Coupled Hydro-Mechanical Simulation of Multi-Phase Fluid Flow in Fractured Shale Reservoirs Using Distinct Element Method

by

Saeed Nazary Moghadam

A thesis submitted in partial fulfillment of the requirements for the degree of

Doctor of philosophy

in

Geotechnical Engineering

Department of Civil and Environmental Engineering
University of Alberta

Abstract

In the present research, a numerical method was developed to solve the equations of motion of coupled hydro-mechanical multi-phase fluid flow through fractured unconventional reservoir rocks with particular application to the simulation of shale reservoirs stimulation by water injection. To this end, a finite volume discrete fracture-matrix approach was developed to numerically formulate flow of immiscible multi-phase fluid, comprised of aqueous and non-aqueous liquids along with dissolved and free gas, through both pore spaces and complex fracture networks. Using this method, compressible multi-phase fluid flow under viscous forces, gravity and interfacial tension was simulated taking into account matrix-matrix, matrix-fracture and fracture-fracture multi-phase fluid transmissibility. An objected oriented C++ code called Finite Volume Black Oil Simulator (FVBOS) was written to implement the developed discrete fracture-matrix approach.

In order to simulate the effects of interaction of solid phase deformation and multi-phase fluid flow, mathematically represented by the coupling between multi-phase flow velocity field and solid phase displacement field in the equations of motion, a novel sequential hydro-mechanical coupling method was developed. In this method, during each time step of fluid flow analysis performed by the discrete fracture-matrix method, aperture and normal stiffness of fractures are iteratively updated based on the displacement field of solid phase obtained by three-dimensional Distinct Element method. The matrix porosity is assumed to be constant during the analyses since the hydro-mechanical coupling is mainly due to the interrelationship between pore fluid pressure and fracture aperture in shale reservoirs. Using distinct element method, fractured porous media is represented

by a densely packed system of blocks separated by complex deformable fracture systems facilitating the simulation of slippage and detachment of intact blocks along and across the fractures. To implement the developed coupled hydro-mechanical multi-phase fluid flow simulation approach, Multi-Phase Discrete Element Simulator (MPDES) was developed by linking FVBOS and 3DEC, Itasca's Three-Dimensional Distinct Element Code, using multi-process programming method.

The coupled hydro-mechanical multi-phase fluid flow through fracture and matrix has not been properly simulated so far in the framework of discrete element approach. In the present research, an enhanced discrete element method was developed to address this shortcoming with particular application to coupled hydro-mechanical modeling of stimulation of shale reservoirs by water injection. The developed computational model makes it feasible to numerically analyze the coupled hydro-mechanical multi-phase fluid flow in both porous matrix and fractures in reservoirs where complex deformable fracture systems are encountered. The developed computational tool paves the way to more sophisticated approaches for the efficiency assessment of hydraulic fracturing and production schemes in shale reservoirs.

Preface

This thesis reflects the authentic intellectual product of the independent research work performed by the author, Saeed Nazary Moghadam, to achieve PhD degree in Geotechnical Engineering under the supervision of Dr. Rick Chalaturnyk at the department of Civil and Environmental Engineering, University of Alberta. Saeed Nazary Moghadam was the principal researcher who was responsible for the development of all the concepts and methodologies behind this research as well as the manuscript composition. Dr. Rick Chalaturnyk was the supervisory author of this research and he was involved throughout the concept formation and manuscript composition. The mathematical formulations, computational codes, numerical models, analytical solutions, data analyses, figures and so forth are developed and compiled by the author. The existing research works utilized in the development of the concepts are cited in the text and mentioned in the reference section at the end of the thesis.

The literature review reflected in chapter 2 and the formulations and concepts presented in chapter 3 for the numerical modeling of discrete solid mechanical problems were based on an extensive study, analysis, clarification and compilation of existing key scientific publications conducted by the author.

The numerical approach presented in chapter 4 has been mathematically formulated by the author enriching the state-of-the-art discrete fracture-matrix methods with the capability of the simulation of compressible multi-phase fluid flow comprised of aqueous and non-aqueous liquids as well as dissolved and free gas through pore spaces and complex fracture networks. The object-oriented C++ computational code Finite Volume Black Oil Simulator (FVBOS) introduced and verified in Chapter 5 has been developed by the author implementing the devised numerical approach.

The concepts behind the coupled hydro-mechanical multi-phase fluid flow simulation approach presented in chapter 6 was developed by the author based on hydro-mechanical coupling of the devised finite volume discrete fracture-matrix approach and distinct element method. The computational tool Multi-Phase Discrete Element Simulator (MPDES) was developed by the author by implementing the devised hydro-mechanical

coupling approach and coupling FVBOS and 3DEC with the aid of multi-process programming.

The source codes of FVBOS and MPDES are not released in this thesis since they are intellectual properties of the author. Instead, in order to demonstrate the general concepts behind the object-oriented programming method used in these codes in a way that can be understood by readers who are not computer programing experts, the C++ code developed by the author for the analytical solution of Buckley-Leverett problem is given in the appendixes. In addition, the most of the 3DEC codes used in MPDES for the simulation of the coupled hydro-mechanical problems discussed in this thesis are given in the appendixes to explain the developed hydro-mechanical approach in more details.

A version of the chapters 2 to 6 has been incorporated into two original research papers that will be submitted in two peer-reviewed journals. In these papers, Saeed Nazary Moghadam is the first and corresponding author and Dr. Rick Chalaturnyk is the second author. In these papers, Saeed Nazary Moghadam was responsible for the development of all the concepts, methodologies, numerical modeling, and manuscript composition. Dr. Rick Chalaturnyk was the supervisory author of these papers and he was involved in the concept formation and manuscript composition.

A version of the chapters 5 and 6 has been incorporated into the following conference paper:

Nazary Moghadam, S., Deisman, N., Zambrano-Narvaez, G., Hazzard, J., Chalaturnyk, R. 2020. Fluid flow model in fractured rock by Finite Volume Black Oil Simulator (FVBOS) and 3DEC. Fifth International Itasca Symposium, Vienna, Austria.

In this paper, Saeed Nazary Moghadam was responsible for the development of all the concepts, methodologies, numerical modeling, and manuscript composition. Dr. Rick Chalaturnyk was the supervisory author of this paper and he was involved in the concept formation and manuscript composition. Dr. Deisman, Dr. Zambrano-Narvaez and Dr. Hazzard were involved in the early stages of concept formation and contributed to manuscript edits.

The author dedicates this thesis to all the brilliant minds who were never appreciated as they deserved in their own time, particularly Dr. Ludwig Boltzmann (1844-1906) and Dr. Alan Turing (1912-1954). Dr. Boltzmann made a substantial contribution to the second law of thermodynamics by interpreting it as a law of disorder and Dr. Turing significantly advanced the theoretical computer science and artificial intelligence.

Acknowledgments

The author of this thesis is profoundly grateful to Dr. Rick Chalaturnyk for supervising this research and for all his supports and constructive ideas. The author is grateful for the detailed and insightful comments and recommendations made by the examination committee members Dr. Richard Wan, Dr. Peichun Tsai and Dr. Renato Macciotta as well as the supervisory committee members Dr. Michael Hendry and Dr. Huazhou Li. The author is also grateful to the chair of the committee Dr. Evan Davies for managing the examination.

The author is deeply thankful to his lovely wife Kimia Nazokkar, his Mother Fatemeh Felezzi Nasiri, his Father Mahmoud Nazary Moghadam and his sisters Samira and Simin Nazary Moghadam for all their encouragements and emotional supports.

The author would like to appreciate Dr. Jim Hazzard, Dr. Gonzalo Zambrano-Narvaez, and Dr. Nathan Deisman for their useful discussions and suggestions during this research.

Finally, the author appreciates the financial and technological supports provided by the sponsors of this research, namely Alberta Innovates, BP, Canadian Natural Resources Ltd., Cenovus Energy, China National Petroleum Corporation, Conoco Phillips, Energi Simulation, Itasca Consulting Group Inc., Nexen-Cnooc, NSERC, Petro China Canada, Shell, Suncor and University of Alberta.

Table of Contents

List of Tables

List of Figures

1 Introduction

1.1 Background and Motivation

Shale formations are constructed from the sedimentation of fine-grained soils mostly containing clay minerals through geological processes under pressure and temperature conditions existing at great depths. During the sedimentation process of some shale formations, considerable amounts of organic substances were buried inside the fine-grained sediments which in turn have been transformed into natural gas and oil. In these shale formations, significant amounts of hydrocarbon resources have been reserved in pore spaces and natural fractures providing a crucial energy resource to deal with the increasing worldwide demand for energy. However, due to the extremely low permeability of shale reservoir rock, unconventional recovery methods are required to make it feasible to extract hydrocarbon resources in these reservoirs (Ma and Holditch, 2015). In shale reservoirs, there exists a complicated pore structure with multi-scale pore size where fluid transfer is performed through different flow mechanisms comprising of desorption and diffusion in intact shale blocks as well as viscous flow in fractures (Javadpour et al., 2007; Javadpour, 2009). Despite the ultralow permeability of intact shale blocks, there exist natural fractures in shale formations with proper permeability to transmit water, oil and gas. However, although complex natural fracture systems exist in shale reservoirs, these fractures are not properly interconnected to effectively enhance the low permeability of shale formations (Ma and Holditch, 2015).

Recently, unconventional methods have been introduced to partly extract the hydrocarbon resources existing in shale layers. These methods mostly involve horizontal drilling of wellbores together with multi-stage hydraulic fracturing through the wellbores (Nicot and Scanlon, 2012). In the process of hydraulic fracturing in shale formations, fracturing fluid, which is a combination of proppant and chemicals, is injected into the formation increasing pore pressure which in turn leads to the creation of hydraulic fractures in shale formations (Ma and Holditch, 2015). These induced hydraulic fractures yield the enhancement of the connectivity of existing fracture systems. This process yields the release of oil and natural gas hindered in pore spaces and directs the released

hydrocarbon towards the production wellbores. In this process, multi-stage hydraulic fracturing is performed along horizontal wellbores to induce hydraulic fractures over a significantly large area in shale reservoirs providing several flow paths with relatively high permeability. Using this method, in addition to the creation of hydraulic fractures, existing natural fractures are connected to the hydraulic fractures producing large highly conductive fracture network system. The created highly conductive area makes it feasible to economically extract the oil and natural gas in shale layers (Warpinski et al., 2009). The region covering the most of highly conductive flow paths provided by the large fracture network system is termed as stimulated reservoir volume (SRV) while the remaining zone where the hydraulic fracturing cannot effectively ameliorate hydraulic conductivity is termed as un-stimulated reservoir volume (USRV). The efficiency of production in shale reservoirs is highly dependent on the extent and hydraulic characteristics of SRV that are relied on the geomechanical attributes of the formation and operation condition (Mayerhofer et al., 2006; Ozkan et al., 2009).

Performing experimental and field studies on the coupled hydro-mechanical fluid flow in fractured shale reservoirs is burdensome and costly, since there exist extreme uncertainty and complexity in these formations. Therefore, in order to assess the efficiency of hydraulic fracturing and production performance in naturally fractured shale reservoirs, it is vitally important to develop numerical models to analyze the geomechanically coupled fluid flow in these formations during both hydraulic fracturing and depletion processes, considering the slippage and detachment of intact blocks as well as complex deformable fracture networks. Such a numerical model provides an economical approach to propose an efficient hydraulic fracturing and production scheme. It also makes it feasible to analyze the probable risks during hydraulic fracturing and production. In shale reservoirs, compressible multi-phase fluid flow through both pore spaces and complex fracture networks is existing during both hydraulic fracturing and depletion. However, in the majority of numerical investigations on fluid flow through fractured porous media, either fluid transfer at matrix-fracture contacts has not been accurately dealt with (Barenblatt et al., 1960; Snow, 1965; Kazemi et al., 1969; Damjanac 1996), or complex fracture networks and compressibility of multi-phase fluid have been neglected (Karimi-Fard et al., 2004; Sandve et al., 2012; Liu et al. 2016; Khoei et al., 2016). In this research, these shortcomings have been addressed by developing a numerical model of coupled

hydro-mechanical multi-phase fluid flow through both pore spaces and complex deformable fracture networks.

1.2 Problem Statement

In shale reservoirs, the efficiency of hydraulic fracturing treatment and production performance is highly dependent on the extent and hydraulic behavior of stimulated reservoir region. Although, in theory, large stimulated regions containing interconnected fracture networks can be created by hydraulic fracturing process, it does not necessarily yield a practical production strategy due to the fact that the existing pressure gradient might not effectively yield the expected production performance. Hence, thorough numerical simulations of multi-phase fluid flow through both pore spaces and complex fracture networks existing in shale reservoirs are required to ensure an efficient production in shale reservoirs. Also, due to the interrelationship between pore fluid pressure and two major geomechanical parameters, namely porosity of intact matrix and fracture aperture, there exists hydro-mechanical coupling in the equations of motion governing the velocity, stress and pressure fields in solid and fluid phases which should be taken into account in the numerical simulations.

Moreover, as it is schematically shown in Figure 1, fracturing fluid leakoff into porous matrix and natural fractures has a significant effect on the hydraulic properties and the extent of SRV. The fracturing fluid leakoff is a multi-phase fluid flow governed by fluid pressure gradient, viscous frictional forces, gravity, interfacial tension as well as geomechanical stress field and constitutive behavior which further emphasizes the vital role of the numerical simulation of coupled hydro-mechanical multi-phase fluid flow in fractured shale reservoirs. In particular, since the highly permeable large-scale fractures dominate the fluid flow in fractured shale reservoirs, these fractures should be explicitly modeled in the numerical analyses.

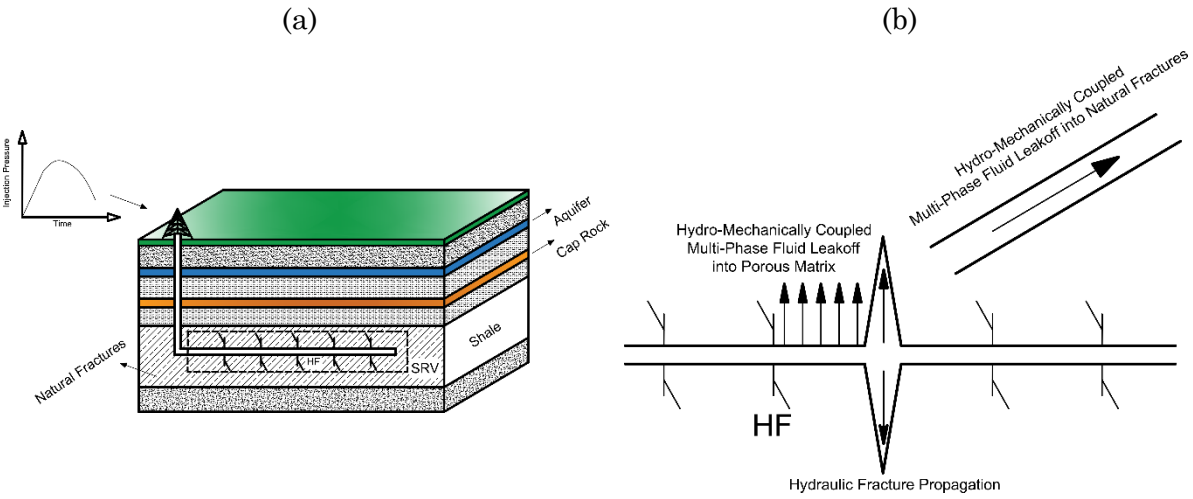

Figure 1: Hydraulic fracturing in shale reservoirs.
(a) Stimulated reservoir volume (b) Hydraulic fracturing fluid leakoff.

1.3 Research Objective and Scope

Experimental and field investigations on the efficiency of hydraulic fracturing treatment and production performance in fractured shale reservoirs are costly and troublesome due to the inherent complication and uncertainty existing in the governing multi-physics processes and geological features. Therefore, developing reliable numerical models is crucial to economically tackle such complex issues. In particular, numerical simulation of coupled hydro-mechanical multi-phase fluid flow through both pore spaces and complex deformable fracture networks plays a vitally important role in the efficiency assessment of hydraulic fracturing and production in shale reservoirs. Although such numerical modeling is highly demanded by the industry, it has not been fully developed to comprehensively take into account the multi-physics processes governing the fluid flow. The primary objective of this research is to develop a computational coupled hydro-mechanical tool addressing this shortcoming. To achieve this primary goal, the following specific objectives have been met:

- A novel numerical method compatible with discrete element method has been formulated to solve the equations of motion governing the multi-phase fluid flow through pore spaces and complex fracture networks. In the numerical formulation, the effects of different agents such as pressure gradient, viscous frictional forces, gravity and interfacial tension on the movement of compressible multi-phase fluid

comprising of aqueous and non-aqueous liquids and dissolved and free gas are taken into account.

- A computational code was then developed to implement the devised numerical formulation based on the object-oriented programming making the code flexible to be upgraded and incorporated in other computational codes.
- In order to account for the influence of displacement field in discontinuous solid phase on the multi-phase flow, a novel hydro-mechanical coupling approach was developed in the framework of discrete element approach capable of simulating the effects of deformation of complex fracture networks.
- Using the coupling approach, the developed computational code for the fluid flow was hydro-mechanically coupled with 3DEC, ITASCA's Three-Dimensional Distinct Element Code, using multi-process programming method.
- Finally, the unique capability and application of the developed coupled hydro-mechanical multi-phase discrete element simulator in modeling stimulation of fractured shale reservoirs by water injection has been demonstrated.

The major focus of this research is to develop a computational tool for the simulation of coupled hydro-mechanical multi-phase fluid flow through fractured formations in general and shale reservoirs in particular during the stimulation of reservoir by water injection. In this research, it is also demonstrated how the developed computational tool can be utilized to evaluate the effectiveness of stimulation of fractured shale reservoirs by water injection. However, detailed hydraulic fracturing and production efficiency assessment are out of the scope of this research. In addition, simulation of thermal effects on fluid flow as well as simulation of the effects of stress singularity at fractures tips and surface energy developed by fracture propagation on fracture initiation and propagation are out of the scope of this research.

1.4 Methodology and Thesis Outline

As it was discussed in the previous sections, currently, there exists a lack of numerical models capable of simulating coupled hydro-mechanical multi-phase fluid flow through porous matrix and complex deformable fracture networks taking into account matrix-matrix, matrix-fracture and fracture-fracture multi-phase fluid transfer. In this research, a numerical method is developed to address this shortcoming.

By only considering mass transport and neglecting thermodynamic processes, this multi-physics problem is approached by numerical formulation of two sets of equations of motion governing the velocity and pressure field in multi-phase fluid as well as displacement field in solid phase. Due to the interrelationship between the fluid flow velocity field and displacement field in solid phase, the two sets of equations of motion are coupled and cannot be solved independently. Such coupled equations of motion can be solved simultaneously using fully coupled approach. Another solution method is sequential coupling approach in which each sets of equations are solved in separate sequences by fixing the major unknown parameters of the other equation sets. These sequences of temporarily uncoupled solutions can be iteratively performed to target the convergence of coupled parameters in the equation sets satisfying a predefined tolerance. Fully coupled approach provides a more stable solution and more accurately takes into account the multi-physics processes involved in the problem compared to sequential coupling method. However, in order to utilize fully coupled approach, the computational source code of both solid phase and fluid phase are needed. Since developing a computational code for the numerical solution of equations of motion of solid phase is out of the scope of this research, and since it is not feasible to have an access to the computational source code of commercial solid mechanical simulators, sequential coupling approach is used in this research.

One of the major focuses of this research is to simulate coupled hydro-mechanical fluid flow through complex deformable fracture systems existing in fractured shale formations. To manage the simulation of such fracture systems, complex dynamic discontinuities are taken into account in the equations of motion of solid phase. For this purpose, the solid phase is modeled as a system of densely packed discrete blocks separated by a complex system of contact planes. Proper constitutive equations are also assigned to the contact planes to evaluate normal and shear displacements of the points located on the contact planes as a function of normal and shear stresses of these points. In order to numerically solve the equations of motion of solid phase represented by the model described above, discrete element method is utilized. To this end, 3DEC, Itasca's 3-Dimensional Distinct Element Code, was employed to numerically solve the equations of motion of discontinuous solid phase during the sequences of hydro-mechanical coupling.

Another principal focus of this research is to simulate the fluid flow through both pore

spaces of discrete porous matrix blocks and complex deformable fracture networks. To this end, a unified grid system discretizing both porous matrix and complex fracture systems is utilized. In order to simulate fluid flow considering such complex geometry, the integral form of equations of motion of fluid flow is discretized using finite volume method. In addition, the matrix-matrix, matrix-fracture and fracture-fracture fluid transmissibility in the unified grid system is dealt with discrete fracture-matrix approach. Consequently, a finite volume discrete fracture-matrix method is formulated in this research to numerically solve the equations of motion of fluid flow through both porous matrix and fractures. The developed finite volume formulation is compatible with discrete element solid mechanical computational codes. With the aid of such compatibility, a novel coupled hydro-mechanical computational approach was developed in this research by sequential coupling of distinct element solid mechanical simulation method and the developed finite volume discrete fracture-matrix fluid mechanical simulation approach.

As it is schematically shown in Figure 2, the developed coupled hydro-mechanical method is comprised of the three dimensional distinct element model of fractured rock formation, finite volume discrete fracture-matrix model of fluid flow taking into account matrix-matrix, matrix-fracture and fracture-fracture multi-phase fluid transfer, highly complex discrete fracture networks and sequential hydro-mechanical coupling method.

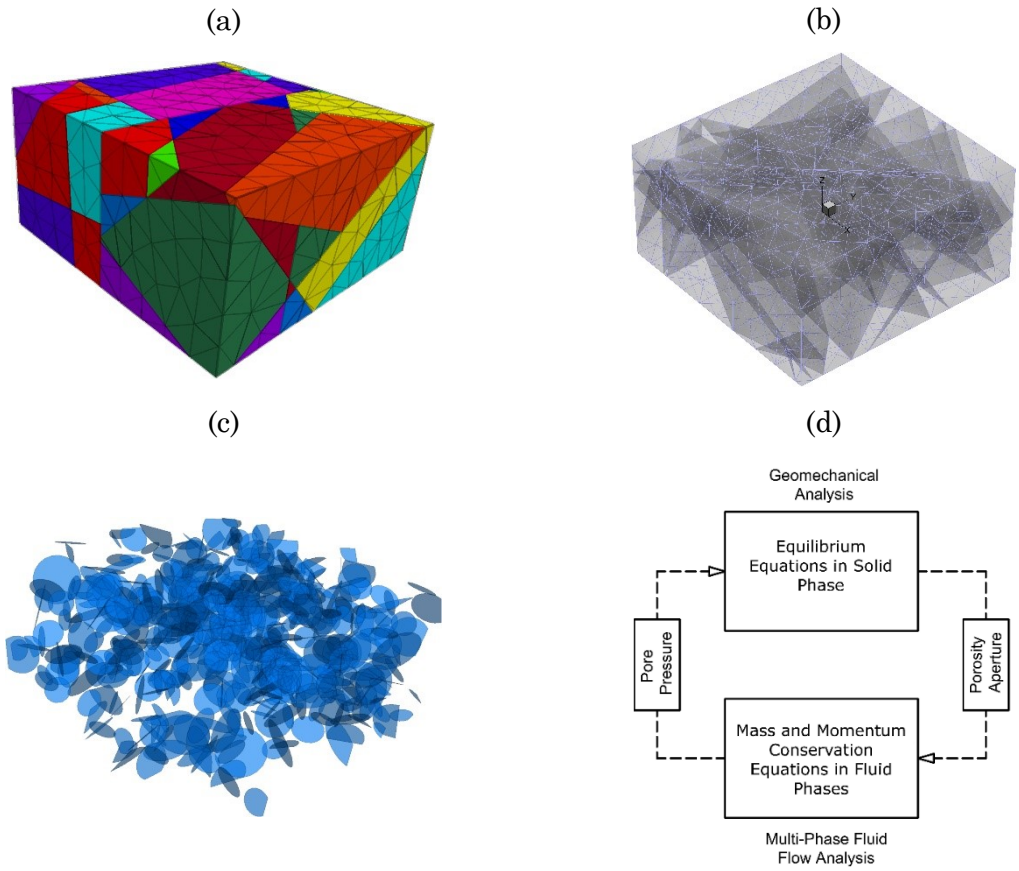

Figure 2: Conceptual numerical model of coupled hydro-mechanical multi-phase fluid flow in fractured shale reservoirs.
(a) Distinct element model of solid phase in fractured reservoir (b) Finite volume discrete fracture-matrix model of fluid phase (c) Discrete fracture network representing fractures and joints existing in the rock formation (d) Sequential coupling approach.

Although the developed computational method is capable of simulating porosity changes in the coupled hydro-mechanical analyses, the major focus of this research is to merely account for aperture change in the analyses. This is due to the fact that the porosity change occurring by pore fluid pressure change is negligible relative to aperture change in fractured shale reservoirs. Therefore, it is assumed that the interrelationship between pore fluid pressure and fracture aperture is the major reason behind hydro-mechanical coupling in shale reservoirs. In the sequentially coupled hydro-mechanical simulations presented in this research, first, the equations of motion of fluid flow through both porous matrix and fracture system is numerically solved using the developed finite volume discrete fracture-matrix approach. Then, the velocity and stress field in the solid phase is determined under the pore fluid pressure updated in the previous sequence using distinct

element method to calculate the fractures apertures. These two sequences can be iteratively performed until a convergence between the pore fluid pressure fields in two consecutive iterations is detected.

This research is also primarily aimed at the numerical simulation of immiscible multi-phase fluid motion taking into account various agents that significantly influence fluid flow in fractured porous media, namely gravity, pressure gradient, viscous frictional force, and interfacial tension. To this end, it is assumed that the multi-phase fluid is comprised of aqueous liquid, none-aqueous liquid and gas which is either free or dissolved in the aqueous and none-aqueous liquids. By assuming that inertial force is negligible relative to other agents in fluid flow through fractured porous media, the momentum conservation equation and constitutive law for the fluid flow through porous matrix and fractures can be respectively simplified into Darcy's law and Reynolds equations. It is also assumed that the effects of interfacial tension can be experimentally approximated by the concepts of relative permeability and capillary pressure. The thermodynamic effects on the multi-phase fluid flow are neglected in this research.

In order to achieve the objectives defined in this research, in the second chapter of this thesis, a brief study is carried out on the state-of-the-art investigations on the reservoir simulation of unconventional formations, numerical simulation of coupled hydro-mechanical multi-phase fluid flow through fractured porous media and hydraulic fracturing. In particular, the capabilities and deficiencies of different numerical approaches in the simulation of coupled hydro-mechanical multi-phase fluid flow are discussed. In this chapter, the exceptional capabilities of distinct element method in dealing with complex deformable fracture systems and its deficiencies in handling multi-phase fluid flow through both pore spaces and fractures are clarified.

In the third chapter of this thesis, a concise study is carried out on the formulation of equations of motion of solid phase with the aim of comprehending the essential concepts behind the distinct element method. Such a theoretical study on the distinct element method plays a vitally important role in the numerical formulation of equations of motion of fluid phase so that it can be compatible with distinct element model of solid phase for the purpose of hydro-mechanical coupling. To this end, kinematics, kinetics and constitutive modeling of a system of discrete blocks separated by complex contact plains

are studied. In particular, rigid body motion of system of blocks, contact detection and updating algorithms as well as constitutive modeling of contacts used in distinct element method are studied.

In the fourth chapter of this thesis, a novel numerical method is formulated using finite volume method by implementing compressible multi-phase fluid flow into discrete fracture-matrix approach. With this aim, first, the equations of motion of single-phase fluid is derived. These equations are then generalized for multi-phase fluid comprising of aqueous and none-aqueous liquids as well as free and dissolved gas. Then, a finite volume discrete fracture-matrix approach is formulated using Gauss's theorem and numerical integration of the derived partial differential equations of motions of multi-phase fluid flow through fractures and porous matrix. The developed finite volume discrete fracture-matrix approach is capable of discretizing porous matrix and complex fracture networks in a unified system of Eulerian mesh generated and updated based on the current Lagrangian distinct element mesh of the solid phase. The developed computational approach for the simulation of multi-phase fluid flow through fractured porous media is compatible with distinct element model of solid phase in the fractured porous media for the purpose of hydro-mechanical coupling.

In the fifth chapter of this thesis, a C++ computer code is developed based on the devised finite volume discrete fracture-matrix approach using object-oriented programming method. Using the object-oriented programming method, the structure of the developed C++ code is designed based on a data structure called class. The defined classes provide the blue print of objects which can be created in the program to deal with different tasks such as processing the data related to grids, material models, initial and boundary conditions along with the numerical solution of equations of motion by the developed finite volume discrete fracture-matrix approach. Such programming method makes it feasible to share object files of different classes of the program with other software developers to be used in different computational codes without any need for being involved in the detailed source codes. The inheritance concept in object-oriented programing also enables the developed classes to be upgraded by adding new member functions and variables to the existing classes to implement new algorithms without being involved in the source codes of the classes.

The accuracy and capabilities of the developed multi-phase fluid flow simulation code are investigated through a comprehensive verification procedure. To this end, the performance of the computational code in simulating different agents affecting the multi-phase fluid flow through fractured porous media is separately assessed through numerical simulation of various benchmark problems. The numerical simulation results are compared to the available theoretical solutions, simplified numerical solutions as well as a widely-used reservoir simulation software. Then, the performance of the developed code in dealing with the numerical simulation of multi-phase fluid flow through porous matrix and complex fracture networks is assessed.

In the sixth chapter of this thesis, a novel coupled hydro-mechanical multi-phase fluid flow simulation approach was developed. In this method, the equations of motion of multi-phase fluid flow through porous matrix and complex fracture networks are numerically solved by the devised finite volume discrete fracture-matrix approach while the distinct element method is utilized to solve the equations of motion of the solid phase in fractured porous media hosting the multi-phase fluid. Then, multi-process programming was utilized to develop a multi-phase discrete element computational tool by coupling the developed coupled hydro-mechanical multi-phase simulation code with 3DEC.

The performance of the multi-phase discrete element computational tool is assessed by numerical simulation of coupled hydro-mechanical multi-phase fluid flow through fractured porous media. In particular, the effects of multi-phase fluid properties and fluid leak off into porous matrix during the stimulation of fractured reservoirs by water injection is investigated. The capabilities of the developed multi-phase discrete element computational tool in numerical simulation of coupled hydro-mechanical multi-phase fluid flow through highly complex deformable fracture networks and discrete porous matrix blocks is also demonstrated. In particular, it is shown how the capabilities of the developed computational tool can be utilized to evaluate the effectiveness of stimulation of fractured reservoirs performed by water injection. It is also demonstrated that the effectiveness of the stimulation process strongly relies on the connectivity of fracture networks as well as geomechanical effects reflected in displacement field in solid phase which is governed by the geomechanical constitutive model and boundary and initial conditions.

In the seventh chapter of this thesis, a short summary of the different stages and principal concepts of this research are given. Then, the capabilities of the developed coupled hydro-mechanical multi-phase fluid flow computational tool are briefly discussed. At the end of this chapter, concluding remarks are made and future research subjects are proposed to further develop the new pathway initiated by the present research in the reservoir simulation of fractured formations.

2 Literature Review

In hydraulically fractured shale reservoirs, there exists multi-phase fluid flow through the pore spaces in intact shale matrix and complex fracture networks (Guo, 2014). In this regard, multiple porous media contribute in the transfer and storage of multi-phase fluid, namely hydraulic fractures, natural fractures and pores in the inorganic and organic constituents (Loucks et al., 2009; Wang and Reed, 2009; Sondergeld, 2010; Curtis et al., 2012; Sakhaee-Pour and Bryant, 2015). Due to the existence of Nano-scale pore spaces in intact shale matrix, different transport mechanisms govern fluid flow in fractured shale reservoirs, e.g. desorption, diffusion and viscous flow. All these transfer mechanisms cannot be comprehensively simulated only by Darcy's law (Javadpour et al., 2007; Shabro et al., 2009). It is also worth mentioning that the wettability of shale matrix cannot be simply defined since it exhibits a mixed behavior including both hydrocarbon and water wet attributes (Xu and Dehghanpour, 2014). Another complexity in characterizing multi-phase fluid flow in fractured shale reservoirs is that the hydraulic properties of fractures are dependent on the fracture roughness and stresses applied on the fracture surface (Babadagli et al., 2015). Taking into account these issues, multi-phase fluid flow through fractured shale reservoirs has not been properly apprehended so far.

2.1 Parameters Affecting Production in Shale Reservoirs

Simulation of fluid flow through fractures and matrix is vitally important in the performance assessment of horizontal wells in hydraulically fractured shale gas reservoirs. With this aim, Xu et al. (2015) developed a semi-analytical model in which three different fluid flow mechanisms, namely desorption, diffusion and viscous flow, were considered. In this model, it was assumed that the shale gas reservoir is comprised of two regions, i.e. SRV and USRV, reflecting two different reservoir characteristics and the discontinuity effects were approximated in a continuum mechanics framework. Afterwards, the developed model was employed to carry out sensitivity analyses on the production performance of hydraulically fractured shale gas reservoirs as a function of different uncertain parameters, namely SRV radius, SRV permeability, geomechanical stress effects and hydraulic fractures conductivity.

It was demonstrated that although creating larger SRV significantly improves the productivity of horizontal wells, it does not necessarily yield more optimized production scheme. This is due to the fact that in the depletion stage, the pressure gradient cannot effectively influence the whole SRV region. Also, analyzing the effects of geomechanical stress highlighted its significant influence on the production of shale gas reservoirs which was also admitted by many researchers (Cho et al., 2013; Franquet et al., 2004; Gutierrez et al., 2000). Furthermore, hydraulic fractures conductivity and SRV permeability were another effective geomechanical parameters in the production of shale gas reservoirs as it was manifested by other researchers (Yu et al., 2014; Wen et al., 2007). Overall, this sensitivity study bears in mind that an optimized hydraulic fracturing strategy can be developed based on the evaluation of production relative to the cost of hydraulic fracturing treatment.

The conductivity and geometry of hydraulic fractures in SRV have a significant effect on the production in multi-stage hydraulically fractured shale gas reservoirs. These parameters are considerably influenced by geomechanical characteristics of the formation and hydraulic fracturing operation conditions. Considering the geomechanical features of the formation, the geometrical parameters of hydraulic fractures, namely fracture spacing, fracture length and fracture angle, can be controlled to achieve more efficient hydraulic fracturing treatment (Kaiser, 2012). In this regard, Liu et al. (2015) developed an analytical model to investigate the effects of hydraulic fractures geometry on the production of shale gas reservoirs. In this model, a dual porosity continuum system representing both porous matrix and fractures was utilized in which energy loss along hydraulic fractures, desorption, adsorption, viscous flow and geomechanical stress effects were taken into account. Using this model, the influence of fracture conductivity, fracture distribution, fracture spacing and fracture length on the effectiveness of hydraulic fracturing was studied through a series of parametric analyses. It was shown that there exists an optimum conductivity for the production operation depending on the shale gas reservoir features. Analyses results indicated that when more fractures are concentrated near the lateral portion of wellbore, shale gas production rate is higher. It was also demonstrated that longer fractures yield higher gas production rate. In particular, by increasing the fractures length near the lateral portion of the well, gas production rate remarkably rises compared to the case where the middle fractures are longer. It can be

concluded that production rate is more affected by the lateral fractures than central fractures and the length of lateral fractures is the chief geometrical parameter affecting the shale gas production rate. Consequently, in hydraulic fracturing operation, it is more efficient to create denser and longer lateral fractures.

2.2 Coupled Hydro-Mechanical Multi-Phase Fluid Flow Simulation

Simulation of geomechanically coupled multi-phase fluid flow consisting of either fluids with different states, i.e. liquid and gas, or immiscible fluids with different chemical properties, e.g. oil and water, is the foremost research subject in petroleum engineering (Chalaturnyk et al. 1992; Chalaturnyk and Scott, 1995; Li and Chalaturnyk, 2007; Azad and Chalaturnyk, 2012, Khoie, et al., 2016; Liu et al, 2016). In particular, extensive investigations have been dedicated to numerically simulate the transport of multi-phase fluids in fractured porous media with particular application to oil and gas production.

In order to model multi-phase fluid flow in fractured porous media, different approaches have been developed, namely equivalent continuum methods, dual porosity methods and Discrete Fracture-Matrix (DFM) methods. In equivalent continuum methods, fluid flow through fractured porous media is analyzed in an equivalent porous matrix where the effects of fractures are taken into account by postulating an equivalent anisotropic permeability (Snow, 1965). In dual porosity methods, fluid flow is formulated in a dual-porosity continuum domain where matrix and fracture system are represented as two continuum porous media (Barenblatt and Zheltov, 1960; Kazemi et al. 1969). In this method, two independent pressure fields are assumed for matrix and fracture system and the fluid exchange between these two media are considered as source or sink terms in the governing equations of each pressure field.

The deficiency of equivalent continuum and dual porosity methods is highlighted when there exist large-scale fractures dominating fluid flow (Wong et al., 2020). In these circumstances, due to the significant difference between permeability of fractures and matrix, it is essential to explicitly simulate the dominating fractures along with the matrix. To address these issues, DFM methods are applied to explicitly model the fluid flow through matrix and a system of interconnected fractures, considering matrix-matrix, matrix-fracture and fracture-fracture fluid transport (Noorishad and Mehran, 1982;

Karimi-Fard et al., 2004; Sandve et al., 2012; Lie, 2016).

Numerical simulation of hydro-mechanically coupled fluid flow in fractured porous media can be performed by three major coupling methods, namely one-way coupling, sequential coupling and full coupling methods. In one-way coupling method, at each time step of fluid flow analysis, the porosity and permeability of porous media are updated under the current pore fluid pressure using geomechanical analyses but no convergence between geomechanical and fluid flow analyses is targeted in terms of pore pressure, porosity and permeability. In contrast, in sequential coupling method, an iterative analysis is performed on both geomechanics and fluid flow until a convergence between these two analyses is obtained (Zienkiewicz et al., 1988; Chalaturnyk et al. 1992). In fully coupled methods, the coupled equations of motion for both solid and fluid phases are formulated in terms of velocity or displacement in solid phase and velocity or pressure in fluid phase. Then, these coupled equations are solved simultaneously (Khoei, et al., 2016).

It is worthwhile to mention that the hydro-mechanical coupling is mainly due to the interrelationship between pore fluid pressure and two major geomechanical parameters, namely porosity of intact matrix and fracture aperture. Therefore, in coupled hydro-mechanical analyses in fractured porous media, the effects of change in both matrix porosity and fracture aperture should be considered based on the physics of the problem. Another issue in the geomechanically coupled multi-phase fluid flow in fractured porous media is the definition of overall pore pressure and effective stress considering the fact that the pressure in fluid phases might be unequal due to surface tension and capillary effects. In this regard, different methods are proposed to define the pore pressure. For instance, the pore pressure can be assumed to be equal to the pressure in the wetting fluid phase or it can be defined in terms of saturation-based weighted average of pressures in different fluid phases. Alternatively, in more sophisticated analyses, the saturation-based weighted average definition of pore pressures can be modified by considering surface tension and capillary effects (Rutqvist et al., 2002; Minkoff et al., 2003; Kim et al., 2013).

In shale reservoirs, conducting experimental and field investigation on the influence of complicated discontinuities, including fracture networks and bedding planes, on multi-phase fluid flow is problematic. This is due to the restricted accessibility to the formation

as well as severe complication, uncertainty and variability existing in governing physical processes, geomechanical features, and so forth. In these circumstances, numerical modeling plays a vitally important role to better understand the Multi-physics processes governing the coupled hydro-mechanical multi-phase fluid flow through fractures, bedding planes and pore spaces of shale reservoirs. In such numerical modeling, the coupled equations of motion governing the velocity, stress and pressure fields in solid and fluid phases should be formulated so that the slippage and detachment of intact blocks along and across discontinuities as well as complex dynamic spatial configuration of fractures can be simulated. In this regard, numerical methods developed based on conventional Finite Element Method (FEM) cannot properly deal with such complicated problems.

Alternatively, in Distinct Element Method (DEM), mechanical behavior of fractured porous media can be simulated as an assemblage of discrete porous blocks separated by complex contact planes. In this method, the constitutive behavior of the discontinuities is defined using distributed stiffness, viscous and plastic slider elements at the blocks contacts. Then, by utilizing efficient contact detection and updating algorithms, the governing dynamic equations of motion of the system are formulated by DEM with no need for mesh updating (Owen and Hinton, 1980; Crisfield, 1991; Bathe, 1996; Zienkiewicz and Taylor, 2005; Jing and Stephansson, 2007; Nazary Moghadam et al., 2012; Nazary Moghadam et al., 2013; Nazary Moghadam et al., 2015). Using this method, any constitutive behavior can be assumed for the discrete blocks and contacts in the framework of large deformation. Indeed, the difficulties of conventional Finite Element Method in dealing with complex dynamic discontinuities are resolved by utilizing effective contact detection and updating algorithms developed based on discrete mathematics, such as graph theory and combinatorial topology, as well as properly defined data structure (Cundall, 1988; Hart et al., 1988; Zienkiewicz and Taylor, 2005; Jing and Stephansson, 2007).

Three-dimensional distinct element method and the computer code 3DEC were introduced by Cundall (1971, 1988) and Hart et al. (1988) to analyze discontinuous rock mechanics problems. In this method, fractured rock domain is simulated by a discrete system of polyhedral deformable blocks which are separated by interfaces or contacts representing discontinuities, e.g. fractures and joints. This method is capable of

effectively storing, updating and applying the data representing the contacts and the blocks, namely faces, edges, vertexes and so on. The successful application of distinct element method has been proven by numerous research works (Deisman et al., 2010; Khazaei et al., 2015; Shilko et al. 2015; Le et al. 2016).

The numerical formulation for the analysis of coupled hydro-mechanical equations of motion for single-phase fluid passing through the fractures has been developed and implemented in 3DEC software (Damjanac, 1996; Itasca Consulting Group, Inc., 2016). However, such numerical formulation has not been properly developed for the simulation of multi-phase fluid flow, fracture-matrix fluid transfer and large displacements. Moreover, the effects of stress singularities at fracture tips as well as strain energy release leading to surface energy development on fracture initiation and propagation have not been formulated in this method so far. In particular, since multi-phase fluid flow through both fractures and matrix is existing in shale reservoirs during both hydraulic fracturing and depletion processes, it is essential to develop DEM for the case of multi-phase fluid flow.

2.3 Numerical Simulation of Hydraulic Fracturing in Unconventional Reservoirs

With the aim of modeling fluid flow through fractures and hydraulic fracturing, Bazant and Ohtsubo (1978) utilized finite element method. However, in the research works carried out by Peirce and Siebrits (2005), it is demonstrated that frequent mesh updating around the fractures is required to track the fracture propagation trajectory in finite element method. To avoid such frequent mesh updating, Lecampion (2009) employed the Extended Finite Element Method (XFEM) to simulate hydraulic fracturing. However, in case the fracture propagation trajectories are not predictable before starting the analyses, extended finite element method needs very fine mesh which makes this method numerically expensive. It should also be mentioned that finite element and extended finite element methods are not efficient to simulate problems where fracture propagation and fracture systems are highly complicated (Hu et al., 2014).

Pine and Cundall (1985) presented one of the original implementations of DEM in the simulation of hydraulic fracturing in rock formations. In that research, geomechanically coupled single-phase fluid flow through rock joints was modeled based on cubic law for

fluid flow through parallel impermeable planes by neglecting the stress singularities at fracture tips, released strain energy and surface energy developed by fracture propagation in the rock mass (Griffith, 1921). Recently, numerical simulations of hydraulic fracturing in rock formations and the resulting micro-seismicity have been effectively performed using 3DEC (Savitski et al., 2013; Zhang et al., 2015).

In DEM, discontinuity planes extend to the boundaries of the surrounding domain. Therefore, fractures with limited extent cannot be defined directly in a block. To approach this issue, different material properties, i.e. shear stiffness, normal stiffness, cohesion and friction angle, can be assigned to different parts of discontinuity planes so that some parts of the plane behave as fractures and some parts as intact rock. In addition, by assigning appropriate material properties and failure criteria to intact parts of the discontinuity planes, fracture initiation and propagation can be simulated along these planes. In particular, fracture propagation in an arbitrary direction can be modeled in a system of blocks provided that adequate number of discontinuity planes with proper intact material properties are defined (Damjanac and Cundall, 2016).

It is also worth mentioning that to mitigate both the deficiencies of FEM and the numerical costliness of DEM in modeling fracture systems, the hybrid Finite-Discrete Element Method was proposed by Munjiza et al. (1995). In hybrid Finite-Discrete Element Method, DEM is utilized to explicitly model complex fracture systems in critical regions, e.g. near-field regions, while other areas, e.g. far-field areas, are simulated using the equivalent continuum FEM model. However, hydro-mechanical coupling has not been properly addressed in the hybrid method so far.

In an article by Hoek and Martin (2014), it is demonstrated that numerical methods developed based on DEM in which the intact rock is represented by a system of grains with well-defined grain size distribution and constitutive behavior at the joints (Cundall and Strak, 1979) are capable of simulating highly complex fracture propagation mechanisms in rocks. Therefore, Distinct Element Method implemented in the software 3DEC, Discontinuous Deformation Analysis (DDA) and Particle Discrete Element Method implemented in the computer code PFC provide promising methods to deal with such problems (Hoek and Martin, 2014; Morgan and Aral, 2015; Wang et al., 2014). Based on this concept, virtual contacts can be utilized in three-dimensional distinct element

method to simulate fracture initiation and propagation. In this method, the intact rock blocks are separated into multiple discrete blocks by virtual joints representing complex potential fracture trajectories in intact rock. Then, proper constitutive properties and failure criteria are assigned to these joints so that this system of tetrahedral blocks behaves as intact rock. Also, three-dimensional discrete fracture networks (DFN) can be stochastically generated based on the parameters fracture persistence, fracture spacing and fracture orientation to represent the existing natural fractures. If the stress state at any points in the virtual joints reaches the critical value defined by the failure criteria, tensile or shear failure occurs, and fractures initiate and develop at those points. Also, by using this method in the simulation of hydraulic fracturing, SRV can be defined based on the area of rock mass where virtual joints are failed due to the increase in the fluid pressure. Such numerical models can be employed to analyze the effects of different parameters such as in situ stresses, fracture fluid properties, injection rate, rock material properties, natural fractures and so forth on the effectiveness of the hydraulic fracturing treatment (Hamidi and Mortazavi, 2014; Zanganeh et al., 2015).

To sum up, three-dimensional distinct element method provides a capable numerical method to simulate coupled hydro-mechanical multi-phase fluid flow in fractured shale reservoirs considering complicated hydraulic fractures initiation and propagation, slippage and detachment of blocks, and complex dynamic spatial configuration of fractures. However, such numerical model has not been properly developed so far to account for the multi-phase fluid flow, matrix-fracture fluid transfer, stress singularities at fracture tips, released strain energy and developed surface energy during fracture propagation as well as large displacements during fluid flow analysis.

3 An Overview of Numerical Simulation of Systems of Discrete Deformable Blocks by Distinct Element Method

3.1 Kinematics of Rigid Body Motion

In the formulation of equations of motion for discontinuum body represented by an assemblage of rigid blocks, a relative local coordinate system together with the global inertial coordinate system is utilized. As it is shown in Figure 3, the time derivative of an arbitrary vector field F can be obtained considering a local relative coordinate system x', y', z' rotating by an angular velocity ω.

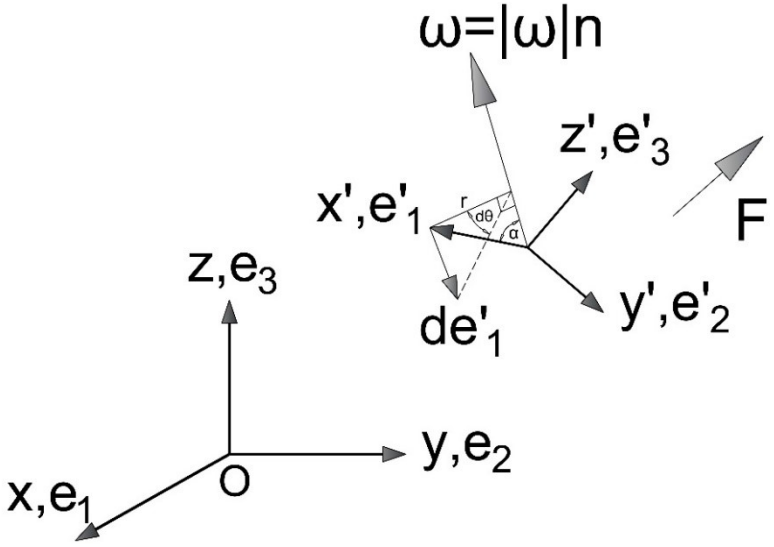

Figure 3: Time variation of the basis vectors of local coordinate system rotating relative to inertial coordinate system.

To this end, the time change of the basis vector e_1' of the relative coordinate system is derived as follows (Spencer, 2004; Reddy, 2007; Belytschko et al., 2013):

$$r = |e_1'| \sin \alpha \qquad \text{Eq. 1}$$

$$de_1' = \frac{\omega \times e_1'}{|e_1'||\omega| \sin \alpha} r d\theta = \frac{\omega \times e_1'}{|e_1'||\omega| \sin \alpha} |e_1'||\omega| \sin \alpha \, dt = \omega \times e_1' dt \qquad \text{Eq. 2}$$

This relation can be extended for every basis vector of relative coordinate system as

$$\frac{de_i'}{dt} = \omega \times e_i' \qquad \text{Eq. 3}$$

Therefore, the time derivative of an arbitrary vector field F defined in the relative coordinate system is achieved as follows:

$$F = f_i e_i' \qquad \text{Eq. 4}$$

$$\frac{dF}{dt} = \frac{df_i}{dt} e_i' + \frac{de_i'}{dt} f_i \qquad \text{Eq. 5}$$

$$\frac{dF}{dt} = \frac{df_i}{dt} e_i' + \omega \times f_i e_i' \qquad \text{Eq. 6}$$

$$\frac{dF}{dt} = \frac{\partial F}{\partial t} + \omega \times F \qquad \text{Eq. 7}$$

Using the above relation, the time derivation of any arbitrary vectors defined in the relative coordinate system can be obtained. To formulate the equations of motion of rigid blocks, the acceleration of an arbitrary point located in the block should be derived in the global inertial coordinate system. Using the relative rotating coordinate system, the acceleration of any arbitrary point located in the block can be calculated based on the position vector of the point relative to local coordinate system as well as the position vector of the origin of the local coordinate system relative to the inertial coordinate system as shown in Figure 4.

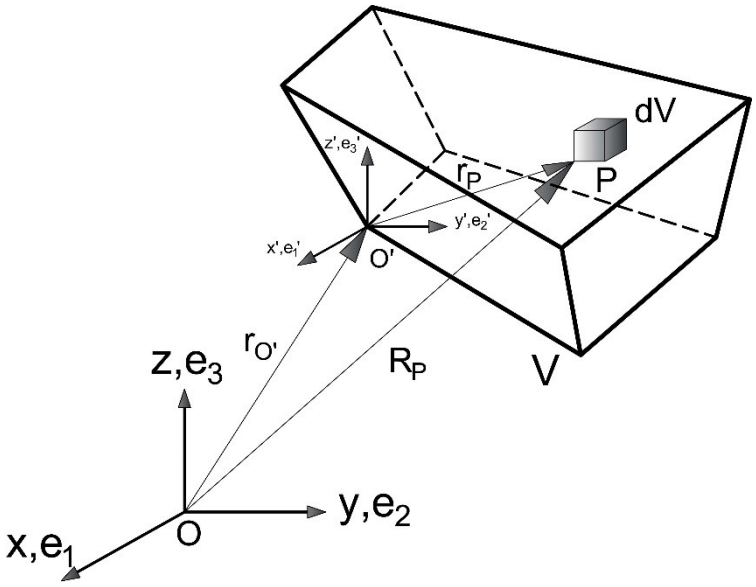

Figure 4: Location of an arbitrary point in relative and inertial coordinate system.

In this regard, by assuming that the initial state of the relative coordinate system is aligned with the inertial coordinate system, the position vector of an arbitrary material point located in the block can be defined as

$$R_p = r_{O'} + r_p = r_{O'} + r'_p \qquad \text{Eq. 8}$$

where R_p represents the position vector of the point in inertial coordinate system, $r_{O'}$ is the position vector of the origin of the relative coordinate system, r'_p denotes the position vector of the point in the relative coordinate system and r_p is the representation of r'_p in inertial coordinate system. The velocity of the point can be achieved by taking the first time derivative of the position vector as

$$\dot{R}_p = \dot{r}_{O'} + \frac{d}{dt}\left(r'_p\right) \qquad \text{Eq. 9}$$

$$\dot{R}_p = v_p = \dot{r}_{O'} + \dot{r}'_p + \omega \times r'_p \qquad \text{Eq. 10}$$

where, $\dot{R}_p$ is the velocity of the point in inertial coordinate system, $\dot{r}_{O'}$ is the velocity of the origin of the relative coordinate system in the inertial coordinate system, $\dot{r}'_p$ represents the velocity of the point in the relative coordinate system, ω is the angular velocity of the relative coordinate system and r'_p is the position vector of the point in relative coordinate system. Similarly, by taking time derivative of velocity of the point p, the acceleration can

be obtained as follows:

$$\ddot{R}_p = \ddot{r}_{O'} + \frac{d}{dt}\left(\dot{r}'_p + \omega \times r'_p\right) \quad \text{Eq. 11}$$

$$\ddot{R}_p = \ddot{r}_{O'} + \ddot{r}'_p + \omega \times \dot{r}'_p + \dot{\omega} \times r'_p + \omega \times \frac{d}{dt}\left(r'_p\right) \quad \text{Eq. 12}$$

$$\ddot{R}_p = \ddot{r}_{O'} + \ddot{r}'_p + \omega \times \dot{r}'_p + \dot{\omega} \times r'_p + \omega \times \left(\dot{r}'_p + \omega \times r'_p\right) \quad \text{Eq. 13}$$

$$\ddot{R}_p = a_p = \ddot{r}_{O'} + \ddot{r}'_p + 2\omega \times \dot{r}'_p + \dot{\omega} \times r'_p + \omega \times \left(\omega \times r'_p\right) \quad \text{Eq. 14}$$

where $\ddot{R}_p$ is the acceleration of the point p in global coordinate system, $\ddot{r}_{O'}$ is the acceleration of the origin of the relative coordinate system in inertial coordinate system, $\ddot{r}'_p$ is the acceleration of the point in relative coordinate system, $2\omega \times \dot{r}'_p$ is called Coriolis acceleration, $\dot{\omega} \times r'_p$ denotes Euler acceleration and $\omega \times \left(\omega \times r'_p\right)$ is called centrifugal acceleration.

3.2 Momentum Conservation Equations for Rigid Body Motion

In order to formulate the rigid body motion of a system of rigid blocks, the laws of linear and angular momentum conservation is applied. The conservation of the linear momentum for an arbitrary material element located in the rigid block is represented in indicial form as follows (Spencer, 2004; Reddy, 2007; Belytschko et al., 2013):

$$\frac{\partial \sigma_{ji}}{\partial x_j} + \rho b_i = \rho a_i \quad \text{Eq. 15}$$

where σ_{ij} is the Cauchy stress in the material element, b_i is the body force applied to the element concentrated in the unit mass of the element, ρ is unit mass of the element and a_i is the acceleration of the element. By integrating the above equation in the volume of the rigid block, the following equation can be derived for the block:

$$\int_V \frac{\partial \sigma_{ji}}{\partial x_j} dV + \int_V \rho b_i dV = \int_V \rho a_i dV \quad \text{Eq. 16}$$

Using the divergence theorem, the first volume integral taken over the volume of the block can be substituted by a surface integral taken over the surface of the block as

follows:

$$\oint_A \sigma_{ji} n_j dA + \int_V \rho b_i dV = \frac{d^2}{dt^2}\left(\int_V \rho r_i dV\right) \quad \text{Eq. 17}$$

where n_j represents the unit normal vector of the surface surrounding the rigid block. By using Cauchy's stress theorem (Spencer, 2004; Reddy, 2007; Belytschko et al., 2013), i.e. $\sigma_{ji} n_j = t_i$ where t_i is the traction force applied on the surface of the block, and the concept of mass center for the rigid block, the above equilibrium equation is simplified as

$$\oint_A t_i dA + \int_V \rho b_i dV = M \bar{a}_i \quad \text{Eq. 18}$$

$$F + T + B = M\bar{a} \quad \text{Eq. 19}$$

where F represents point forces applied to the block, T represents surface forces applied on the block surface, B represents body forces applied to the mass of the block, $\bar{a}$ is the acceleration of the mass center of the block which is defined as $\int_V \rho r_i dV$. Also, the differential form of the angular momentum conservation law is represented by the symmetry of the Cauchy stress at each arbitrary material element of the block as follows:

$$\sigma_{ij} - \sigma_{ji} = 0 \quad \text{Eq. 20}$$

By using the definition of the permutation tensor ϵ_{ijk}, the above equation can be represented as (Spencer, 2004; Reddy, 2007; Belytschko et al., 2013)

$$\epsilon_{ijk}\sigma_{jk} = 0 \quad \text{Eq. 21}$$

Also, the cross product of relative position vector of the material element and the equilibrium equation for the element can be substituted in the right-hand side of the above equation as

$$\epsilon_{ijk}\sigma_{jk} = \epsilon_{ijk} r'_j \left(-\frac{\partial \sigma_{lk}}{\partial x_l} - \rho b_k + \rho a_k\right) \quad \text{Eq. 22}$$

By taking the integration of the above equation over the block volume, the following equations are obtained:

$$\int_V \epsilon_{ijk}\sigma_{jk}dV = \int_V \epsilon_{ijk} r_j' \left(-\frac{\partial \sigma_{lk}}{\partial x_l} - \rho b_k + \rho a_k\right) dV \quad \text{Eq. 23}$$

$$\int_V \epsilon_{ijk} \left(\sigma_{jk} + r_j' \frac{\partial \sigma_{lk}}{\partial x_l} + r_j' \rho b_k\right) dV = \int_V \epsilon_{ijk} r_j' \rho a_k dV \quad \text{Eq. 24}$$

$$\int_V \epsilon_{ijk} \left(\sigma_{jk} + r_j' \frac{\partial \sigma_{lk}}{\partial x_l}\right) dV + \int_V \epsilon_{ijk} r_j' \rho b_k dV = \int_V \epsilon_{ijk} r_j' \rho a_k dV \quad \text{Eq. 25}$$

Substituting σ_{jk} with $\delta_{jl}\sigma_{lk}$, where δ_{jl} is the Kronecker delta, and using chain rule of derivation, the above equation can be rewritten as

$$\int_V \epsilon_{ijk} \left(\delta_{jl}\sigma_{lk} + r_j' \frac{\partial \sigma_{lk}}{\partial x_l}\right) dV + \int_V \epsilon_{ijk} r_j' \rho b_k dV = \int_V \epsilon_{ijk} r_j' \rho a_k dV \quad \text{Eq. 26}$$

$$\int_V \frac{\partial}{\partial x_l} \left(\epsilon_{ijk} r_j' \sigma_{lk}\right) dV + \int_V \epsilon_{ijk} r_j' \rho b_k dV = \int_V \epsilon_{ijk} r_j' \rho a_k dV \quad \text{Eq. 27}$$

The first volume integral in the left-hand side of the equation can be replaced by a surface integral taken over the surface surrounding the block based on the divergence theorem as follows:

$$\oint_A \epsilon_{ijk} r_j' \sigma_{kl} n_l dA + \int_V \epsilon_{ijk} r_j' \rho b_k dV = \int_V \epsilon_{ijk} r_j' \rho a_k dV \quad \text{Eq. 28}$$

In the above equation, $\sigma_{kl}n_l$ can be substituted by traction force applied on the surface surrounding the block using Cauchy's stress theorem as

$$\oint_A \epsilon_{ijk} r_j' t_k dA + \int_V \epsilon_{ijk} r_j' \rho b_k dV = \int_V \epsilon_{ijk} r_j' \rho a_k dV \quad \text{Eq. 29}$$

The above indicial representation of the angular momentum conservation law for the block can be rewritten as follows:

$$\oint_A r' \times t dA + \int_V r' \times b\rho dV = \int_V r' \times a\rho dV \quad \text{Eq. 30}$$

$$M_F + M_T + M_B = \int_V r' \times a\rho dV \quad \text{Eq. 31}$$

where M_F, M_T and M_B represent the moment of point forces, traction forces and body forces about the origin of the relative coordinate system, respectively. By substituting the expression of acceleration of an arbitrary point in the rotating relative coordinate system which is attached to the block, and considering $\ddot{r}_p' = \dot{r}_p' = 0$ due to the rigidity of the block,

the angular momentum conservation law is represented as

$$M_F + M_T + M_B = \int_V r' \times \left[\ddot{r}_{O'} + \ddot{r}' + \omega \times \dot{r}' + \dot{\omega} \times r' + \omega \times (\omega \times r')\right] \rho dV \qquad \text{Eq. 32}$$

Since the acceleration of the origin of the relative coordinate system do not change in the block volume and by using the concept of mass center, the above equation is simplified as:

$$M_F + M_T + M_B = M\bar{r}' \times \ddot{r}_{O'} + \int_V r' \times [\dot{\omega} \times r' + \omega \times (\omega \times r')] \rho dV \qquad \text{Eq. 33}$$

where $\bar{r}'$ is the position vector of the mass center of the rigid block.

3.3 Coupled Hydro-Mechanical Multi-Phase Solid-Fluid Equations of Motion in Deformable Fractured Porous Media

In rock engineering problems, if the displacements of a system of rock blocks are mostly due to the rigid body motion of the blocks with negligible blocks deformations, such as rockslides, the equations of motion derived for rigid body motion are adequate for analyzing the problem (Jing and Stephansson, 2007). However, in a problem where the contribution of the blocks deformations is considerable, continuum mechanics should be applied to simulate the deformation of the separate blocks which is coupled with the displacement field resulted from the rigid body motion of the discrete system of blocks.

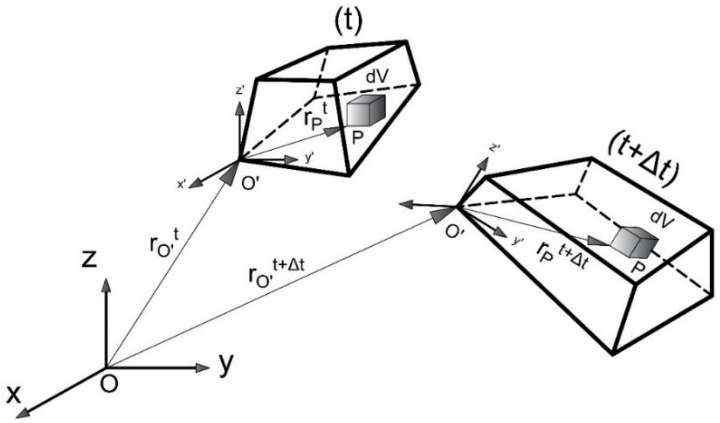

Figure 5: Rigid body motion and deformation.

If the material behavior of the rock blocks is assumed to be elastic, deformation and rigid body motion can be decoupled, and the total motion of any material points can be decomposed into the rigid body motion and elastic deformation. In these circumstances, the relative coordinate systems can be attached to the blocks, and the rigid body motion relative to these local coordinate systems can be cancelled. As it is schematically shown in Figure 5, the rigid body motion of the blocks can be formulated based on the translational and rotational motion of the local coordinate system relative to the inertial coordinate system. Hence, the rigid body displacements, inertial forces and interaction forces at the blocks' interfaces can be calculated by assuming the rigidity of the blocks. Then, under these forces, the elastic deformation of the blocks can be calculated relative to the local coordinate systems and superimposed on the rigid body motion. Using this method, large displacements, large rotations and small elastic strain of a system of rock blocks can be analyzed (Zienkiewicz and Taylor, 2005; Jing and Stephansson, 2007).

On the other hand, in order to analyze the large displacement and rotation of a system of rock blocks with inelastic material behavior, the deformation and rigid body motion cannot be decoupled. In these problems, distributed stiffness, viscous and plastic slider elements are defined at the blocks' contacts representing the constitutive behavior of the rock joints. Then, by utilizing a proper contact updating algorithm, the equations of motion of the whole block system can be formulated using momentum conservation law, kinematic equations relating derivation of displacement field and strains as well as constitutive equations in the contacts and discrete deformable blocks (Zienkiewicz and Taylor, 2005; Jing and Stephansson, 2007). Using this method, any constitutive behavior can be assumed for the rock blocks and contacts in the framework of large deformation. In these circumstances, the equations of momentum conservation or equilibrium equations, can be written for an arbitrary material element of the deforming body as follows:

$$\frac{\partial \sigma_{ji}}{\partial x_j} + \rho b_i - \rho \frac{d^2 r_i}{dt^2} - c \frac{dr_i}{dt} = 0 \qquad \text{Eq. 34}$$

where σ_{ij} is the true or Cauchy stress tensor measured at the material point in the current configuration of the body, and r_i, dr_i/dt and d^2r_i/dt^2 are position vector, velocity vector and the acceleration vector of the material element due to rigid body motion and

deformation, and *c* represents the viscous damping coefficient.

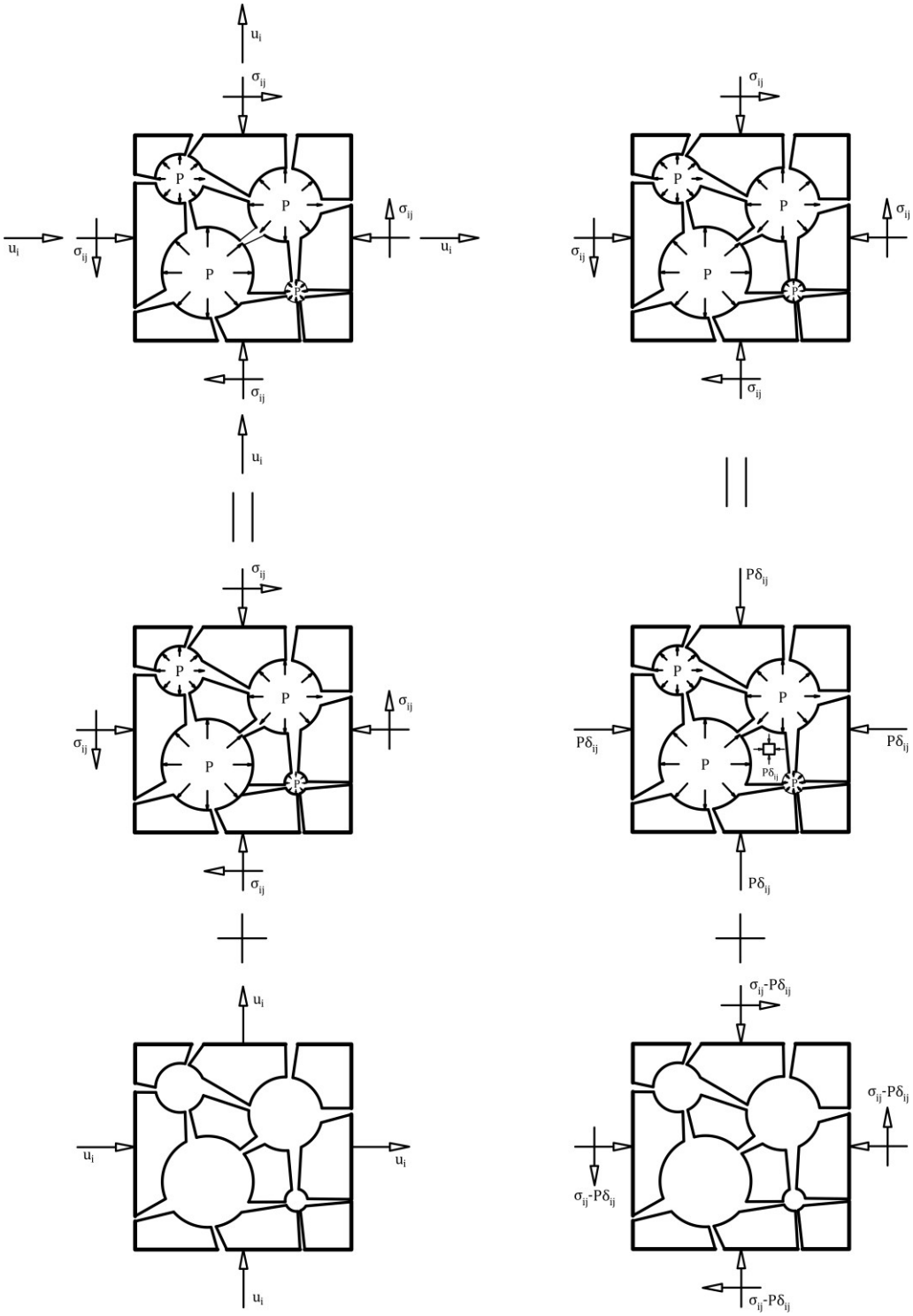

Figure 6: Decomposition of coupled hydromechanical multi-phase processes in fractured porous media.

In the case of multi-phase solid-fluid fractured porous media where the displacement field

in solid phase and velocity field in pore fluid phases are hydro-mechanically coupled, the above equations of motion derived for single solid phase can be extended based on the decomposition of the hydro-mechanical processes as it is schematically shown in Figure 6. As it is demonstrated in this figure, the hydro-mechanical processes can be decomposed into the velocity field of pore fluid defined relative to solid phase and the displacement field in the fractured porous media containing pore fluid which is immobile relative to the solid phase. Therefore, two sets of equations of motion govern the multi-phase mechanisms. The first set of governing equations is the equations of motion of porous solid phase, through pore spaces and fractures of which fluid phase moves. This set of equations of motion is obtained as follows:

$$\frac{\partial \sigma_{ji}}{\partial x_j} + \rho b_i - \rho \frac{d^2 r_i}{dt^2} - c \frac{dr_i}{dt} - \mathcal{I}_i^{\mathcal{F}} = 0 \qquad \text{Eq. 35}$$

where σ_{ij} represents the total stress vector applied on the boundaries of an element of porous media, b_i is the body force applied on the element of porous media, dr_i/dt and d^2r_i/dt^2 respectively denote the acceleration and velocity of solid phase, c represents the viscous damping coefficient in the solid phase, and $\mathcal{I}_i^{\mathcal{F}}$ is the inertial force of pore fluid phase. In this equation, two sets of inertial forces are taken into account. The first set of inertial force represented by the term $\rho\, d^2r_i/dt^2$ is the inertial force due to the acceleration of the element of porous media containing pore fluid phases which are immobile relative to the solid phase. Therefore, this inertial force is obtained by the multiplication of the acceleration of solid phase, d^2r_i/dt^2, and the bulk density calculated as $\rho = \phi\rho^{\mathcal{F}} + (1-\phi)\rho^{\mathcal{S}}$ where ρ is bulk density of porous media, $\rho^{\mathcal{F}}$ denotes average density of pore fluid phases, $\rho^{\mathcal{S}}$ represents the density of solid constituents and ϕ is porosity. The second inertial force represented by $\mathcal{I}_i^{\mathcal{F}}$ is applied to the element of porous media as a result of the movement of pore fluid through pore spaces and fractures of porous media relative to the solid phase which is defined as follows:

$$\mathcal{I}_i^{\mathcal{F}} = -\rho^{\mathcal{F}} \left[\frac{\partial u_i}{\partial t} + u_j \frac{\partial u_i}{\partial x_j} \right] \qquad \text{Eq. 36}$$

In this equation, u_i represents the velocity field of the fluid phase relative to solid phase and the above expression is the multiplication of the density and acceleration of fluid phase. In the problems considered in this research, since the movement of fluid relative

to solid phase occurs with negligible velocities, the inertial force due to the relative movement of pore fluid is neglected and the equilibrium equation is simplified to a form very similar to the single solid phase. In this case, the only difference is that the stresses applied on the porous media are called total stresses and the bulk density is used to account for the fluid phase in the gravitational force applied to the element of porous media.

The above equations of motion of solid phase are derived based on total stresses applied on a material element which is comprised of fractured porous solid phase and fluid phases which are immobile relative to the solid phase. In these circumstances, by neglecting the shear stresses in immobile pore fluid developed due to the fluid viscosity and velocity gradient in the solid phase, as it is shown in Figure 6, the total stress field applied to the element of fractured porous media can be decomposed into two parts as follows:

$$\sigma_{ij} = \sigma_{ij}' + P\delta_{ij} \qquad \text{Eq. 37}$$

where σ_{ij}' is the effective stress tensor developed between the constituents of the solid phase and P represents the pressure in pore fluid which is immobile relative to solid phase. As it is illustrated in Figure 6 and implied by the above equation, the total stresses applied on an element of porous media containing immobile pore fluid is equilibrated by effective stresses and pore fluid pressure (Terzaghi, 1943; Biot, 1941; Zienkiewicz, 1984). Based on the decomposition of the total stress into effective stress and pore pressure, the constitutive relations for solid phase in fractured porous media can be formulated. In fact, the part of the total stresses equilibrated with internal pore fluid pressure only contribute in the undrained volumetric deformation of the porous matrix due to the compressibility of pore fluid and solid constituents of porous media.

In contrast, the effective stresses contribute in the drained volumetric and drained shear deformation of the fractured porous media. While the volumetric deformation of the solid phase in undrained condition is negligible relative to that in drained condition in soils, it cannot be ignored in fractured rock mass (Biot, 1941). Therefore, as it is discussed in more details in Appendix A, the fraction of the total stress tensor contributing in the deformation of solid phase in fractured porous media can be defined by Biot's effective stress as follows:

$$\sigma_{ij} = \sigma_{ij}'' + \alpha P \delta_{ij} \quad \text{Eq. 38}$$

where σ_{ij}'' is Biot's effective stress tensor and α is Biot's coefficient which is derived in Appendix A in elastic condition.

Consequently, the equations of motion of fractured porous media containing immobile pore fluid is formulated based on 3 momentum conservation equations written in terms of total stresses for a Lgrangian, i.e. material, element. In these equations, by neglecting the pore fluid acceleration and viscosity, there exist 9 unknowns comprised of 6 unknown total stress components, and 3 unknown components of solid phase displacement field. In order to solve these equations, the 3 components of solid phase displacement field are related to 6 components of strains in solid phase element using 6 kinematic equations as follows:

$$d\varepsilon_{ij} = \mathbb{D}(dw_i) \quad \text{Eq. 39}$$

where ε_{ij} is the total strain tensor of the solid phase in the Lagrangian element of fractured porous media, w_i is the displacement field in the solid phase, and $\mathbb{D}$ denotes the derivative operator converting the displacement field into strain vector which can be defined based on different kinematic relations for large or small displacements and strains (Owen and Hinton, 1980; Crisfield, 1991; Bathe, 1996; Spencer, 2004; Reddy, 2007; Zienkiewicz and Taylor, 2005; Belytschko et al., 2013; Nazary Moghadam et al., 2012; Nazary Moghadam et al., 2013; Nazary Moghadam et al., 2015). Then, constitutive relations are defined to relate the 6 components of solid phase strains to 6 components of total stresses. To this end, as it is illustrated in Figure 6, the total stresses are decomposed into effective stresses and the part equilibrated with the pore fluid pressure. With the aid of this decomposition, constitutive relations can be defined based on material models existing for dry solid phase and experimental data as follows:

$$d\varepsilon_{ij} = \mathbb{K}\left(d\varepsilon_{ij}^{d}, d\varepsilon_{ij}^{u}\right) \quad \text{Eq. 40}$$

$$d\varepsilon_{ij}^{d} = \mathbb{F}\left(d\sigma_{ij}'\right) \quad \text{Eq. 41}$$

$$d\varepsilon_{ij}{}_{\mathcal{V}}^{u} = \mathbb{G}(dP) \quad \text{Eq. 42}$$

$$d\phi = \mathbb{H}\left(dP, d\sigma_{ij}{}'\right) \qquad \text{Eq. 43}$$

where $d\varepsilon_{ij}^{d}$ and $d\varepsilon_{ij}^{u}$ represent the strains of solid phase in respectively drained and undrained element of fractured porous media, $d\varepsilon_{ij}{}_{v}^{u}$ is the volumetric strain of solid phase in undrained element of fractured porous media, $\mathbb{K}$ is a function which can be defined based on kinematics and experimental data, and $\mathbb{F}$, $\mathbb{G}$ and $\mathbb{H}$ are constitutive functions defined based on experimental data. In the above equations, it should be noted that the porosity change as a function of pore pressure change can be taken into account depending on pore fluid compressibility.

To sum up, the coupled hydromechanical equations of motion of solid phase in fractured porous media involve 15 equations, namely 3 momentum conservation equations, 6 kinematic equations relating displacement field and strains in solid phase, and 6 constitutive equations relating stress and strains in solid phase. In these equations, there are 16 major unknowns, including 3 unknown components of displacement field, 6 unknown components of total stress tensor, 6 unknown components of total strain tensor and 1 unknown pore fluid pressure. Therefore, an additional set of equations is needed to solve the problem.

The additional set of equations of motion in such multi-phase problems is the one that governs the movement of pore fluid through pore spaces and fractures relative to solid phase. This set of equations of motion formulate the velocity field and pore pressure in the fluid phases which will be discussed in more details in the next chapter. The final set of hydro-mechanical equations of motion of porous media are coupled and the displacement field in solid phase and velocity field in fluid phase cannot be determined independently. Therefore, either these equations shall be solve simultaneously using fully coupled methods or a sequentially coupled approach have to be utilized to approach this problem.

3.4 Derivation of Integral Form of Equations of Motion by Weighted Residual Approach

In order to solve the coupled hydro-mechanical equations of motion of fractured porous media, the differential form of momentum conservation equation derived in the previous section can be converted into integral form using weighted residual approach. Using this method, the weak form, i.e. integral form, of equations of motion is obtained. Using this approach, a weaker requirement for the continuity of the unknown displacement field of the solid phase is adequate in the numerical solution. This is due to the fact that by integrating the differential form of momentum conservation equation, the requirement for continuity of first derivative of the unknown displacement field is removed and the continuity of the displacement field suffices. Therefore, using the weighted residual approach, the integral form of coupled hydro-mechanical momentum conservation equation for a Lagrangian, i.e. material, element of fractured porous media containing immobile pore fluid is derived as follows:

$$\int_V \mathcal{W}_i \left[\frac{\partial \sigma_{ji}}{\partial x_j} + \rho b_i - \rho \frac{d^2 r_i}{dt^2} - c\frac{dr_i}{dt}\right] dV = 0 \qquad \text{Eq. 44}$$

where $\mathcal{W}_i$ is a properly defined weighting vector field, V represents the volume of the closed surface bounding the fractured porous domain, and dV is the volume of the material element of fractured porous media containing relatively immobile pore fluid. The boundary conditions of the problem are also defined by the following equations:

$$\left[n_j \sigma_{ji}\right]_{A_t} = \tau_i \qquad \text{Eq. 45}$$

$$[w_i]_{A_w} = \omega_i \qquad \text{Eq. 46}$$

where A represents the closed surface bounding the fractured porous domain with normal vector n_j, A_t and A_w denotes the sections of the boundary surface where traction and displacement boundary conditions are applied, respectively. The first boundary condition states that the traction on the A_t boundary of the fractured porous domain is equal to the predefined traction vector τ_i. The second boundary condition imposes the predefined boundary displacement vector denoted by ω_i on the A_w boundary.

3.4.1 Discretization of Integral form of Equations of Motion by Finite Element Method

By utilizing a virtual displacement field compatible with the displacement boundary conditions in the definition of the weighting field $\mathcal{W}_{\mathrm{i}}$ in the integral form of momentum conservation equation, the resulting integral equation can be spatially discretized by finite element approach. To this end, as schematically shown in Figure 7, by applying the virtual differential deformation field $\delta\mathcal{U}_i$ which is compatible with boundary conditions, the differential form of momentum conservation equation can be expressed in an integral form as follows (Galerkin, 1915; Owen and Hinton, 1980; Crisfield, 1991; Bathe, 1996; Spencer, 2004; Zienkiewicz and Taylor, 2005; Reddy, 2007; Belytschko et al., 2013; Nazary Moghadam et al., 2012; Nazary Moghadam et al., 2013; Nazary Moghadam et al., 2015):

$$\delta W = \int_V \left(\frac{\partial \sigma_{ji}}{\partial x_j} + \rho b_i - \rho \ddot{r}_i - c\dot{r}_i\right) \delta\mathcal{U}_i dV = 0 \qquad \text{Eq. 47}$$

$$\delta W = \int_V \left[\frac{\partial(\sigma_{ji}\delta\mathcal{U}_i)}{\partial x_j} - \sigma_{ji}\frac{\partial \delta\mathcal{U}_i}{\partial x_j} + \rho b_i \delta\mathcal{U}_i - \rho \ddot{r}_i \delta\mathcal{U}_i - c\dot{r}_i\right] dV = 0 \qquad \text{Eq. 48}$$

where δW denotes the virtual work due to all internal and external forces appled to the body and $\partial\delta\mathcal{U}_i/\partial x_j$ represents the virtual displacement gradient of the material element which can be decomposed into two symmetric and anti-symmetric tensors as follows:

$$\frac{\partial \delta\mathcal{U}_i}{\partial x_j} = \frac{1}{2}\left[\frac{\partial \delta\mathcal{U}_i}{\partial x_j} + \frac{\partial \delta\mathcal{U}_j}{\partial x_i}\right] + \frac{1}{2}\left[\frac{\partial \delta\mathcal{U}_i}{\partial x_j} - \frac{\partial \delta\mathcal{U}_j}{\partial x_i}\right] = \delta\varepsilon_{ij} + \delta\Omega_{ij} \qquad \text{Eq. 49}$$

where $\delta\varepsilon_{ij}$ is the virtual true strain change while $\delta\Omega_{ij}$ is the virtual rotation change. The true strain change denotes the differential relative deformation of a material point in the current configuration of the body (Crisfield, 1991; Spencer, 2004; Reddy, 2007; Belytschko et al., 2013). By substituting the above expression in the virtual work equation, using divergence theorem, and considering $\int_V \sigma_{ji}\delta\Omega_{ij}dV = 0$, the integral form of momentum conservation equation rewritten as follows:

$$\delta W = \oint_A \sigma_{ji} n_j \delta\mathcal{U}_i dA - \int_V \sigma_{ji}\delta\varepsilon_{ij}dV + \int_V (\rho b_i - \rho\ddot{r}_i - c\dot{r}_i)\delta\mathcal{U}_i dV = 0 \qquad \text{Eq. 50}$$

As it can be seen, the true strain change is the work conjugate to the Cauchy stress (Crisfield, 1991; Spencer, 2004; Reddy, 2007).

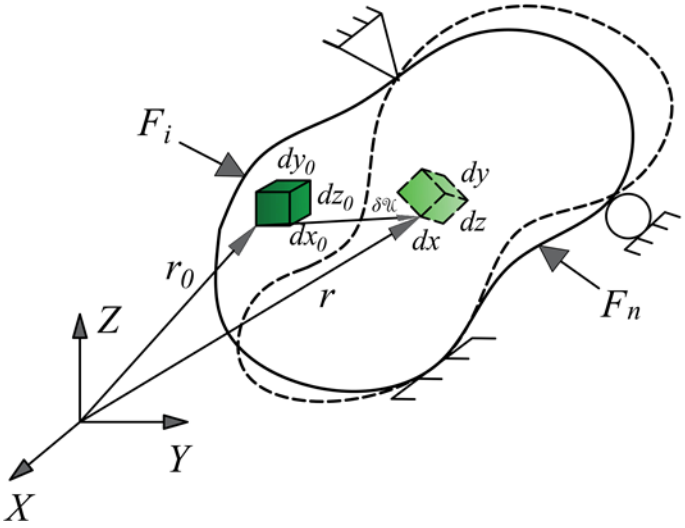

Figure 7: Virtual deformation in the local coordinate system.

Using Cauchy's theorem, the integral form of momentum conservation equation is derived as follows:

$$\delta W = \oint_A t_i \delta \mathcal{U}_i dA - \int_V \sigma_{ji} \delta \varepsilon_{ij} dV + \int_V (\rho b_i - \rho \ddot{r}_i - c\dot{r}_i) \delta \mathcal{U}_i dV = 0 \qquad \text{Eq. 51}$$

where t_i represents the traction force. The above equation represents the principle of virtual work. Based on this principle, a continuum body is in equilibrium if the virtual work of all forces acting on the body under a virtual displacement is zero. Using finite element method, fractured porous media can be spatially discretized into Lagrangian subdomains, i.e. finite elements, where the displacement field is interpolated as follows:

$$u_i = \mathcal{N}_{ij} \tilde{u}_j \qquad \text{Eq. 52}$$

where $\tilde{u}_j$ and $\mathcal{N}_{\mathrm{ij}}$ denotes the nodal displacements and interpolation functions, i.e. shape functions, in the finite elements, respectively. Consequently, using the displacement field interpolated by the above relation, the integral form of momentum conservation equation obtained by virtual work principle can be approximated in finite elements resulting in the discretized momentum conservation equation.

3.4.2 Discretization of Integral Form of Equations of Motion by Finite Volume Method

By applying the weighted residual approach to both momentum conservation equation and boundary conditions, the governing equations of motion is obtained in integral form as follows (Zienkiewicz and Onate, 1992; Demirdzic and Martinovic, 1993; Bailey and Cross, 1995):

$$\int_V \mathcal{W}_i \left[\frac{\partial \sigma_{ji}}{\partial x_j} + \rho b_i - \rho \frac{d^2 r_i}{dt^2} - c\frac{dr_i}{dt}\right] dV + \int_{A_t} \mathcal{W}_i^t \left[n_j \sigma_{ji} - \tau_i\right] dA + \int_{A_w} \mathcal{W}_i^w [w_i - \omega_i] = 0 \quad \text{Eq. 53}$$

In the above equation, the weighting vector field defined for displacement boundary condition, $\mathcal{W}_i^w$, is assumed to be equal to zero to ensure the satisfaction of displacement boundary conditions. In addition, the weighting vector field of $\mathcal{W}_i^t = -\mathcal{W}_i$ is assumed for the traction boundary condition. Therefore, the integral form of governing coupled hydro-mechanical equations of motion in solid phase is rewritten as follows:

$$\int_V \mathcal{W}_i \frac{\partial \sigma_{ji}}{\partial x_j} dV + \int_V \mathcal{W}_i \left[\rho b_i - \rho \frac{d^2 r_i}{dt^2} - c\frac{dr_i}{dt}\right] dV - \int_{A_t} \mathcal{W}_i n_j \sigma_{ji} dA + \int_{A_t} \mathcal{W}_i \tau_i dA = 0 \quad \text{Eq. 54}$$

In the above equation, since the boundary of the porous media is the union of the traction and displacement boundaries, $A = A_t \cup A_w$, the third integral can be performed using the relation $\int_{A_t} \varphi d\varphi = \int_A \varphi d\varphi - \int_{A_w} \varphi d\varphi$. Therefore, the above equation can be rewritten as

$$\int_V \mathcal{W}_i \frac{\partial \sigma_{ji}}{\partial x_j} dV + \int_V \mathcal{W}_i \left[\rho b_i - \rho \frac{d^2 r_i}{dt^2} - c\frac{dr_i}{dt}\right] dV - \int_A \mathcal{W}_i n_j \sigma_{ji} dA + \int_{A_w} \mathcal{W}_i n_j \sigma_{ji} dA + \int_{A_t} \mathcal{W}_i \tau_i dA = 0 \quad \text{Eq. 55}$$

In the above equation, using the divergence theorem, the third surface integral can be replaced by a volume integral as follows:

$$\int_V \mathcal{W}_i \frac{\partial \sigma_{ji}}{\partial x_j} dV + \int_V \mathcal{W}_i \left[\rho b_i - \rho \frac{d^2 r_i}{dt^2} - c \frac{dr_i}{dt}\right] dV - \int_V \left[\mathcal{W}_i \frac{\partial \sigma_{ji}}{\partial x_j} - \sigma_{ji} \frac{\partial \mathcal{W}_i}{\partial x_j}\right] dV + \int_{A_w} \mathcal{W}_i n_j \sigma_{ji} dA + \int_{A_t} \mathcal{W}_i \tau_i dA = 0 \quad \text{Eq. 56}$$

$$\int_V \frac{\partial \mathcal{W}_i}{\partial x_j} \sigma_{ji} dV + \int_V \mathcal{W}_i \left[\rho b_i - \rho \frac{d^2 r_i}{dt^2} - c \frac{dr_i}{dt}\right] dV + \int_{A_w} \mathcal{W}_i n_j \sigma_{ji} dA + \int_{A_t} \mathcal{W}_i \tau_i dA = 0 \quad \text{Eq. 57}$$

Finally, the integral form of governing coupled hydro-mechanical equations of motion of fractured porous media can be achieved by assuming $\mathcal{W}_i = \{1 \quad 1 \quad 1\}^T$ as follows:

$$\int_V \mathcal{W}_i \left[\rho b_i - \rho \frac{d^2 r_i}{dt^2} - c \frac{dr_i}{dt}\right] dV + \int_{A_w} \mathcal{W}_i n_j \sigma_{ji} dA + \int_{A_t} \mathcal{W}_i \tau_i dA = 0 \quad \text{Eq. 58}$$

By discretizing the fractured porous media into Lagrangian subdomains, i.e. finite volumes, the integral form of governing coupled hydro-mechanical equations of motion of fractured porous media represented by the above equation can be spatially discretized. Moreover, by using constitutive equations, stresses are related to strains which are in turn related to displacement field. Therefore, a numerical procedure is required to determine the derivatives of the displacement field. To this end, displacement field in finite volumes is interpolated based on the displacements at the finite volume vertices, $\tilde{u}_j$, using the relation $u_i = \mathcal{N}_{ij} \tilde{u}_j$. With the aid of defining proper shape functions, $\mathcal{N}_{ij}$, the required derivatives of displacement field can be obtained in terms of the derivatives of shape functions and displacements at the finite volume vertices.

3.5 Time Integration Scheme

In the governing equations of motion of solid phase in fractured porous media, a numerical integration method is required to discretize the equations in time domain. To this end, the time derivatives of the location vector in the governing equation are approximated using Newmark's method as follows (Newmark, 1959; Clough and Penzien, 2003):

$$(r_i)^{n+1} = (r_i)^n + \left(\frac{dr_i}{dt}\right)^n \delta t + \left[(1-2\beta)\left(\frac{d^2 r_i}{dt^2}\right)^n + 2\beta \left(\frac{d^2 r_i}{dt^2}\right)^{n+1}\right] \frac{\delta t^2}{2} \quad \text{Eq. 59}$$

$$\left(\frac{dr_i}{dt}\right)^{n+1} = \left(\frac{dr_i}{dt}\right)^{n} + \left[(1-\gamma)\left(\frac{d^2r_i}{dt^2}\right)^{n} + \gamma\left(\frac{d^2r_i}{dt^2}\right)^{n+1}\right]\delta t \qquad \text{Eq. 60}$$

where n represents the time step number, i.e. $t^{n+1} = t^n + \Delta t$, and β and γ are Newmark's time integration weighting coefficients. Assuming the values of $\beta = 1/4$ and $\gamma = 1/2$, Newmark's method results in an unconditionally stable time integration scheme. Taking the variation of the above equations yields

$$(\delta r_i)^{n+1} = (\delta r_i)^{n} + \left(\frac{d\delta r_i}{dt}\right)^{n}\delta t + \left[(1-2\beta)\left(\frac{d^2\delta r_i}{dt^2}\right)^{n} + 2\beta\left(\frac{d^2\delta r_i}{dt^2}\right)^{n+1}\right]\frac{\delta t^2}{2} \qquad \text{Eq. 61}$$

$$\left(\frac{d\delta r_i}{dt}\right)^{n+1} = \left(\frac{d\delta r_i}{dt}\right)^{n} + \left[(1-\gamma)\left(\frac{d^2\delta r_i}{dt^2}\right)^{n} + \gamma\left(\frac{d^2\delta r_i}{dt^2}\right)^{n+1}\right]\delta t \qquad \text{Eq. 62}$$

Therefore, in the above equations, the location vector r_i can be replaced by displacement field $w_i = \delta r_i$ as follows:

$$(w_i)^{n+1} = (w_i)^{n} + (\dot{w}_i)^{n}\delta t + [(1-2\beta)(\ddot{w}_i)^{n} + 2\beta(\ddot{w}_i)^{n+1}]\frac{\delta t^2}{2} \qquad \text{Eq. 63}$$

$$(\dot{w}_i)^{n+1} = (\dot{w}_i)^{n} + [(1-\gamma)(\ddot{w}_i)^{n} + \gamma(\ddot{w}_i)^{n+1}]\delta t \qquad \text{Eq. 64}$$

where $\dot{w}_i = dw_i/dt = dr_i/dt$ and $\ddot{w}_i = d^2w_i/dt^2 = d^2r_i/dt^2$ denotes velocity and acceleration of the solid phase in fractured porous media. Using the above relations together with the momentum conservation equation, the displacement, velocity and acceleration fields are iteratively obtained during each time steps.

3.6 Numerical Solution of Discretized Equations of Motion by Newton-Raphson Method

The discretized coupled hydro-mechanical equations of motions derived in previous sections for the solid phase in fractured porous media are nonlinear necessitating the utilization of iterative methods such as Newton-Raphson method to solve the equations during each time step of numerical solution. To this end, internal force, external force and out-of-balance force vectors are defined for finite element solution using virtual work principle (Owen and Hinton, 1980; Crisfield, 1991; Bathe, 1996; Spencer, 2004; Reddy, 2007; Zienkiewicz and Taylor, 2005; Belytschko et al., 2013; Nazary Moghadam et al., 2012; Nazary Moghadam et al., 2013; Nazary Moghadam et al., 2015). In the case of finite

volume solution, the following equations are used to define internal force, external force, and out-of-balance force vectors:

$$q_{int} = \int_{A_u} \mathcal{W}_i n_j \sigma_{ji} dA \quad \text{Eq. 65}$$

$$q_{ext} = \int_V \mathcal{W}_i \left[\rho b_i - \rho \frac{d^2 r_i}{dt^2} - c \frac{dr_i}{dt}\right] dV + \int_{A_t} \mathcal{W}_i \tau_i dA \quad \text{Eq. 66}$$

$$g = q_{int} - q_{ext} \quad \text{Eq. 67}$$

where q_{int}, q_{ext} and g, are internal force, external force and out-of-balance or residual force vectors. Hence, during each time step of numerical solution, the solution of discretized equations of motion is achieved by iteratively decreasing the out-of-balance force vector. With this aim, in Newton-Raphson method, the above equations are linearized with respect to unknown displacements at finite volume vertices using Taylor series expansion as follows:

$$g^{i+1} = g^i + \left(\frac{\partial g}{\partial \tilde{u}}\right)^i \delta \tilde{u}^{i+1} = 0 \quad \text{Eq. 68}$$

$$\mathcal{K}_t^i = \left(\frac{\partial g}{\partial \tilde{u}}\right)^i = \left(\frac{\partial q_{int}}{\partial \tilde{u}}\right)^i \quad \text{Eq. 69}$$

$$\delta \tilde{u}^{i+1} = -\left(\mathcal{K}_t^i\right)^{-1} g^i \quad \text{Eq. 70}$$

where i is the Newton-Raphson iteration number, $\tilde{u}$ denotes the displacements at finite volume vertices, $\mathcal{K}_t^i$ is the tangent stiffness matrix, and $\delta \tilde{u}^{i+1}$ represents the updated displacement increment vector at the finite volume vertices at the end of each Newton-Raphson iterations. Therefore, the total displacements at the end of iterative solutions, $\Delta \tilde{u}$, is obtained as follows:

$$\Delta \tilde{u} = \sum_{i=1}^{r} \delta \tilde{u}^i \quad \text{Eq. 71}$$

where r represents the total number of iterations which is controlled by a predefined tolerance for out-of-balance force vector as well as a predefined maximum number of iterations.

3.7 Simulation of Discontinuities by Distinct Element Method

Distinct element method is one of the widely-used approaches, particularly in rock mechanics, for the numerical solution of equations of motion of a system of deformable discrete blocks. In this method, a properly linked data structure is employed to manage the storage and updating of data representing the time-dependent position and geometry of discrete system of blocks involving vertices, edges, faces and contacts of the blocks. One of the crucial components of this data structure is the dynamic data representing contacts between discrete blocks. The contact data are updated at each time step of numerical analysis based on the displacement field determined by the solution of equations of motion of the discrete system of blocks. The efficiency of contact detection and updating algorithms implemented in distinct element method plays a vital role in overall performance of the method.

Contacts between adjacent discrete blocks are numerically recognized when the minimum distance between the blocks decreases below a predefined tolerance. In general, for three-dimensional polyhedral blocks, 6 different contact types can be identified, namely, vertex-to-face, edge-to-face, face-to-face, vertex-to-edge, edge-to-edge and vertex-to-vertex. In case of convex polyhedral blocks, all these contact types can be identified based on two primary types of contacts, e.g. vertex-to-face and edge-to-face. In this regard, vertex-to-vertex contact is identified at a particular point when there exist three or more vertex-to-face contacts at the point. Similarly, vertex-to-edge contact is recognized at a point where two vertex-to-face contacts is existing. Also, edge-to-edge contact is recognized at a particular edge-to-face contact provided that two edge-to-face contacts are existing at the edge. Finally, face-to-face contact is represented by three or more edge-to-face contacts (Cundall, 1988; Zienkiewicz and Taylor, 2005; Jing and Stephansson, 2007).

The contact detection approach in distinct element method, not only recognizes the contact types, but also determines the unit normal vector at the contact point along which the gap between the contacting blocks and the normal contact force is defined. This unit normal vector also determines the contact tangent plane on which the contacting blocks can slide, and the shear contact forces are applied. With this aim, numerical treatments are needed to manage the situations where such contact plains cannot be defined theoretically, e.g. in the case of vertex-to-vertex contact. Since contact detection and

updating is a time-consuming process, an efficient algorithm should be defined to handle this process.

The most straightforward and robust contact detection method is called direct contact search in which all vertices, edges and faces of a block is checked for any contact possibilities with other blocks. However, this method is not usually the most efficient method for contact detection in three-dimensional problems (Zienkiewicz and Taylor, 2005; Jing and Stephansson, 2007). Therefore, an alternative more efficient method for contact detection in three-dimensional problems is developed by Cundall (1988). In this method, as it is shown in Figure 8, an imaginary tangential plane called common plane is defined at the void space between the contacting blocks located at a maximum distance from the closest vertices of the blocks. The location and direction of the common plane is also updated based on the relative motion of the blocks at each time step of analysis so that the common plane is always tangent to the contacting blocks and located at the maximum distance from the closest vertices of the blocks.

Using common plane concept, the contact detection process becomes more numerically economical as the number of contact tests is considerably decreased and all the possible contacts between two blocks can be simply recognized by vertex-to-plane contacts between the vertices of convex blocks and the common plane. For instance, when there exist three vertex-to-plane contacts for both contacting blocks, the contact type is face-to-face. In case of deformable blocks where the blocks are discretized by finite difference or finite volume nodes, the nodes located on the contact planes called sub-contacts are numerically treated as vertices. Then, normal and shear springs, plastic sliders and viscous dampers can also be effectively defined at sub-contact points discretizing the contact plane represented by common plane. Consequently, the discrete displacement fields of each block can be related to those of neighboring blocks which makes it feasible to numerically solve the equations of motion of system of discrete blocks.

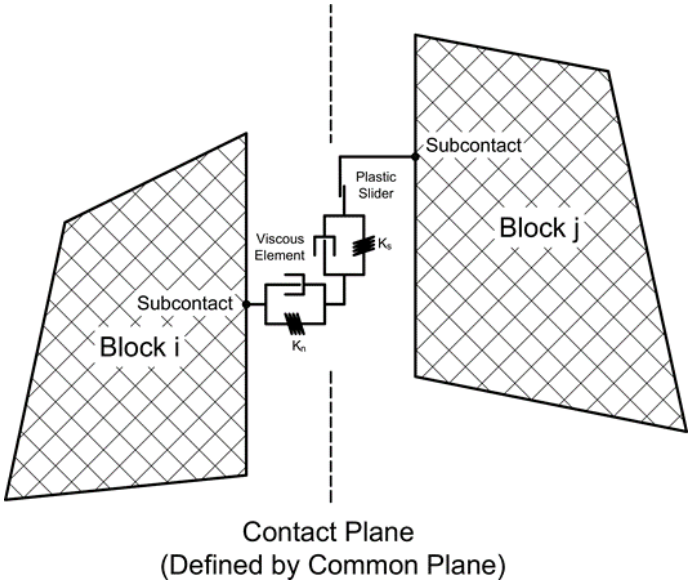

Figure 8: Deformable blocks and representation of contacts by common plane concept in distinct element method.

Another benefit of using the concept of common plane is that the contact tangent plane and its unit normal vector is simply defined by the common plane and its unit normal vector. In particular, in the case of vertex-to-vertex or edge-to-edge contacts, the concept of common plane is significantly useful in the definition of the contact tangent plane. The utilization of the concept of common plane is efficient for the case of tightly connected blocks as it is usually the case in rock mechanics problems (Cundall, 1988; Zienkiewicz and Taylor, 2005; Jing and Stephansson, 2007). However, in order to simulate granular materials motion or extremely large movement of block systems, e.g. in the case of explosion, where loosely connected blocks are encountered, direct contact search method might be more efficient.

In order to increase the efficiency of the contact detection algorithm in distinct element method, the contact search for each block can be restricted to the neighboring blocks by Cell Mapping method as it is shown in Figure 9. In this method, a spatial mesh comprising of simply-shaped cells, e.g. rectangular cells, is mapped into the block system. Then, in the contact detection process, each block is only tested for contact with the blocks having common overlapping cells with the tested block (Cundall, 1988; Zienkiewicz and Taylor, 2005; Jing and Stephansson, 2007). In other words, using the Cell Mapping method, a neighborhood is defined for each block by the area enveloping the cells overlapping the block. Then, each block is checked for contact only with the blocks overlapping the

neighborhood of the tested block.

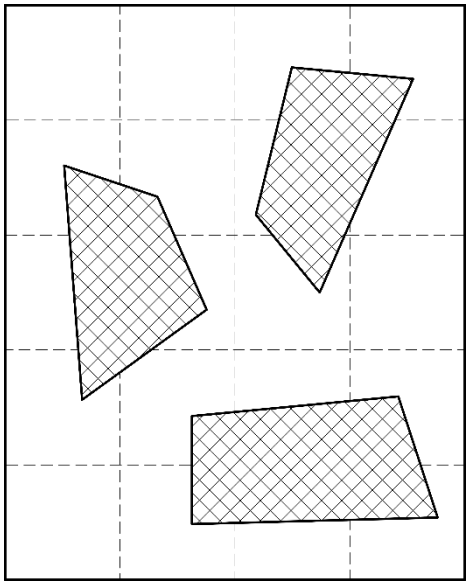

Figure 9: Estimation of neighboring blocks using cell mapping in distinct element method.

It should be mentioned that by increasing the number of spatial cells, i.e. by using smaller cells, the numerical effort needed to manage the cells, e.g. mapping and remapping, is increased. On the other hand, smaller cells result in smaller number of contact tests needed for each block due to the decrease in the number of neighboring blocks. Therefore, an optimum spatial cell numbers can be theoretically determined. In the case of tightly connected block systems, except for limited excessively changing areas, most of the blocks do not move out of their current cells and their contacts do not change too much. In these cases, cell remapping and contact updating process is limited to the relatively small areas. Therefore, contact detection algorithm based on Cell Mapping and Common Plane concept is efficient for tightly connected block systems (Cundall, 1988; Zienkiewicz and Taylor, 2005; Jing and Stephansson, 2007). However, in the case of granular materials motion or extremely large movement of block systems, the direct contact search between each block and all other blocks might be needed and the Cell Mapping method would not be efficient.

After the definition of contacts between discrete blocks and assigning proper constitutive models to the blocks and contacts, the integral form of equations of motion of the system of discrete deformable blocks can be numerically solved using finite volume or finite element method.

In distinct element method, the material behavior at contact planes are formulated based

on forces and displacements at sub-contacts. For instance, elastic-perfectly plastic Mohr-Coulomb failure can be utilized to simulate the constitutive behavior of joints in the analyses. In this model, elastic displacements at the contacts are modeled by defining normal and tangential springs at the sub-contacts considering normal and tangential stiffness as elastic material parameters. The perfectly plastic response is modeled by placing frictional slider at the sub-contacts with material parameters of cohesion, friction angle and dilation angle. Also, in order to damp the vibrations caused by springs, dashpots, with material parameters represented by viscous damping coefficients, are placed at the sub-contacts (Zienkiewicz and Taylor, 2005; Jing and Stephansson, 2007). Therefore, at the sub-contacts, the relative displacement of the contacting blocks induces contact forces based on the stiffness, damping, cohesion and friction of the contact planes. The incremental normal and tangential interaction forces at the sub-contacts are calculated in terms of incremental relative normal and tangential displacements of the contacting blocks as follows:

$$dF_n = K_n du_n \qquad \text{Eq. 72}$$

$$dF_t = \begin{cases} K_s du_t & if: F_t < c + F_n tan\phi \ (without\ slide) \\ c + dF_n tan\varphi & if: F_t \geq c + F_n tan\phi \ (with\ slide) \end{cases} \qquad \text{Eq. 73}$$

where du_n represents the interpenetration of the contacting blocks at the sub-contacts, and K_n and K_s are normal and shear stiffness, respectively. In addition, when sliding occurs, the incremental normal displacement causing dilation at the sub-contacts, du_n, is calculated based on dilation angle, ψ, and incremental tangential displacement, du_t, as follows:

$$du_n = du_t tan\psi \qquad \text{Eq. 74}$$

In order to define the material parameters specifying the damping at sub-contacts, the concept of Rayleigh damping is utilized. In this method, mass-proportional damping is employed to damp the vibrations with low frequency caused mostly by the vibrations of the whole system of blocks. Also, the stiffness-proportional damping is utilized to dissipate vibrations with high frequencies in which individual blocks vibrate relative to their neighboring blocks (Clough and Penzien, 2003; Chopra, 2012). In order to more sophisticatedly consider the effects of joint roughness in the constitutive modeling of

contact planes, instead of Mohr-Coulomb model, Barton-Bandis model can be implemented in which the effects of joint roughness and the compressive strength of joint walls are taken into account. In addition, in order to consider the damage of joints and the related reduction in friction angle due to shear displacement, the Continuously-Yielding model can be applied (Jing and Stephansson, 2007). It should also be mentioned that in order to model fluid flow through the fractures and rock joints, the hydraulic aperture is calculated by the following equation:

$$e = e_0 + \delta u_n \qquad \text{Eq. 75}$$

where e is the hydraulic aperture at a flow plane node located on contact plane, e_0 is the hydraulic aperture at the node for zero normal stress, and the δu_n is the change in the gap between the contacting blocks with positive values representing opening calculated based on the normal displacements at the corresponding sub-contacts. Also, the hydraulic aperture is bounded between two values called residual aperture, e_{res}, and maximum aperture, e_{max}, as $e_{res} \leq e \leq e_{max}$ (Damjanac, 1996; Itasca Consulting Group, Inc., 2007). The constitutive behavior of the hydraulic aperture is schematically shown in Figure 10.

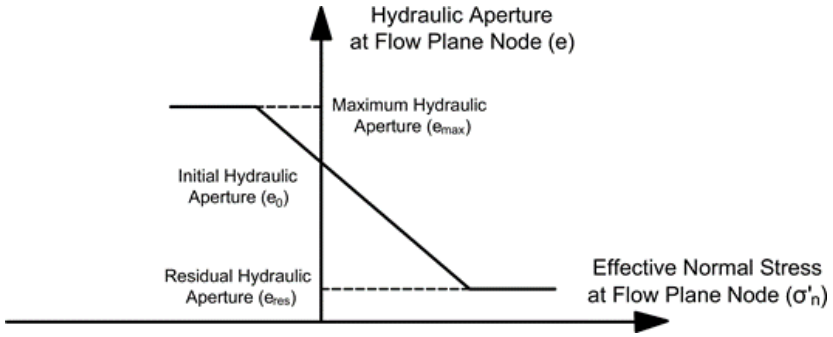

Figure 10: Constitutive behavior of hydraulic aperture in Distinct Element Method.

In this research, the capabilities of distinct element method in the numerical solution of equations of motion of system of discrete blocks, taking into account complex deformable discontinuities, are utilized to develop a novel coupled hydro-mechanical multi-phase fluid flow simulation approach with particular application to simulation of hydro-mechanical processes in fractured shale reservoirs. To this end, in the next chapter, , a novel numerical approach compatible with distinct element method is developed for the simulation of multi-phase fluid flow through both pore spaces and complex fracture networks in a system of discrete deformable blocks.

4 Numerical Formulation of Finite Volume Discrete Fracture-Matrix Approach for Compressible Multi-Phase Fluid Flow

4.1 Conservation Equations for Single-Phase Fluid Flow in Fractured Porous Media

In order to formulate the equations of motion of a physical system, a specification approach is needed to measure the changes of the variables of the physical system. In classical mechanics, Lagrangian and Eulerian approaches are the two widely-used specification approaches for the measurement of the changes in the unknown variables, e.g. velocity or position, based on which the equations of motion are formulated. In Eulerian approach, the equations of motion of material particles are formulated based on the velocity of the moving particles measured at a point in space specified by the position vector of the spatial point. In contrast, in Lagrangian method, the equations of motion of material particles are formulated based on the velocity or position of the moving particles measured at a material point attached to the particle.

In the formulation of equations of motion of fluid flow, Eulerian method is conventionally preferred to Lagrangian approach since fluid particles follows complicated movement paths which makes it burdensome to track the path of the fluid particles in space. Although Lagrangian approach cause difficulties when large deformations and displacements are encountered in the movement of material particles, this approach is widely used in the formulation of equations of motion of solid materials since it provides a practical method to determine the position of material particles by time making it feasible to track the movement of interfaces and boundaries. In order to transform the conservation laws expressed based on Lagrangian approach to an expression defined based on Eulerian method, Reynolds transport theorem is utilized which is schematically illustrated in Figure 11.

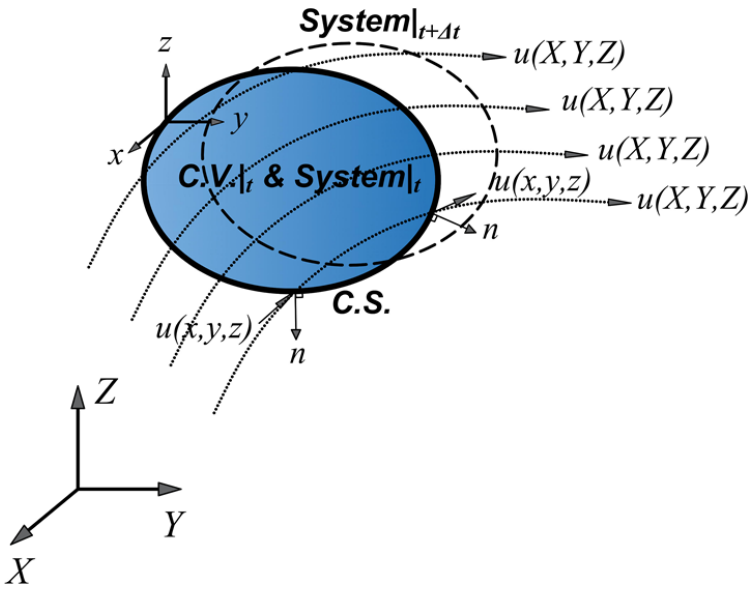

Figure 11: Schematic representation of Reynolds transport theorem.

By the utilization of Reynolds transport theorem, the change in a parameter measured by Lagrangian approach can be related to its corresponding expression defined based on Eulerian approach as follows (Shames, 2003; Spencer, 2004; Reddy, 2007; Belytschko et al., 2013):

$$\left.\frac{dN}{dt}\right|_{System} = \frac{DN}{Dt} = \frac{\partial}{\partial t}\int_{C.V.}\eta dV + \oint_{C.S.}\eta u(x,y,z,t).ndA \qquad \text{Eq. 76}$$

where u represents the velocity of an arbitrary material particle, N is an scalar-valued function or a vector field contained in material volume which can be transformed by the material velocity and η is the amount of N per unit volume of the control volume, i.e. $N = \int_{C.V.}\eta dV$. In this equation, *C.V.* stands for control volume which is a volume of space where an amount of fluid mass, i.e. system, is passing from at time t. Also, x, y and z represent local coordinate system attached to the control volume while X, Y and Z denote the inertial coordinate system. Also, the term *C.S.* denotes the control surface which is the surface surrounding the control volume with the normal vector of n. For immobile control volume, the local and global coordinate systems are aligned, and the Reynolds transport theorem is defined as follows:

$$\left.\frac{dN}{dt}\right|_{System} = \frac{DN}{Dt} = \frac{\partial}{\partial t}\int_{C.V.}\eta dV + \oint_{C.S.}\eta u(X,Y,Z,t).ndA \qquad \text{Eq. 77}$$

Using the Reynolds transport theorem, mass conservation equation can be formulated

using Eulerian method by considering $N = M = \int \rho dV$ by the following equation:

$$\frac{DM}{Dt} = \frac{D}{Dt}\int_{System} \rho dV = \frac{\partial}{\partial t}\int_{C.V.} \rho dV + \oint_{C.S.} \rho u.ndA = 0 \qquad \text{Eq. 78}$$

where ρ is the mass per unit volume of fluid. Using the divergence and Leibnitz's theorem, the above equation can be rewritten as

$$\frac{DM}{Dt} = \frac{D}{Dt}\int_{System} \rho dV = \int_{C.V.} \left(\frac{\partial \rho}{\partial t} + \nabla.\rho u\right) dV = 0 \qquad \text{Eq. 79}$$

Therefore, the above integral equation can be written in differential form as follows:

$$\frac{\partial \rho}{\partial t} + \nabla.\rho u = 0 \qquad \text{Eq. 80}$$

The above mass conservation equation is formulated using Reynolds transport theorem for a control volume which is totally occupied by fluid. However, in the fluid flow through porous media, the control volume is filled with both porous solid phase and fluid phase moving through the pore spaces of the solid phase. Therefore, in order to account for the portion of control volume occupied by porous solid phase, Reynolds transport theorem shall be modified as follows:

$$\left.\frac{dN}{dt}\right|_{System} = \frac{DN}{Dt} = \frac{\partial}{\partial t}\int_{C.V.} \eta\phi dV + \oint_{C.S.} \eta u.ndA \qquad \text{Eq. 81}$$

where V is the volume of porous media and ϕ is the porosity representing the ratio of the pore volume to the total volume of porous media. By neglecting the fillings in fractures, porosity for fractures is assumed to be equal to 1. Therefore, the mass conservation equation for porous media in integral and differential form is derived as

$$\frac{\partial}{\partial t}\int_{C.V.} \rho\phi dV + \oint_{C.S.} \rho u.ndA = 0 \qquad \text{Eq. 82}$$

$$\frac{\partial(\phi\rho)}{\partial t} + \nabla.\rho u = 0 \qquad \text{Eq. 83}$$

Using the same procedure, the linear momentum conservation equation can be achieved in Eulerian method by considering $N = \int \rho u dV$ as

$$\oint_{C.S.} tdA + \int_{C.V.} \rho b dV = \frac{D}{Dt}\int_{System} \rho u dV = \frac{\partial}{\partial t}\int_{C.V.} \rho u dV + \oint_{C.S.} \rho uu.ndA \quad \text{Eq. 84}$$

where t is traction applied on control surface and b denotes the body force per unit mass. Using Cauchy's theorem, the above equation can be rewritten as follows:

$$\oint_{C.S.} \sigma.ndA + \int_{C.V.} \rho b dV = \frac{\partial}{\partial t}\int_{C.V.} \rho u dV + \oint_{C.S.} \rho uu.ndA \quad \text{Eq. 85}$$

where σ is Cauchy's stress tensor representing forces per unit surface of material differential elements with current deformed configuration. Using divergence theorem, the surface integrals in the above equation can be replaced by volume integrals as

$$\int_{C.V.} (\nabla.\sigma + \rho b) dV = \frac{\partial}{\partial t}\int_{C.V.} \rho u dV + \oint_{C.V.} u\nabla.(\rho u) dV \quad \text{Eq. 86}$$

Using Leibnitz's theorem, the above equation can be rearranged as follows:

$$\int_{C.V.} \left[\frac{\partial(\rho u)}{\partial t} + u\nabla.(\rho u) - \nabla.\sigma - \rho b\right] dV = 0 \quad \text{Eq. 87}$$

Therefore, the linear momentum conservation equation is derived in the differential form as follows:

$$\frac{\partial(\rho u)}{\partial t} + u\nabla.(\rho u) - \nabla.\sigma - \rho b = 0 \quad \text{Eq. 88}$$

Using the Stokes constitutive law for the material behavior of the fluid particles, the deviatoric stress tensor τ_{ij} is related to the rate of strains tensor $\dot{\varepsilon}$ as follows (Spencer, 2004; Shames, 2003, Reddy, 2007):

$$\tau_{ij} = 2\mu\dot{\varepsilon}_{ij} \quad \text{Eq. 89}$$

$$\sigma_{ij} = \frac{\sigma_{kk}}{3}\delta_{ij} + \tau_{ij} = -P\delta_{ij} + \tau_{ij} \quad \text{Eq. 90}$$

where μ is dynamic viscosity of fluid and P is pressure. The rate of strains $\dot{\varepsilon}$ is defined based on the velocity gradient which is schematically shown in Figure 12.

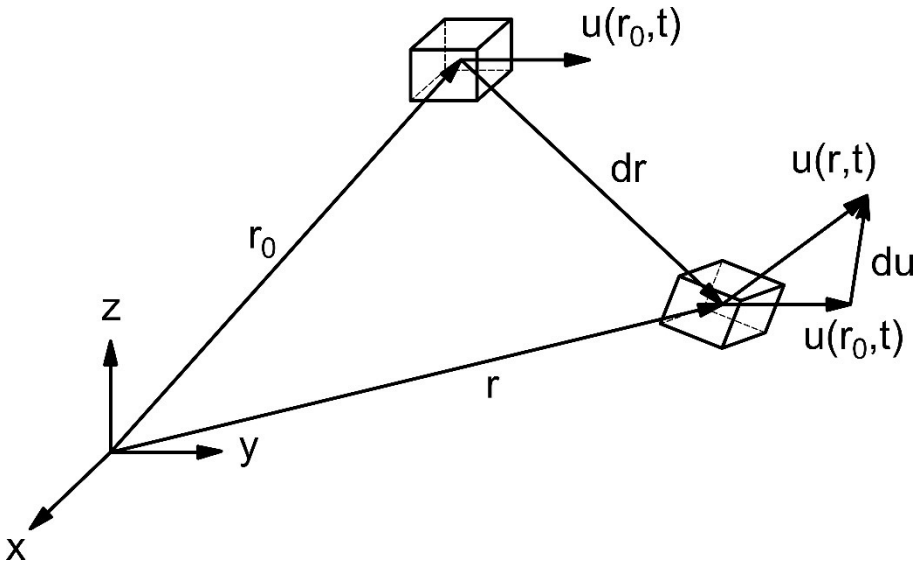

Figure 12: Schematic representation of velocity gradient of fluid particles.

The velocity gradient of fluid particles can be decomposed into symmetric and anti-symmetric tensors called rate of strain and rate of rotation tensors, respectively, as follows:

$$\nabla u = \frac{\partial u_i}{\partial x_j} = \dot{\varepsilon}_{ij} + \dot{\Omega}_{ij} \qquad \text{Eq. 91}$$

$$\dot{\varepsilon}_{ij} = \frac{1}{2}\left(\frac{\partial u_i}{\partial x_j} + \frac{\partial u_j}{\partial x_i}\right) \qquad \text{Eq. 92}$$

$$\dot{\Omega}_{ij} = \frac{1}{2}\left(\frac{\partial u_i}{\partial x_j} - \frac{\partial u_j}{\partial x_i}\right) \qquad \text{Eq. 93}$$

where $\dot{\Omega}$ is the rate of rotation tensor. Finally, by combining the Stokes constitutive equations and the linear momentum conservation equation, the Navier-Stokes equations of motion for incompressible fluid can be derived as follows:

$$\rho\left(\frac{\partial u}{\partial t} + u.\nabla u\right) = -\nabla P + \mu(\nabla^2 u) + \rho b \qquad \text{Eq. 94}$$

where the left-hand side of the above equation represents the inertial force, which is the multiplication of mass density and material acceleration Du/Dt. The material acceleration is defined as (Spencer, 2004; Shames, 2003; Reddy, 2007)

$$\frac{Du_i}{Dt} = \frac{\partial u_i}{\partial t} + \frac{\partial u_i}{\partial x_j}\frac{\partial x_j}{\partial t} = \frac{\partial u_i}{\partial t} + \frac{\partial u_i}{\partial x_j}u_j \quad \text{Eq. 95}$$

If it is assumed that the only body force acting on the material is the gravitational force and vertical coordinate z is aligned with the direction of gravity with upward positive direction, the Navier-Stokes equations for incompressible fluid can be rewritten as

$$\rho\frac{Du}{Dt} = -\nabla(P - \rho g z) + \mu(\nabla^2 u) \quad \text{Eq. 96}$$

In the case of fluid flow through porous media, by assuming small fluid velocity, the inertial force term in the Navier-Stokes equations can be neglected. Using this assumption, by volume averaging of Navier-Stokes equations in a porous medium volume, the Darcy's equation can be derived as follows (Hubbert, 1956):

$$u_i = -\frac{K}{\mu}\frac{\partial}{\partial x_i}(P - \rho g z) \quad \text{Eq. 97}$$

where u is the Darcy velocity of the fluid representing the average velocity of the fluid per unit area of the porous media. The parameters P, μ, ρ and g respectively denote the pressure, dynamic viscosity, specific mass of the fluid and gravitational acceleration. In addition, the parameter K is the permeability of the porous matrix determining the extent to which the porous matrix can allow the fluid to pass through it. Permeability is a scalar by assuming isotropic porous media and a tensor for anisotropic porous media.

Moreover, Navier-Stokes equations can be simplified to Reynolds equation for fluid flow through parallel planes assuming no-slip boundary conditions, negligent inertial force, zero flow velocity perpendicular to the planes, and negligent second derivative of velocity in the directions parallel to the planes (Reynolds, 1886). Reynolds equation can be used to model fluid flow through fractures by assuming zero velocity for the fracture planes and assuming that the gap between the fracture planes called aperture does not change in the plane of fracture. Based on these assumptions, Navier-Stokes equations are simplified as follows:

$$\frac{\partial^2 u_i}{\partial z^2} = \frac{1}{\mu}\frac{\partial}{\partial x_i}(P - \rho g z) \quad \text{Eq. 98}$$

where x_i represents x and y coordinates in the directions parallel to the fracture

surfaces while z denotes the coordinate perpendicular to the fracture. By integrating the above equations in the direction normal to the fracture plane and applying boundary conditions at the fracture surfaces, the average velocity passing through the gap between the fracture surfaces in the plane of fracture is derived as (Zimmerman and Bodvarsson, 1996)

$$u_i = -\frac{K}{\mu}\frac{\partial}{\partial x_i}(P - \rho g z) \qquad \text{Eq. 99}$$

$$K = \frac{e^2}{12} \qquad \text{Eq. 100}$$

where K denotes the permeability of fracture and e is the fracture aperture. By multiplying the above equation with the aperture, the flow rate passing through the fractures can be represented by the fallowing equation called the cubic law (Zimmerman and Bodvarsson, 1996):

$$q_i = -\frac{e^3}{12\mu}\frac{\partial}{\partial x_i}(P - \rho g z) \qquad \text{Eq. 101}$$

4.2 Conservation Equations for Multi-Phase Fluid Flow in Fractured Porous Media

In this research, in order to mathematically formulate the transport of multi-phase fluid through fractured porous media, the black-oil model is employed. In this model, the multi-phase fluid is assumed to be a continuum media comprised of three major immiscible fluids, namely non-aqueous liquid, e.g. oil, aqueous liquid, i.e. water, and gas which is either free or dissolved in aqueous and non-aqueous liquids. In such formulation, instead of applying the conservation equations in microscopic pore level, the equations are derived for an average connected pore volume as a fraction of the whole porous media volume using the concept of average porosity which is a macroscopic scalar.

As it was demonstrated in the derivation of equations of motion for single-phase fluid, the Navier-Stokes equations can be simplified into Darcy's law and Reynolds equation in the case of fluid flow through pore spaces and fractures, respectively. Therefore, the utilization of Darcy's law and Reynolds equation implies that the momentum

conservation equation and constitutive relations between stress and rate of strain in fluid are satisfied. Darcy's law can be extended for the case of multi-phase Newtonian fluid flow in porous media under gravitational force, pressure gradient, viscous frictional force, and interfacial tension by assuming that the inertial force can be ignored. Based on such extension, the generalized Darcy's law for multi-phase fluid flow is represented as follows (Fanchi et al., 1982; Trangenstein and Bell, 1989; Wu, 2016):

$$\{u_i^{\mathscr{p}}\}_{Porous\ Matrix} = -\frac{Kk_r^{\mathscr{p}}}{\mu^{\mathscr{p}}}\nabla(P^{\mathscr{p}} - \rho^{\mathscr{p}} gz) \qquad \text{Eq. 102}$$

where $\mathscr{p}$ is an index representing the fluid phases, i.e. $\mathscr{p} = o$ for oil phase, $\mathscr{p} = g$ for gas phase and $\mathscr{p} = w$ for water phase, and $u_i^{\mathscr{p}}$ is the Darcy velocity of the fluid phase $\mathscr{p}$ representing the average velocity of the fluid phase per unit area of the porous media. The parameters $P^{\mathscr{p}}$, $\mu^{\mathscr{p}}$ and $\rho^{\mathscr{p}}$ respectively denote the pressure, viscosity and specific mass of the fluid phase $\mathscr{p}$. Also, based on the indicial or Einstein notation, the term $\frac{\partial}{\partial x_i}$ represents gradient and x_i denotes the three components of the coordinate system where *i=1* and *2* represents *x* and *y* or horizontal coordinates while *i=3* represents *z* or vertical coordinate aligned with gravity direction with upward positive direction. In addition, the parameter K is absolute permeability, which is a scalar by assuming isotropic porous media and a tensor for anisotropic porous media, while $k_r^{\mathscr{p}}$ is the relative permeability of the fluid phase $\mathscr{p}$.

It should be mentioned that although in Darcy's law the inertial force is neglected, it can be generalized for the condition where the flow velocity is so high that the inertial effects cannot be neglected, i.e. Reynolds number is greater than 10. In this regard, extra terms can be added to the Darcy's law to consider inertial effects. Also, in the case of non-Newtonian fluid, a variable viscosity can be defined for the fluid phases as a function of different variables. As it was demonstrated in previous section, in the case of fluid flow through fractures, the Navier-Stokes equation is simplified to the Reynolds equation or cubic law which is generalized for multi-phase fluid flow as follows (Karimi-Fard et al., 2004):

$$\{u_i^{\mathscr{p}}\}_{Fracture} = -\frac{Kk_r^{\mathscr{p}}}{\mu^{\mathscr{p}}}\nabla(P^{\mathscr{p}} - \rho^{\mathscr{p}} gz) \qquad \text{Eq. 103}$$

As it was shown in the previous section, absolute permeability of fracture denoted by K is related to squared fracture aperture as $K=e^2/12$. In the problems where hydro-mechanical coupling of multi-phase flow is considered, porosity, absolute permeability and fracture aperture are dependent on pore fluid pressure as well as stress field and constitutive model in solid phase.

In multi-phase fluid flow through fractured porous media, transport of fluid phases are mainly governed by gravitational force, viscous frictional force, pressure gradient and the effects of interfacial tension at the interface of fluid phases as well as the interface of fluid phases and solid phase. In this regard, the effects of interfacial tension is frequently taken into account by defining the concepts of capillary pressure and relative permeability. In multi-phase fluid flow through porous media, due to the intermolecular forces, the degree of maintaining in contact with solid phase called wettability is different for each liquid phases. Therefore, one of the liquid phases, e.g. water or oil, wets the solid phase called wetting phase. Wettability of each fluid phase results from the interaction of adhesive forces, existing between the molecules of a fluid phase and solid phase, and cohesive forces, existing between the fluid phase molecules. Wettability can be approximated based on contact angles and depends on the mineral properties of solid phase, composition of the fluid phases and history of saturation. It should also be mentioned that in conventional situations, natural gas is non-wetting phase.

Based on the concept of wettability in multi-phase fluid flow, two distinct transport processes can be defined, namely imbibition and drainage. In the imbibition process, multi-phase fluid flow leads to the increase in the saturation of the wetting fluid phase, while, in the drainage process, the saturation of the wetting phase decreases (Wu, 2016). Due to the different wettability of fluid phases and interfacial tension existing between fluid interfaces, pressure in different phases are not equal and the pressure in the less-wetting phase is higher. This phenomenon implies the concept of capillary pressure which is defined as the difference between the pressures in different fluid phases. Consequently, in the case of three-phase oil-gas-water fluid flow, two capillary pressures can be defined, namely oil-gas and oil-water capillary pressures, by assuming the existence of two interfaces between the fluid phases. Capillary pressure primarily relies on the properties of solid phase and fluid phases, pore sizes in the solid phase and saturation of each fluid phases. However, by assuming that the properties of fluid phases and solid phase are

constant during the numerical analyses and by neglecting the capillary pressure change due to porosity variation, it can be assumed that capillary pressure only changes as a function of the saturation of different fluid phases.

Moreover, in multi-phase fluid flow, the permeability of different phases through porous media is defined by effective permeability. In numerical simulation, it is more desirable to normalize the effective permeability of each fluid phase by absolute permeability to obtain relative permeability of the phases. Relative permeability of fluid phases mainly relies on the saturation of the fluid phase, wettability, distribution of pore size and history of saturation. It is also slightly influenced by fluid phases as well as solid phase properties and flow rate (Wu, 2016). However, it is frequently assumed that the only time varying parameter affecting the relative permeability is the saturation of fluid phases. Therefore, relative permeability of a fluid phase can be defined as a function of the saturation of the fluid phase. It should also be mentioned, capillary pressures in fractures can be assumed to be equal to zero, and also the relative permeability functions for fractures can be approximated by straight lines (Wu, 2016).

In the formulation of equations of motion of multi-phase fluid through fractured porous media, the other conservation equation which should be satisfied in control volumes, containing pore spaces in porous matrix and planar fluid conduits in fractures, is the mass conservation equation. To this end, at the reservoir condition for pressure and temperature, the Reynolds transport theorem is rewritten as follows:

$$dN|_{System} = d\int_{C.V.} \eta\phi dV + \oint_{C.S.} \eta u.ndAdt + \int qdVdt \qquad \text{Eq. 104}$$

In this equation, the term $u.ndAdt$ represents the volume of fluid entering or exiting the control volume from control surface and q denotes the flow rate of N per unit volume of porous media either entering the control volume, i.e. source or injector case with $q \geq 0$, or exiting control volume, i.e. sink or producer case with $q \leq 0$. Based on the above equation, the mass conservation for each fluid phases are satisfied by the following equation:

$$dM^{\mathcal{P}}|_{System} = d\int_{C.V.} \left[\frac{\rho_{SC}^{\mathcal{P}}}{B^{\mathcal{P}}} S^{\mathcal{P}} + \sum_{i=1}^{3} \frac{R_{s\mathcal{P}}^{\mathcal{P}_i}\rho_{SC}^{\mathcal{P}}}{B^{\mathcal{P}_i}} S^{\mathcal{P}_i}\right] \phi dV + \oint_{C.S.} \left[\rho_{SC}^{\mathcal{P}} \frac{u^{\mathcal{P}}.ndAdt}{B^{\mathcal{P}}} + \sum_{i=1}^{3} R_{s\mathcal{P}}^{\mathcal{P}_i}\rho_{SC}^{\mathcal{P}} \frac{u^{\mathcal{P}_i}.ndAdt}{B^{\mathcal{P}_i}}\right] + \int q^{\mathcal{P}} dVdt = 0 \qquad \text{Eq. 105}$$

where ϕ is effective porosity, $S^{\mathscr{p}}$ is saturation of the fluid phase $\mathscr{p}$, $\rho_{SC}^{\mathscr{p}}$ is the density of the fluid phase $\mathscr{p}$ in standard temperature and pressure condition, i.e. 16° C and 101.33 KPa, and $u^{\mathscr{p}}$ is the velocity of the fluid phase $\mathscr{p}$. Also, n is the unit vector normal to the control surface and $q^{\mathscr{p}}$ denotes the mass source or sink of fluid phase $\mathscr{p}$ in the control volume. In this equation, the parameter $B^{\mathscr{p}}$ represents volume factor of fluid phase $\mathscr{p}$ which is the ratio of the volume of fluid phase $\mathscr{p}$ in reservoir condition, $V_{RC}^{\mathscr{p}}$, to that in standard condition, $V_{SC}^{\mathscr{p}}$, i.e. $B^{\mathscr{p}} = V_{RC}^{\mathscr{p}}/V_{SC}^{\mathscr{p}}$. In addition, the parameter $R_{s\mathscr{p}}^{\mathscr{p}_i}$ denotes the solubility of a dissolved fluid phase in other fluid phases which is defined as the ratio of the volume of dissolved fluid phase represented by $V_{SC}^{DS\,\mathscr{p}\,in\,\mathscr{p}_i}$ in fluid phase $\mathscr{p}_i$ in standard condition to the volume of fluid phase $\mathscr{p}_i$ in standard condition, $V_{SC}^{\mathscr{p}_i}$, i.e. $R_{s\mathscr{p}}^{\mathscr{p}_i} = V_{SC}^{DS\,\mathscr{p}\,in\,\mathscr{p}_i}/V_{SC}^{\mathscr{p}_i}$. The above equation can be rearranged as

$$\left.\frac{dM^{\mathscr{p}}}{dt}\right|_{System} = \frac{\partial}{\partial t}\int_{C.V.}\left[\frac{\rho_{SC}^{\mathscr{p}}}{B^{\mathscr{p}}}S^{\mathscr{p}} + \sum_{i=1}^{3}\frac{R_{s\mathscr{p}}^{\mathscr{p}_i}\rho_{SC}^{\mathscr{p}}}{B^{\mathscr{p}_i}}S^{\mathscr{p}_i}\right]\phi dV + \oint_{C.S.}\left[\rho_{SC}^{\mathscr{p}}\frac{u^{\mathscr{p}}.ndA}{B^{\mathscr{p}}} + \sum_{i=1}^{3}R_{s\mathscr{p}}^{\mathscr{p}_i}\rho_{SC}^{\mathscr{p}}\frac{u^{\mathscr{p}_i}.ndA}{B^{\mathscr{p}_i}}\right] + \int q^{\mathscr{p}}dV = 0 \quad \text{Eq. 106}$$

Using the divergence and Leibnitz's theorem, the above equation can be rewritten as

$$\left.\frac{dM^{\mathscr{p}}}{dt}\right|_{System} = \int_{C.V.}\left[\frac{\partial}{\partial t}\left(\frac{\rho_{SC}^{\mathscr{p}}}{B^{\mathscr{p}}}S^{\mathscr{p}}\phi + \sum_{i=1}^{3}\frac{R_{s\mathscr{p}}^{\mathscr{p}_i}\rho_{SC}^{\mathscr{p}}}{B^{\mathscr{p}_i}}S^{\mathscr{p}_i}\phi\right) + \nabla.\left(\frac{\rho_{SC}^{\mathscr{p}}}{B^{\mathscr{p}}}u^{\mathscr{p}}\right) + \sum_{i=1}^{3}\nabla.\left(\frac{R_{s\mathscr{p}}^{\mathscr{p}_i}\rho_{SC}^{\mathscr{p}}}{B^{\mathscr{p}_i}}u^{\mathscr{p}_i}\right) + q^{\mathscr{p}}\right]dV = 0 \quad \text{Eq. 107}$$

Therefore, the above integral equation can be rewritten in differential form as follows:

$$\frac{\partial}{\partial t}\left(\frac{\rho_{SC}^{\mathscr{p}}}{B^{\mathscr{p}}}S^{\mathscr{p}}\phi + \sum_{i=1}^{3}\frac{R_{s\mathscr{p}}^{\mathscr{p}_i}\rho_{SC}^{\mathscr{p}}}{B^{\mathscr{p}_i}}S^{\mathscr{p}_i}\phi\right) + \nabla.\left(\frac{\rho_{SC}^{\mathscr{p}}}{B^{\mathscr{p}}}u^{\mathscr{p}}\right) + \sum_{i=1}^{3}\nabla.\left(\frac{R_{s\mathscr{p}}^{\mathscr{p}_i}\rho_{SC}^{\mathscr{p}}}{B^{\mathscr{p}_i}}u^{\mathscr{p}_i}\right) + q^{\mathscr{p}} = 0 \quad \text{Eq. 108}$$

By assuming that gas is the only fluid phase which can be dissolved in other fluid phases, i.e. oil and water, the mass conservation equation for each phases is derived in differential form as follows (Fanchi et al., 1982; Trangenstein and Bell, 1989):

$$\frac{\partial}{\partial t}\left(\frac{S^{w}\phi}{B^{w}}\right)+\nabla.\left(\frac{u^{w}}{B^{w}}\right)+\frac{q^{w}}{\rho_{SC}^{w}}=0 \qquad \text{Eq. 109}$$

$$\frac{\partial}{\partial t}\left(\frac{S^{o}\phi}{B^{o}}\right)+\nabla.\left(\frac{u^{o}}{B^{o}}\right)+\frac{q^{o}}{\rho_{SC}^{o}}=0 \qquad \text{Eq. 110}$$

$$\frac{\partial}{\partial t}\left[\left(\frac{S^{g}}{B^{g}}+\frac{R_s^{w}S^{w}}{B^{w}}+\frac{R_s^{o}S^{o}}{B^{o}}\right)\phi\right]+\nabla.\left(\frac{u^{g}}{B^{g}}+\frac{R_s^{w}u^{w}}{B^{w}}+\frac{R_s^{o}u^{o}}{B^{o}}\right)+\frac{q^{g}}{\rho_{SC}^{g}}=0 \qquad \text{Eq. 111}$$

where $R_s^{w}=V_{SC}^{DS\,g\,in\,w}/V_{SC}^{w}$ and $R_s^{o}=V_{SC}^{DS\,g\,in\,o}/V_{SC}^{o}$ denote the solubility of gas in water and oil, respectively. Also, the saturation of the fluid phases should satisfy the following equation:

$$S^{w}+S^{o}+S^{g}=1 \qquad \text{Eq. 112}$$

In the three-phase oil-gas-water fluid, due to the interfacial tension existing at the interface of fluid phases as well as the interface of fluid phases and solid phase, there exist differences between the pressures of each fluid phases which can be represented by the capillary pressure concept as follows:

$$P^{o}-P^{w}=P_c^{ow} \qquad \text{Eq. 113}$$

$$P^{g}-P^{O}=P_c^{go} \qquad \text{Eq. 114}$$

where P_c^{ow} and P_c^{go} are oil-water and gas-oil capillary pressures, respectively, and it is assumed that water is the wetting phase. As it can be seen, in the governing differential equations of black oil model, there are 9 unknowns, namely 3 velocities, 3 pressures and 3 saturations of the three fluid phases. Also, there are 9 equations, namely 3 equations represented by Darcy's law or cubic law, 3 mass conservation equations, 2 capillary pressure equations and one equation for the saturation summation. Therefore, the partial differential equations of motion of multi-phase fluid flow through fractured porous media can be solved numerically provided that the material parameters in these equations are determined based on experimental data. In this regard, the mass density of different phases is calculated as follows:

$$\rho^{w}=\left(\frac{V_{Res}^{w}}{B^{w}}\rho_{SC}^{w}+\frac{R_s^{w}V_{Res}^{w}}{B^{w}}\rho_{SC}^{g}\right)/V_{Res}^{w}=\frac{1}{B^{w}}\left(\rho_{SC}^{w}+R_s^{w}\rho_{SC}^{g}\right) \qquad \text{Eq. 115}$$

$$\rho^{o} = \left(\frac{V_{Res}^{o}}{B^{o}}\rho_{SC}^{o} + \frac{R_s^{o}V_{Res}^{o}}{B^{o}}\rho_{SC}^{g}\right)/V_{Res}^{o} = \frac{1}{B^{o}}\left(\rho_{SC}^{o} + R_s^{o}\rho_{SC}^{g}\right) \quad \text{Eq. 116}$$

$$\rho^{g} = \left(\frac{V_{Res}^{g}}{B^{g}}\rho_{SC}^{g}\right)\Big/V_{Res}^{g} = \frac{\rho_{SC}^{g}}{B^{g}} \quad \text{Eq. 117}$$

Ideally, in order to determine the capillary pressures and relative permeability, three-phase experimental data should be employed. However, so far, very few experimental and theoretical investigations have been carried out on the determination of capillary pressure and relative permeability in three-phase condition compared to the two-phase condition. Therefore, in order to deal with this lack of constitutive modeling, the capillary pressure and relative permeability for three-phase condition are usually approximated based on the experimental data existing for separate two-phase systems (Wu, 2016). Therefore, the capillary pressure can be determined based on two series of experiments performed on two-phase fluid systems. In this regard, the oil-water capillary pressure can be assumed to be a function of water saturation, i.e. $P_c^{ow} = f(S^w)$, and it can be determined based on two-phase oil-water experimental data. Also, using the same procedure, oil-gas capillary pressure can be determined by assuming that it is a function of gas saturation, $P_c^{og} = f(S^g)$, and it can be estimated based on experimental data available for two-phase oil-gas condition. Similarly, as there is a lack of experimental data to determine the relative permeability relations for three-phase fluid system, these relations are usually approximated based on available experimental data for two-phase fluid (Wu, 2016).

The parameters viscosity and formation volume factors for different fluid phases and the ratios of solution gas to oil and water are determined based on pressure-volume-temperature (PVT) experimental and field data for specific reservoir fluids and rock formation. In this regard, by assuming an isothermal condition, i.e. constant temperature, the formation volume factor, gas solubility and viscosity of phases are assumed to be a function of pressure in the corresponding phase. It should be mentioned that the non-aqueous fluid phase in which gas is assumed to be dissolved, e.g. oil, show two different behaviors for the pressures lower than the bubble point pressure and those greater than the bubble point pressure (Fanchi et al., 1982). For the pressures lower than bubble point pressure, the undersaturation response is observed where, by increasing pressure, the

gas solubility increases, and as a result the viscosity of the fluid phase decreases. Also, an increase in the dissolved gas raises the fluid phase volume which results in the growth of volume factor of the fluid phase. In contrast, when the pressure is greater than bubble point pressure, the fluid phase is saturated and the volume of dissolved gas and gas solubility in the fluid phase remains constant by increasing the pressure. Therefore, for pressures higher than bubble point pressure, by increasing pressure, the viscosity of the fluid increases while the volume of the fluid phase decreases resulting in the reduction in its volume factor.

Finally, as it is discussed in more details in Appendix B, by combining the mentioned 9 governing equations, the following pressure partial differential equation is achieved in which the only unknown is the oil pressure:

$$(B^w - R_s^w B^g)\left[\nabla.K\frac{k_r^w}{B^w\mu^w}\nabla P^o + CG^w - \frac{q^w}{\rho_{SC}^w}\right] + (B^o - R_s^o B^g)\left[\nabla.K\frac{k_r^o}{B^o\mu^o}\nabla P^o + CG^o - \frac{q^o}{\rho_{SC}^o}\right] + B^g\left[\nabla.K\left(\frac{k_r^g}{B^g\mu^g} + \frac{R_s^w k_r^w}{B^w\mu^w} + \frac{R_s^o k_r^o}{B^o\mu^o}\right)\nabla P^o + CG^g - \frac{q^g}{\rho_{SC}^g}\right] = \frac{\partial(C_t P^o)}{\partial t} \quad \text{Eq. 118}$$

As it can be seen in the above equation, P^o is the only unknown parameter that its time derivative is existing in the equation. Therefore, all the parameters in the above equation except for P^o can be assumed to be known from the previous time step. In the derivation of the above equation, it is assumed that volume factors, gas solubility and porosity are dependent on the oil pressure. Therefore, the compressibility of oil, C^o, compressibility of water, C^w, compressibility of gas, C^g, compressibility of solid phase or rock, C^{ro}, as well as the total compressibility, C^t, are defined relative to oil pressure, P^o, by the following equations (Fanchi et al., 1982; Trangenstein and Bell, 1989):

$$C^w = -\frac{1}{B^w}\frac{\partial B^w}{\partial P^o} + \frac{B^g}{B^w}\frac{\partial R_s^w}{\partial P^o} \quad \text{Eq. 119}$$

$$C^o = -\frac{1}{B^o}\frac{\partial B^o}{\partial P^o} + \frac{B^g}{B^o}\frac{\partial R_s^o}{\partial P^o} \quad \text{Eq. 120}$$

$$C^g = -\frac{1}{B^g}\frac{\partial B^g}{\partial P^o} \quad \text{Eq. 121}$$

$$C^{r\sigma} = -\frac{1}{\phi}\frac{\partial \phi}{\partial P^{\sigma}} \quad \text{Eq. 122}$$

$$C^{t} = C^{w}S^{w} + C^{\sigma}S^{\sigma} + C^{g}S^{g} + C^{r\sigma} \quad \text{Eq. 123}$$

In the above equations, the compressibility of solid phase in fractured porous media, i.e. rock compressibility, is defined relative to oil pressure, i.e. $C^{r\sigma}$. However, in order to update the rock compressibility based on the solid mechanical analyses during hydro-mechanical coupling iterations, the rock compressibility relative to average pore fluid pressure and its relation with rock compressibility relative to oil pressure shall be defined. To this end, the average pore fluid pressure, P, is defined by the following equations:

$$P = S^{\sigma}P^{\sigma} + S^{w}P^{w} + S^{g}P^{g} \quad \text{Eq. 124}$$

$$P = S^{\sigma}P^{\sigma} + S^{w}(P^{\sigma} - P_c^{\sigma w}) + S^{g}\left(P^{\sigma} + S^{g}P_c^{g\sigma}\right) \quad \text{Eq. 125}$$

$$P = P^{\sigma} + S^{g}P_c^{g\sigma} - S^{w}P_c^{\sigma w} \quad \text{Eq. 126}$$

Therefore, the compressibility of solid phase in fractured porous media relative to average pore fluid pressure, C^{r}, is defined as follows:

$$C^{r} = -\frac{1}{\phi}\frac{\partial \phi}{\partial P} \quad \text{Eq. 127}$$

In addition, the relation between rock compressibility relative to average pore fluid pressure, C^{r}, and rock compressibility relative to oil, non-aqueous pore fluid phase, pressure, $C^{r\sigma}$, is obtained by the following equations:

$$C^{r\sigma} = -\frac{1}{\phi}\frac{\partial \phi}{\partial P^{\sigma}} = -\frac{1}{\phi}\frac{\partial \phi}{\partial P}\frac{\partial P}{\partial P^{\sigma}} \quad \text{Eq. 128}$$

$$C^{r\sigma} = -\frac{1}{\phi}\frac{\partial \phi}{\partial P}\left[1 + \frac{\partial\left(S^{g}P_c^{g\sigma} - S^{w}P_c^{\sigma w}\right)}{\partial P^{\sigma}}\right] \cong C^{r} \quad \text{Eq. 129}$$

In coupled hydro-mechanical multi-phase fluid flow problems, the saturation of fluid phases are mostly in a range that the term $\frac{\partial\left(S^{g}P_c^{g\sigma} - S^{w}P_c^{\sigma w}\right)}{\partial P^{\sigma}}$ can be neglected relative to 1 implying $C^{r\sigma} \cong C^{r}$.

In the case of fluid flow through fractures, in the above partial differential equation, the

porosity of fracture is assumed to be equal to 1 if the fracture fillings are assumed to be negligible. However, this assumption makes a difficulty in the definition of the volume change in fracture control volumes as a function of pressure. Therefore, in order to utilize the above partial differential equation for the numerical simulation of fluid flow through fractures, a modification shall be applied to account for the compressibility of fractures by relating aperture change to pressure inside the fracture. In this research, a conceptual parameter called relative aperture is introduced, denoted by ϕ^*, to take into account fracture aperture changes in the pressure partial differential equation for the case of multi-phase fluid flow through fractures as follows:

$$\phi^* = \frac{V}{V_0} = \frac{e}{e_0} \qquad \text{Eq. 130}$$

where V and e are respectively current fracture volume and aperture while V_0 and e_0 are initial fracture volume and aperture, respectively. The current fracture aperture can be updated based on the current pressure in the fracture as a function of initial aperture, normal stiffness of fracture and displacement field in solid phase using the following equation:

$$e = e_0 + \frac{P}{k_n} \qquad \text{Eq. 131}$$

This equation can be written in terms of pressure change and fracture aperture in the previous time step of analysis as follows:

$$e^{t+\Delta t} = e^t + \frac{\Delta P}{k_n} \qquad \text{Eq. 132}$$

$$\frac{\partial e}{\partial P} = \frac{1}{k_n} \qquad \text{Eq. 133}$$

where k_n is the normal stiffness of fracture which is dependent on the displacement filed and constitutive model of solid phase. Consequently, using the introduced relation, compressibility of fracture control volumes can be expressed by the following equation:

$$C^r = \frac{1}{\phi^*}\frac{\partial \phi^*}{\partial P} = \frac{1}{e}\frac{\partial e}{\partial P} \qquad \text{Eq. 134}$$

In the pressure partial differential equation, the parameters CG^w, CG^o and CG^g represent the gravity and capillary pressures effects and are defined as follows:

$$CG^w = -\nabla.\left[\frac{Kk_r^w}{B^w\mu^w}\nabla(\rho^w gZ + P_c^{ow})\right] \qquad \text{Eq. 135}$$

$$CG^o = -\nabla.\left[\frac{Kk_r^o}{B^o\mu^o}\nabla(\rho^o gZ)\right] \qquad \text{Eq. 136}$$

$$CG^g = \nabla.\left[\frac{Kk_r^g}{B^g\mu^g}\nabla\left(P_c^{go} - \rho^g gZ\right) - R_s^w\frac{Kk_r^w}{B^w\mu^w}\nabla(P_c^{ow} + \rho^w gz) - R_s^o\frac{Kk_r^o}{B^o\mu^o}\nabla(\rho^o gz)\right] \qquad \text{Eq. 137}$$

After the numerical solution of the pressure partial differential equation and calculating the oil pressure at the end of each time step, the water and gas pressures can be updated based on the capillary pressure equations. Also, the saturation of water, oil and gas phases can be updated using the following equations:

$$\nabla.K\frac{k_r^w}{B^w\mu^w}\nabla P^o + CG^w - \frac{q^w}{\rho_{SC}^w} = \frac{\partial}{\partial t}\left(\frac{S^w\phi}{B^w}\right) \qquad \text{Eq. 138}$$

$$\nabla.K\frac{k_r^o}{B^o\mu^o}\nabla P^o + CG^o - \frac{q^o}{\rho_{SC}^o} = \frac{\partial}{\partial t}\left(\frac{S^o\phi}{B^o}\right) \qquad \text{Eq. 139}$$

4.3 Numerical Formulation by Finite Volume Discrete Fracture-Matrix Method

Although compressible multi-phase fluid flow through porous matrix represented by black-oil model has been numerically approached by finite difference method (Funchi et al. 1982) as well as finite volume and finite element methods (Bergamaschi et al., 1999), it has not been implemented in the framework of discrete fracture-matrix method so far. In this research, in order to numerically simulate the multi-phase fluid flow in fractured porous media, finite volume discrete fracture matrix method is utilized to discretize the pressure partial differential equation derived based on black-oil model in previous

section. To this end, the pressure equation is integrated over the finite control volumes, representing fractures and porous matrix, as follows:

$$\int (B^w - R_s^w B^g)\left[\nabla . K\frac{k_r^w}{B^w\mu^w}\nabla P^o + CG^w - \frac{q^w}{\rho_{SC}^w}\right]dV + \int (B^o - R_s^o B^g)\left[\nabla . K\frac{k_r^o}{B^o\mu^o}\nabla P^o + CG^o - \frac{q^o}{\rho_{SC}^o}\right]dV + \int B^g\left[\nabla . K\left(\frac{k_r^g}{B^g\mu^g} + \frac{R_s^w k_r^w}{B^w\mu^w} + \frac{R_s^o k_r^o}{B^o\mu^o}\right)\nabla P^o + CG^g - \frac{q^g}{\rho_{SC}^g}\right]dV = \int \frac{\partial C_t P^o}{\partial t}dV \quad \text{Eq. 140}$$

where V denotes the volume of the finite control volumes. By assuming isotropic permeability and constant total compressibility during each time step, the above integral equation is rearranged as

$$(B^w - R_s^w B^g)\int \nabla . \frac{k_r^w}{B^w\mu^w}K\nabla P^o dV + (B^w - R_s^w B^g)\int CG^w dV - \frac{(B^w - R_s^w B^g)}{\rho_{SC}^w}\int q^w dV + (B^o - R_s^o B^g)\int \nabla . \frac{k_r^o}{B^o\mu^o}K\nabla P^o dV + (B^o - R_s^o B^g)\int CG^o dV - \frac{(B^o - R_s^o B^g)}{\rho_{SC}^o}\int q^o dV + B^g\int \nabla . \left(\frac{k_r^g}{B^g\mu^g} + \frac{R_s^w k_r^w}{B^w\mu^w} + \frac{R_s^o k_r^o}{B^o\mu^o}\right)K\nabla P^o dV + B^g\int CG^g dV - \frac{B^g}{\rho_{SC}^g}\int q^g dV = C_t\frac{\partial}{\partial t}\int P^o dV \quad \text{Eq. 141}$$

The volume integrals of the divergence of pressure gradient can be replaced by surface integrals using divergence theorem as

$$(B^w - R_s^w B^g)\oint \frac{k_r^w}{B^w\mu^w}K\nabla P^o . ndA + C_{CG^w} + C_{q^w} + (B^o - R_s^o B^g)\oint \frac{k_r^o}{B^o\mu^o}K\nabla P^o . ndA + C_{CG^o} + C_{q^o} + B^g\oint \left(\frac{k_r^g}{B^g\mu^g} + \frac{R_s^w k_r^w}{B^w\mu^w} + \frac{R_s^o k_r^o}{B^o\mu^o}\right)K\nabla P^o . ndA + C_{CG^g} + C_{q^g} = C_t\frac{\partial\overline{P^o}}{\partial t}V \quad \text{Eq. 142}$$

where A denotes the surface surrounding the finite volumes. In this equation, the contribution of capillary pressures and gravity for water, oil and gas phases are respectively represented by the terms C_{CG^w}, C_{CG^o} and C_{CG^g} defined as follows:

$$C_{CG^w} = -(B^w - R_s^w B^g)\int \nabla.\left[\frac{Kk_r^w}{B^w \mu^w}\nabla(\rho^w gZ + P_c^{ow})\right]dV \quad \text{Eq. 143}$$

$$C_{CG^o} = -(B^o - R_s^o B^g)\int \nabla.\left[\frac{Kk_r^o}{B^o \mu^o}\nabla(\rho^o gZ)\right]dV \quad \text{Eq. 144}$$

$$C_{CG^g} = B^g\int \nabla.\left[\frac{Kk_r^g}{B^g\mu^g}\nabla\left(P_c^{go} - \rho^g gZ\right) - R_s^w\frac{Kk_r^w}{B^w\mu^w}\nabla(P_c^{ow} + \rho^w gZ) - R_s^o\frac{Kk_r^o}{B^o\mu^o}\nabla(\rho^o gZ)\right]dV \quad \text{Eq. 145}$$

Also, the flow rate of injected or produced water, oil and gas phases are respectively accounted for by the terms C_{q^w}, C_{q^o} and C_{q^g} defined as

$$C_{q^w} = -\frac{(B^w - R_s^w B^g)}{\rho_{SC}^w}\int q^w dV \quad \text{Eq. 146}$$

$$C_{q^o} = -\frac{(B^o - R_s^o B^g)}{\rho_{SC}^o}\int q^o dV \quad \text{Eq. 147}$$

$$C_{q^g} = -\frac{B^g}{\rho_{SC}^g}\int q^g dV \quad \text{Eq. 148}$$

As the finite volumes are assumed to be polyhedral, the surface integrals in the pressure partial differential equation are calculated over a finite number of planar faces. Therefore, using the finite volume approach, the pressure partial differential equation is discretized based on the average values of parameters as follows:

$$\begin{gathered}(B^w - R_s^w B^g)\sum_{i=1}^m \frac{\overline{k_r^w}_i}{\overline{B^w}_i\overline{\mu^w}_i}\overline{K}_i\overline{\nabla P^o}_i.n_i A_i + C_{CG^w} + C_{q^w} + \\ (B^o - R_s^o B^g)\sum_{i=1}^m \frac{\overline{k_r^o}_i}{\overline{B^o}_i\overline{\mu^o}_i}\overline{K}_i\overline{\nabla P^o}_i.n_i A_i + C_{CG^o} + C_{q^o} + \\ B^g\sum_{i=1}^m\left(\frac{\overline{k_r^g}_i}{\overline{B^g}_i\overline{\mu^g}_i} + \frac{\overline{R_s^w}_i\overline{k_r^w}_i}{\overline{B^w}_i\overline{\mu^w}_i} + \frac{\overline{R_s^o}_i\overline{k_r^o}_i}{\overline{B^o}_i\overline{\mu^o}_i}\right)\overline{K}_i\overline{\nabla P^o}_i.n_i A_i + C_{CG^g} + C_{q^g} = \\ C_t\frac{\partial\overline{P^o}}{\partial t}V\end{gathered} \quad \text{Eq. 149}$$

where m is the number of the faces of the finite volumes. Also, the overbar refers to the average values of parameters defined at the center of a surface or volume over which surface integrals or volume integrals are approximated using the single point Gaussian

numerical integration method. Using an implicit pressure-explicit saturation method, the pressure partial differential equation is discretized in time domain such that the pressures are defined at the current time step while the other parameters, particularly saturations, are defined at the previous time step as follows:

$$\sum_{i=1}^{m} \bar{\Lambda}_i{}^{\mathfrak{N}} \bar{K}_i{}^{\mathfrak{N}} \overline{\nabla P^{\sigma}}_i{}^{\mathfrak{N}+1} . n_i A_i + C_{CG^{w}}{}^{\mathfrak{N}} + C_{q^{w}}{}^{\mathfrak{N}} + C_{CG^{o}}{}^{\mathfrak{N}} + C_{q^{o}}{}^{\mathfrak{N}} + C_{CG^{g}}{}^{\mathfrak{N}} + C_{q^{g}}{}^{\mathfrak{N}} = C_t{}^{\mathfrak{N}} V^{\mathfrak{N}} \frac{\overline{P^{\sigma}}^{\mathfrak{N}+1} - \overline{P^{\sigma}}^{\mathfrak{N}}}{\Delta t} \quad \text{Eq. 150}$$

where $\mathfrak{N}$ represents the time at the previous time step, $\mathfrak{N}+1$ represents the time at the current time step, Δt is the time step length and $\bar{\Lambda}_i$ is defined as

$$\bar{\Lambda}_i = (B^{w} - R_S^{w} B^{g}) \frac{\overline{k_r^{w}}_i}{\overline{B^{w}}_i \overline{\mu^{w}}_i} + (B^{o} - R_S^{o} B^{g}) \frac{\overline{k_r^{o}}_i}{\overline{B^{o}}_i \overline{\mu^{o}}_i} + B^{g} \left(\frac{\overline{k_r^{g}}_i}{\overline{B^{g}}_i \overline{\mu^{g}}_i} + \frac{\overline{R_S^{w}}_i \overline{k_r^{w}}_i}{\overline{B^{w}}_i \overline{\mu^{w}}_i} + \frac{\overline{R_S^{o}}_i \overline{k_r^{o}}_i}{\overline{B^{o}}_i \overline{\mu^{o}}_i} \right) \quad \text{Eq. 151}$$

In order to approximate the average pressure gradient at the middle of the finite volume faces, i.e. $\overline{\nabla P^{\sigma}}_i$, the two-point flux approximation is utilized. To this end, as it is schematically shown in Figure 13, the flux passing through the ith face of a finite volume, $q_i^{P^{\sigma}}$, due to the pressure gradient can be approximated based on the difference between the pressure at the face midpoint and the pressures at the center of the finite volume and its ith adjacent finite volume as follows:

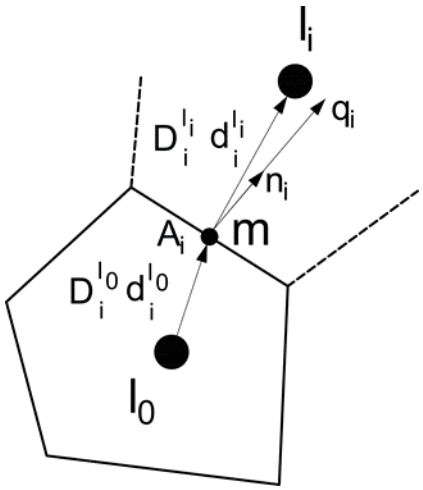

Figure 13: Matrix-matrix and matrix-fracture fluid transport in two-point flux approximation.

$$q_i^{P^\sigma} = \bar{\Lambda}_i \bar{K}_i \overline{\nabla P^\sigma}_i . n_i A_i = \bar{\Lambda}_i K_{l_0} \frac{\overline{P^\sigma}_{m_i} - \overline{P^\sigma}_{l_0}}{L_i^{l_0}} l_i^{l_0} . n_i A_i \quad \text{Eq. 152}$$

$$q_i^{P^\sigma} = \bar{\Lambda}_i K_{l_i} \frac{\overline{P^\sigma}_{l_i} - \overline{P^\sigma}_{m_i}}{L_i^{l_i}} l_i^{l_i} . n_i A_i \quad \text{Eq. 153}$$

Rearranging the above equations, the difference between the pressure at the face middle point and the finite volume centers is obtained as

$$\frac{1}{\bar{\Lambda}_i} \frac{1}{\alpha^{l_0}} q_i^{P^\sigma} = \overline{P^\sigma}_{m_i} - \overline{P^\sigma}_{l_0} \quad \text{Eq. 154}$$

$$\frac{1}{\bar{\Lambda}_i} \frac{1}{\alpha^{l_i}} q_i^{P^\sigma} = \overline{P^\sigma}_{l_i} - \overline{P^\sigma}_{m_i} \quad \text{Eq. 155}$$

$$\alpha^{l_i} = \frac{K_{l_i} A_i}{L_i^{l_i}} \left(l_i^{l_i} . n_i \right) \quad \text{Eq. 156}$$

Removing the pressure at the middle of the ith face, $\overline{P^\sigma}_{m_i}$, gives

$$\frac{1}{\bar{\Lambda}_i} \left(\frac{1}{\alpha^{l_0}} + \frac{1}{\alpha^{l_i}} \right) q_i^{P^\sigma} = \overline{P^\sigma}_{l_i} - \overline{P^\sigma}_{l_0} \quad \text{Eq. 157}$$

Therefore, the flux passing through the ith face of the finite volume is approximated based on the difference between pressures at the center of the finite volume and its adjacent finite volume as

$$q_i^{P^\sigma} = \bar{\Lambda}_i \bar{K}_i \overline{\nabla P^\sigma}_i . n_i A_i = \bar{\Lambda}_i \frac{\alpha^{l_0} \alpha^{l_i}}{\alpha^{l_0} + \alpha^{l_i}} \left(\overline{P^\sigma}_{l_i} - \overline{P^\sigma}_{l_0} \right) \quad \text{Eq. 158}$$

The above equation represents the two-point flux approximation method used for approximation of pressure gradient. By defining the term geometric transmissibility $T_{l_0 l_i}$ between the l_0th finite volume and its ith adjacent finite volume, i.e. l_ith finite volume, the two-point flux approximation is rewritten as follows:

$$T_{l_0 l_i} = \frac{\alpha^{l_0} \alpha^{l_i}}{\alpha^{l_0} + \alpha^{l_i}} \quad \text{Eq. 159}$$

$$q_i^{P^\sigma} = \bar{\Lambda}_i \bar{K}_i \overline{\nabla P^\sigma}_i . n_i A_i = \bar{\Lambda}_i T_{l_0 l_i} \left(\overline{P^\sigma}_{l_i} - \overline{P^\sigma}_{l_0} \right) \quad \text{Eq. 160}$$

In the formulation of fluid transmissibility at fracture intersections, infinitesimal control volumes appear at the intersections distributing the flux receiving from one of the fractures to the other fractures connected to the intersection. Considering such infinitesimal finite volumes in the discretization of fractured porous media, Numerical difficulties occur in multi-phase fluid flow simulation (Karimi-Fard et al., 2004). In order to resolve this issue, fluid transmissibility between intersecting fracture finite volumes, is obtained by satisfying mass conservation at fracture intersections. Using this method, there is no need to explicitly consider the infinitesimal fracture intersection finite volumes in the discretization of fractured porous media.

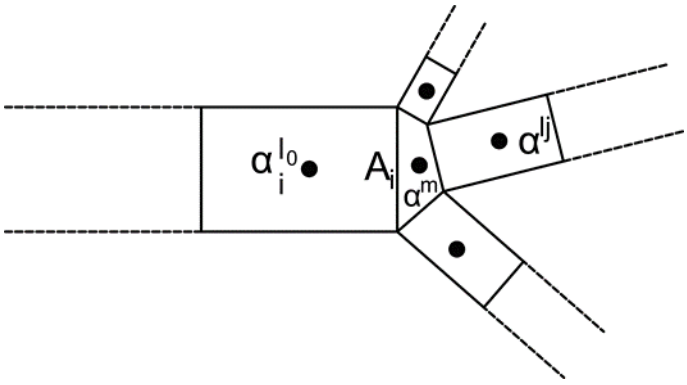

Figure 14: Fluid transmissibility at intersection of multiple fractures.

By satisfying mass conservation at the fracture intersection schematically shown in Figure 14, the following equations are achieved:

$$q_i^{P^\sigma} = \bar{\Lambda}_i \bar{K}_i \overline{\nabla P^\sigma}_i . n_i A_i = \bar{\Lambda}_i T_{l_0 m} \left(\overline{P^\sigma}_m - \overline{P^\sigma}_{l_0} \right) \quad \text{Eq. 161}$$

$$q_i^{P^\sigma} = \sum_{j=1}^{n} q_j^{P^\sigma} \quad \text{Eq. 162}$$

$$q_j^{P^\sigma} = \bar{\Lambda}_i T_{l_j m} \left(\overline{P^\sigma}_{l_j} - \overline{P^\sigma}_m \right) \quad \text{Eq. 163}$$

By combining the above equations, the relation between the flux entering the fracture intersection through one of the fractures can be related to the flux distributed to the other fractures at the fracture intersection as follows:

$$\bar{\Lambda}_i T_{l_0 m} \left(\overline{P^\sigma}_m - \overline{P^\sigma}_{l_0} \right) = \sum_{j=1}^{n} \bar{\Lambda}_i T_{l_j m} \left(\overline{P^\sigma}_{l_j} - \overline{P^\sigma}_m \right) \quad \text{Eq. 164}$$

By rearranging the above equation, pressure at the center of fracture intersection finite volume can be obtained by the following equation:

$$\overline{P^\sigma}_m = \frac{\sum_{j=1}^{n} T_{l_j m} \overline{P^\sigma}_{l_j} + T_{l_0 m} \overline{P^\sigma}_{l_0}}{\sum_{j=1}^{n} T_{l_j m} + T_{l_0 m}} \quad \text{Eq. 165}$$

In mass conservation equation at fracture intersections, by substituting pressure at the center of intersection finite volumes by the above relation, the following equation is obtained:

$$q_i^{P^\sigma} = \bar{\Lambda}_i \bar{K}_i \overline{\nabla P^\sigma}_i . n_i A_i = \bar{\Lambda}_i T_{l_0 m} \left(\frac{\sum_{j=1}^{n} T_{l_j m} \overline{P^\sigma}_{l_j} + T_{l_0 m} \overline{P^\sigma}_{l_0}}{\sum_{j=1}^{n} T_{l_j m} + T_{l_0 m}} - \overline{P^\sigma}_{l_0} \right) \quad \text{Eq. 166}$$

The above equation can be rewritten as

$$q_i^{P^\sigma} = \sum_{j=1}^{n} q_j^{P^\sigma} = \bar{\Lambda}_i T_{l_0 m} \frac{\sum_{j=1}^{n} T_{l_j m} \left(\overline{P^\sigma}_{l_j} - \overline{P^\sigma}_{l_0} \right)}{\sum_{j=1}^{n} T_{l_j m} + T_{l_0 m}} \quad \text{Eq. 167}$$

In the above equation, transmissibility between intersection finite volume and the fracture finite volume through which fluid is entering fracture intersection is approximated as follows:

$$L_i^{l_0} \gg L^m, \; K_{l_0} \simeq K_m \rightarrow T_{l_0 m} = \frac{\alpha^{l_0} \alpha^m}{\alpha^{l_0} + \alpha^m} \simeq \alpha^{l_0} \quad \text{Eq. 168}$$

$$L_i^{l_i} \gg L^m,\ K_{l_i} \simeq K_m \rightarrow T_{l_j m} = \frac{\alpha^{l_j}\alpha^m}{\alpha^{l_j}+\alpha^m} \simeq \alpha^{l_j} \quad \text{Eq. 169}$$

Therefore, the resulting flux equation can be simplified as follows:

$$q_j^{P^\sigma} = \bar{\Lambda}_i \frac{T_{l_0 m} T_{l_j m}}{\sum_{j=1}^{n} T_{l_j m} + T_{l_0 m}} \left(\overline{P^\sigma}_{l_j} - \overline{P^\sigma}_{l_0}\right) \quad \text{Eq. 170}$$

Finally, the flux equation at fracture intersection and fluid transmissibility at the intersection of fractures is achieved by the following equations:

$$q_j^{P^\sigma} = \bar{\Lambda}_i T_{l_0 l_j} \left(\overline{P^\sigma}_{l_j} - \overline{P^\sigma}_{l_0}\right) \quad \text{Eq. 171}$$

$$T_{l_0 l_j} = \frac{\alpha^{l_0}\alpha^{l_j}}{\sum_{j=1}^{n} \alpha^{l_j} + \alpha^{l_0}} \quad \text{Eq. 172}$$

Using the two-point flux approximation method and defining the parameters C_{CG} and C_q, the finite volume discretization of the pressure differential equation is achieved for l_0th finite volume as follows:

$$\sum_{i=1}^{m} \bar{\Lambda}_{i\,l_0}^{\Re} T_{l_0 l_i}^{\Re} \left(\overline{P^\sigma}_{l_i}^{\Re+1} - \overline{P^\sigma}_{l_0}^{\Re+1}\right) + C_{CG\,l_0}^{\Re} + C_{q\,l_0}^{\Re} = C_{t\,l_0}^{\Re} V_{l_0}^{\Re} \frac{\overline{P^\sigma}_{l_0}^{\Re+1} - \overline{P^\sigma}_{l_0}^{\Re}}{\Delta t} \quad \text{Eq. 173}$$

$$C_{CG\,l_0}^{\Re} = C_{CG^w\,l_0}^{\Re} + C_{CG^\sigma\,l_0}^{\Re} + C_{CG^\phi\,l_0}^{\Re} \quad \text{Eq. 174}$$

$$C_{q\,l_0}^{\Re} = C_{q^w\,l_0}^{\Re} + C_{q^\sigma\,l_0}^{\Re} + C_{q^\phi\,l_0}^{\Re} \quad \text{Eq. 175}$$

To determine the parameter $\bar{\Lambda}_{i\,l_0}^{\Re}$ in the above equation, the average values $\overline{B^{\mathcal{P}}}_{i\,l_0}^{\Re} = \left(B^{\mathcal{P}}{}_{l_i}^{\Re} + B^{\mathcal{P}}{}_{l_0}^{\Re}\right)/2$, $\overline{\mu^{\mathcal{P}}}_{i\,l_0}^{\Re} = \left(\mu^{\mathcal{P}}{}_{l_i}^{\Re} + \mu^{\mathcal{P}}{}_{l_0}^{\Re}\right)/2$ and $\overline{R_s^{\mathcal{P}}}_{i\,l_0}^{\Re} = \left(R_s^{\mathcal{P}}{}_{l_i}^{\Re} + R_s^{\mathcal{P}}{}_{l_0}^{\Re}\right)/2$ are utilized. Also, the average value $\overline{k_r^{\mathcal{P}}}_{i\,l_0}^{\Re}$ is assumed to be equal to the relative permeability of the finite volume which has the larger phase potential, $\Phi^{\mathcal{P}} = P^{\mathcal{P}} + \rho^{\mathcal{P}} g Z$. In order to approximate the capillary and gravity effect terms, C_{CG^w}, C_{CG^σ} and C_{CG^ϕ}, the same method as that used for pressure is employed. In this regard, the volume integrals are replaced by surface integrals using divergence theorem as

$$C_{CG^w} = -(B^w - R_s^w B^g) \oint \frac{k_r^w}{B^w \mu^w} K \nabla (\rho^w g Z + P_c^{ow}).ndA \quad \text{Eq. 176}$$

$$C_{CG^o} = -(B^o - R_s^o B^g) \oint \frac{k_r^o}{B^o \mu^o} K \nabla (\rho^o g Z).ndA \quad \text{Eq. 177}$$

$$C_{CG^g} = B^g \oint \frac{k_r^g}{B^g \mu^g} K \nabla \left(P_c^{go} - \rho^g g Z\right).ndA - B^g \oint \frac{R_s^w k_r^w}{B^w \mu^w} K \nabla (P_c^{ow} + \rho^w g Z).ndA - B^g \oint \frac{R_s^o k_r^o}{B^o \mu^o} K \nabla (\rho^o g Z).ndA \quad \text{Eq. 178}$$

The surface integrals in the capillary and gravity effect terms are obtained based on the average values as follows:

$$C_{CG^w} = -(B^w - R_s^w B^g) \sum_{i=1}^{m} \frac{\overline{k_r^w}_i}{\overline{B^w}_i \overline{\mu^w}_i} \bar{K}_i \overline{\nabla (\rho^w g Z + P_c^{ow})}_i . n_i A_i \quad \text{Eq. 179}$$

$$C_{CG^o} = -(B^o - R_s^o B^g) \sum_{i=1}^{m} \frac{\overline{k_r^o}_i}{\overline{B^o}_i \overline{\mu^o}_i} \bar{K}_i \overline{\nabla (\rho^o g Z)}_i . n_i A_i \quad \text{Eq. 180}$$

$$C_{CG^g} = B^g \sum_{i=1}^{m} \frac{\overline{k_r^g}_i}{\overline{B^g}_i \overline{\mu^g}_i} \bar{K}_i \overline{\nabla \left(P_c^{go} - \rho^g g Z\right)}_i . n_i A_i - B^g \sum_{i=1}^{m} \frac{\overline{R_s^w}_i \overline{k_r^w}_i}{\overline{B^w}_i \overline{\mu^w}_i} \bar{K}_i \overline{\nabla (P_c^{ow} + \rho^w g Z)}_i . n_i A_i - B^g \sum_{i=1}^{m} \frac{\overline{R_s^o}_i \overline{k_r^o}_i}{\overline{B^o}_i \overline{\mu^o}_i} \bar{K}_i \overline{\nabla (\rho^o g Z)}_i . n_i A_i \quad \text{Eq. 181}$$

Using the two-point flux approximation, the above equations are approximated based on the values of the parameters at the center of finite volumes and their ith adjacent finite volumes as

$$C_{CG^w} = -(B^w - R_s^w B^g) \sum_{i=1}^{m} \frac{\overline{k_r^w}_i}{\overline{B^w}_i \overline{\mu^w}_i} T_{l_0 l_i} \left(g \overline{\rho^w}_{l_i} \bar{Z}_{l_i} + \overline{P_c^{ow}}_{l_i} - g \overline{\rho^w}_{l_0} \bar{Z}_{l_0} - \overline{P_c^{ow}}_{l_0} \right) \quad \text{Eq. 182}$$

$$C_{CG^o} = -(B^o - R_s^o B^g) \sum_{i=1}^{m} \frac{\overline{k_r^o}_i}{\overline{B^o}_i \overline{\mu^o}_i} T_{l_0 l_i} \left(g \overline{\rho^o}_{l_i} \bar{Z}_{l_i} - g \overline{\rho^o}_{l_0} \bar{Z}_{l_0} \right) \quad \text{Eq. 183}$$

$$C_{CG^g} = B^g \sum_{i=1}^{m} \frac{\overline{k_r^g}_i}{\overline{B^g}_i \overline{\mu^g}_i} T_{l_0 l_i} \left(\overline{P_c^{g\sigma}}_{l_i} - g\overline{\rho^g}_{l_i} \bar{Z}_i - \overline{P_c^{g\sigma}}_{l_0} + g\overline{\rho^g}_{l_0} \bar{Z}_{l_0} \right) -$$

$$B^g \sum_{i=1}^{m} \frac{\overline{R_s^w}_i \overline{k_r^w}_i}{\overline{B^w}_i \overline{\mu^w}_i} T_{l_0 l_i} \left(\overline{P_c^{\sigma w}}_{l_i} + g\overline{\rho^w}_{l_i} \bar{Z}_{l_i} - \overline{P_c^{\sigma w}}_{l_0} - g\overline{\rho^w}_{l_0} \bar{Z}_{l_0} \right) - \quad \text{Eq. 184}$$

$$B^g \sum_{i=1}^{m} \frac{\overline{R_s^\sigma}_i \overline{k_r^\sigma}_i}{\overline{B^\sigma}_i \overline{\mu^\sigma}_i} T_{l_0 l_i} \left(g\overline{\rho^\sigma}_{l_i} \bar{Z}_{l_i} - g\overline{\rho^\sigma}_{l_0} \bar{Z}_{l_0} \right)$$

where the overbar refers to the average values at the finite volume center. Also, the injection-production terms are approximated based on the average values at the center of the finite volumes as

$$C_{q^w} = -\frac{(B^w - R_s^w B^g)}{\rho_{SC}^w} \overline{q^w} V \quad \text{Eq. 185}$$

$$C_{q^\sigma} = -\frac{(B^\sigma - R_s^\sigma B^g)}{\rho_{SC}^\sigma} \overline{q^\sigma} V \quad \text{Eq. 186}$$

$$C_{q^g} = -\frac{B^g}{\rho_{SC}^g} \overline{q^g} V \quad \text{Eq. 187}$$

Finally, after calculating the oil pressure, pressures in other phases can be calculated using the capillary pressures and the phase saturations are evaluated by integrating saturation equations over the finite control volumes as follows:

$$\int \nabla . K \frac{k_r^w}{B^w \mu^w} \nabla P^\sigma dV + \int CG^w dV - \int \frac{q^w}{\rho_{SC}^w} dV = \int \frac{\partial}{\partial t} \left(\frac{S^w \phi}{B^w} \right) dV \quad \text{Eq. 188}$$

$$\int \nabla . K \frac{k_r^\sigma}{B^\sigma \mu^\sigma} \nabla P^\sigma dV + \int CG^\sigma dV - \int \frac{q^\sigma}{\rho_{SC}^\sigma} dV = \int \frac{\partial}{\partial t} \left(\frac{S^\sigma \phi}{B^\sigma} \right) dV \quad \text{Eq. 189}$$

Therefore, using finite volume method, the phase saturations are calculated by the following equations:

$$\sum_{i=1}^{m}\frac{\overline{k_r^{w}}^{\Re}_{i_{l_0}}}{\overline{B^{w}}^{\Re}_{i_{l_0}}\overline{\mu^{w}}^{\Re}_{i_{l_0}}}T^{\Re}_{l_0 l_i}\left(\overline{P^{\sigma}}^{\Re+1}_{l_i}-\overline{P^{\sigma}}^{\Re+1}_{l_0}\right)+\frac{C_{CG^{w}}{}^{\Re}_{l_0}}{\left(B^{w}{}^{\Re}_{l_0}-R_s^{w}{}^{\Re}_{l_0}B^{g}{}^{\Re}_{l_0}\right)}+\frac{C_{q^{w}}{}^{\Re}_{l_0}}{\left(B^{w}{}^{\Re}_{l_0}-R_s^{w}{}^{\Re}_{l_0}B^{g}{}^{\Re}_{l_0}\right)}=\frac{\phi^{\Re}_{l_0}}{B^{w}{}^{\Re}_{l_0}}V^{\Re}_{l_0}\frac{\overline{S^{w}}^{\Re+1}_{l_0}-\overline{S^{w}}^{\Re}_{l_0}}{\Delta t}} \quad \text{Eq. 190}$$

$$\sum_{i=1}^{m}\frac{\overline{k_r^{\sigma}}^{\Re}_{i_{l_0}}}{\overline{B^{\sigma}}^{\Re}_{i_{l_0}}\overline{\mu^{\sigma}}^{\Re}_{i_{l_0}}}T^{\Re}_{l_0 l_i}\left(\overline{P^{\sigma}}^{\Re+1}_{l_i}-\overline{P^{\sigma}}^{\Re+1}_{l_0}\right)+\frac{C_{CG^{\sigma}}{}^{\Re}_{l_0}}{\left(B^{\sigma}{}^{\Re}_{l_0}-R_s^{\sigma}{}^{\Re}_{l_0}B^{g}{}^{\Re}_{l_0}\right)}+\frac{C_{q^{\sigma}}{}^{\Re}_{l_0}}{\left(B^{\sigma}{}^{\Re}_{l_0}-R_s^{\sigma}{}^{\Re}_{l_0}B^{g}{}^{\Re}_{l_0}\right)}=\frac{\phi^{\Re}_{l_0}}{B^{\sigma}{}^{\Re}_{l_0}}V^{\Re}_{l_0}\frac{\overline{S^{\sigma}}^{\Re+1}_{l_0}-\overline{S^{\sigma}}^{\Re}_{l_0}}{\Delta t}} \quad \text{Eq. 191}$$

After the pressure and saturation of phases are calculated, the velocity of each fluid phase can be calculated by the Darcy's law and cubic law as follows:

$$\Phi^{\mathcal{P}}=P^{\mathcal{P}}-\rho^{\mathcal{P}}gZ \quad \text{Eq. 192}$$

$$u_i^{\mathcal{P}}=-\sum_{j=1}^{m}\frac{\overline{k_r^{\mathcal{P}}}}{\overline{\mu^{\mathcal{P}}}}\overline{K}\overline{\nabla\Phi^{\mathcal{P}}} \quad \text{Eq. 193}$$

$$u_i^{\mathcal{P}}=-\sum_{j=1}^{m}\frac{\overline{k_r^{\mathcal{P}}}_{l_0 l_j}}{\overline{\mu^{\mathcal{P}}}_{l_0 l_j}}\frac{T_{l_0 l_j}}{A_j}\left(\overline{\Phi^{\mathcal{P}}}_{l_j}-\overline{\Phi^{\mathcal{P}}}_{l_0}\right)n_i^j \quad \text{Eq. 194}$$

In the above equation, n_i^j and A_j are the unit normal vector and area of the jth face of the control volume, and also the average relative permeability of phases $\overline{k_r^{\mathcal{P}}}$, average viscosity of phases $\overline{\mu^{\mathcal{P}}}$ and the transmissibility are calculated the same as before.

4.4 Time Stepping Method

In the developed finite volume discrete fracture-matrix approach, the pressure partial differential equation was integrated in time domain using an explicit method. In this method, the parameters involved in pressure equation are estimated based on their values in the previous time step. Therefore, the utilized time integration scheme is conditionally stable, and its accuracy is strongly affected by the time increment sizes chosen during the numerical solution. If the time step sizes are not controlled properly,

unstable numerical results might be encountered which brings about physically unsound numerical solution and unacceptable material balance errors. In order to ensure stable numerical solutions, an automatic time stepping scheme is utilized. In this time stepping method, the numerical solution is started with a predefined initial time step size. Then, at the end of each time step, the maximum pressure and saturation increment calculated in the finite volumes are compared with predefined tolerable values. If each of the maximum calculated pressure or saturation change is greater than the tolerances, the solution is repeated with a decreased time step size defined as follows:

$$\begin{cases} \boldsymbol{IF}\left\{max_{i=1}^{nz}\left(\delta\overline{P^{\sigma}}_i^r\right) > \Pi \ \boldsymbol{OR}\ max_{i=1}^{nz}\left(\delta\overline{S^{\wp}}_i^r\right) > \Psi\right\}\boldsymbol{THEN}\ \Delta t^{r+1} = \theta\Delta t^r \\ \boldsymbol{ELSE}\ \Delta t^{r+1} = \Theta\Delta t^r \end{cases} \quad \text{Eq. 195}$$

where nz is the number of finite volumes, $\delta\overline{P^{\sigma}}_i^r$ and $\delta\overline{S^{\wp}}_i^r$ respectively represent the calculated pressure and saturation increments in the ith finite volume at the rth repetition of current time step, and the operator max finds the maximum value of the parameter in the finite volumes. In this equation, parameters Π and Ψ respectively denote the predefined tolerance for pressure and saturation increments at the end of each time step, Δt^r and Δt^{r+1} respectively represent the time step sizes at the rth and $r+1$th repetition, and θ is the multiplication factor decreasing time step in the case where pressure or saturation increments exceed the tolerances. It should also be noted that in order to accelerate the solution in the case of slight pressure and saturation changes, the next time step size might be increased by the multiplication factor Θ if the pressure or saturation increments do not exceed the tolerances. In addition to the utilized time stepping scheme, as an additional numerical stability control, the material balance error which is the difference between the net total amounts of fluid phases injected into the porous media and the change in the amount of stored fluid phases in porous media, shall be monitored during the numerical analysis.

The finite volume discrete fracture-matrix approach numerically formulated in this chapter can be used to simulate multi-phase fluid flow through fractured porous media using a unified finite volume mesh for both fractures and porous matrix. The resulting linearized set of equations can be numerically solved using iterative methods as it is discussed in more details in Appendix C. In the next chapter, the numerical formulation devised for the finite volume discrete fracture-matrix approach is implemented in a

computational code developed in this research to numerically solve the equations of motion of multi-phase fluid flow through fractured porous media. The developed finite volume discrete fracture-matrix approach is also compatible with solid mechanical distinct element simulators. With the aid of this compatibility, a coupled hydro-mechanical multi-phase computational tool will be developed in sixth chapter of this thesis. In the following chapters, it is demonstrated how the developed numerical formulation can be utilized in the simulation of coupled hydro-mechanical multi-phase fluid flow through both pore spaces and complex fracture networks existing in fractured shale reservoirs.

5 Finite Volume Black Oil Simulator (FVBOS)

5.1 Implementation of the Developed Multi-Phase Fluid Flow Model

The finite volume discrete fracture-matrix formulation developed in the previous section for the simulation of coupled hydro-mechanical multi-phase fluid flow in fractured porous media is implemented into an object-oriented code using C++ programming language. The resulting finite volume code has been named Finite Volume Black Oil Simulator (FVBOS). In the following sections, the structure of the program as well as its input-output data are discussed, and the developed code is verified with different benchmark problems. The verification cases are designed to separately investigate the performance of the program in simulating pressure gradient, viscose frictional forces, gravity and interfacial tension in both matrix and fractures along with mass conservation at fracture intersections.

5.2 Structure of the Developed Object-Oriented C++ Code

In this research, in order to manage the computer programming of the coupled hydro-mechanical multi-phase fluid flow problem mathematically formulated in the previous sections, the structure of the program was designed with the aid of object-oriented programming approach using C++ programming language. Utilizing this method, all the processes required to be performed in the simulation are split into seven major components each of which concentrated on accomplishing specific objectives. The seven major components are designated to deal with the following tasks:

1. Processing finite volume grid data, creation of the link between proper material models and parameters and zones, and recognition of the neighboring zones attached to faces of each zone.
2. Storage of material properties of the multi-phase fluid and the hosting fractured porous media and performing the calculations needed to update these data during the numerical analysis.
3. Storage of the initial condition data defined for the fluid flow and creating the link

between these data and proper finite volume zones.

4. Processing the data representing boundary conditions as well as control parameters of numerical solution algorithms.
5. Coordination of external solid mechanics simulator processes during coupled hydro-mechanical simulations.
6. Conducting the numerical analysis of multi-phase fluid flow by using finite volume discrete fracture-matrix approach formulated in the previous section.
7. Extracting the numerical analysis results after accomplishing the solution at each time step for post-processing purposes such as creating graphs, contours and vector plots.

In order to write the C++ code performing the function of these components, the data type called class is utilized which is a user-defined data structure comprised of a number of member functions and variables. To this end, seven major classes were defined in the code, namely Grid, Material, InitialCondition, BondSolinCont, ExternalSimulatorProcess, Analysis and PostProcess. The functions and variables needed to perform the mentioned major processes are separately defined in the corresponding classes. The schematic structure of these seven major classes are illustrated in Figure 15.

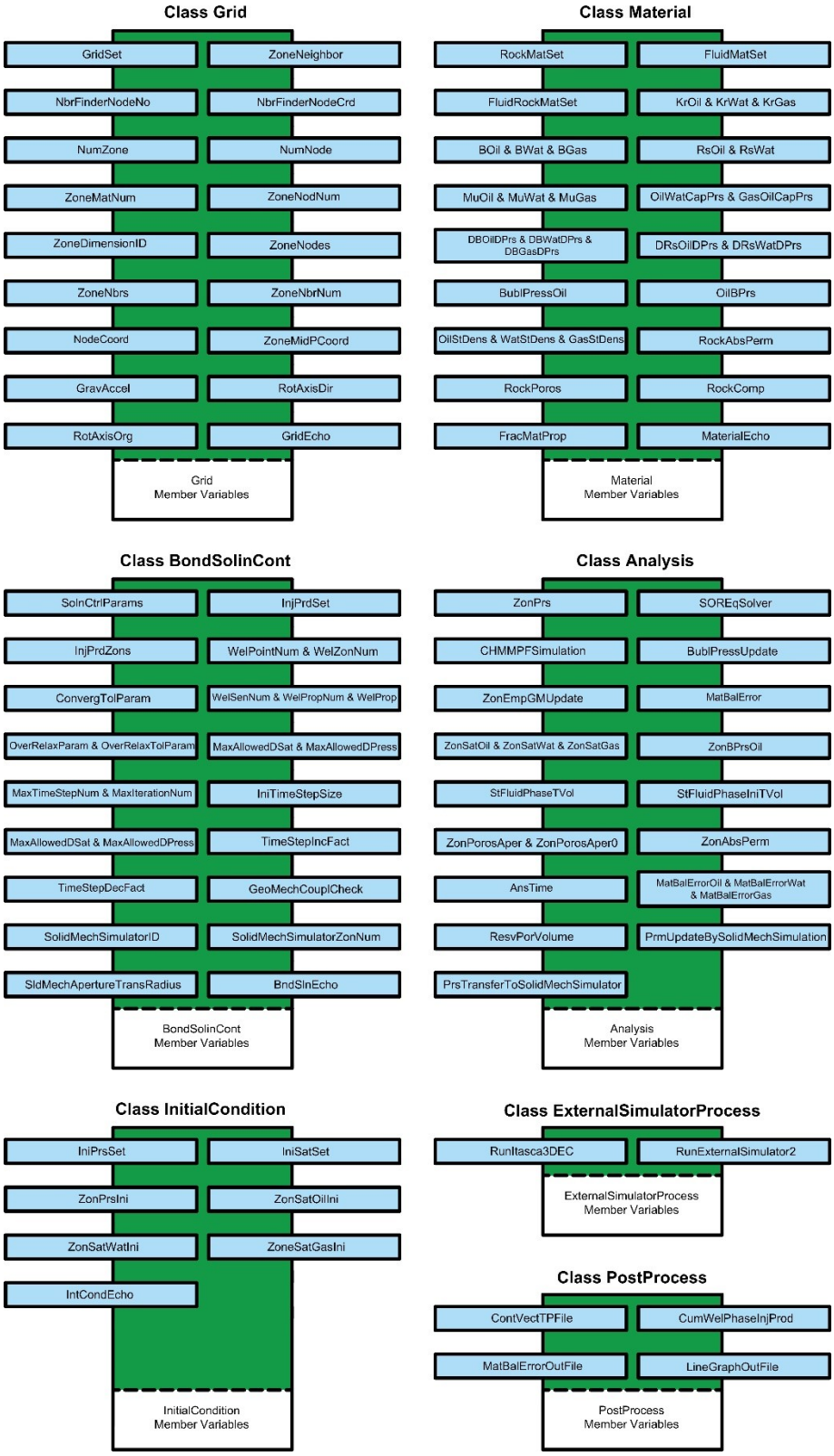

Figure 15: Schematic structure of seven major classes of FVBOS.

In order to write the code for the computational procedure developed in the previous section, vector, matrix and higher order tensor variables and operations are needed to be defined inside the member functions of the mentioned seven major classes. To facilitate the definition of matrix, vector and higher order tensor variables as well as the needed operations, the complementary class TensorField was coded. Therefore, C++ objects can be created based on the class TensorField representing vectors, matrices and higher order tensors and operations such as vector inner and outer products, matrix multiplication, matrix inversion, matrix determinant and other tensor operations can be performed.

It should also be mentioned that, in the Analysis and PostProcess classes, to avoid redundant coding and data storage at the finite volume zones, two more complementary classes are defined, namely ZonParams and ZonPostProcess. Objects of the class ZonParams and ZonPostProcess can be defined for each finite volume zone creating all the temporary parameters and functions for the zones needed either for the numerical analysis during each time step or extraction of numerical results at the end of each time step. Using such objects, all the temporary parameters and functions can be created whenever it is needed by the object constructor, once the object is declared, and they can be terminated by the object destructor as soon as the lifespan of the object is ended in the algorithm. The structure of the three complementary classes TensorField, ZonParams, and ZonPostProcess are exhibited in Figure 16.

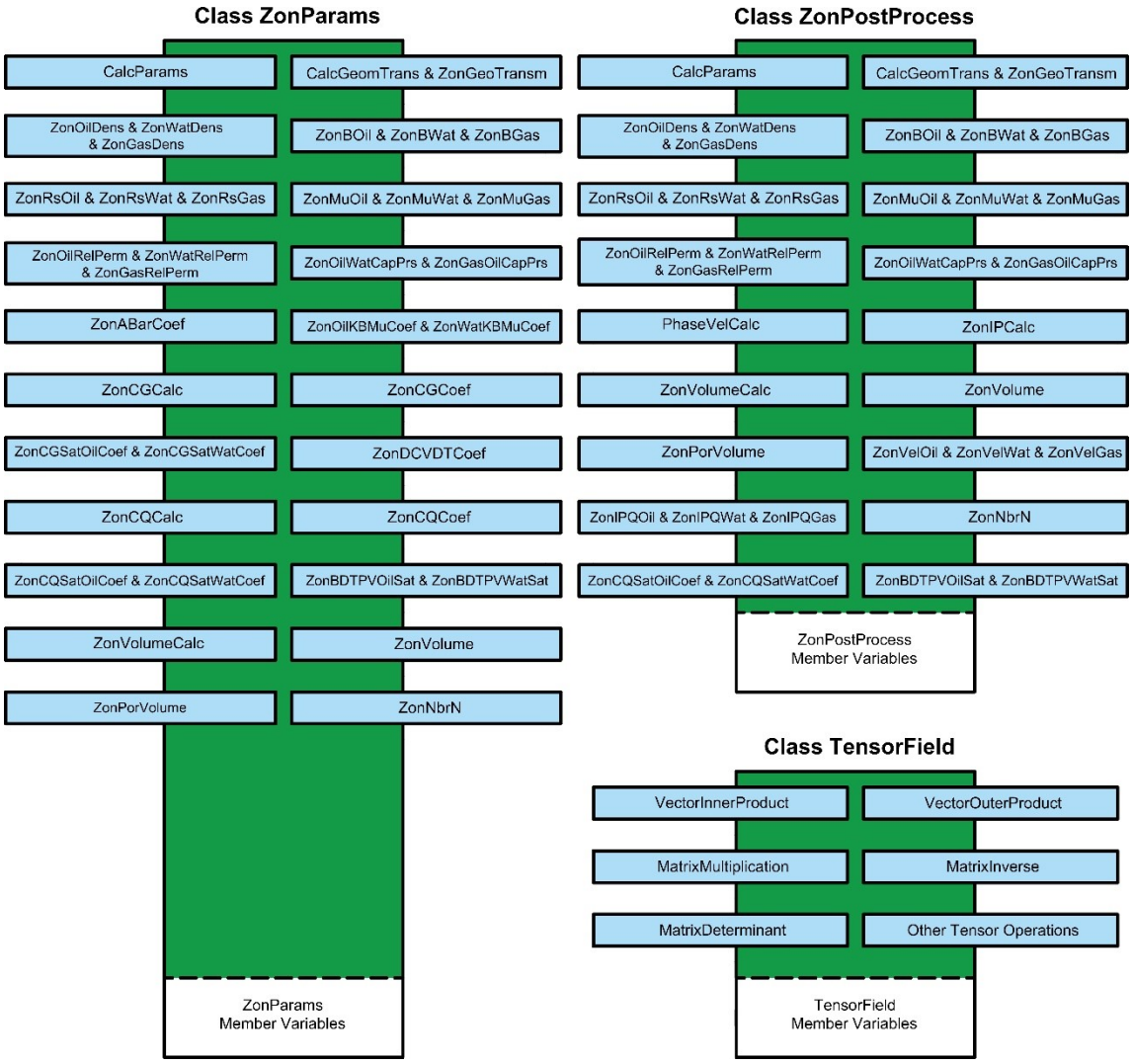

Figure 16: Schematic structure of the three complementary classes of FVBOS.

The seven major classes Grid, Material, InitialCondition, BondSolinCont, ExternalSimulatorProcess, Analysis and PostProcess together with the three complementary classes TensorField, ZonParams, and ZonPostProcess provide the blueprints based on which the needed objects can be created to handle the implementation of the developed computational algorithms in FVBOS. In other words, in the main function of FVBOS, the developed Finite Volume Discrete Fracture-Matrix method is implemented with the aid of the seven major objects FlowGrid, FluidRockMat, FlowIniCond, FlowBondSolCtr, FlowAnalysis, SolidMechSimulator and FlowPostProcess defined based on the blueprints as it is schematically illustrated in Figure 17.

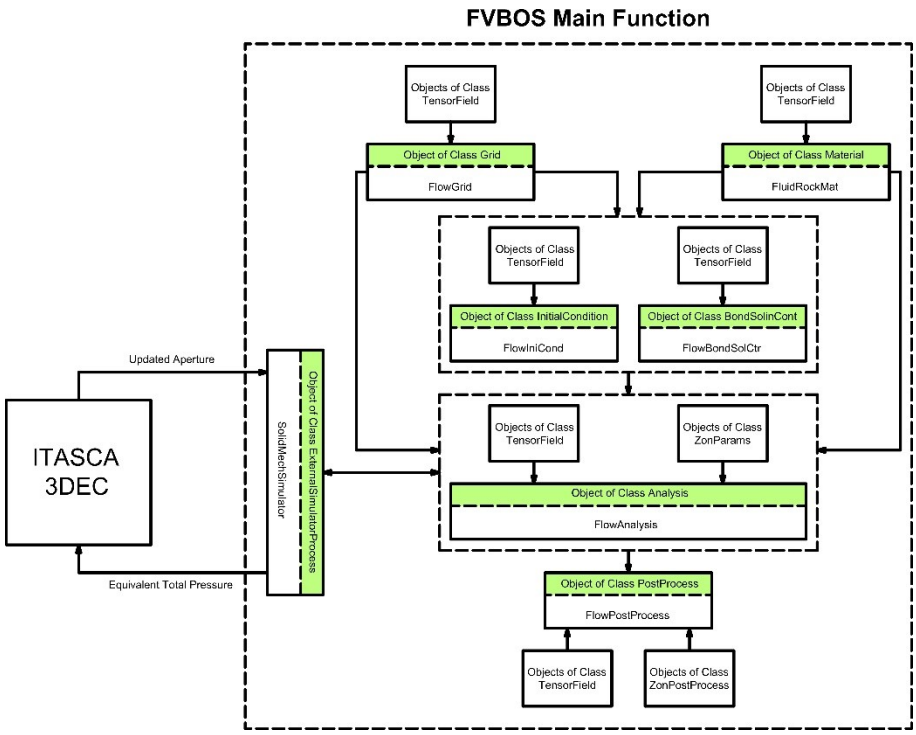

Figure 17: Object-oriented overall flowchart of FVBOS coupled with 3DEC.

The designed object-oriented structure of FVBOS facilitates dealing with complicated algorithms needed to implement the developed coupled multi-phase fluid flow model using powerful objects created based on the defined classes inside the program. In particular, as the functions and variables are accessed through their corresponding objects with intuitive names, the final written code is highly readable and organized. Above all, using this method, it is also feasible to share only the object files of the compiled classes, instead of the source code, with other programmers to use them in their own codes and use them based on provided instructions without being involved in the detailed codes and complications behind the classes. Furthermore, the defined classes make it much more feasible and efficient to add FVBOS code to other computational programs such as 3DEC and FLAC to enable them for the simulation of coupled hydro-mechanical multi-phase fluid flow through fractured porous media. The object-oriented structure of FVBOS also facilitates upgrading this code by adding more features such different multi-phase fluid flow models, other than the current black oil model, into the finite volume discrete fracture-matrix framework existing in FVBOS.

The current application of FVBOS as a multi-phase fluid mechanical simulator coupled with a distinct element solid mechanical simulator is illustrated in the current main

function of the software shown in Figure 18. The main function of FVBOS exhibited in this figure, shows how objects can be created based on the compiled classes to handle coupled multi-phase fluid flow simulation. As it is demonstrated in the current main function of FVBOS, it is fairly straightforward to create objects using the blueprints provided by the compiled classes and to assemble these objects on the basis of an algorithm defined by the software developer, to accomplish a specific outcome such as coupled multiphase fluid flow simulation using black oil model. To achieve this objective, the only resources the software developer requires are the object files of the compiled classes along with an instruction about the available member functions of the different classes and their applications.

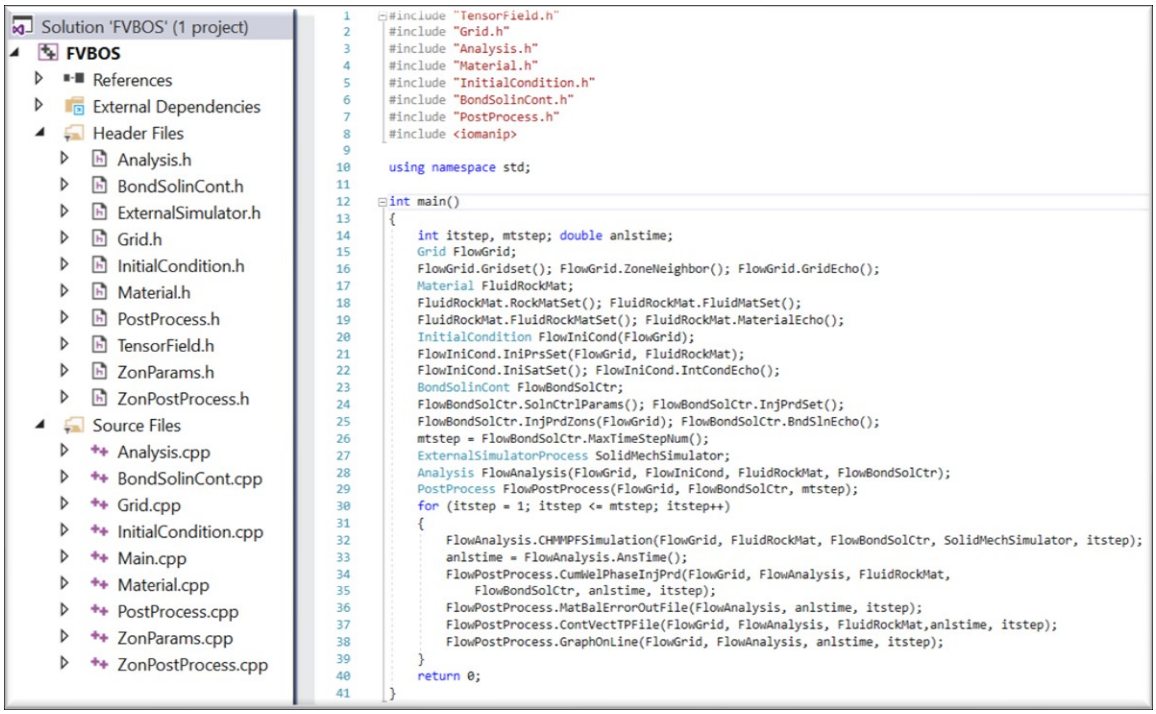

Figure 18: FVBOS main function C++ code.

It is also feasible for a software developer to add more features to the current code by defining new classes using inheritance concept of object-oriented programming. Using this concept, the developer can define new classes inheriting the member functions and variables of the available classes of FVBOS. Then, the developer can add more member functions and variables to the class, e.g. with the aim of adding new multi-phase fluid model and so on, without being engaged in the source code of FVBOS which makes the

upgrading of FVBOS much more efficient particularly when a team of software developers are independently working on different aspects of the software.

5.3 Finite Volume Discrete Fracture-Matrix Discretization in FVBOS

Using the finite volume discrete fracture-matrix method implemented into FVBOS, cell-based finite volume zones can be generated to discretize porous matrix and fractures. Both structured and unstructured finite volume zones are available in this code for the discretization of porous matrix and fractures. Using this approach, the fluid flow through fractured porous media can be simulated taking into account the matrix-matrix, matrix-fracture and fracture-fracture multi-phase fluid transfer. In this discretization method, it is not required to define finite volume zones at the intersection of fractures since the mass conservation at the intersections are automatically satisfied in the formulations developed for this method. Therefore, the issues arising from the presence of minuscule finite volume zones at fracture intersections are alleviated by this approach.

As it is discussed in the previous sections, the discretization of fractures are handled by two-dimensional triangular or quadrilateral finite volume zones while porous matrix is discretized with the aid of three-dimensional tetrahedral or hexahedral finite volume zones. Using this approach, it is feasible to efficiently simulate complex discrete fracture networks along with porous matrix by avoiding cumbersome numerical efforts emerging from the extremely small fracture zones satisfying the need for proper aspect ratio considering small fracture apertures. Hence, it is numerically viable to simulate stochastically generated complex discrete fracture networks representing natural fractures as well as joints using FVBOS.

The mechanisms of matrix-matrix, matrix-fracture and fracture-fracture multi-phase fluid transport together with the finite volume discrete fracture-matrix discretization available in FVBOS are schematically illustrated in Figure 19. As it is schematically implied in this figure, fluid flow through both three-dimensional finite volume matrix zones and a system of interconnected fractures explicitly modeled by two-dimensional finite volume zones can be simulated.

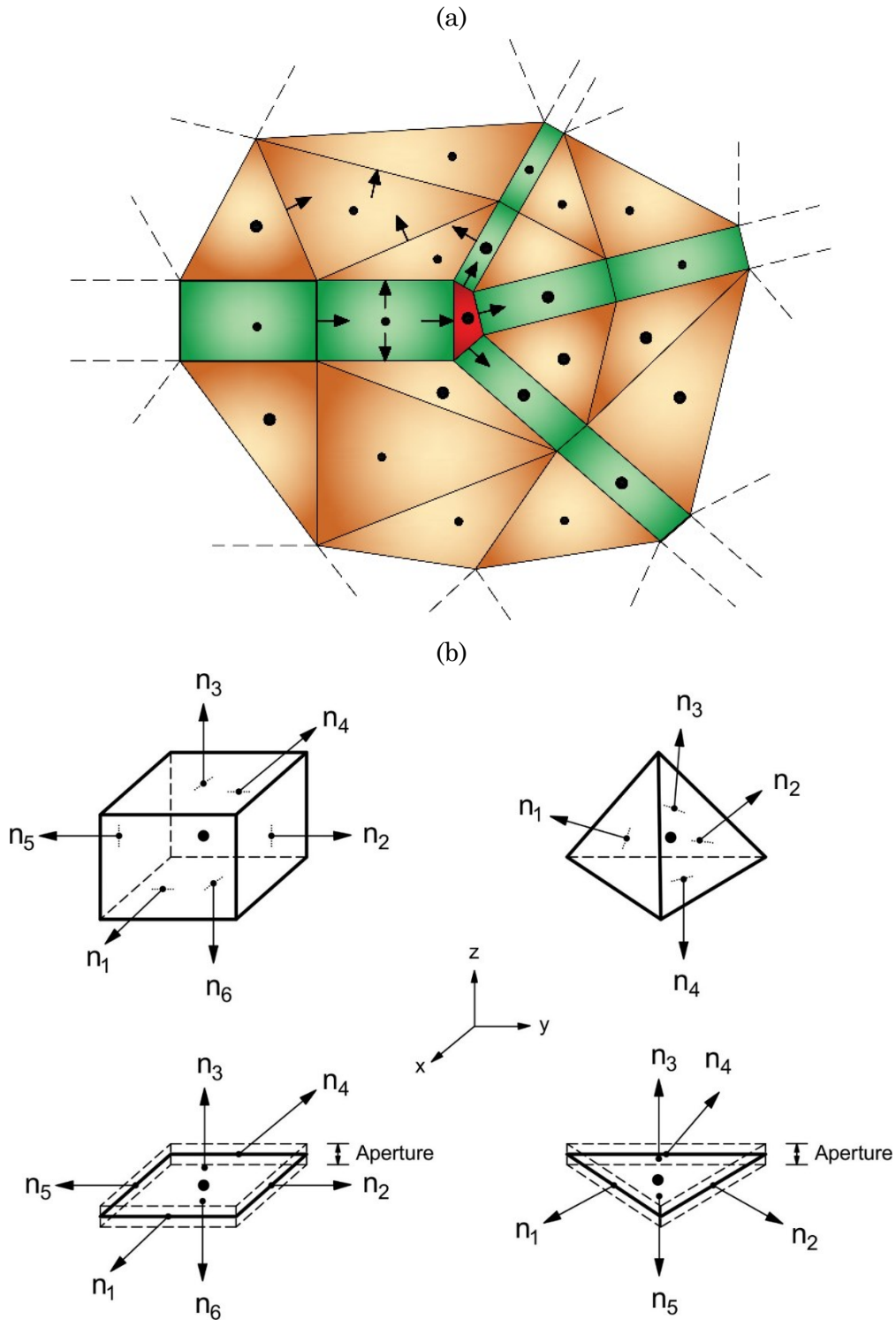

Figure 19: Finite volume discrete fracture-matrix discretization available in FVBOS.
(a) Matrix-matrix, matrix-fracture and fracture-fracture multi-phase fluid transport in FVBOS (b) Tetrahedral and hexahedral finite volume zones for porous matrix along with triangular and quadrilateral finite volume zones for fractures.

5.4 Verification of the Developed Multi-Phase Fluid Flow Model Implemented in FVBOS

In order to verify the devised numerical formulation of multi-phase fluid flow through fractured porous media, on the basis of which the software FVBOS was developed, a comprehensive verification study was carried out. The verification study involves numerical simulation of various benchmark problems. Each of these benchmark problems is concentrated on specific agents influencing the fluid flow, namely pressure gradient, viscous frictional force, gravity force, multi-phase fluid compressibility effects, interfacial tension and capillary pressure effects as well as mass conservation at fracture intersections. In these simulations, the applicability and accuracy of the developed formulation in the simulation of different aspects of multi-phase fluid flow in fractured porous media are demonstrated.

5.4.1 Simulation of Incompressible Two-Phase Flow under Pressure Gradient, Viscous Frictional Force and Fluid-Solid Interfacial Tension

One of the major agents driving the fluid flow through porous media is pressure gradient. In the case of two-phase flow, pressure gradient can be applied by the injection of an immiscible fluid phase into a porous media saturated by a resident fluid phase. While the pressure gradient due to the injection of the invading fluid phase tends to displace the resident fluid phase in porous media, the frictional force due to the viscosity of the fluid phases resists against this displacement. As long as the flow velocity is relatively small, another agent affecting the fluid flow is interfacial tension at the contact surface of fluid phases and the hosting porous media. The effect of this interfacial tension is empirically taken into account in the concept of relative permeability and capillary pressure. The problem of displacing a resident fluid phase by an immiscible invading fluid phase considering the pressure gradient, viscous frictional force and interfacial tension at the contact of fluid phases and porous media can be analytically solved using the method formulated by Buckley and Leverett (1941). This problem is schematically illustrated in Figure 20.

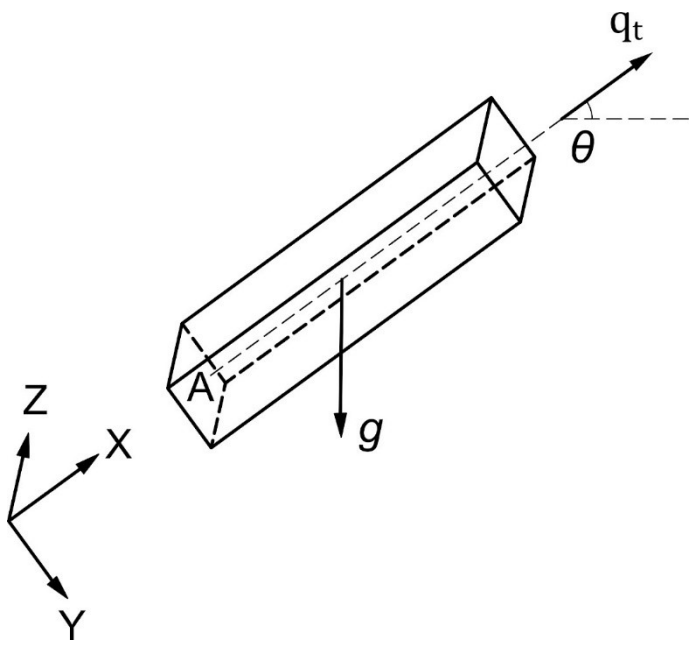

Figure 20: Configuration of Buckley-Leverett problem.

In this method, it is assumed that the fluid phases are incompressible which simplifies the mass conservation equation into fractional relation as follows:

$$q^t = q^w + q^o \quad \text{Eq. 196}$$

$$q^w = F_w q^t \quad \text{Eq. 197}$$

where q^t, q^w and q^o are respectively total, water and oil mass flow rates. The incompressibility of flow implies that the total mass flow rate is constant in the domain of fluid flow and water mass flow rate can be defined as a fraction of total mass flow rate represented by F_w. Consequently, by substituting water and oil flow rates by the corresponding total mass flow rate using the fractional relation in the Darcy's law, the following equations can be obtained:

$$F_w q^t = q^w = -\frac{AKk_r^w}{\mu^w}\left(\frac{\partial p^w}{\partial x} + \rho^w g sin\alpha\right) \quad \text{Eq. 198}$$

$$(1 - F_w)q^t = q^o = -\frac{AKk_r^o}{\mu^o}\left(\frac{\partial p^o}{\partial x} + \rho^o g sin\alpha\right) \quad \text{Eq. 199}$$

where A is the cross section of porous medium through which the two-phase flow is occurring. In the above equations, it is assumed that flow rate in the domain cross section is negligible and fluid flow is inclined relative to the direction of gravity force with an

inclination angle of $\pi/2-\theta$. In the above equation, gradient of oil pressure can be written in terms of water pressure gradient using capillary pressure concept and by combining these equations and removing water pressure gradient terms, the following relation can be achieved for the water fraction coefficient as follows:

$$F_w = \frac{1+\frac{AKk_r^o}{\mu^o q^t}\left[\frac{\partial p_c}{\partial x}-(\rho^w-\rho^o)gsin\alpha\right]}{1+\frac{\mu^w k_r^o}{\mu^o k_r^w}} \qquad \text{Eq. 200}$$

In order to be able to theoretically solve the equations of motion for this simplified fluid flow problem, the following exponential relations for the relative permeability of water and oil are assumed:

$$k_r^w = k_{rm}^w\left(\frac{S^w-S_c^w}{1-S_c^w-S_r^o}\right)^{n_w}$$
$$k_r^o = k_{rm}^o\left(\frac{1-S^w-S_r^o}{1-S_c^w-S_r^o}\right)^{n_o} \qquad \text{Eq. 201}$$

where n_w and n_o are the parameters which are determined by experimental measurements. By neglecting the fluid flow in the cross section of porous media, mass conservation equation for this problem can be obtained as

$$Q^w+\frac{\partial q^w}{\partial x}=-\phi A\frac{\partial S^w}{\partial t} \qquad \text{Eq. 202}$$

where Q^w is the water flow rate injection at the left side of the model and ϕ denotes the porosity of the porous media. Hence, by substituting the water flow rate in terms of water fraction coefficient, the following equation can be obtained:

$$\frac{\partial S^w}{\partial t}=-\frac{1}{\phi A}\left(q_t\frac{\partial F_w}{\partial x}+Q^w\right) \qquad \text{Eq. 203}$$

In the above equation, as the water fraction coefficient is a function of water saturation, the only unknown is water saturation. In order to analytically solve this equation, by assuming constant viscosity for water and oil, the total differential of water saturation is derived as follows:

$$dS^w(x,t)=\frac{\partial S^w}{\partial t}dt+\frac{\partial S^w}{\partial x}dx \qquad \text{Eq. 204}$$

Then, the total derivative of water saturation with respect to time can be obtained as follows:

$$\frac{dS^w}{dt} = \frac{\partial S^w}{\partial t} + \frac{\partial S^w}{\partial x}\frac{dx}{dt} \quad \text{Eq. 205}$$

Using the above equation, the rate of advance of constant saturation front can be derived by equating the total time derivative of water saturation to zero as follows:

$$\left[\frac{dx}{dt}\right]_{S^w=cons} = -\frac{\frac{\partial S^w}{\partial t}}{\frac{\partial S^w}{\partial x}} = \frac{q_t}{\phi A}\left[\frac{dF_w}{dS^w}\right]_{S^w=cons} \quad \text{Eq. 206}$$

Therefore, the location of this constant saturation front can be achieved by integrating the above equation with respect to x as follows:

$$[x]_{S^w=cons} = \frac{q_t t}{\phi A}\left[\frac{dF_w}{dS^w}\right]_{S^w=cons} \quad \text{Eq. 207}$$

Based on the mass conservation law, the total volume of water in the pore spaces of the porous media should be equal to the total volume of water injected from the left side of the model. Therefore, the water saturation distribution along the x axis obtained by the above equation is only valid up to a certain point which should be determined based on mass conservation of water as follows:

$$\int_0^{\Delta t} Q^w dt = \int_0^{\Delta x} \phi S^w A dx \quad \text{Eq. 208}$$

In the above equation, based on the assumption of incompressibility of fluid phases, Q^w is equal to q_t. Therefore, by integrating the above equation, the spatial validity interval of Buckley-Leverett theoretical solution is obtained as

$$\Delta x = \frac{q_t \Delta t}{\phi A S^w} \quad \text{Eq. 209}$$

Hence, water saturation distribution along x axis can be determined by Buckley-Leverett theoretical solution up to the point located at $x = \Delta x$ which can be calculated at any time $t = \Delta t$ while water saturation at the locations represented by $x > \Delta x$ is equal to the connate water, i.e. $S^w = S_c^w$.

If the interfacial tension at the interface of fluid phases represented by capillary pressure is neglected, the Buckley-Leverett solution will be decoupled and the distribution of water saturation in space can be determined at different times analytically. This analytical solution has been implemented into an object-oriented C++ code reflected in Appendix D. Buckley-Leverett problem in different situations has been analytically solved using the

developed C++ code and the results were compared to the corresponding numerical results obtained by FVBOS. The comparison of the theoretical and numerical results demonstrates the capability of FVBOS in the simulation of different agents affecting multi-phase flow, namely pressure gradient, viscous frictional force, gravity, interfacial tension and capillary pressure effects as well as mass conservation at fracture intersections, in the both porous matrix and fractures. The results of these analyses are discussed in the following sections.

In the first series of analyses, the major focus is on the assessment of the performance of FVBOS in simulating pressure gradient, viscous frictional force and the effect of interfacial tension between fluid phases and porous media empirically estimated by the concept of relative permeability in porous matrix and fracture. In this regard, it is assumed that the capillary pressure is negligible and gravitational acceleration is equal to zero. Then, the Buckley-Leverett problem is solved by the analytical method explained earlier as well as numerical method using FVBOS. The comparison of the analytical and numerical solution at different times for porous matrix is shown in Figure 21.

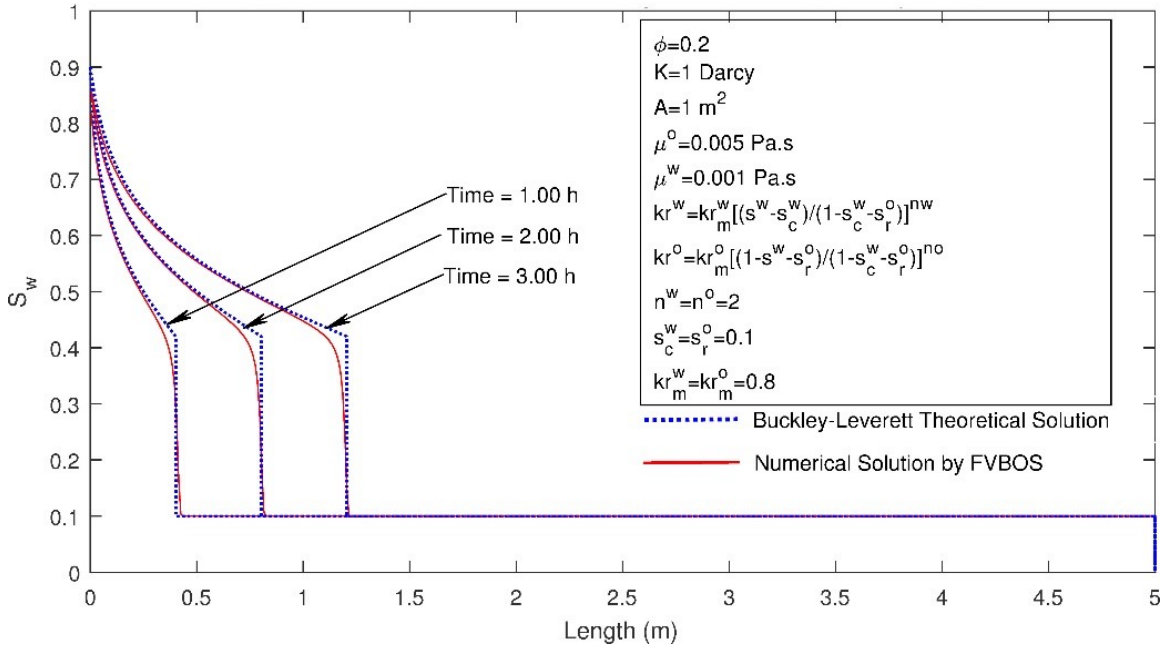

Figure 21: Verification of FVBOS with Buckley-Leverett theoretical solution for the case of finite volume discretization size of 0.01 m in porous matrix.

As it can be observed in this figure, the parameters used to perform these analyses are reflected in the figure and the utilized relative permeability relation is illustrated in

Figure 22.

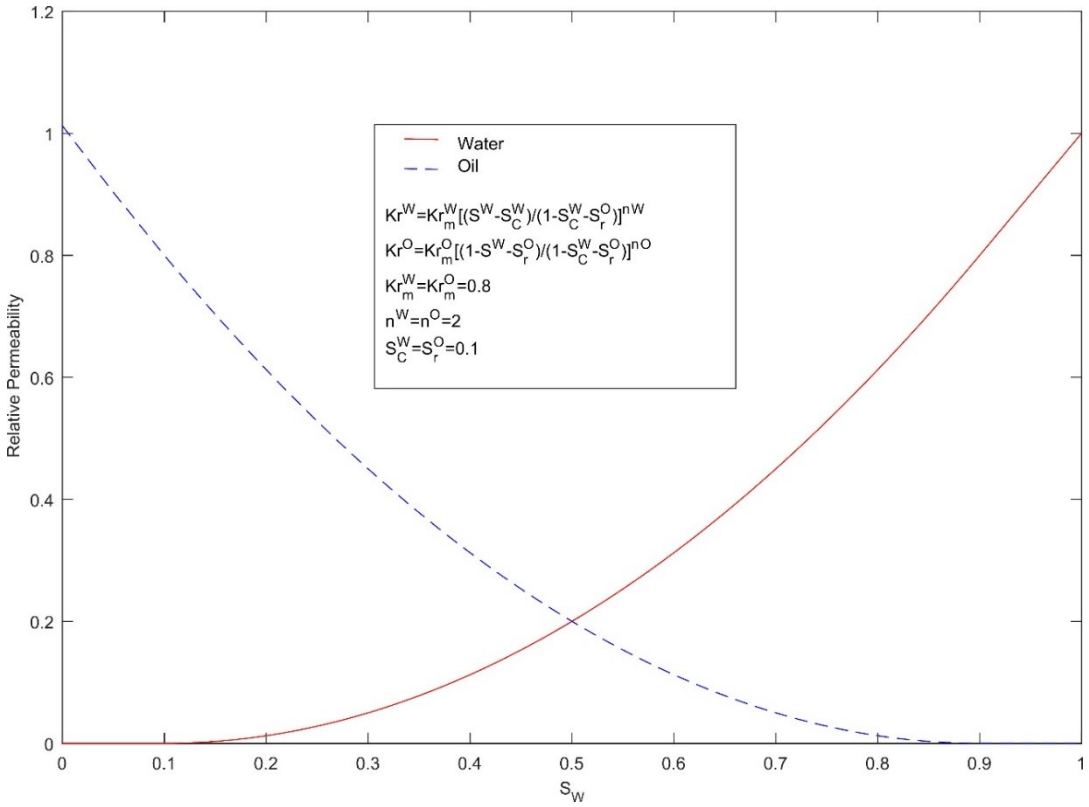

Figure 22: Relative permeability relation used in Buckley-Leverett problem.

As it is demonstrated in Figure 21, the numerical model implemented in FVBOS is in a good agreement with the Buckley-Leverett theoretical solution. A negligible discrepancy between the two analyses results can be seen right at the left side of the model and at the saturation shock front. The discrepancy at the left side of the model is due to the fact that, in the Buckley-Leverett theoretical solution, it is assumed that the the point right at the beginning of the conceptual sample instantaneously reaches to 100 percent water saturation. However, in numerical analysis by FVBOS, it takes time for the finite volume zone located at the left side of the model to reach to 100 percent water saturation since the finite volumes, unlike mathematical points, possess volume which takes time to be fully saturated by water. For the same reason, the finite volumes located at the shock front cannot exactly capture the instantaneous water saturation fall off to the connate water saturation predicted by the Buckley-Leverett theoretical solution. In other words, the values of unknown function, i.e. saturation here, is averaged over a finite number of finite volumes, while, in the theoretical solution, the space domain is divided into infinite

number of mathematical points with zero volume. Unlike the finite volume numerical approximation, the theoretical representation makes it possible to predict the value of the unknown function at infinitesimal space increments resulting in prediction of the instantaneous water saturation decrease or increase. Therefore, by reducing the size of finite volumes along the fluid flow domain, the discrepancy between the numerical results and the theoretical solution can be diminished. In order to investigate on the effect of the size of finite volumes on the accuracy of the results, the same problem was numerically analyzed with a larger discretization size as it is shown in Figure 23.

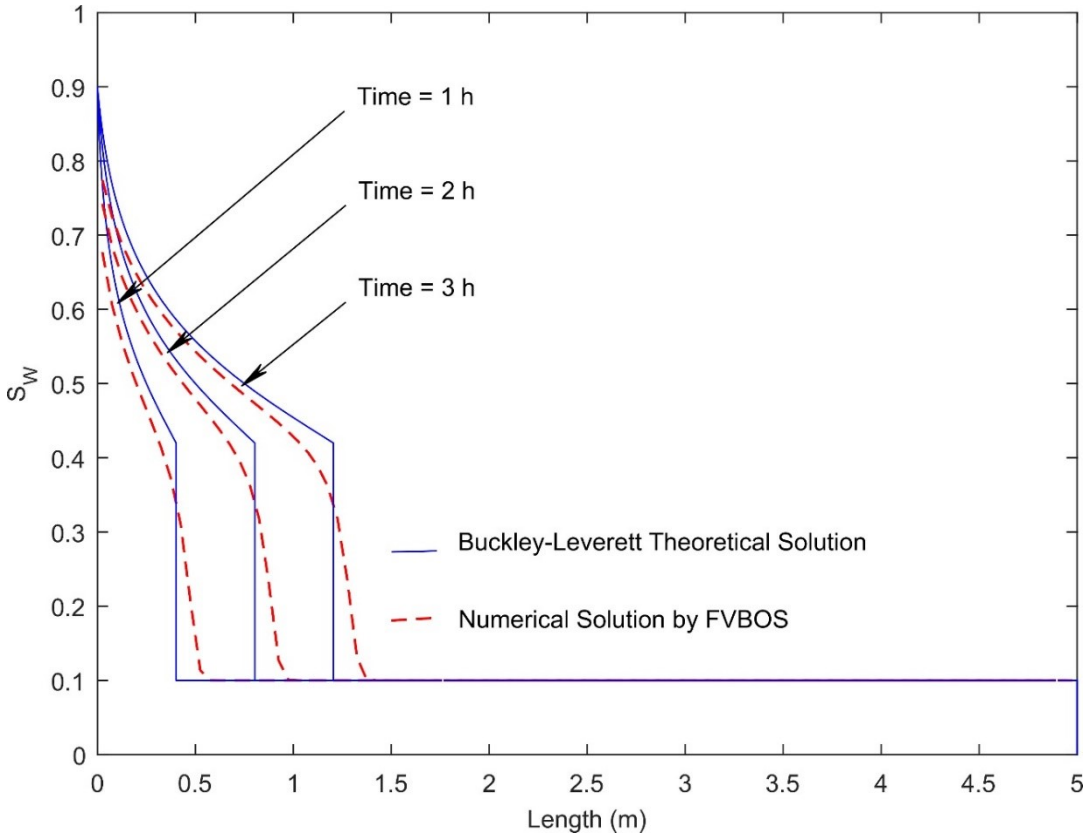

Figure 23: Comparison of FVBOS numerical results with Buckley-Leverett theoretical solution in the case of discretization size of 0.05 m in porous matrix.

As it can be seen, by increasing the size of finite volumes, the accuracy of the results deteriorates due to the numerical dispersion as it is discussed above.

Verification of FVBOS with Buckley-Leverett theoretical solution discussed in this section demonstrates that FVBOS is capable of accurately simulate pressure gradient, viscous frictional force and the effect of interfacial tension between fluid phases and porous media in the case of incompressible fluid flow through porous matrix. It is worth

mentioning that since the numerical formulation implemented in FVBOS is an implicit pressure-explicit saturation approach, the pressures are first calculated implicitly by solving the pressure equation at the finite volumes and then the saturation of fluid phases are explicitly determined in the finite volumes based on the calculated pressures. Therefore, the accuracy of the calculated pressures is higher than the accuracy of the calculated saturations. Consequently, validation of saturation results is adequate to conclude that the pressure results are also valid.

Numerical simulation results obtained by FVBOS for Buckley-Leverett problem neglecting capillary pressure effect and gravity is summarized in Figure 24 for the case of water-oil two-phase flow in porous matrix after 3 hours of water injection at the left side of the model. In this figure, pressure, water saturation and oil saturation contours are exhibited.

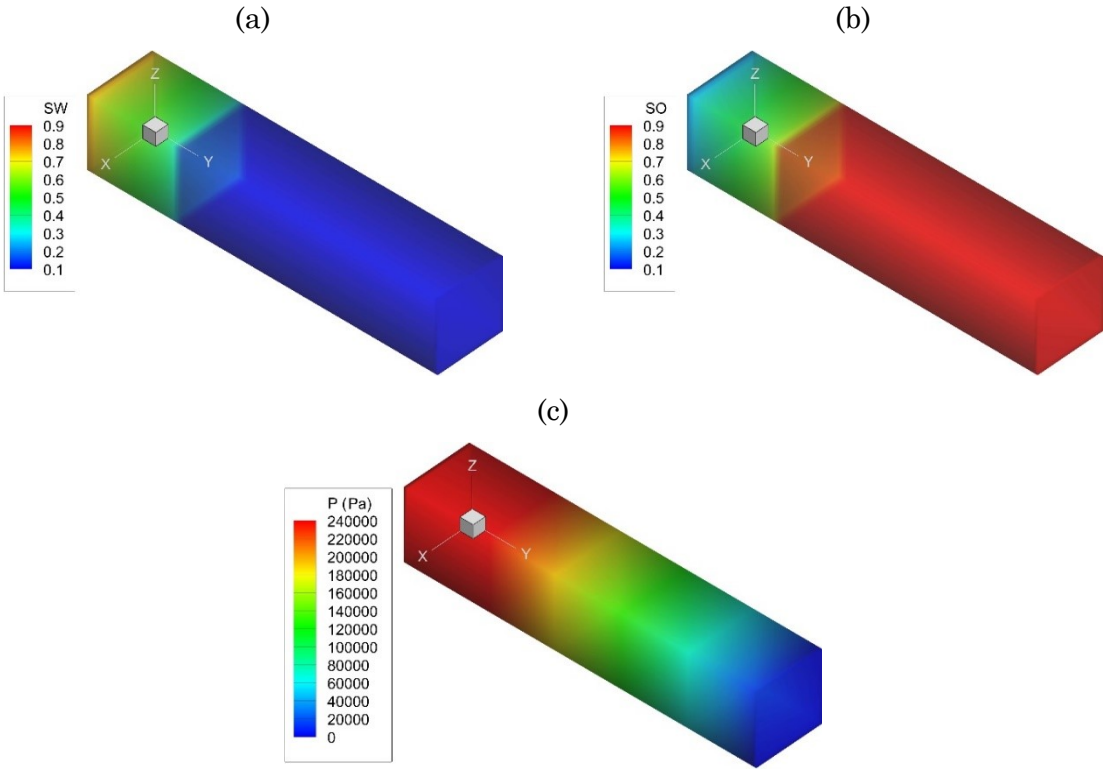

Figure 24: FVBOS numerical simulation results for Buckley-Leverett problem in porous matrix after 3 hours of water injection at the left side of the model.
(a) Water saturation contour (b) Oil saturation contour (c) Pressure contour.

In the next series of analyses, the Buckley-Leverett problem neglecting capillary pressure and gravity in a single fracture is numerically simulated by FVBOS and the results are

verified by the theoretical solution derived earlier.

In FVBOS, fractures are spatially discretized by planar finite volume zones, e.g. triangular or quadrilateral zones. Then, for the purpose of simulation of fluid flow through fractures, two distinct cases are taken into account, namely fracture-matrix and fracture-fracture fluid transfer. In the case of fracture-matrix fluid transfer, the fracture finite volumes are considered as 3 dimensional zones with fracture aperture as the third dimension and the Darcy's law and mass conservation equations are used to simulate the multi-phase flow the same as the case of matrix-matrix fluid transfer. In this case, since the permeability of fracture zones are much higher than those of porous matrix zones, and since the dimension of fracture zones perpendicular to fluid flow, i.e. aperture here, are much smaller than those of porous matrix zones, the transmissivity of fracture zones are much higher than those of porous matrix zones. Hence, face transmissibility at fracture-matrix contacts are simplified into the transmissivity of the matrix zone. Consequently, fluid flow simulation in this case is the same as the matrix-matrix fluid transfer which was previously verified by Buckley-Leverett theoretical solution.

In the case of fracture-fracture fluid transfer, the fluid flow is simulated by mass conservation equation together with Reynolds equation (Reynolds, 188; Zimmerman and Bodvarsson, 1996). In this case, as it was discussed in the previous chapter, by integrating the fluid flow through the fracture aperture, flow velocity is defined by an equation similar to the Darcy's law by assuming that the absolute permeability of fracture is equal to one-twelfth of squared aperture. Therefore, this problem can also be analytically simulated using Buckley-Leverett theoretical solution. To this end, incompressible water-oil two-phase fluid flow through single fracture is numerically simulated by FVBOS and the numerical results are verified with Buckley-Leverett theoretical solution. In the Buckley-Leverett theoretical solution, a porous media with a cross section area equal to fracture height multiplied by fracture aperture and absolute permeability equal to one-twelfth of squared fracture aperture is analytically solved. The comparison of numerical results obtained by FVBOS and Buckley-Leverett theoretical solution is displayed in Figure 25.

(a)

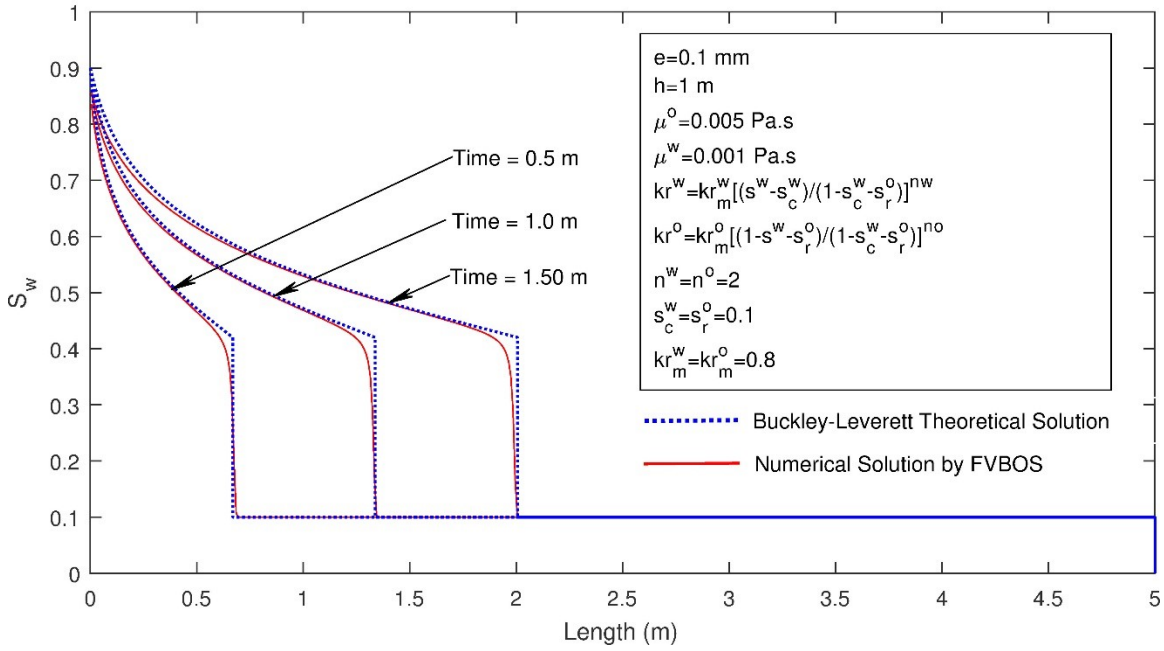

(b)

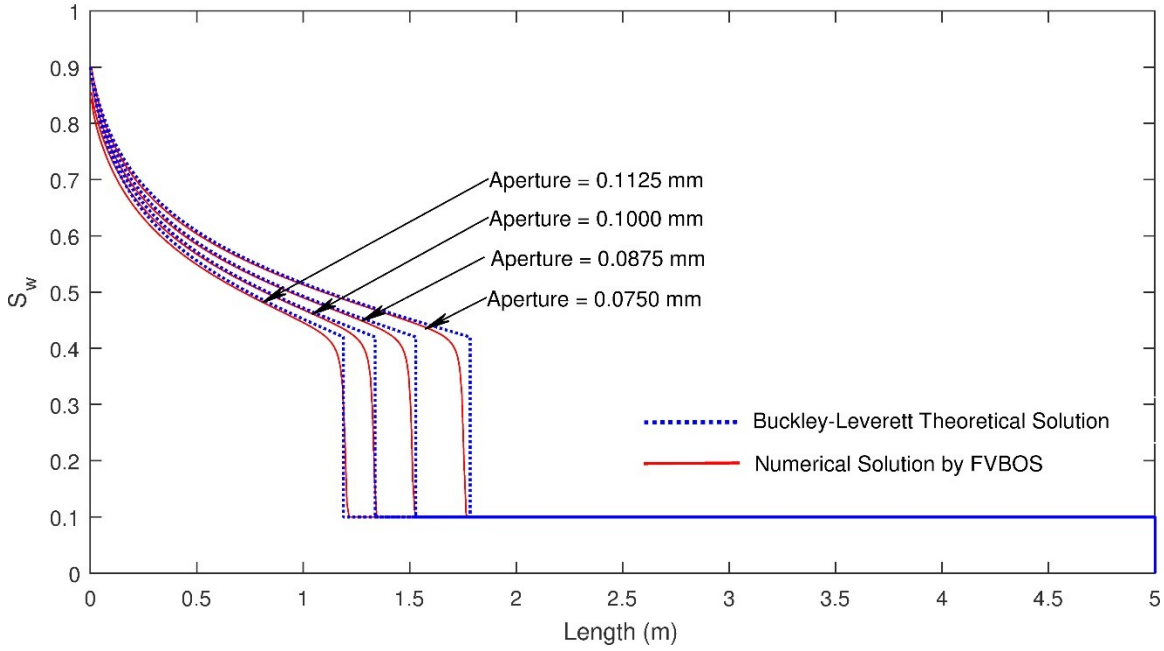

Figure 25: Verification of FVBOS with Buckley-Leverett theoretical solution for the case of single fracture.
(a) Water saturation distribution at different times for the fracture aperture of 0.1 mm (b) Water saturation distribution for different fracture apertures after 1 minute of water injection at the left side of the model.

In these simulations, first, constant fracture aperture of 0.1 mm was used in models and

the water saturation at different times after water injection at the left side of the model is plotted. In the next case, different fractures with different apertures ranging in the interval 0.075-0.1125 mm were considered and the water saturation distribution after 1 minute of water injection at the left side of the model is plotted. As it is demonstrated in Figure 25, the numerical results achieved by FVBOS are in a good agreement with the analytical results obtained by Buckley-Leverett theoretical solution.

In Figure 26, pressure contour, water saturation contour and oil saturation contour are displayed.

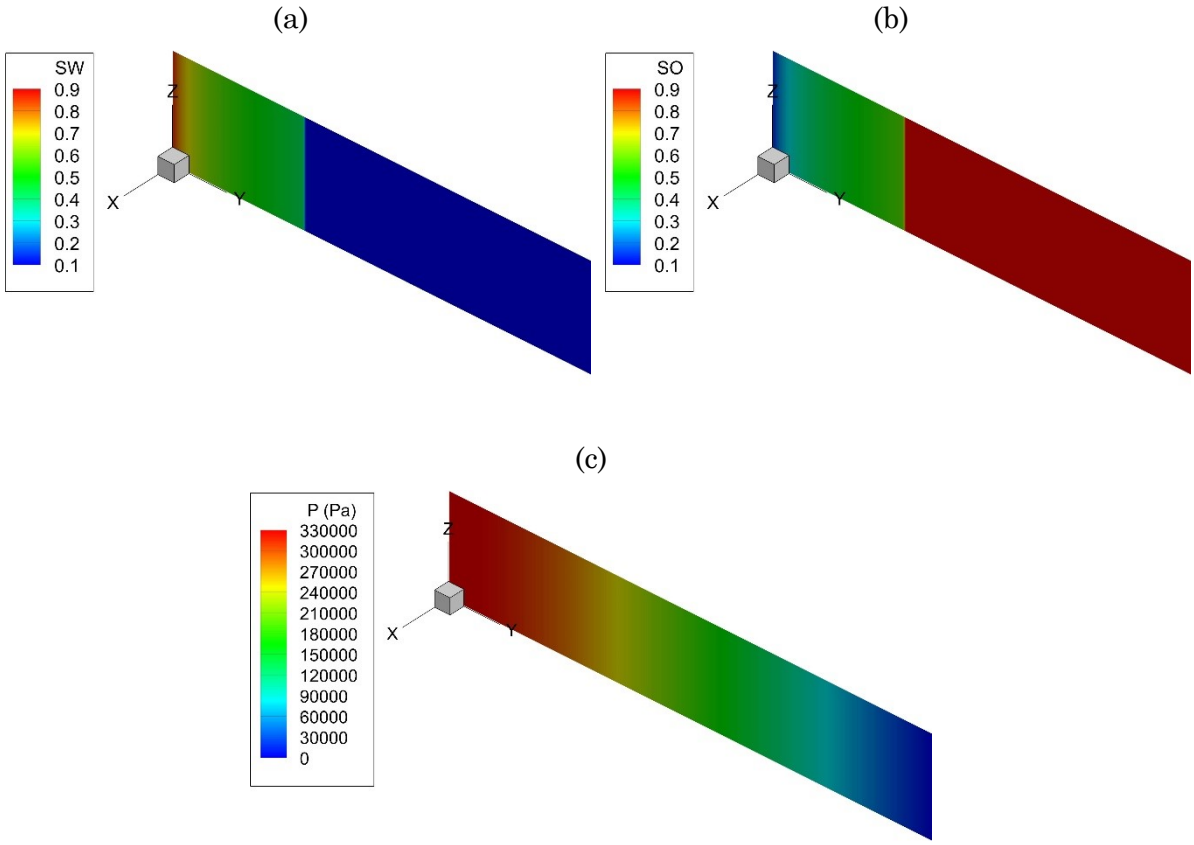

Figure 26: FVBOS numerical simulation results for Buckley-Leverett problem in single fracture after 1 minutes of water injection at the left side of the model.
(a) Water saturation contour (b) Oil saturation contour (c) Pressure contour.

In these numerical simulations, incompressible fluid flow through fractures are modeled by assigning volume factor of unity for fluid phases and large fracture normal stiffness. As it can be observed in Figure 25(a), as the saturation front moves forward by elapsing time, the deviation between water saturation approximated by FVBOS and that obtained by Buckley-Leverett theoretical solution increases at the injection point. This is due to

the fact that it is not possible to exactly simulate the theoretical incompressible fluid flow by the numerical methods taking into account the accumulation terms in mass conservation equations. Indeed, in order to approximate incompressible fluid flow where the accumulation term is assumed to be zero, in addition to assuming a low compressibility for the fluid phases, a low compressibility for porous matrix and high fracture normal stiffness should be assumed in numerical simulations. However, in the limiting case where the compressibility of fluid phases are extremely low and either fracture normal stiffness is extremely high or matrix compressibility is extremely low, the accumulation term in mass conservation equation approaches to zero which makes the mass conservation differential equations to approach singularity. In this situation, it is either impossible for the numerical solution to converge to a unique solution or a large number of iterations and a great deal of time is required for the numerical solution to converge to a stable solution. Hence, in practice, in order to simulate the incompressible fluid flow by FVBOS, having assumed incompressible fluid phases, a fairly large fracture normal stiffness and quite small porous matrix compressibility was assumed in the numerical analyses. In these circumstances, not only the numerical results approximate the incompressible theoretical solutions with a reasonable accuracy, but also the numerical solutions can converge into a stable solution in a practical time span.

As it is demonstrated, although the numerical solution approximates the theoretical solution for incompressible fluid flow with a reasonable accuracy, in the numerical solution, the accumulation term in mass conservation equation increases by time which makes the numerical results to gradually deviate from theoretical results by the passage of time. This situation is heightened in the case of simulating incompressible fluid flow through fractures due to the low cross section of fracture finite volumes relative to that of porous matrix finite volumes. In the case of simulating fluid flow through fractures, although a large value is assumed for the normal fracture stiffness, by the passage of time and continuing water injection at the left side of the model, the pressure increase is so high that the fracture aperture increases in spite of the large value assumed for the fracture normal stiffness. Therefore, by continuing injection at the left side of the model, the accumulation term increases which brings about the deviation of numerical solution from theoretical solution for incompressible fluid flow. This deviation is higher at the injection point due to the higher pressure and higher accumulation term.

Overall, numerical results obtained by FVBOS for Buckley-Leverett problem demonstrates the accuracy and applicability of the code in the simulation of multi-phase fluid flow through both porous matrix and fractures. As it was demonstrated, simulation of multi-phase fluid flow through both fracture and matrix are handled based on an analogous numerical approach. Therefore, in order to verify the performance of FVBOS in the simulation of gravity and capillary pressure effects, it is only required to design the verification problem either in the framework of porous matrix or fracture.

5.4.2 Simulation of the Effect of Gravity Force on Incompressible Two-Phase Flow

In the previous section, the accuracy of FVBOS in the simulation of multi-phase fluid flow through porous matrix and fractures was demonstrated taking into account pressure gradient, viscous frictional force and the effects of interfacial tension between fluid phases and porous media. In this section, the performance of FVBOS in the simulation of gravity force is assessed. With this aim, as it was discussed in the previous section, it is adequate to design the verification case either for porous matrix using three-dimensional finite volumes or for fracture using two-dimensional finite volumes. Without loss of generality, the verification problem for assessing the performance of FVBOS in simulating gravity is designed only in the case of porous matrix. The same problem would be simulated in fracture, but it is avoided for the sake of conciseness.

In order to verify the performance of FVBOS in simulating the effect of gravity on the multi-phase fluid flow, two verification problems were designed such a way that they can be solved by Buckley-Leverett theoretical solution. In these verification problems, porous matrix with the same geometry, rock and fluid material properties, as well as initial and boundary conditions as those chosen in the previous section were used in the numerical models. In particular, in the first verification problem, the standard density of the resident fluid phase, i.e. oil here, and the invading fluid phase, i.e. water here, used in this simulation are summarized in Table 1.

Table 1: Standard density of fluid phases used in the simulation of the effect of gravity force on incompressible two-phase flow by FVBOS.

	Resident Fluid phase (Oil)	Invading Fluid Phase (Water)
Standard Density (kg/m^3)	800	1000

Note: Standard condition is assumed to be represented by temperature and pressure of 16°C and 101.33 KPa, respectively.

In this verification problem, the length of porous matrix is aligned with the direction of gravitational acceleration, i.e. vertical direction here, and water is injected at the bottom of the model so that the fluid flow direction is in the opposite direction of gravitational force. Then, the two cases, i.e. with gravitational acceleration equal to 9.81 and without gravitational acceleration, were analyzed both numerically by FVBOS and analytically using Buckley-Leverett theoretical solution. The comparison of numerical and analytical results for the two cases are displayed in Figure 27.

As it can be observed in Figure 27, the effect of gravity is properly simulated by FVBOS with a reasonable accuracy compared to the Buckley-Leverett analytical results. As it is demonstrated in this figure, by neglecting gravitational force, water saturation front moves faster and water saturation behind it increases slower compared with the case where gravitational force is taken into account. This is due to the fact that, based on the Darcy's law, gravitational force applied in the opposite direction of fluid flow tends to decrease the velocity of both phases. In this regard, the higher the density of a fluid phase, i.e. water here, the higher the decrease in the velocity of the fluid phase.

On the basis of mass conservation equation, the decrease in the velocity of a fluid phase results in the rise in the saturation of the fluid phase. Therefore, in the case of verification problem discussed in this section, taking into account the gravitational force, the velocity of both phases, i.e. water and oil, is diminished compared to the case where gravity is ignored. Since the density of the water phase is higher than the oil phase, the decrease in the velocity of water is more significant than that of oil phase. Therefore, mass conservation implies that water saturation increase is faster behind the water saturation front by considering gravity compared to the case where gravity is neglected. Moreover, based on the mass conservation law, the total volume of water injected at the bottom of the model should be equal to the total volume of the water stored in the pore spaces. Therefore, considering the fact that water injection rate is the same in the two cases of

with and without gravity, mass conservation law necessitates that faster water saturation increase behind water saturation front should be accompanied by slower water saturation front movement. In other words, the higher the water saturation behind the water saturation front, the lower the distance water saturation front moves in the direction of fluid flow. That is why the water saturation front moves slower in the case where the gravitational force is taken into account.

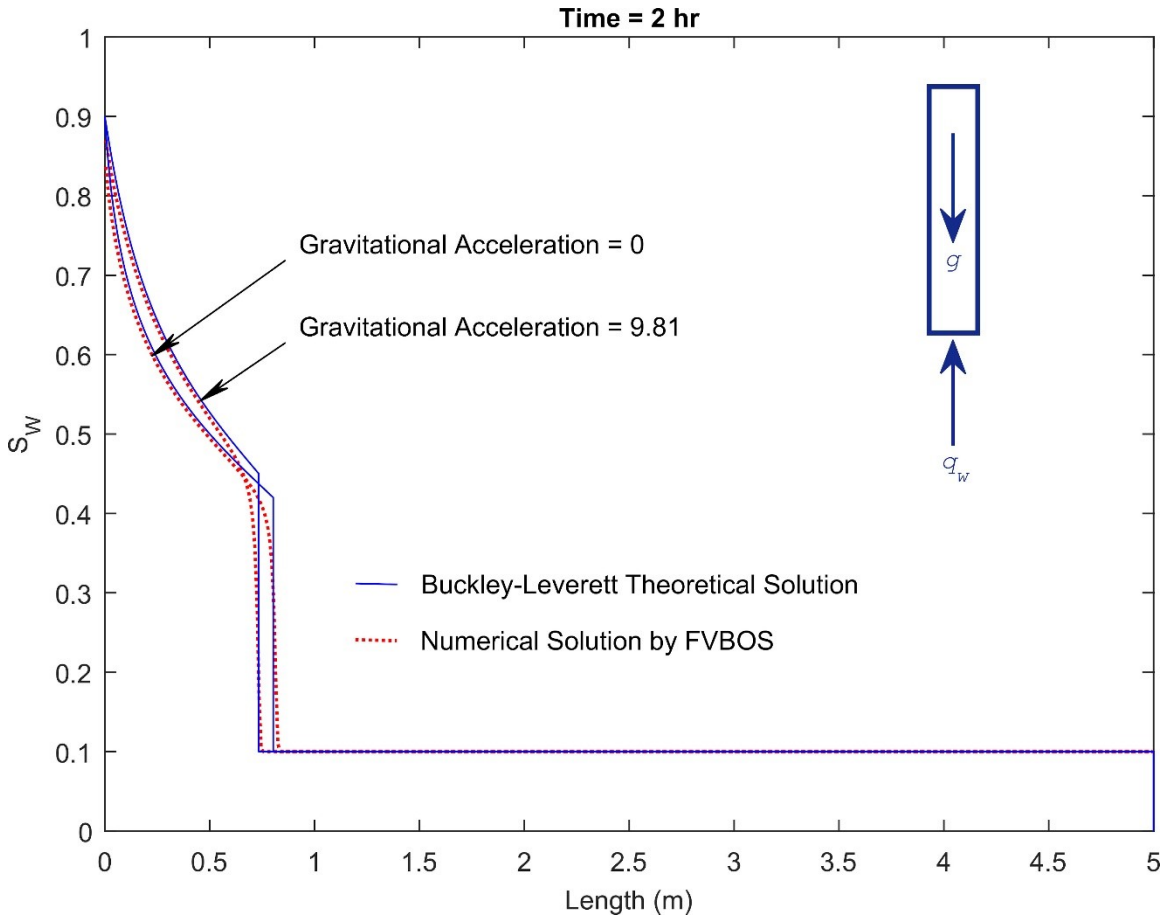

Figure 27: Verification of FVBOS with Buckley-Leverett theoretical solution taking into account gravitational force.

The physical interpretation of the effect of gravity described above is that, by considering the gravitational force, the mobility of both water and oil phase decreases due to the presence of gravity. Since the density of water is higher than oil, the decrease in the mobility of water is higher than that in the oil mobility. Therefore, in the case where gravity is considered, water saturation front moves slower in the direction of fluid flow, and in turn more water saturation in pore spaces is needed to balance the amount of water injected at the bottom of the model, compared to the case were gravity is neglected.

In contrast, in the case where gravity is neglected, the difference in the mobility of the phases is solely controlled by the difference between the viscosities of the phases, i.e. the higher the viscosity of a phase, the lower the mobility of it. Consequently, in the case where gravity is neglected, since the mobility of oil is lower than that of water, due to higher viscosity of oil, more volume of injected water penetrates into the area which is mostly saturated by oil. Therefore, lower water saturation is left in pore spaces behind the water saturation front compared to the case where gravity is taken into account.

In order to further highlight the effect of gravitational force on the two-phase fluid flow discussed above, the second verification problem was designed. In the second verification problem, the two-phase fluid flow described earlier is simulated by FVBOS for two cases of resident fluid phase standard densities summarized in Table 2.

Table 2: Standard density of the two cases of resident fluid phases used in the simulation of the effect of gravity force on incompressible two-phase flow by FVBOS.

Resident Fluid phase	Case 1	Case 2
Standard Density (kg/m^3)	800	300

Note: Standard condition is assumed to be represented by temperature and pressure of 16°C and 101.33 KPa, respectively.

In these verification cases, the standard water density for the both cases were assumed to be equal to 1000 kg/m^3. This problem were also analytically solved using Buckley-Leverett method and the analytical results were compared with the numerical results achieved by FVBOS as it is illustrated in Figure 28.

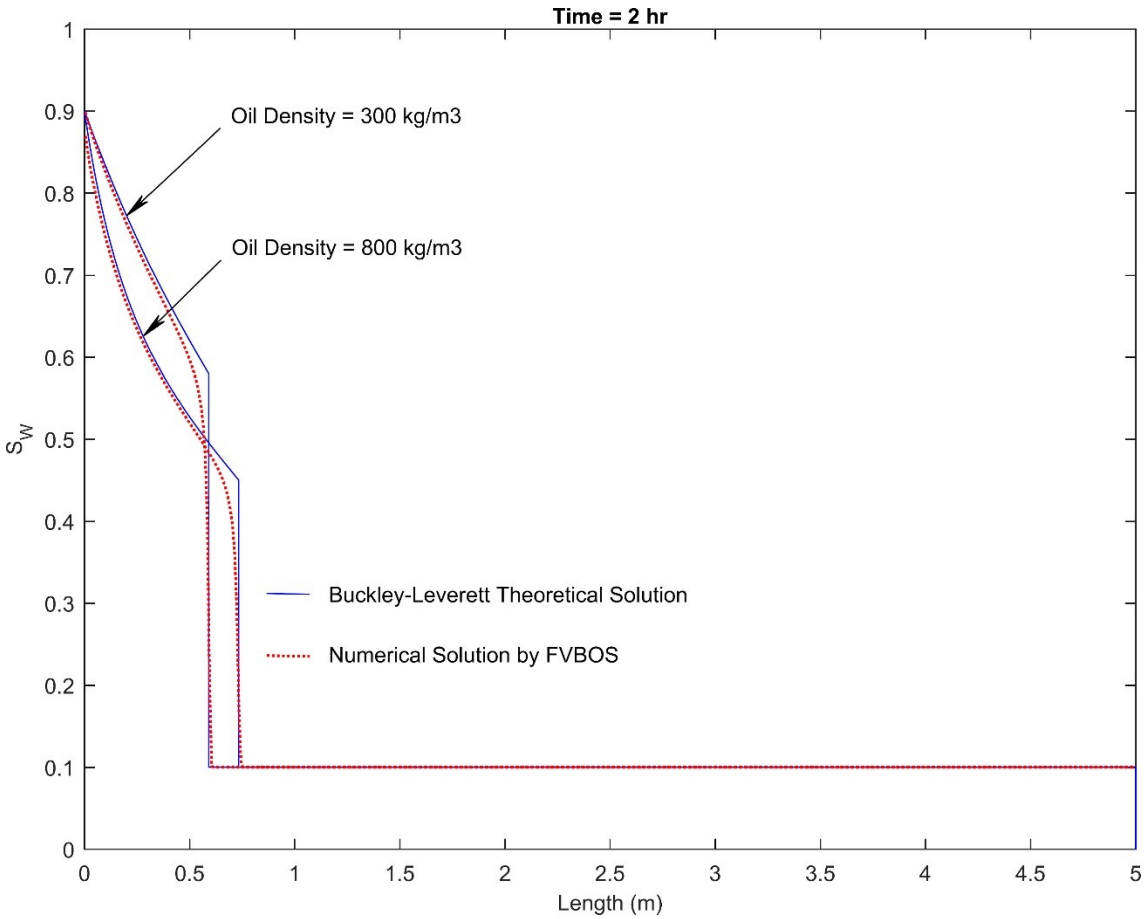

Figure 28: Verification of FVBOS with Buckley-Leverett theoretical solution evaluating the effect of resident fluid phase density.

As it can be seen, in the second verification problem designed for the simulation of gravity force effects, the numerical results obtained by FVBOS demonstrates proper precision relative to the Buckley-Leverett theoretical solution. In this case, it is further demonstrated how gravitational force influences the advance of water saturation front. As it can be observed in Figure 28, the higher the density of the resident fluid phase, the faster the advance of water saturation front and the lower the water saturation behind the water saturation front. This is due to the fact that the decrease in the density of the resident fluid phase results in the higher velocity of the resident fluid phase, according to Darcy's law, which in turn yields both faster decrease of resident fluid phase saturation and faster water saturation increase behind the water saturation front, according to mass conservation law. Furthermore, based on mass conservation law, as the water injection rate is the same for the two cases, the faster water saturation rise behind the water saturation front yields a slower advance of water saturation front. As it was discussed

earlier, the physical interpretation of such phenomena is that an increase in the density of resident fluid phase reduces the mobility of this fluid phase. Such a reduction in the mobility of the resident fluid phase forces the injected water to further penetrate into the resident fluid phase which yields a faster advance of water saturation front leaving less water saturation behind it.

Finally, the pressure and water saturation contours obtained by FVBOS along the porous matrix is exhibited in Figure 29 for the three cases of neglected gravitational force together with the presence of gravity force with resident fluid phase standard density of 800 and 300 kg/m^3. In this figure, the water saturation front can be recognized and compared in the three-dimensional contours. As it can be observed, the presence of gravity force causes a slower advance of water saturation front and higher water saturation behind it. It is also demonstrated that, considering gravitational force, a decrease in the resident fluid phase density decelerates the advance of water saturation front and rises the water saturation behind it. What is further illustrated in these contours is that, pressure in the porous media rises due to the presence of gravitational force and it increases if the density of resident fluid phase is heightened. This pressure response further demonstrates that the multi-phase fluid flow simulated by FVBOS is physically sound and valid.

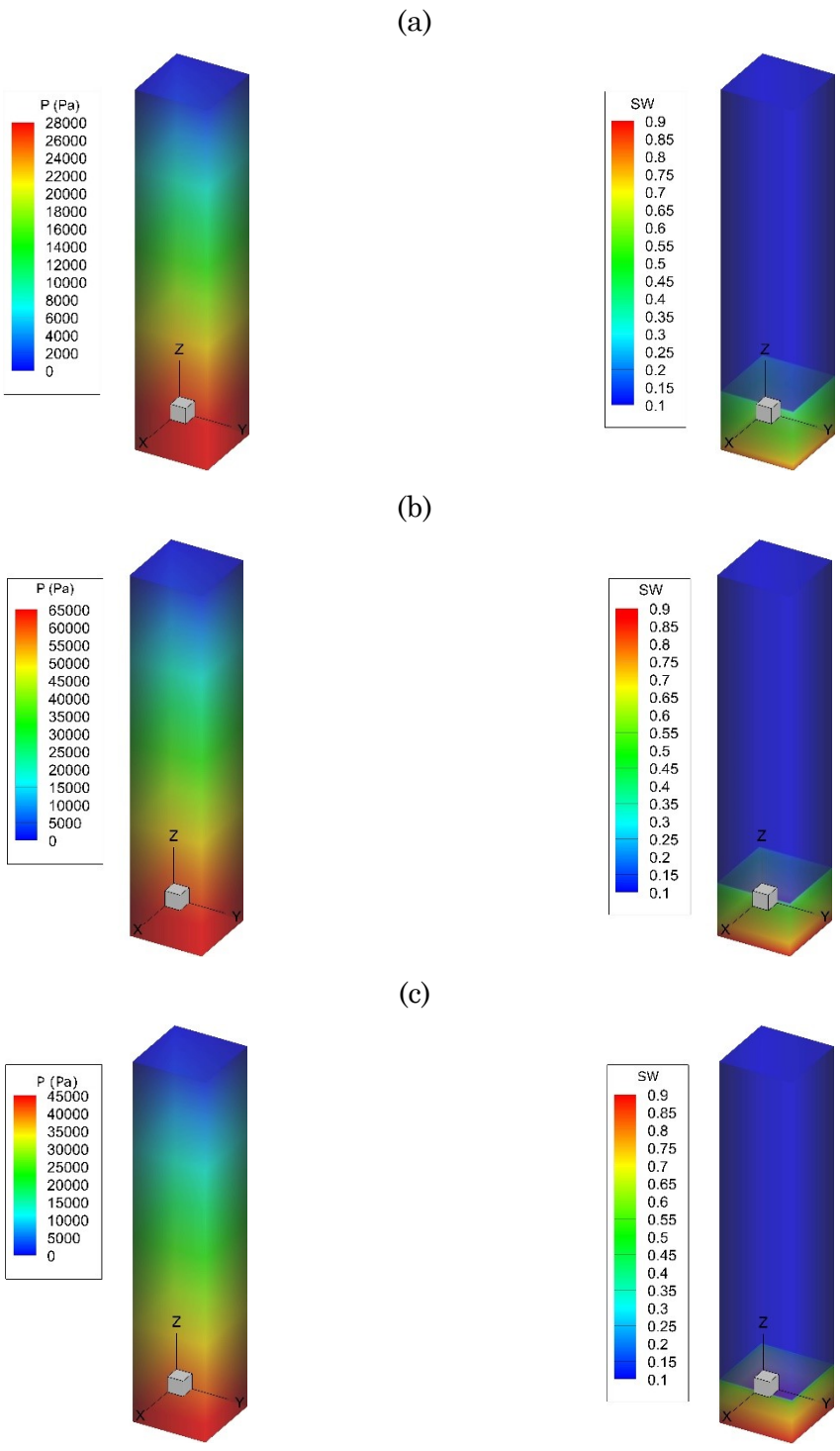

Figure 29: Numerical simulation results by FVBOS for Buckley-Leverett problem in porous matrix after 2 hours of water injection at the bottom of the model.
(a) Neglected gravity force (b) With gravity force and oil density of 800 kg/m^3 (c) With gravity force and oil density of 300 kg/m^3.

5.4.3 Simulation of Immiscible Three-Phase Oil-Water-Gas Gravity Segregation

In the previous section, the effect of gravity on incompressible two-phase fluid flow was simulated by FVBOS and the numerical results were verified with analytical results. In this section, the focus is on the assessment of the performance of FVBOS in the simulation of the tendency of a uniform immiscible three-phase oil-water-gas fluid mixture to be separated into three distinct fluid layers by the movement of heavier fluid phases underneath the lighter ones due to the gravitational force. In the simulation of multi-phase fluid flow, if gravitational force is taken into account, this phenomenon called gravity segregation is always coupled with the effect of other agents. To simulate this phenomenon, the same geometry and rock and fluid material properties as those chosen in the previous section were used in the numerical models. In particular, the standard density and viscosity of the fluid phases used in this simulation are summarized in Table 3.

Table 3: Standard density and viscosity of the fluid phases used in the simulation of gravity segregation of three-phase oil-water-gas fluid by FVBOS.

	Oil Phase	Water Phase	Gas Phase
Standard Density (Kg/m^3)	800	1000	1
Standard Dynamic Viscosity (Pa.s)	0.005	0.001	0.00001

Note: Standard condition is assumed to be represented by temperature and pressure of 16°C and 101.33 KPa, respectively.

In this model, the same relative permeability relation as those used for water and oil was also chosen for gas phase. It is also assumed that the porous media is initially uniformly saturated by the three phases of oil, water and gas, i.e. $S^o = S^w = S^g = 1/3$. Then, the fluid phases are allowed to flow under the influence of gravity until a certain time when the three fluid phases are almost separated. In this model, no flow boundary condition was applied at all boundary surfaces of the model and the length of the model is aligned with the gravitational acceleration, i.e. vertical direction here. The simulation results obtained by FVBOS are exhibited in Figure 30 in terms of contour plots of the saturation of three phases at three different times illustrating the gradual processes of segregation of the fluid phases under gravitational force.

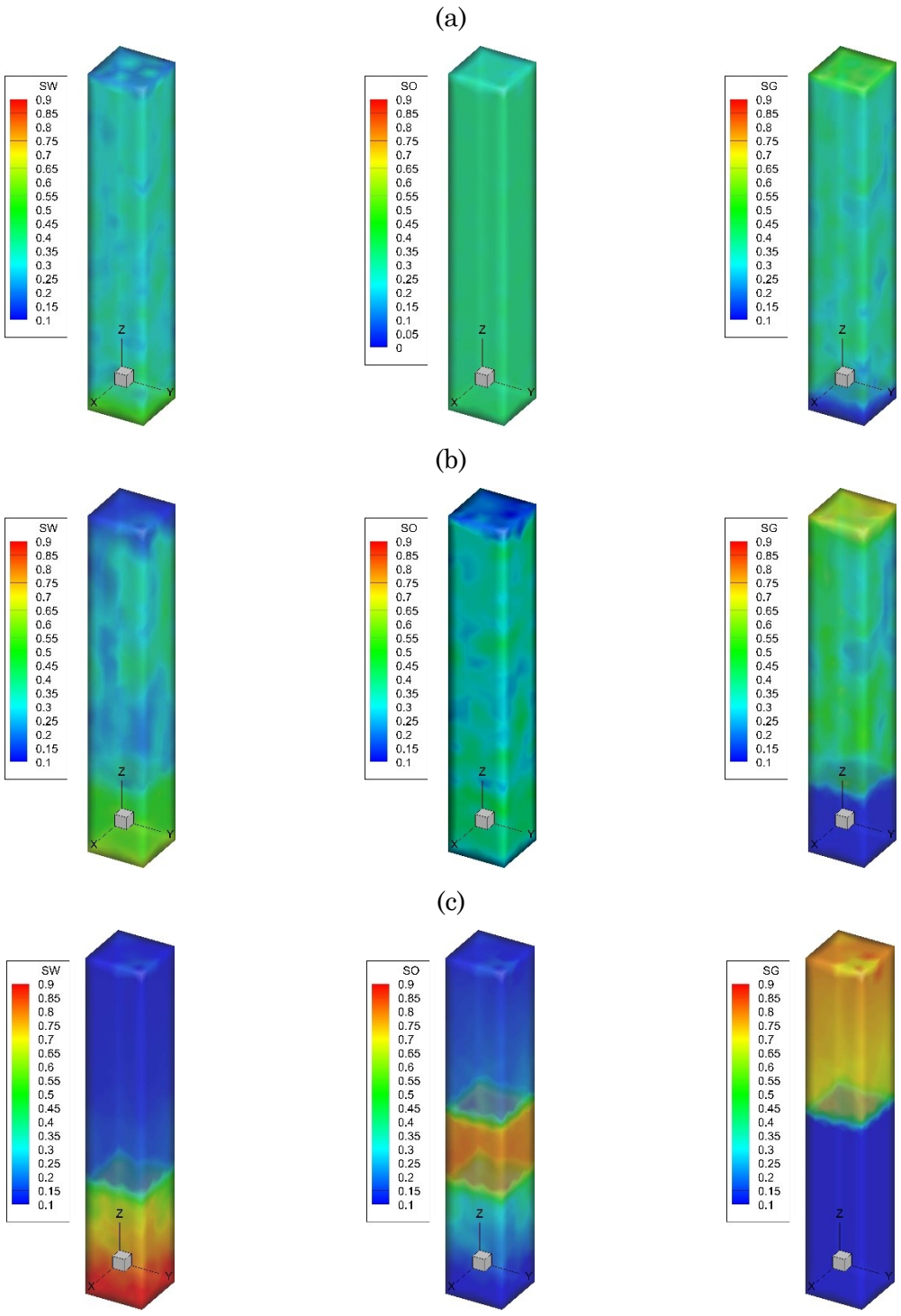

Figure 30: Simulation of gravity segregation of three-phase oil-water-gas fluid by FVBOS. (a) Contour plots of oil, water and gas saturation after 5 minutes (b) Contour plots of oil, water and gas saturation at after 30 minutes (c) Contour plots of oil, water and gas saturation after 6 hours.

As it is demonstrated in Figure 30, the three phases of oil, water and gas move such a way that gas tends to be located on the top of the other two phases while water tends to be located underneath all fluid phases and oil tends to be located between gas and water in the middle. This behavior predicted by FVBOS is confirmed by the fact that, in gravity segregation, the lightest fluid phase, i.e. gas here, has the tendency to be located at the top, while the heaviest fluid phase, which is water here, is inclined to be located at the bottom. Also, the fluid phase with the density between the other two fluid phases, i.e. oil here, tends to be located between the the other two fluid phases. It can also be observed that the separation process occurs for gas phase faster than the other two fluid phases while slowest separation process occurs for the oil phase. This is due to the fact that the gas phase possesses the lowest viscosity which makes the gas mobility higher than the other two phases while oil phase has the highest viscosity implying that oil has the lowest mobility in the three-phase oil-water-gas system. To sum up, the simulation results presented in this section, demonstrate that FVBOS is capable of properly capturing the separation process of immiscible multi-phase fluid phases under gravity.

In the verification problems discussed in the previous sections, the accuracy and capability of FVBOS in precisely simulating the effects of pressure gradient, viscous frictional force, interfacial tension effects between fluid phases and porous media as well as gravitational force on multi-phase fluid flow was demonstrated. In the verification cases, the numerical results obtained by FVBOS were compared with analytical results achieved by Buckley-Leverett theoretical solution. Having assured the validity of the numerical approach implemented into FVBOS in the simulation of the mentioned agents, the next verification case is designed to validate FVBOS in the simulation of the effect of interfacial tension between fluid phases which is approximated by the concept of capillary pressure.

5.4.4 Simulation of the Effect of Capillary Pressure on Incompressible Two-Phase Flow

In the previous sections, incompressible oil-water two-phase fluid flow simulated in the porous media by FVBOS and the results were verified with Buckley-Leverett theoretical solution demonstrating the accuracy of the developed code. In previous sections, the interfacial tension effects between fluid phases and porous media were taken into account

in terms of relative permeability concept neglecting the effect of interfacial tension between the fluid phases. These simulations resulted in a saturation distribution for the invading fluid phase, i.e. water, along the flow direction with a sharp saturation front. In this section, the effect of interfacial tension between the fluid phases approximated in terms of capillary pressure is taken into account in the problem of two-phase oil-water flow where water is injected into a porous media initially saturated by the oil phase. The geometry and material parameters used in these simulations for the porous media and fluid phases are the same as the previous models. In these simulations, the effect of gravity is neglected and the capillary pressure relation used in the analyses is illustrated in Figure 31.

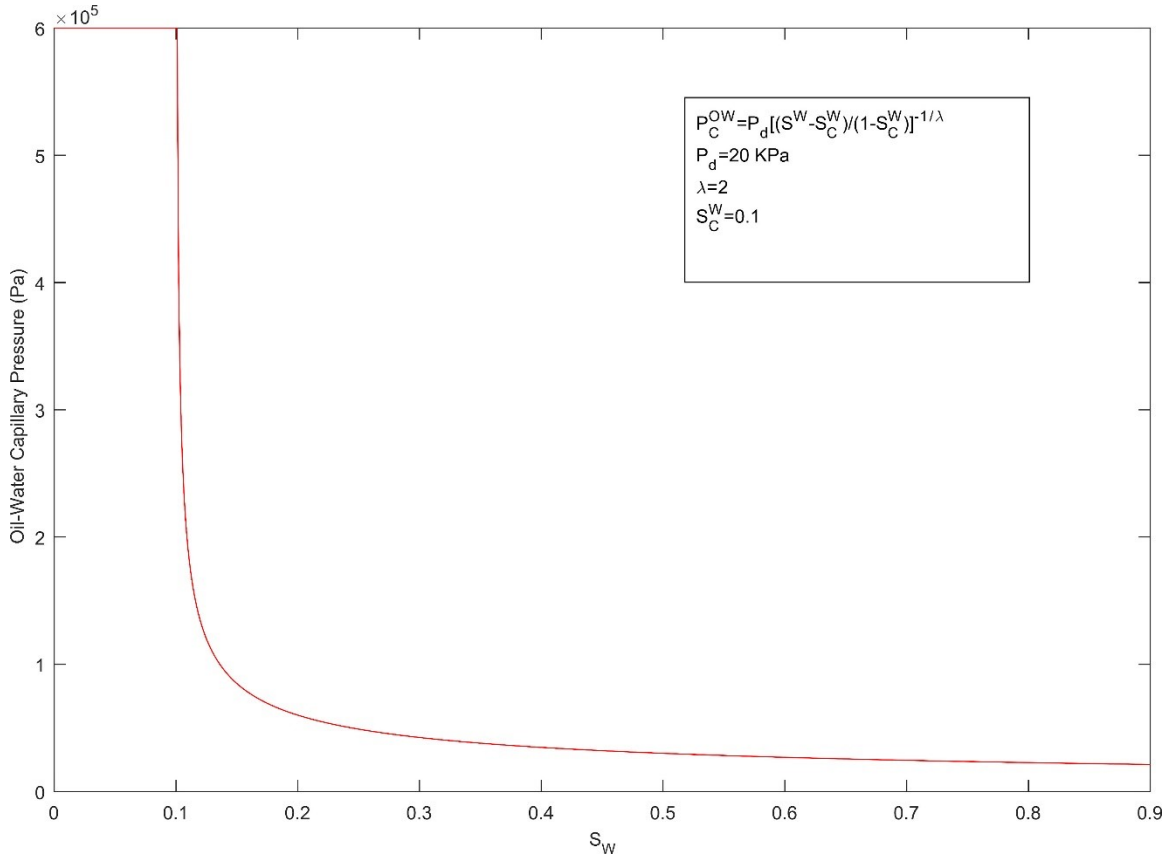

Figure 31: Capillary pressure relation used in Buckley-Leverett problem.

Since considering capillary pressure term in the Buckley-Leverett fractional equation makes the equation coupled, a one-dimensional finite difference method is utilized to solve this equation. Then, the results obtained by FVBOS is compared with the one-dimensional finite difference solution of the fractional equation as it is shown in Figure

32.

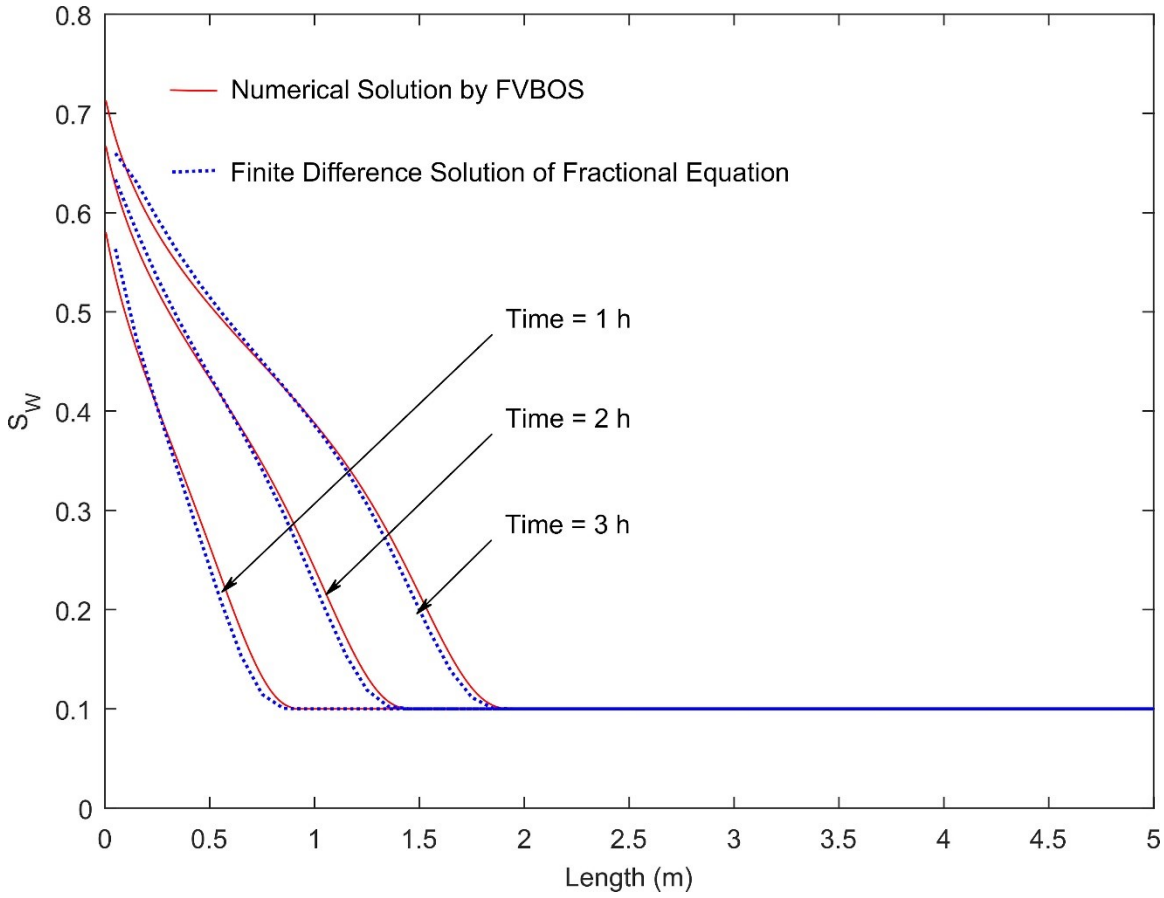

Figure 32: Verification of FVBOS with finite difference solution of fractional equation taking into account the effect of capillary pressure.

As it can be seen, the numerical results obtained by FVBOS is in a good agreement with the one-dimensional finite difference solution of Buckley-Leverett fractional equation taking into account capillary pressure effects. As it is shown in Figure 32, instead of the sharp saturation front observed in the case neglecting capillary pressure, a smooth transition is observed in the water saturation front by taking into account the capillary pressure effects. This smooth transition is due to the fact that, since the water phase is considered as the wetting phase in the capillary pressure relation used in the analyses, in addition to the pressure gradient and viscous force, the multi-phase fluid flow is also affected by the interfacial tension existing between the fluid phases and the porous media. The capillary pressure resulting from the interfacial tension between fluid phases causes the imbibition of the wetting phase, i.e. water, here. This imbibition effect converts the sharp water saturation front resulted from the pressure gradient and viscous force to a

smooth water saturation distribution.

The numerical results obtained by FVBOS for Buckley-Leverett fractional equation considering capillary pressure effect is displayed in terms of pressure contour as well as water and oil saturation contours in Figure 33. In the displayed contour plots of saturation of the water and oil phase, a blurry water saturation front can be observed instead of a distinct one due to the capillary pressure effect.

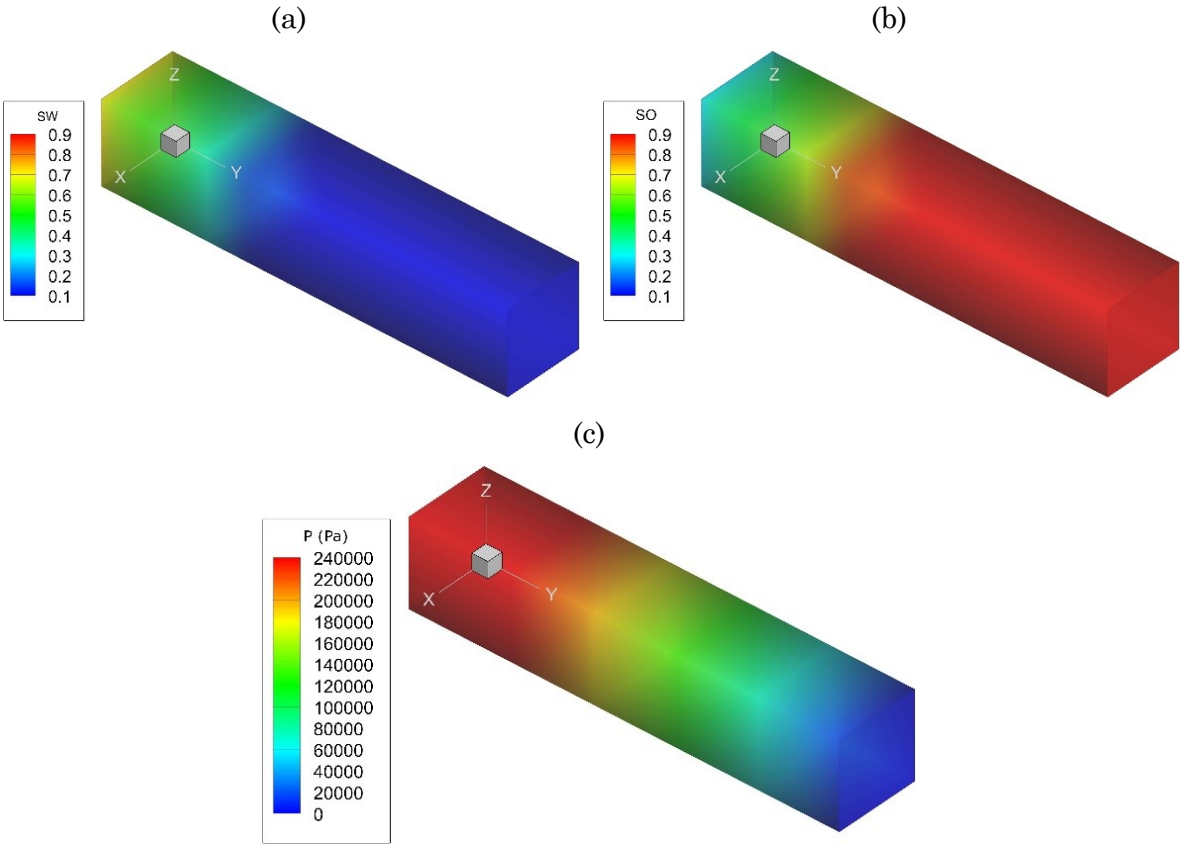

Figure 33: FVBOS numerical simulation results for Buckley-Leverett problem in porous matrix considering capillary pressure effects after 3 hours of water injection at the left side of the model.
(a) Water saturation contour (b) Oil saturation contour (c) Pressure contour.

Overall, it can be concluded that the formulated numerical approach implemented in FVBOS provides an accurate and effective method for the simulation of multi-phase fluid flow considering pressure gradient, viscous frictional force, gravity and capillary pressure. In the next sections, additional verification problems are designed to assess the capability of FVBOS in the simulation of the other aspects of the multi-phase fluid flow such as fluid phases compressibility, mass conservation at fracture intersections and so

forth.

5.4.5 Simulation of the Effect of Fluid Compressibility on Two-Phase Flow

In the previous verification problems, the validity of FVBOS in the simulation of incompressible multi-phase fluid flow through fractures and porous matrix under viscous forces, gravity and interfacial tension was demonstrated. In this section, FVBOS is utilized to simulate compressible multi-phase fluid flow through porous media and the results are compared with CMG-IMEX which is one of the widely-used reservoir simulation codes. As it was discussed in the previous sections, for the sake of conciseness, the numerical simulation verifying FVBOS in the analysis of compressible multi-phase fluid flow is performed only for the case of porous matrix without the loss of the generality of the verification case for both porous matrix and fractures.

To this end, compressible two-phase oil-water fluid flow through porous matrix is simulated by both FVBOS and CMG-IMEX and the results are compared with the incompressible case analytically solved by Buckley-Leverett method. In the simulation of compressible two-phase flow, water is assumed to be incompressible without any dissolved gas with the constant viscosity of 0.001 Pa.s. In contrast, oil is assumed to be compressible with pressure dependent viscosity, volume factor and solution gas-oil ratio shown in Figure 34 as well as bubble point pressure of 15 MPa. The properties of oil phase were determined based on the black-oil correlations as it is discussed in more details in Appendix E. As it was discussed in chapter 3, the compressibility of oil is calculated based on its volume factor and solution gas ratio in the numerical simulation of multi-phase flow by FVBOS. In this regard, up to bubble point pressure, higher pressure results in more dissolved gas inside oil phase which in turn increases solution gas-oil ratio and volume factor of oil and decreases oil viscosity. However, as the pressure goes beyond the bubble point pressure, the dissolved gas inside oil remains constant which means that, for pressures higher than bubble point pressure, pressure increase causes reduction in oil volume factor and rise in oil viscosity.

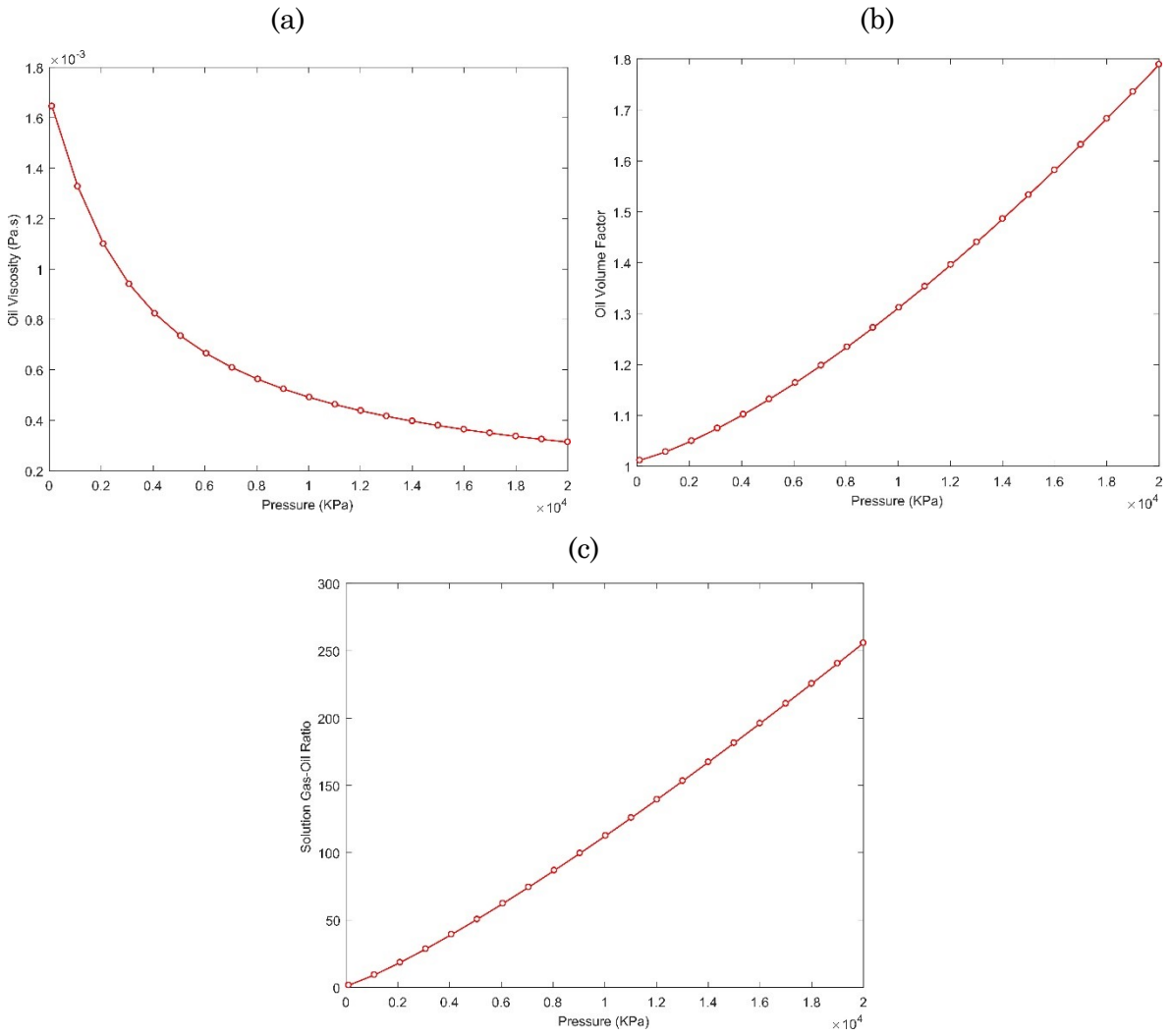

Figure 34: Pressure dependent properties of oil phase below bubble point pressure used in the verification of FVBOS in the simulation of compressible multi-phase flow.
(a) Variation of oil viscosity with pressure (b) Variation of oil volume factor with pressure (c) Variation of solution gas-oil ratio with pressure.

The results obtained by FVBOS and CMG-IMEX for this verification case are displayed in Figure 35. In addition to the numerical results for compressible flow, the analytical results obtained by Buckley-Leverett method for incompressible flow are also reflected in this figure to illustrate the effects of multi-phase fluid compressibility on the mass transport occurring in this problem.

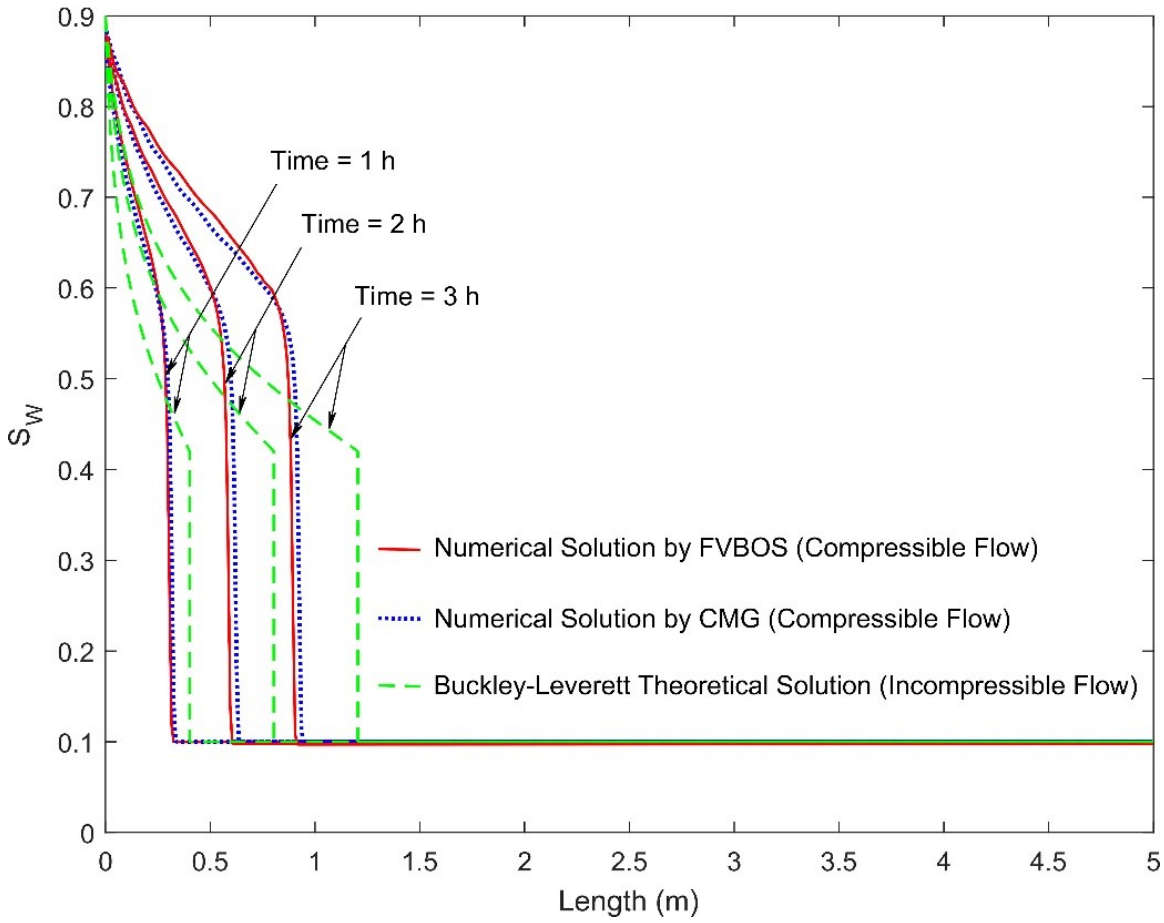

Figure 35: Verification of FVBOS with Buckley-Leverett theoretical solution accounting for the effect of resident fluid phase compressibility.

As it is demonstrated in Figure 35, the numerical results obtained by FVBOS is in a good agreement with CMG_IMEX which demonstrates the validity of FVBOS in the simulation of compressible multi-phase fluid flow. The comparison of the results obtained for compressible and incompressible fluid flow indicates that water saturation front in the case of compressible fluid flow moves slower than the case of incompressible flow. This is due to the fact that the compressibility of fluid results in more accumulation of fluid mass inside the pore spaces which in turn decreases the outflow rate of the pore spaces slowing down the water saturation front advance. As it is illustrated in Figure 35, due to this excess mass accumulation resulted from the fluid compressibility, water saturation behind the water saturation front is higher than that in incompressible flow case.

As it can be observed in Figure 35, the results achieved by FVBOS are numerically stable.

In particular, to examine the numerical stability of the solution obtained by FVBOS in more detail, the material balance error for oil and water fluid phases produced during the analysis has been displayed in Figure 36. The material balance error was defined as the difference between the net amount of fluid mass injected into the porous media and the change in the amount of fluid mass accumulated in the porous media in the current time step divided by the amount of fluid mass stored in the porous media in the previous time step. According to Figure 36, the material balance error generated by FVBOS is negligible and decreases by time which indicates the numerical stability of the solution achieved by FVBOS.

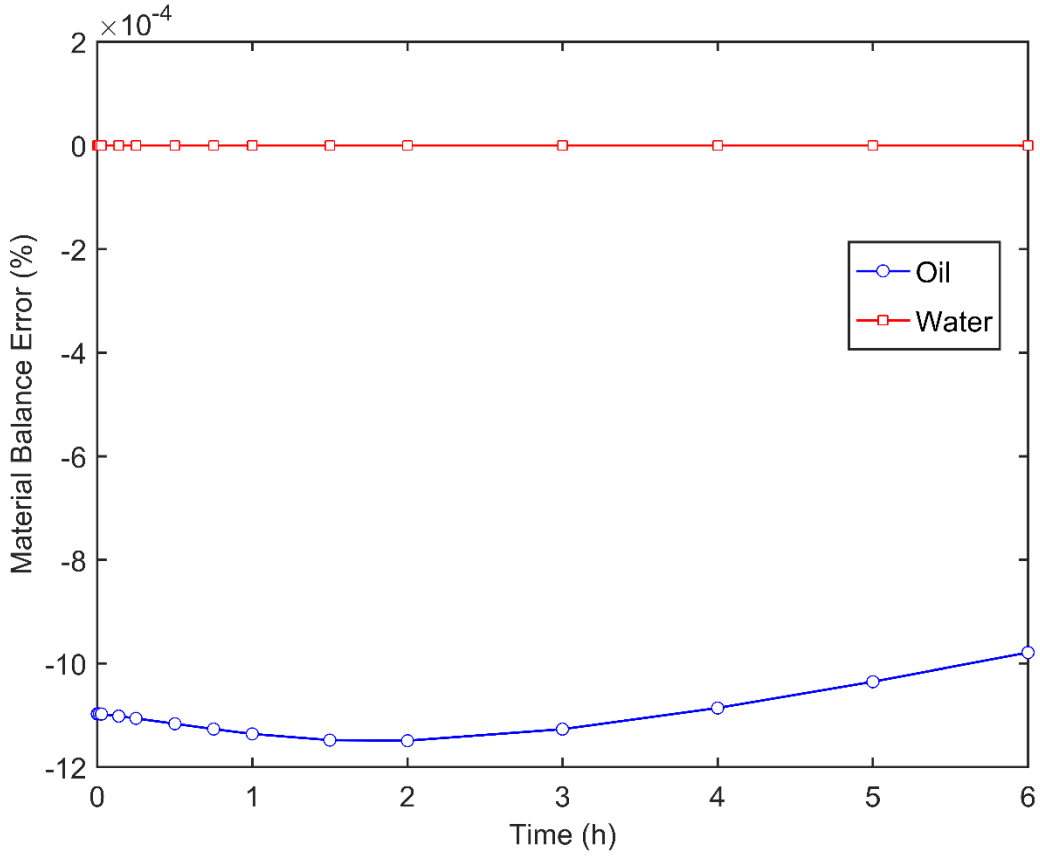

Figure 36: Material balance error generated by the numerical solution performed by FVBOS.

In the verification problems simulated by FVBOS, the competence of this code in the simulation of fundamental physical processes behind multi-phase fluid flow through fractures and porous matrix has been proven. In the final verification case, the accuracy of the numerical treatment formulated based on mass conservation at the intersection of

multiple fractures, implemented into FVBOS to avoid extremely small finite volumes at the intersections, is assessed.

5.4.6 Simulation of the Effect of Mass Conservation at Fractures Intersection on Two-Phase Fluid Flow through Multiple Fractures

In previous sections, the performance of FVBOS in modeling matrix-matrix, matrix-fracture and fracture-fracture multiphase fluid transfer was assessed by verifying FVBOS numerical simulation results with Buckley-Leverett analytical solution for the incompressible two-phase fluid flow demonstrating the accuracy and capabilities of the developed numerical approach. However, in the simulation of fracture-fracture multi-phase fluid transfer, the case of multiple intersecting fractures was not considered in the verification problems. In case multiple intersecting fractures are required to be numerically modeled, the mechanism of fracture-fracture multi-phase fluid transfer is partly different from the case of two neighboring fracture finite volumes.

If multiple intersecting fractures are existing in the model, a fluid distribution approach is utilized at the fracture intersections satisfying mass conservation at the intersection. In this regard, the direct approach is to consider separate finite volumes at the fracture intersections to distribute fluid between the finite volumes representing intersecting fractures satisfying mass conservation. However, the size of such finite volumes at fracture intersections are so small relative to neighboring finite volumes that it necessitates extremely fine spatial discretization around fracture intersections making the numerical simulations dramatically time consuming.

A more efficient approach used in the numerical method developed in this research is to eliminate these infinitesimal finite volumes by utilizing modified transmissibility at the fracture intersections formulated by satisfying mass conservation at fracture intersections. Using this approach, multiple intersecting fractures encountered in complex discrete fracture networks can be effectively simulated. In order to verify the numerical treatment at fracture intersections, a verification case was designed based on Buckley-Leverett problem. In this verification problem, incompressible two-phase oil-water fluid flow is numerically simulated by FVBOS in a set of three intersecting fractures and the numerical result is compared with an analytical solution obtained based

on Buckley-Leverett method as it is shown in Figure 37 and Figure 38.

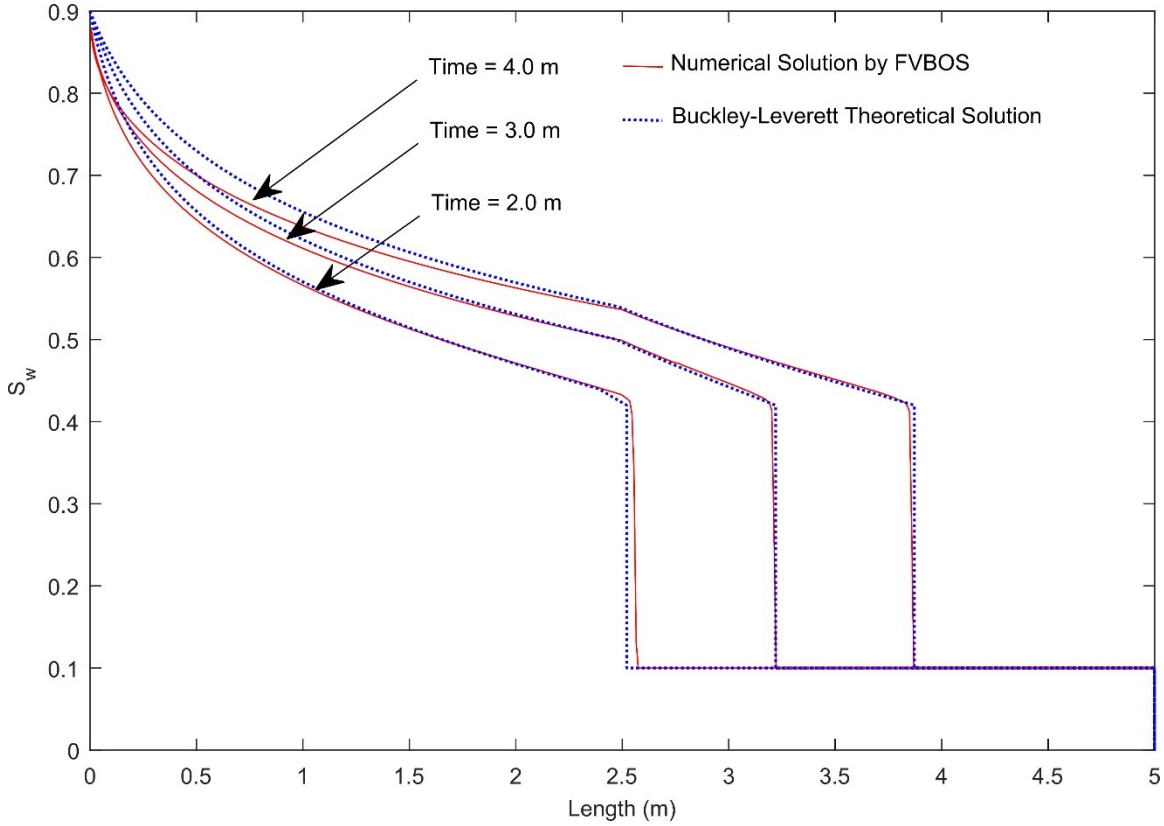

Figure 37: Verification of FVBOS with Buckley-Leverett theoretical solution in the case of multiple fractures intersections.

In the numerical simulation, the same material parameters and initial conditions as those used in the single fracture verification problem were utilized. In this model, water is injected from the left side of the intersecting fractures, which are saturated by oil, and the simulation is continued until water saturation increases up to a noticeable amount in the right side of the fractures intersection.

In the analytical solution, the multi-phase fluid flow in the fracture located at the left side of the intersection is analytically solved using Buckley-Leverett method based on the total injection flow rate applied at the left side of the model up to the intersection point. Then, as soon as the invading fluid phase reaches the intersection point, based on mass conservation law, the multi-phase fluid flow problem in the fractures at the right side of the intersection is analytically solved using Buckley-Leverett method considering half of the total flow rate injected at the left side of the model. As it is shown in Figure 37 and Figure 38, the numerical solution achieved by FVBOS approximates the analytical

solution with a reasonable accuracy.

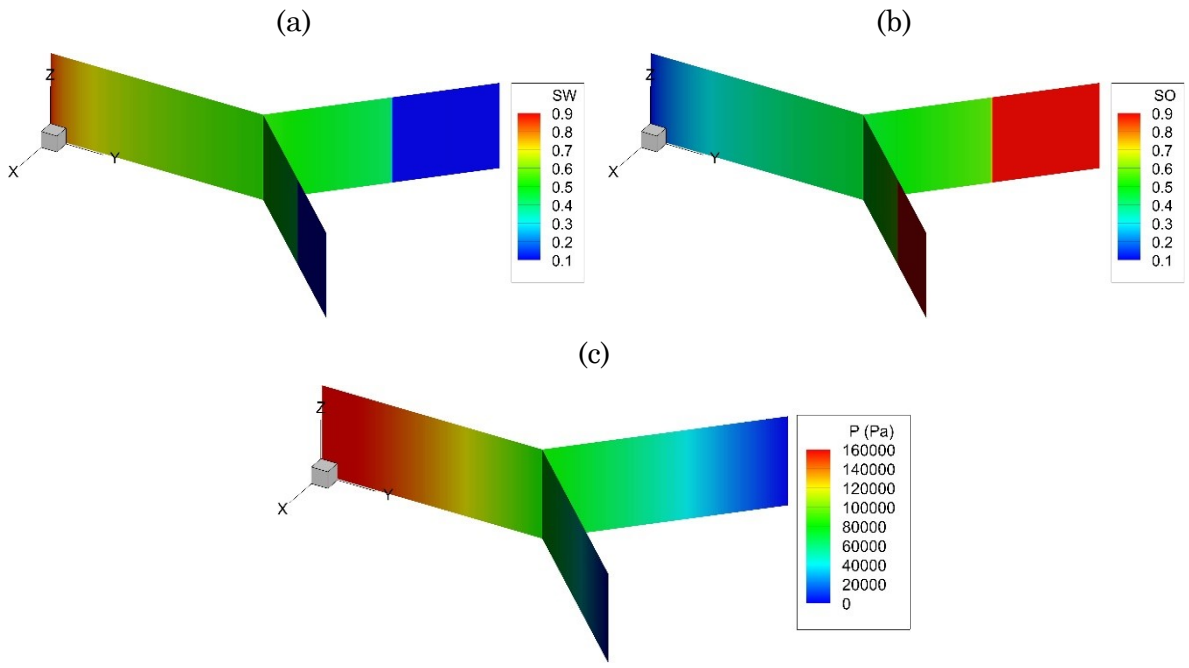

Figure 38: FVBOS numerical simulation results for Buckley-Leverett problem in multiple fractures after 4 minutes of water injection at the left side of the model.
(a) Water saturation contour (b) Oil saturation contour (c) Pressure contour.

As it is demonstrated in Figure 37 and Figure 38, the water saturation front predicted by Buckley-Leverett theoretical solution for incompressible flow as well as mass conservation at the fracture intersection are precisely approximated by FVBOS. As it can be observed, the water saturation distribution approximated by FVBOS at the right side of the fracture intersection matches with the analytical results with a much higher accuracy than those approximated at the left side of the fracture intersection. In particular, in the area adjacent to the injection point, a recognizable deviation between numerical and analytical results can be perceived after the water saturation front passes the fracture intersection. This deviation is mainly due to the fact that the flow regime assumed in the left side of the fracture intersection in the Buckley-Leverett theoretical solution changes when the water saturation front passes the fracture intersection.

In the theoretical solution developed for this problem, two separate Buckley-Leverett analytical solutions were assumed for the fracture at the left side of the intersection and the fractures at the right side of the intersection. The theoretical solution used for the fracture at the left side of the intersection, assumes that the fracture is extended at the

right side of the intersection with the same geometrical properties. However, the summation of the cross-sectional area of the two fractures located at the right side of the intersection is twice as large as the fracture located at the left side of the intersection. Such geometrical discrepancy brings about the deviation of the theoretical solution used to represent the fluid flow in the fracture located at the left side of the intersection from the numerical results by FVBOS. In spite of this discrepancy, the theoretical solution developed for the fractures located at the right side of the fracture intersection precisely represents the multi-phase fluid flow occurring in these fractures.

As it was discussed in detail in the verification case for single fracture, the mentioned discrepancy between analytical and numerical solutions is further magnified due to the incompressibility assumption in theoretical solution. This is due to the fact that the numerical method implemented in FVBOS is formulated for the general multi-phase fluid flow condition where compressibility of the fluid phases and porous matrix as well as the fracture aperture change due to pressure change is taken into account. In other words, in FVBOS, an accumulation term dependent on both fluid and porous media compressibility is considered in the mass conservation equations. Therefore, it is not practical to simulate the exactly incompressible fluid flow by FVBOS since as the compressibility of both fluid phases and porous media simultaneously approaches to zero, the accumulation term in mass conservation equation approaches to zero which brings the mass conservation differential equations closer to singular condition. In such conditions, either a large number of iterations are needed for FVBOS to converge to an acceptable solution, or it is not conceivable to achieve stable numerical results.

In order to practically approximate the incompressible fluid flow condition assumed in Buckley-Leverett method, a slight compressibility either for fluid phases or for porous media should be considered in FVBOS. In the numerical solutions carried out for the verification of FVBOS with Buckley-Leverett theoretical solution, a slight compressibility, i.e. porous matrix porosity or fracture aperture change due to pressure change, was assumed in the analyses. The slight compressibility assumed for porous media allows a slight fluid accumulation in the finite volumes which magnifies the deviation of the numerical solution obtained by FVBOS from those obtained based on incompressibility assumption. Such accumulation term rises by pressure increase since it causes an increase in the volume of the finite volumes, which in turn brings about the

deviation between the numerical results from the incompressible theoretical solutions. This situation is intensified for fractures due to the fact that fracture aperture is so small that the fluid injection increases the pressure inside fracture so fast resulting in more fluid accumulation and deviation from incompressible theoretical results. Overall, in spite of the negligible deviation from analytical solutions in the fracture at the left side of the intersection, the numerical results obtained by FVBOS demonstrate a reasonable precision in the simulation of mass conservation at the fracture intersections.

5.4.7 Simulation of Multi-Phase Fluid Flow in Porous Media Containing Stochastically Generated Discrete Fracture Network

In the previous sections, a comprehensive procedure was designed to verify the developed finite volume discrete fracture-matrix method implemented into FVBOS. To this end, the multi-phase fluid flow problem through fractured porous media was simplified into a number of verification cases such a way that each case can be a representative of the effects of separate agents, namely gravity, viscous forces, interfacial tension, fluid compressibility and mass conservation at fracture intersections. The performance of FVBOS in the simulation of the verification cases was assessed by comparing its numerical results with available theoretical solutions, simplified numerical solutions as well as a widely-used reservoir simulation software. The verification study demonstrated the accuracy and capabilities of FVBOS in the simulation of multi-phase fluid flow through fractured porous media.

The exceptional capability of FVBOS is that it can deal with the numerical simulation of compressible multi-phase fluid flow through both pore spaces of porous matrix and highly complex discrete fracture networks in the framework of a unified finite volume mesh. This unique capability makes FVBOS a powerful computational tool in the simulation of multi-phase fluid flow through naturally fractured reservoirs in general and shale reservoirs in particular.

In this section, the capability of FVBOS in dealing with numerical simulation of multi-phase fluid flow through discontinuous porous media involving complex fracture networks is demonstrated. The complex discrete fracture network and the finite volume mesh needed by FVBOS for the numerical simulation of such problem are generated with

the aid of 3DEC, Itasca's three-dimensional distinct element code. To this end, first, a discrete fracture network was stochastically generated by 3DEC. Then, a porous matrix block with the length, width and heights respectively equal to 10 m, 10 m, and 5 m were cut by the fracture network. The discrete matrix blocks along with the discrete fracture network were discretized into distinct element zones by 3DEC. Afterwards, using an algorithm implemented into the class Grid in FVBOS, the finite volume mesh needed for the discretization of porous matrix and discrete fracture network required for the multi-phase fluid flow analysis is generated. This algorithm implemented into FVBOS generates the required mesh based on the coordinates of the grid points of the distinct element zones generated by 3DEC. Then, another algorithm implemented into the class Grid in FVBOS is utilized to recognize the neighboring zones of each finite volume zone for the purpose of fluid transmissibility calculations. The discrete fracture network stochastically generated by 3DEC is exhibited in Figure 39.

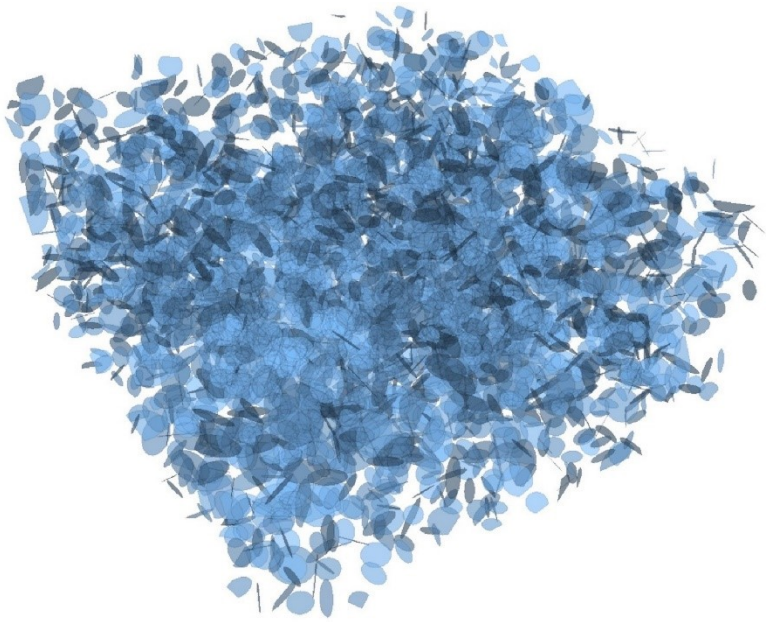

Figure 39: Discrete fracture network stochastically generated by 3DEC representing complex fracture system existing in shale reservoir formations.

The porous matrix block cut by the discrete fracture network as well as the distinct element mesh discretizing porous matrix blocks and discrete fracture networks generated by 3DEC are shown in Figure 40. In this figure, the finite volume mesh generated by FVBOS based on 3DEC grid point coordinates is also illustrated.

(a)

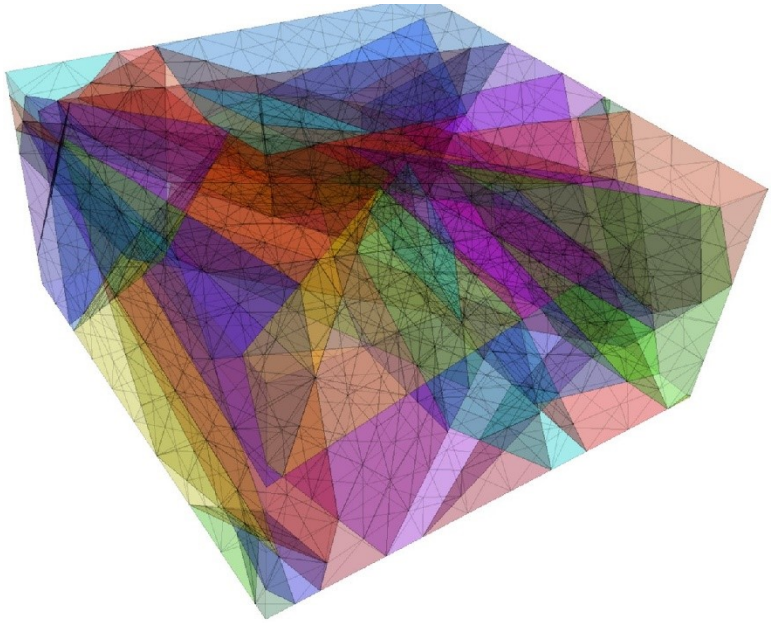

(b)

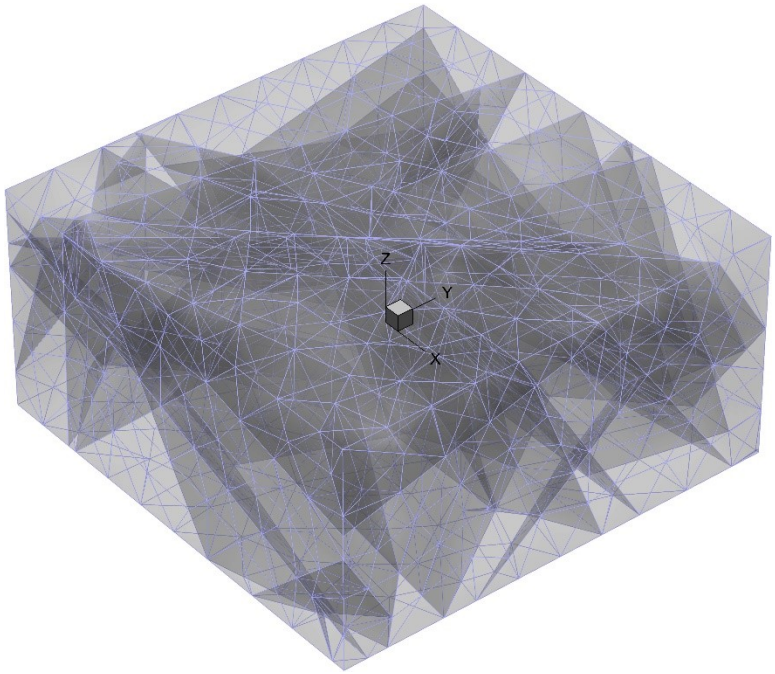

Figure 40: distinct element and finite volume mesh discretizing porous matrix blocks and stochastically generated fracture network.
(a) Distinct element mesh generated by 3DEC (b) Finite volume mesh generated by FVBOS.

In this problem, it is assumed that the fractured porous media is 20 percent saturated by

water, 20 percent saturated by oil and 60 percent saturated by gas. The fluid properties for water and oil are the same as those assumed in the section 5.4.5 for the simulation of compressible two-phase oil-water flow. The fluid properties used to simulate the behavior of gas are shown in Figure 41. The properties of gas phase were determined based on the black-oil correlations as it is discussed in more details in Appendix E.

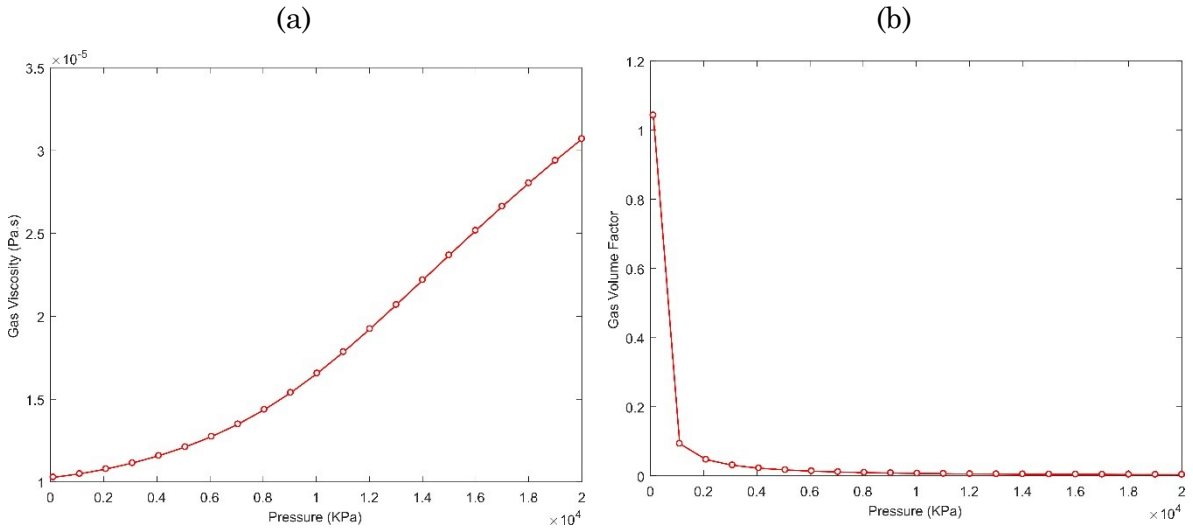

Figure 41: Pressure dependent properties of gas phase used in the simulation of multi-phase fluid flow through porous matrix and stochastically generated discrete fracture network by FVBOS.
(a) Variation of gas viscosity with pressure (b) Variation of gas volume factor with pressure.

As it is shown in Figure 41, the gas phase is simulated as a compressible fluid with viscosity increasing by pressure. The volume factor of gas drastically decreases up to the pressure of around 2 MPa implying a highly compressible behavior while for pressures greater than 2 MPa the volume factor gradually diminishes by pressure rise indicating a relatively moderate compressibility. In this problem, a hydrostatic initial pressure distribution with the pressure equal to 200 KPa at the center of the block is assumed. Then, water is injected at the center of the fractured block with the flow rate of 0.001 m^3/s increasing the pressure in the porous media. It is also assumed that the initial, residual and maximum aperture of the fractures are respectively equal to 0.05 mm, 0.05 mm and 10 mm. Also, the normal stiffness of the fractures is assumed to be equal to 1 GN/m. The pressure contour as well as water, oil and gas saturation contours obtained by FVBOS after 30 minutes of water injection are shown in Figure 42.

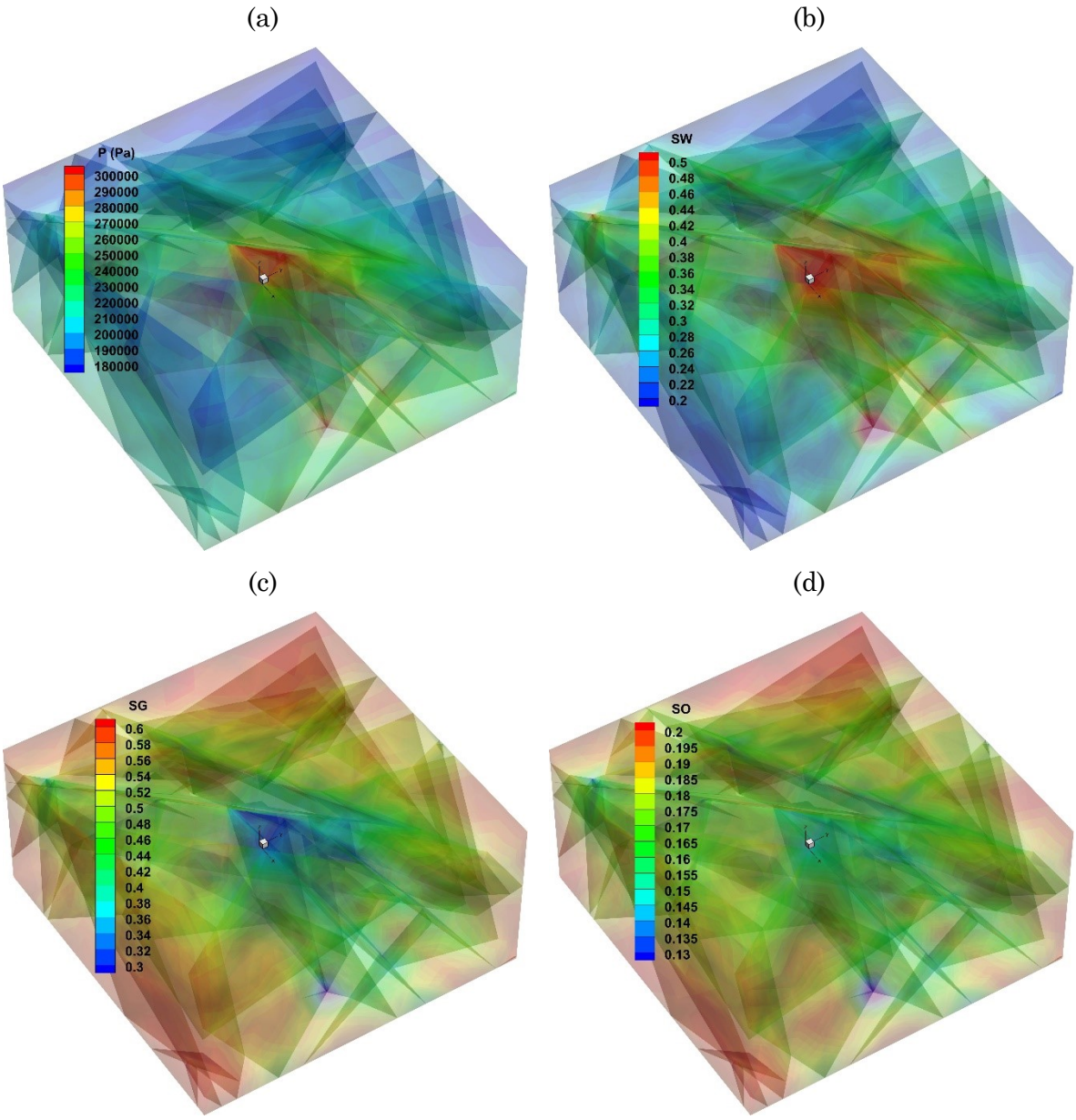

Figure 42: Numerical results obtained by FVBOS for multi-phase fluid flow through porous matrix and stochastically generated discrete fracture network.
(a) Pressure contour (b) Water saturation contour (c) Gas saturation contour (d) Oil saturation contour.

According to Figure 42, by the injection of water, water saturation rises mostly at the center of the fractured porous block creating pressure gradient which in turn pushes back oil and gas phases towards the outer boundaries of the block. As it can be seen, the injected water flows mostly through the fracture network providing flow paths with higher permeability. Also, while most of the injected water is trapped at the center of the

block due the limitation of fractures lengths, gravitational force directs some of the water flow through the permeable connected paths towards the bottom of the block. It can be observed that, at the areas with higher density of fracture intersections at the bottom of the block, the water flow through the fractures are joined together creating areas with high water saturation and lower gas and oil saturation. The pore fluid pressure rise due to the water injection yields an increase in the fractures aperture as it is demonstrated in the fracture aperture contour shown in Figure 43.

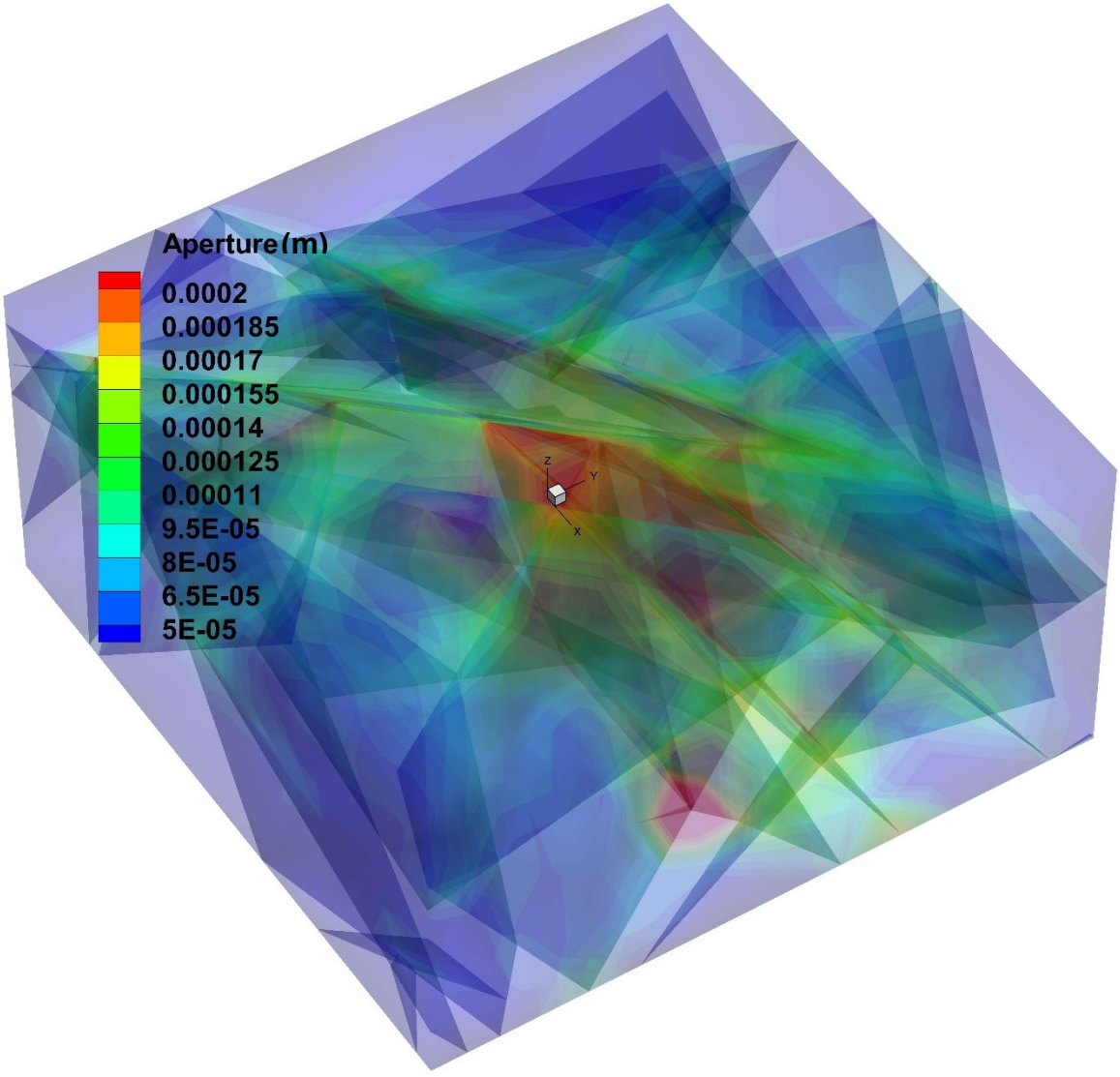

Figure 43: Aperture contour obtained by the numerical simulation of multi-phase fluid flow through porous matrix and stochastically generated discrete fracture network using FVBOS.

As it can be seen in Figure 42 and Figure 43, the higher the saturation of water, the higher the pore fluid pressure and fracture aperture. It should also be noted that the fracture aperture increase predicted by FVBOS is distributed almost throughout the fractured porous block. Such fracture increase pattern has been predicted based on the pore fluid pressure increase merely calculated by fluid flow simulation. However, in reality, fracture aperture is a function of the displacement field in solid phase which in turn depends not only on pore fluid pressure, but also the stress field and boundary condition in the solid phase. Therefore, in order to have a more realistic estimation of the fracture aperture change and multi-phase fluid flow, the effects of hydro-mechanical coupling have to be taken into account. In fact, considering highly complicated geometries encountered due to the existence of complex natural fracture networks, it is not reliable to assume a stress field without justifiable solid mechanical analyses. In particular, simulation of such complicated discontinuities in the solid mechanical analyses necessitates sophisticated numerical approaches such as discrete element method to account for the deformation of the complex fracture networks involving the slippage and detachment of the discrete blocks. In the next chapter, such numerical model is addressed by developing a coupled hydro-mechanical multi-phase computational tool using the devised discrete fracture-matrix approach implemented into FVBOS and 3DEC, Itasca's three-dimensional distinct element code.

6 Multi-Phase Discrete Element Simulator (MPDES)

In the previous sections, the detailed formulation of the developed finite volume discrete fracture-matrix method was presented. As it was discussed, the partial differential equations of motion of multi-phase fluid flow through porous matrix and fractures were developed by satisfying momentum and mass conservation laws. Then, the multi-phase fluid material model along with relative permeability and capillary pressure concepts were utilized to combine the system of partial differential equations of motion to achieve a single compact equation where pressure of one of the fluid phases is the only unknown to be solved. In the next stage, a finite volume discrete fracture-matrix approach was formulated to discretize the compact governing partial differential equation. It was also demonstrated how both porous matrix and fractures can be discretized in a unified grid system using the formulated matrix-matrix, matrix-fracture and fracture-fracture fluid transmissibility. An implicit pressure-explicit saturation method was also used to discretize the compact partial differential equation in time domain.

Afterwards, an object-oriented C++ code called FVBOS was developed to implement the finite volume discrete fracture matrix method and the numerical results generated by FVBOS were verified for different benchmark problems solved either by available theoretical solutions or by the widely used commercial reservoir simulation software CMG IMEX. The verification results demonstrated the acceptable precision and unique capabilities of FVBOS in the simulation of multi-phase fluid flow through both porous matrix and complex discrete fracture networks.

One of the major benefits of FVBOS is that the finite volume discrete fracture-matrix approach implemented in this software for multi-phase fluid flow analysis is compatible with discrete element solid mechanical simulators for hydro-mechanical coupling purposes. In particular, this advantage is highlighted considering the fact that FVBOS is capable of simulating compressible multi-phase fluid flow through complex discrete fracture networks and the surrounding porous matrix in a unified finite volume grid system. These unique capabilities of FVBOS makes it feasible to develop a powerful

coupled hydro-mechanical multi-phase simulator by coupling this software with discrete element solid mechanics codes. In spite of substantial potential capabilities of such discrete element hydro-mechanical multi-phase simulator in unraveling fluid flow problems in unconventional oil and gas reservoirs involving complex fracture networks, it has not been properly approached so far and the major focus of this research is to address this shortcoming.

In the following sections, a novel numerical approach is developed by coupling the devised finite volume discrete fracture-matrix approach implemented in FVBOS for multi-phase fluid flow simulation and discrete element method for solid mechanics simulation based on the coupled hydro-mechanical equations of motion discussed in chapter 3 and 4. To this end, 3DEC, Itasca's 3-dimensional distinct element code, was used to undertake discrete element solid mechanical analyses needed for the hydro-mechanical coupling. It is worth mentioning that although 3DEC was chosen as the solid mechanical discrete element simulator in this research, the developed methodology and the computer program for coupled hydro-mechanical multi-phase simulation in fractured porous media is universal. Using the developed hydro-mechanical method, any discrete element, finite element, finite volume or finite difference solid mechanical simulation codes can be used to be coupled with FVBOS.

6.1 Hydro-Mechanical Coupling Approach

As it was discussed in detail in chapter 3 and 4, equations of motion governing the displacement and velocity field in porous media along with velocity and pressure field in multi-phase fluid flow are formulated by satisfying mass conservation, momentum conservation and constitutive laws. To this end, momentum conservation and constitutive laws were satisfied for a multi-phase system comprised of fractured porous media containing multi-phase pore fluid with negligible movement relative to solid phase. In this stage, equilibrium condition is satisfied for total stresses applied on a differential Lagrangian system of mass involving the solid phase and the pore fluid, which is immobile relative to solid phase. In the resulting equilibrium equations, total stresses can be substituted by strains developed in the differential Lagrangian system of mass using constitutive equations.

In order to be able to utilize the available constitutive equations developed for pure solid

phase, without any need for developing totally new ones for the multi-phase differential element, the effective stress concept is extensively utilized. In this concept, it is postulated that the total stress applied on the differential multi-phase mass element is equilibrated by two components, namely pore fluid pressure developed inside the element and the stress developed between the contacts of solid phase constituents. In these circumstances, a portion of the volumetric deformation of the multi-phase element occurs due to the volumetric deformation of the pore fluid under pore pressure and it is assumed that shear stress developed in the pore fluid is negligible. Therefore, by subtracting the contribution of the pore fluid pressure from the total stresses, the remaining volumetric deformation as well as shear deformation is developed in the solid phase due to the remaining portion of the stresses called effective stress. Consequently, effective stresses can be related to the strains of the differential Lagrangian element using constitutive relations developed for pure solid phase. To this end, constitutive parameters shall be determined based on laboratory measurements and employing constitutive equations previously developed for pure solid phase. Finally, by using proper kinematic relations depending on the type of large or small deformation analyses, strains can be substituted by derivatives of displacement or velocity field of porous media. Using such methodology, the final equations of motion of the the porous media containing relatively immobile multi-phase fluid can be formulated based on the unknown displacement or velocity field in porous media as well as unknown pore fluid pressure field.

Another physical process, which should be taken into account in the equations of motion, is the movement of the multi-phase fluid through the pore spaces and fractures of the porous media relative to the solid phase. This mechanism has been formulated for an Eulerian control volume attached to the porous media in chapter 4 and implemented and verified in chapter 5. In this regard, Navier-Stokes equations which are the combination of momentum conservation law and constitutive equations for fluid flow were simplified to Darcy's law for fluid flow through porous matrix and Reynolds equation for fluid flow through fractures. Then, the generalization of these equations for multi-phase fluid flow together with mass conservation equations were utilized to formulate the equations of motion of multi-phase fluid flow relative to porous media based on pressure or velocity field of the multi-phase pore fluid flow. In these equations, the unknowns are either pore fluid pressure or fluid flow velocity along with porosity and aperture. Porosity and

aperture change, which are functions of pore fluid pressure and total stress field, can also be formulated based on the constitutive laws used in the equations of motion of porous media using effective stress concept.

In summary, in the two sets of equations of motion, one set of major unknowns can be defined as displacement field in a Lagrangian system of porous media containing relatively immobile pore fluid. Another major set of unknowns comprises pressure and saturation of fluid phases in an Eulerian control volume attached to the porous media representing pore spaces and fractures through which multi-phase fluid moves relative to porous media. Additional internal unknowns are also involved in the final system of equations such as capillary pressure, relative permeability, viscosity, porosity, fracture aperture and so on which are related to pressure, saturation and displacement using constitutive equations, equations of state and effective stress concept. All these unknowns can be implicitly obtained by simultaneously solving all the mentioned governing equations leading to the methodology called fully coupled approach.

In theory, the finite volume discrete fracture-matrix method, developed in chapter 4 and implemented in FVBOS in chapter 5, can be incorporated into solid mechanical discrete element methods to numerically analyze coupled hydro-mechanical multi-phase fluid flow through fractured porous media using fully coupled approach. In practice, however, in order to apply fully coupled approach, the source code of a discrete element solid mechanical simulator is needed so that the developed discrete fracture-matrix approach can be incorporated into the code. Since developing a solid mechanical discrete element code is out of the scope of this research, and since it is not feasible to have access to the source code of 3DEC, a sequential hydro-mechanical coupling approach was developed instead. In this research, the sequential coupling approach was utilized to couple FVBOS and 3DEC to numerically analyze coupled hydro-mechanical multi-phase fluid flow through fractured porous media. In the developed hydro-mechanical coupling method, instead of simultaneously solving equations of motion of both solid phase and fluid phase as a unified set of partial differential equations, the equations of motion of solid phase containing immobile pore fluid is solved using 3 dimensional discrete element method with the aid of 3DEC. In addition, the equations of motion of multi-phase fluid moving through pore spaces and fractures are solved using the developed finite volume discrete fracture matrix method implemented into FVBOS.

Two different coupled hydro-mechanical problems can be approached by the developed sequential coupling method. The first problem involves stress field changes in porous media, e.g. due to loading or unloading of porous media, which also affects fluid flow through pore spaces and fractures. In these problems, first, the equations of motion of solid phase containing immobile multi-phase pore fluid discretized by Lagrangian solid mechanical zones is solved using 3DEC. Then, pore pressure, porosity and fracture apertures updated by solid mechanical solution is transferred to FVBOS to solve the equations of motion of multi-phase fluid flow through fractured porous media discretized by Eulerian fluid mechanical zones. Such problems are encountered in staged construction or removal of embankments, transferring structural loads to the ground through foundations, seismic loading of earth dams, and so on.

The second coupled hydro-mechanical problem involves changes in pore pressure field under a somewhat constant stress field in porous media, e.g. by the injection of fluid into the porous media either to push the resident fluid occupying the pore spaces and fractures towards production wells or to induce hydraulic fractures. In these problems, first FVBOS can be utilized to solve the equations of motion of multi-phase fluid flow through pore spaces and fractures represented by Eulerian fluid mechanical zones, and then the updated pore pressure field can be transferred to 3DEC to solve the equations of motion of porous media containing immobile multi-phase fluid using the Lagrangian zones.

Although the first coupled hydro-mechanical problem mentioned above can be handled by the computational tool developed in this chapter, numerical simulation of these problems is out of the scope of this thesis. The major focus of this research is to develop a numerical tool to simulate coupled hydro-mechanical multi-phase fluid flow involved in the second problem mentioned above with a particular focus on shale reservoir rock as the porous media. It should also be mentioned that the injection of fluid into shale reservoirs mostly changes the configuration of fracture systems with negligible change in porosity relative to fractures aperture change. Therefore, in this research, the major focus of the numerical analyses carried out by the developed hydro-mechanical simulation tool is on fractures aperture change and the porosity change is neglected.

As it is outlined above, in this research, a sequential hydro-mechanical coupling approach is developed to implement the devised finite volume discrete fracture-matrix method into

distinct element approach to equip this approach with the capability of simulation of coupled hydro-mechanical multi-phase fluid flow through fractured porous media. To this end, a computational tool called Multi-Phase Discrete Element Simulator (MPDES) is developed using object-oriented C++ programming by coupling FVBOS and 3DEC based on the developed coupling approach. The schematic algorithm used in MPDES is illustrated in Figure 44.

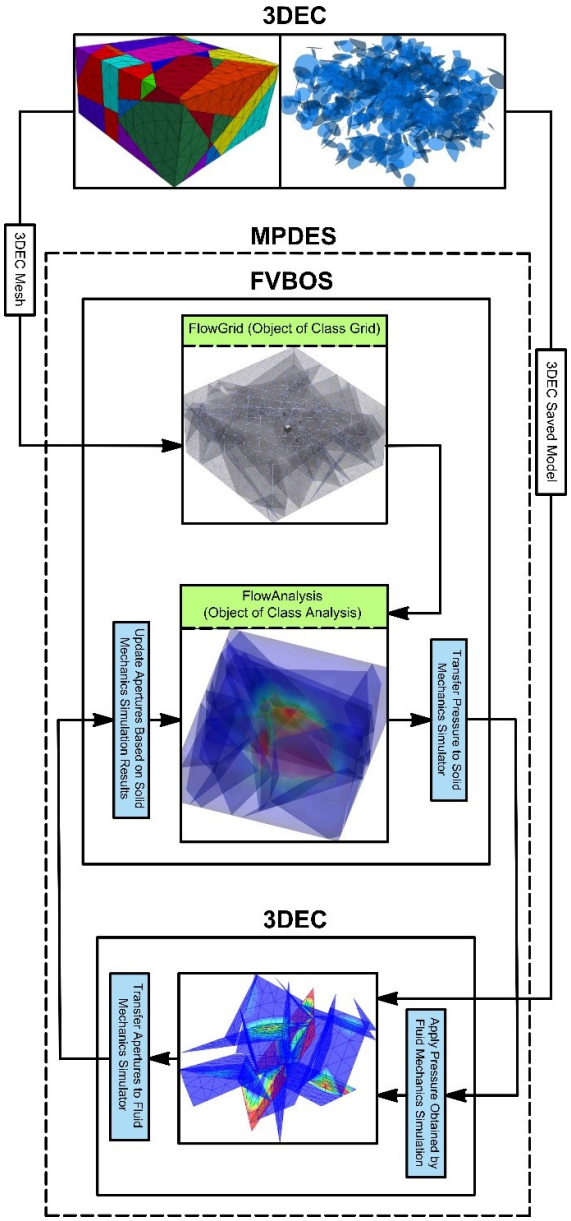

Figure 44: Overall flowchart of sequential coupling method implemented into MPDES.

In the coupling approach used in MPDES, a number of modifications to conventional

sequential coupling approaches are introduced to solve coupled hydro-mechanical problems fairly similar to fully coupled methods. To this end, a Lagrangian computational mesh, attached to the system of mass representing the configuration of solid phase in porous media, is generated by 3DEC to discretize the porous media. In the computational mesh generated by 3DEC, 3-dimensional tetrahedral zones can be used to discretize intact blocks while 2-dimensional trilateral zones can be used for the discretization of the discontinuities such as joints, fractures and faults. The major benefit of the discrete element mesh generated by 3DEC is that it makes it feasible to discretize both discrete blocks and highly complex stochastically generated discrete fracture networks separating the blocks. In order to exploit this capability for the simulation of fluid flow through complex fracture networks, an Eulerian finite volume mesh is generated based on the Lagrangian grid produced by 3DEC to discretize the space occupied by the porous media representing pore spaces and fractures. Such fluid mechanical mesh can be updated based on current configuration of solid mechanical mesh at each time step matching the two mesh systems during the analyses which makes the coupling method more similar to fully coupled approach.

Although the discrete element mesh generated by 3DEC directly provides the grid points needed for generating the Eulerian finite volume mesh, the grid data required to be processed to generate the data structure representing finite volume mesh. This data structure stores finite volume zones, grid points belonging to each finite volume zone as well as the connectivity of finite volume zones at the surfaces for the calculation of transmissibility between finite volume zones. Furthermore, in order to convert distinct element mesh generated by 3DEC to finite volume mesh in FVBOS, two major difficulties are encountered. The first difficulty is due to the numbering convention used in 3DEC for grid points and zones. In this numbering convention, grid points and zones located in a discrete block are numbered independent of those located in other blocks. Another difficulty arises due to the definition of three sets of grid points at the contacts of the discrete blocks, two for each of the blocks and one at the contact plane. These two difficulties make it challenging to convert discrete element mesh generated by 3DEC to finite volume mesh needed in FVBOS. To deal with these issues, an algorithm was developed and implemented into the class Gird in FVBOS processing discrete element grid data produced by 3DEC, including zones and coordinates of the grid points

surrounding the zones. This algorithm generates a data structure defining finite volume zones and their grid points as well as the connectivity between the zones for the purpose of transmissibility calculations.

As it is illustrated in Figure 44, the finite volume mesh generated by FlowGrid object, based on the grid coordinates produced by 3DEC, is passed to FlowAnalysis object which coordinates the multi-phase fluid flow analysis using the finite volume discrete fracture-matrix method developed in this research. After each time step of multi-phase fluid flow analysis, pressures, saturations and velocity of fluid phases are determined at the center of every finite volume zone. Then, the calculated pressures and saturations are transferred to 3DEC to perform distinct element solid mechanical analysis. The solid mechanical analysis performed by 3DEC updates the stress state and configuration of fractured porous media considering deformations in both fracture system and discrete blocks.

In MPDES, three sets of data updated by 3DEC based on solid mechanical analysis can be transferred to FVBOS for either next time step of fluid mechanical analysis or next iteration of hydro-mechanical coupling. The three sets of updated data involve the updated coordinates of finite volume grid points considering the deformation of discrete blocks and fracture network, updated porosity and aperture at the center of finite volume zones. Since the porosity update is out of the scope of this research, in the numerical models presented in this thesis, only fracture apertures are updated based on solid mechanical analyses. It is also worth mentioning that, in 3DEC, large deformation is neglected in coupled hydro-mechanical analyses. Consequently, in this thesis, large deformation is not taken into account in the numerical simulations carried out by MPDES. This is due to the fact that the finite volume mesh used in FVBOS is generated based on the discrete element mesh produced by 3DEC, and the pressures calculated by FVBOS should be applied at the center of flow plane zones in 3DEC for the purpose of hydro-mechanical analysis.

It should also be noted that additional member functions for class Analysis was developed in FVBOS, and also 3DEC fish functions were written in order for MPDES to be able to manage data transfer between FVBOS and 3DEC. To illuminate the codes behind MPDES, the overall flowchart of MPDES is illustrated in more details in Figure 45.

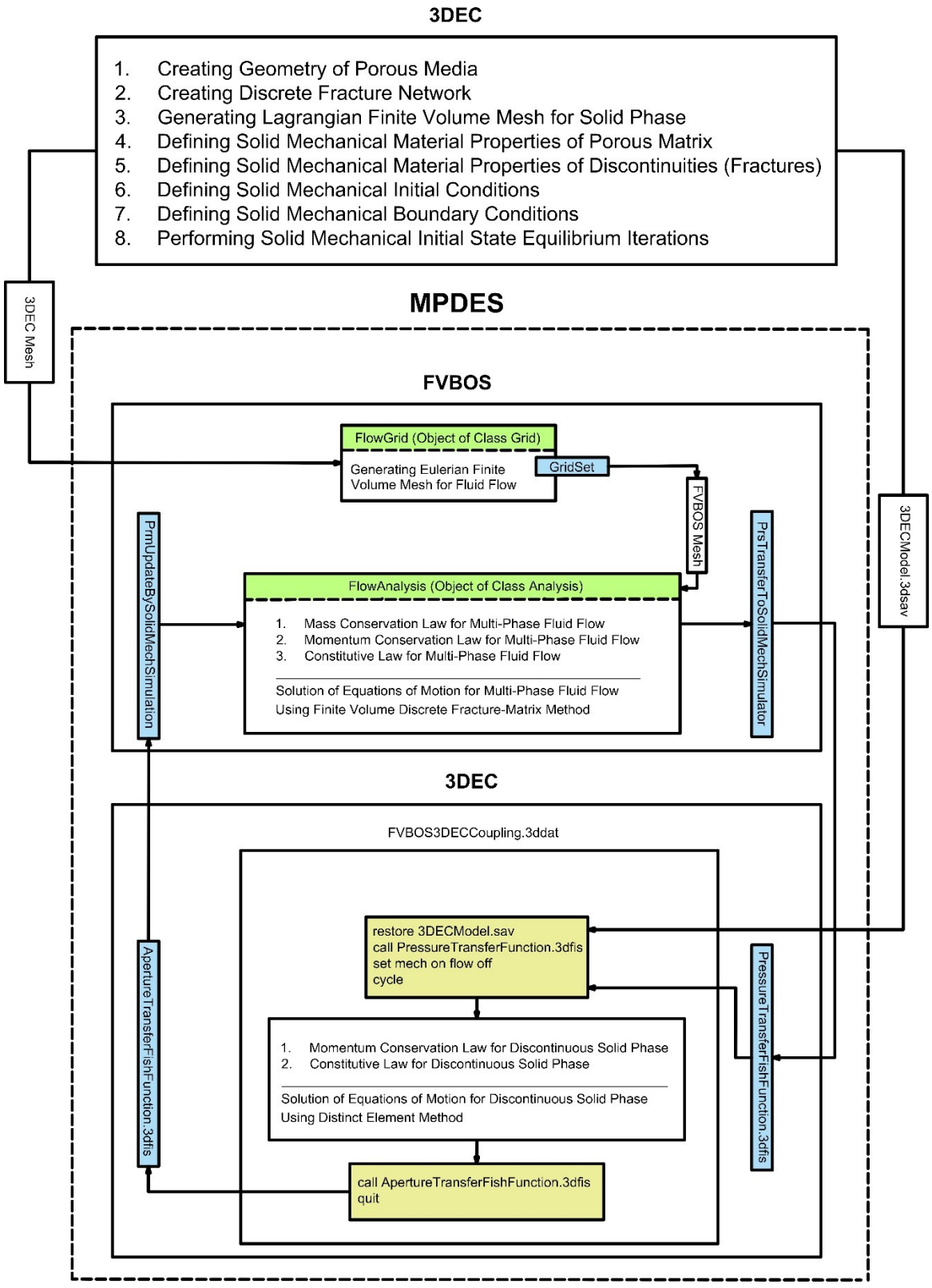

Figure 45: Coupled hydro-mechanical simulation procedure in MPDES.

According to Figure 45, the procedure of performing coupled hydro-mechanical multi-phase fluid flow analysis by MPDS involves 3 major steps. In the first step, the required 3DEC codes are written to generate distinct element solid mechanical model of fractured porous media. In this stage, first, the geometry of porous media including discrete blocks and stochastic discrete fracture network are created. Then, the model is discretized by distinct element mesh, and also solid mechanical material models for discrete blocks as well as fractures are defined. Next, boundary and initial conditions are defined and the 3DEC model is saved producing 3DEC saved file to be restored by 3DEC during hydro-mechanical analysis iterations.

In the second step, grid coordinates generated by 3DEC for discrete blocks and discrete fracture networks along with input files representing fluid mechanical model, including material model of multi-phase fluid flow and fluid mechanical boundary and initial conditions, are passed to FVBOS. Based on the provided data, FVBOS generates finite volume mesh for porous matrix and fracture system and assigns proper material properties together with initial and boundary conditions to the finite volume zones. Afterwards, multi-phase fluid flow analysis is carried out using finite volume discrete fracture-matrix method to calculate pressure, saturation and velocity field in fluid phases.

In the third step, as it is schematically shown in Figure 46, the calculated pressure and saturation by fluid mechanical analysis are transferred to 3DEC based on which the distinct element solid mechanical analysis is performed to update the stress state, configuration of fractured porous media and fracture aperture. To this end, the pressure field transferred to 3DEC is applied to the finite volume vertices of solid mechanical model located at the contacts, i.e. sub-contacts, as it is schematically shown in Figure 46. The updated saturation field is also used to update the bulk density of solid mechanical finite volume zones in 3DEC. At the end of this stage, there are two options for hydro-mechanical coupling process. The first option is to pass the updated solid mechanical data to FVBOS and start the next time step of fluid mechanical analysis which makes the hydro-mechanical coupling one-way. In the next option, before starting the next time step of fluid mechanical analysis, fluid and solid mechanical analyses are iteratively proceeded to iteratively update fluid and solid mechanical parameters until either a predefined maximum allowable number of iterations or a convergence tolerance for two consecutive pressure fields is reached. The second option of hydro-mechanical analysis yields a

coupling approach which is closely analogous to fully coupled approach.

During the hydro-mechanical coupling, MPDES handles the data transfer between FVBOS and 3DEC with the aid of data transfer functions in FVBOS and fish functions in 3DEC. In this regard, two member functions called PrsTransferToSolidMechSimulator and PrmUpdateBySolidMechSimulation are added to the class Analysis inside FVBOS transferring updated pressure field to 3DEC and receiving updated aperture field from it, respectively. In addition, two fish functions named PressureTransferFishFunction and ApertureTransferFishFunction are written to be called inside 3DEC code at the beginning and end of solid mechanical analyses, respectively, to receive updated pressure field from FVBOS and transfer aperture field to it. The mentioned transfer functions in FVBOS and 3DEC map received updated parameters using interpolation based on location. For the mapping purpose, in both FVBOS and 3DEC, a search for finite volume midpoints, for aperture update in FVBOS, or flow knots, for pressure update in 3DEC, is conducted over an area covering the finite volume or distinct element zone containing the location of transferred parameter. After finding the FVBOS finite volume midpoints or 3DEC flow knots located inside the mapping area, an interpolation based on the location of each points relative to the other points is performed using the following formula:

$$\phi^{r_i} = \left[\frac{1/\xi_i}{\sum_{i=1}^{i=n} 1/\xi_i}\right]_{\Omega^r} \Phi^r \qquad \text{Eq. 210}$$

where Ω^r denotes the mapping area containing the point with position vector r specifying the location of the updated value of the parameter to be mapped. The parameter Φ^r is the value of the updated parameter at the point with position vector r, and ξ_i is the distance from the ith point located in the mapping area with position vector r_i to the point with position vector r. In the above equation, ϕ_i represents the interpolated value of the updated parameter at the location specified by r_i, and n is the number of points representing either flow knots in 3DEC or finite volume midpoints in FVBOS located in the mapping area Ω^r.

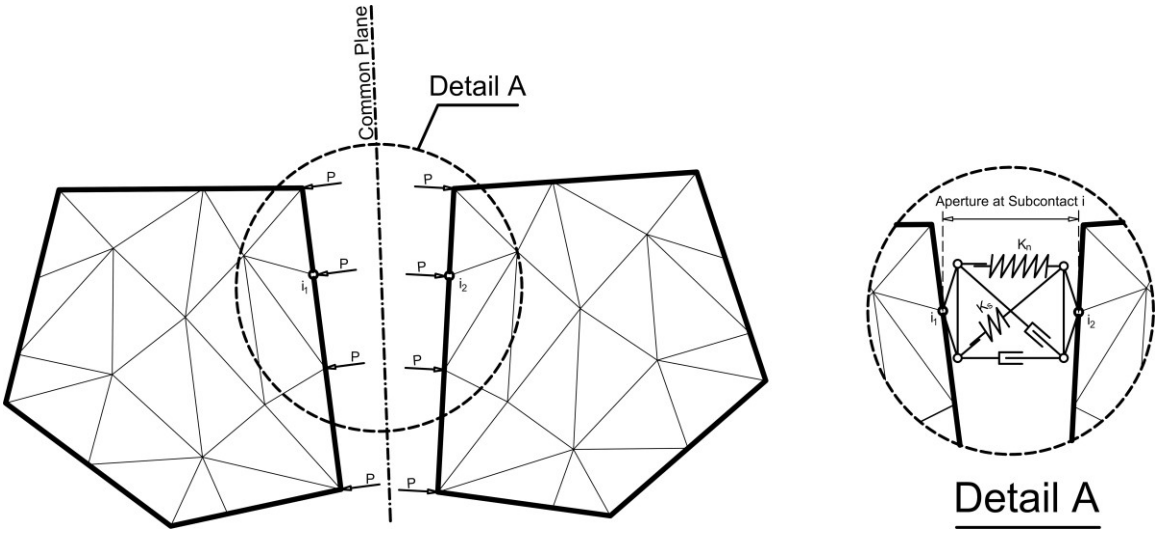

Figure 46: Aperture update by 3DEC using the pressure updated by FVBOS.

During the sequential hydro-mechanical coupling iterations, a relationship between compressibility of solid phase and pore fluid pressure is required to be defined to account for the effects of deformation of porous media on the accumulation term in pore fluid mass conservation equation. In uncoupled fluid mechanical analyses, compressibility of porous media is empirically estimated as a function of pore fluid pressure while the effects of stress field as well as solid mechanical boundary conditions and constitutive relations are neglected. To resolve this issue, in the developed sequential hydro-mechanical coupling approach, the solid phase compressibility is updated at each iteration of hydro-mechanical coupling based on stress field, pore pressure, the deformation of solid phase and solid mechanical constitutive relations. Although such method can be used to determine compressibility of porous media arising from the porosity change in porous matrix, it cannot be used to account for compressibility arising from deformation of fractures, i.e. fracture aperture change as a function of stress field, pore pressure change and solid mechanical boundary conditions and constitutive relations. In this research, to deal with this issue and in order for the developed sequential hydro-mechanical method to behave closely analogous to fully coupled methods, the compressibility of solid phase due to fracture aperture change is estimated based on successive solid mechanical solutions. In this regard, considering the fact that the porosity change in porous matrix is neglected, the compressibility of solid phase is approximated for finite volumes discretizing fractures as follows:

$$k_n = \left[\frac{dP}{de}\right]_n = \frac{P^n - P^{n-1}}{e^n - e^{n-1}} \qquad \text{Eq. 211}$$

where P is pore pressure, e is fracture aperture, k_n is fracture normal stiffness needed for the compressibility calculation, and n denotes the current time step of solid mechanical analysis.

Finally, in order for MPDES to be able to manage the multitasking required to conduct the sequential coupling of FVBOS and 3DEC, a multi-process programming method was applied. The multi-process programming approach utilized in MPDES is schematically demonstrated in Figure 47. As it is illustrated in this figure, to synchronize the operation of FVBOS and 3DEC during sequential hydro-mechanical coupling, a parent process is created where the computational threads of FVBOS are executed running the FlowAnalysis object. The parent process solves the equations of motion of multi-phase fluid moving through the pore spaces and fractures relative to solid phase using finite volume discrete fracture-matrix approach. In this stage, displacement, stress and aperture fields in solid phase are remained unchanged and fluid mechanical finite volume mesh and fracture apertures are generated based on the distinct element grid coordinates and aperture field updated in the previous iteration. After the fluid mechanical analyses reach to an acceptable solution for pressure and saturation fields, RunItasca3DEC which is a member function of SolidMechSimulator object is called which applies a temporary pause in the execution of computational threads of FVBOS and makes them wait until they are resumed at the proper time.

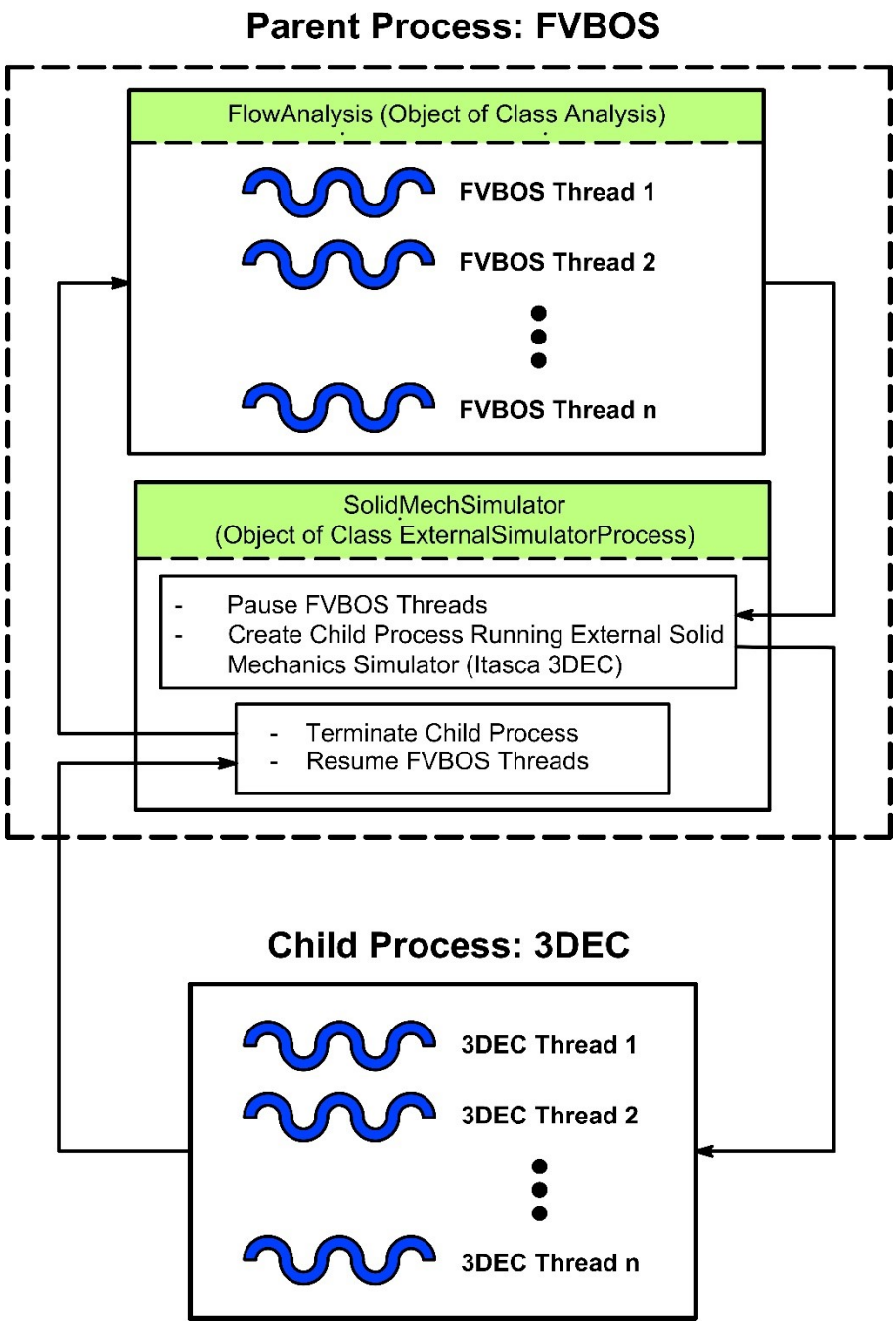

Figure 47: Computing processes and threads in MPDES.

Then, RunItasca3DEC creates a child process where computational threads of 3DEC are executed solving the equations of motion of solid phase containing relatively immobile pore fluid under the pore pressure updated in the previous iteration of hydro-mechanical coupling, solid mechanical stress filed, as well as solid mechanical boundary and initial conditions. As soon as 3DEC reaches to the end of solid mechanical simulation, it is quit

and RunItasca3DEC terminates the child process and resumes FVBOS threads to start the next fluid mechanical iteration or time step, depending on the hydro-mechanical coupling approach and predefined convergence limits.

After the implementation of the developed coupled hydro-mechanical discrete element method into MPDES, the performance of this computational tool shall be assessed. In this regard, the accuracy and capabilities of MPDES in multi-phase fluid flow simulation has been demonstrated through an extensive verification testing conducted on FVBOS in the previous chapter. In addition, 3DEC is the discrete element solid mechanical simulator employed in MPDES which has been widely used in the simulation of discontinuous solid mechanical problems by many researchers and its validity has been proven through numerous investigations. In the following sections, a benchmark problem with available theoretical solution is chosen to verify the hydro-mechanical coupling method implemented into MPDES. Moreover, coupled hydro-mechanical multi-phase fluid flow through porous matrix and complex deformable fracture network is numerically analyzed to demonstrate the computational capabilities of MPDES in dealing with reservoir simulation of fractured formations.

6.2 Simulation of Coupled Hydro-Mechanical Two-Phase Air-Water Flow through a Single Fracture Located inside a Porous Matrix Block

In order to verify the developed coupled hydro-mechanical multi-phase discrete element approach, two-phase air-water flow in a porous matrix block containing a single fracture is numerically simulated by MPDES. In this problem, the unique capabilities of MPDES in the simulation of the effects of both fluid leakoff into porous matrix and multi-phase fluid properties on the extent of opening of the fracture is also demonstrated. To this end, two-phase air-water fluid flow in the porous matrix block containing a single vertical fracture shown in Figure 48 under the injection of water from one side of the fracture is simulated by MPDES. In this problem, it is assumed that the fractured block is 90 percent saturated by air and 10 percent saturated by connate water.

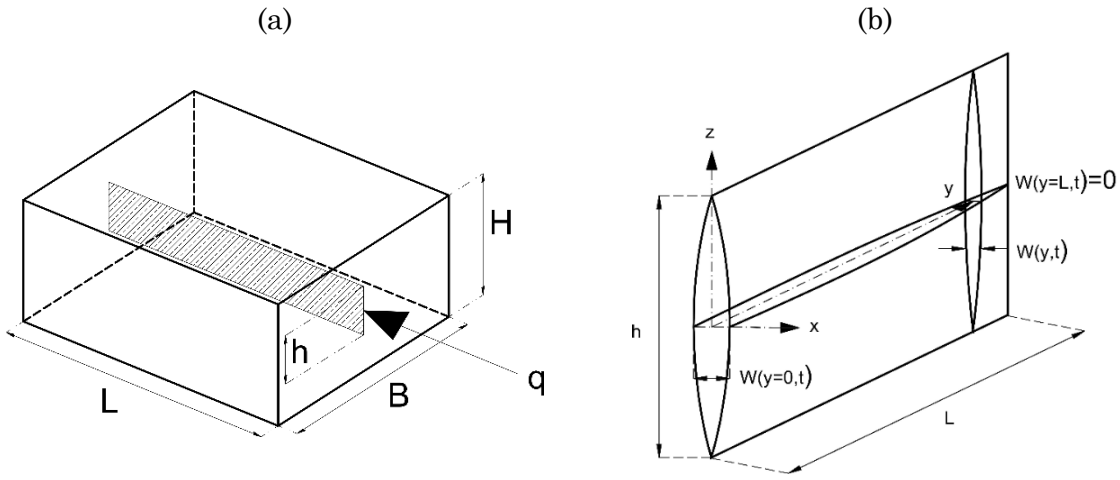

Figure 48: Schematic representation of coupled hydro-mechanical (HM) multi-phase fluid flow through a single fracture located inside porous matrix simulated by MPDES.
(a) Geometric configuration of the problem (b) Conceptual aperture change along and across the single fracture based on the assumptions made by Sneddon (1946) to derive a theoretical relationship between the crack shape and pressure inside the fracture by the theory of elasticity.

In this numerical model, it is demonstrated how the aperture of the single fracture, which is assumed to be initially equal to 0.05 mm, increases along and across the fracture due to the injection of water as a function of pore fluid pressure as well as mechanical properties of porous matrix block, fracture and multi-phase fluid. As it is demonstrated by Perkins and Kern (1961), ignoring the effects of stress concentration at fracture tip and released surface energy due to fracture propagation, and solely considering longitudinal fracture growth, the fracture opening pattern simulated in this model can represent hydraulic fracture propagation at one side of injection point. In this method, it is also assumed that the fracture propagation is symmetrical about the plane perpendicular to the fracture passing through the injection point. In this regard, a theoretical solution has been developed by Sneddon (1946) using the theory of elasticity relating the shape of fracture opening to the pore fluid pressure inside the fracture and elastic properties of the block containing the fracture. The schematic configuration of fracture opening assumed in the Sneddon theoretical solution is illustrated in Figure 48. The fracture opening configuration at an arbitrary cross section specified by *y* coordinate can be estimated by an elliptical shape obtained by Sneddon theoretical solution as follows:

$$e = \frac{8\mathbb{p}h(1-\upsilon^2)}{\pi E}\sqrt{1-\left(\frac{z}{h}\right)^2} \qquad \text{Eq. 212}$$

where e is the fracture aperture at a point specified by z coordinate in the fracture plane and $\mathbb{p}$ denotes the amount by which pore pressure inside the fracture exceeds the stress normal to the fracture surface at a cross section specified by y coordinate. In this equation, h is the fracture height, z represents the vertical coordinate from the fracture mid-height in the plane of fracture, and E and υ are respectively elastic modulus and Poison's ratio of the block. As it is schematically shown in Figure 48, the maximum fracture aperture at different cross sections occurs at the middle of fracture height, i.e. at $z=0$. The properties of porous matrix block, fracture and two-phase fluid used in the numerical simulations carried out by MPDES are reflected in Table 4.

Table 4: Material parameters of intact rock, fracture and fluid.

Porous matrix	
Elastic modulus (GPa)	1
Poison's ratio	0.2
Absolut permeability (Darcy)	0.01
Porosity	0.2
Fracture	
Normal stiffness (GN/m)	1
Aperture at zero normal stress (mm)	0.05
Residual aperture (mm)	0.05
Maximum aperture (mm)	10
Fluid	
Dynamic viscosity of water (Pa.s)	0.001
Dynamic viscosity of air (Pa.s)	0.0002
Density of water (Kg/m^3)	1000
Density of air (Kg/m^3)	1

Note: Density of the porous block is not needed since the effect of gravity on the stress state is ignored.

The constitutive parameters of rock joints are discussed in more details in Appendix F. In the numerical simulations, the dimensions of the block represented by L, B and H are

assumed to be equal to 5 m, 4 m and 6 m, respectively, while the fracture height denoted by h is assumed to be equal to 2 m. Also, assuming the symmetry of the problem about the horizontal plane passing from the middle of the fracture, only the upper half of the block is modeled by MPDES. The pressure contour and uniform vector plot of the velocity of water obtained by coupled hydro-mechanical two-phase air-water flow analysis performed by MPDES together with the configuration of the porous matrix block as well as the fracture are displayed in Figure 49. The water velocity vector plot shown in this figure is not scaled and velocity vectors are shown by equally-sized arrows in spite of the fact that the length of velocity vectors towards the porous matrix are much smaller than the ones directed along the fracture due to the very low permeability of the porous matrix relative to the fracture. This uniform vector plot is shown to more clearly demonstrate the leakoff of the injected water into the pore spaces of the porous matrix surrounding the fracture.

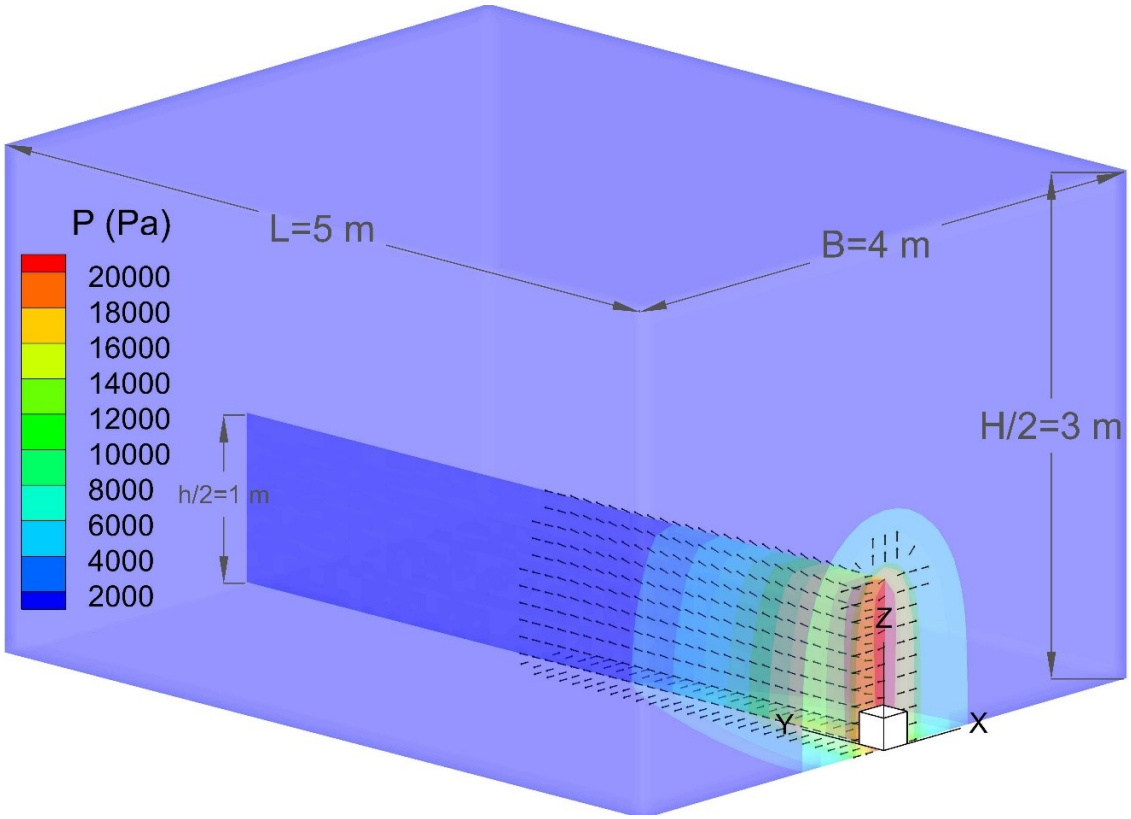

Figure 49: Pressure contour and uniform water velocity vector plot obtained by MPDES for coupled hydro-mechanical two phase air-water flow through a single fracture located inside porous matrix.

As it can be seen, by the injection of water, pore fluid pressure increases around the

injection area creating pressure gradient which in turn causes water and gas to flow through the fractured porous media with higher flow rates along the fracture due to the higher permeability of fracture relative to porous matrix. The higher flow rates along the fracture directs the pore fluid pressure expansion mostly along the fracture. Also, much higher pressure gradient is observed along the fracture than across the fracture leading to much higher air and water flow rates along the fracture compared to the direction aligned with the fracture height. In order to better demonstrate the two-phase air-water flow through the fracture, air and water saturation contours along with scaled vector plot of air and water velocities are exhibited along the fracture in Figure 50.

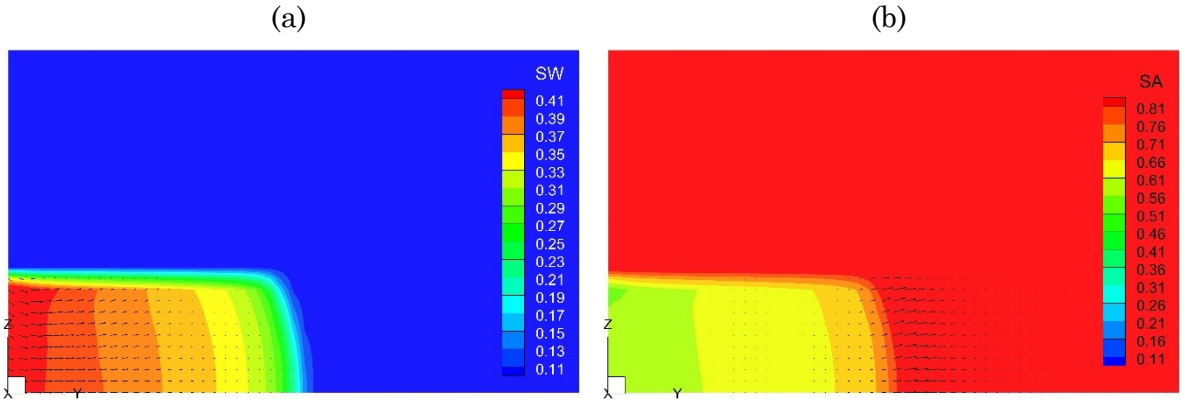

Figure 50: Saturation contours and scaled velocity vector plots obtained by MPDES for coupled hydro-mechanical two phase air-water flow through a single fracture located inside porous matrix.
(a) Water saturation contour and water velocity vector plot (b) Air saturation contour and air velocity vector plot.

In the saturation contours depicted along the fracture, it is demonstrated that the dominant water and air flow occurs along the fracture while the air and water flow across the fracture are relatively negligible. As it can be seen in the figures, the highest water velocity occurs at the water injection area and water velocity decreases towards the water saturation front. In contrast, the highest air velocity can be observed near the water saturation front which is due to the fact that water is pushing the air out of the pore spaces mostly around the water saturation front. The numerical results presented in the contour and vector plots show that the numerical results generated by MPDES reasonably capture the physical processes behind the two-phase air-water flow through the fractured porous matrix block.

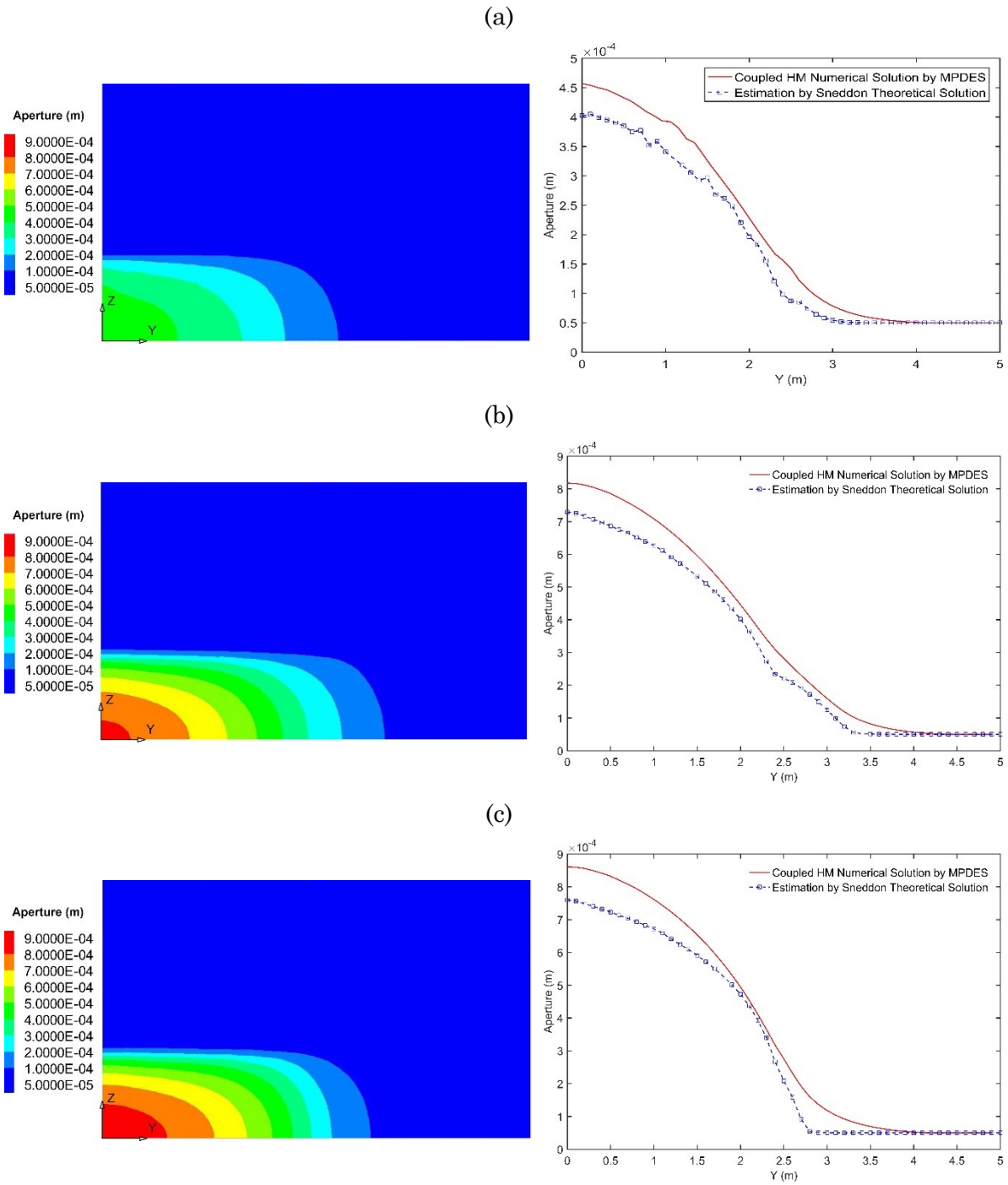

Figure 51: Aperture contours in the single fracture along with the graphs of mid-height aperture variation along the fracture obtained by coupled hydro-mechanical multi-phase fluid flow analyses carried out by MPDES and compared with Sneddon theoretical solution for fracture aperture.

(a) Two-phase air-water flow with leakoff into porous matrix (b) Two-phase air-water flow without leakoff into porous matrix (c) Single phase water flow without leakoff into porous matrix.

The unique capability of MPDES compared to other computational codes is that it is capable of simulating multi-phase fluid flow through both pore spaces of porous matrix and fractures taking into account the interaction of the fluid flow with discontinuous solid mechanical response of the hosting porous media. This capability has been utilized to more realistically simulate the interrelation between the pore fluid pressure and the fracture aperture, as it is demonstrated in Figure 51. In this figure, aperture contour along the fracture as well as the graph of variation of mid-height fracture aperture along the fracture due to the injection of water is demonstrated for three cases, namely two-phase air-water flow considering fluid leakoff into porous matrix, two-phase air-water flow neglecting the fluid leakoff, and single phase water flow without the fluid leakoff. In this figure, the numerical results obtained by MPDES for mid-height fracture aperture change along the fracture are also compared with the Sneddon theoretical solution.

As it can be observed in Figure 51, the numerical results obtained by MPDES for the mid-height aperture variation along the fracture is in a reasonably good agreement with Sneddon theoretical results demonstrating that the hydro-mechanical coupling between FVBOS and 3DEC is properly performed in MPDES. In the case of considering fluid leakoff, a noisy mid-height fracture response can be observed which is due to the effect of size of finite volume zones discretizing the fracture. In this case, pore fluid pressure gradient towards the porous matrix, i.e. perpendicular to fracture surface, directs some of fluid flow towards the porous matrix decreasing the pressure inside fracture. The effect of such pressure decreases along the fracture due to the fluid leakoff on fracture aperture variation can be simulated with a smoother response if the size of Eulerian finite volumes discretizing the fracture is decreased.

The fracture aperture responses for the three cases of analyses, shown in Figure 51, clearly demonstrate that fluid leakoff from the fracture surface into the pore spaces of the surrounding porous matrix dramatically diminishes aperture along the fracture. It is also worthwhile to note that the aperture change is not uniform and it is dependent on the pore fluid pressure as well as the solid mechanical displacement field which is a function of constitutive model, stress field and boundary conditions in solid phase. Such behavior can only be simulated by considering hydro-mechanical coupling effects. Another factor assessed in the three cases of analyses is the effects of multi-phase fluid properties on the aperture response along the fracture. This effect is more clearly illustrated in Figure 52.

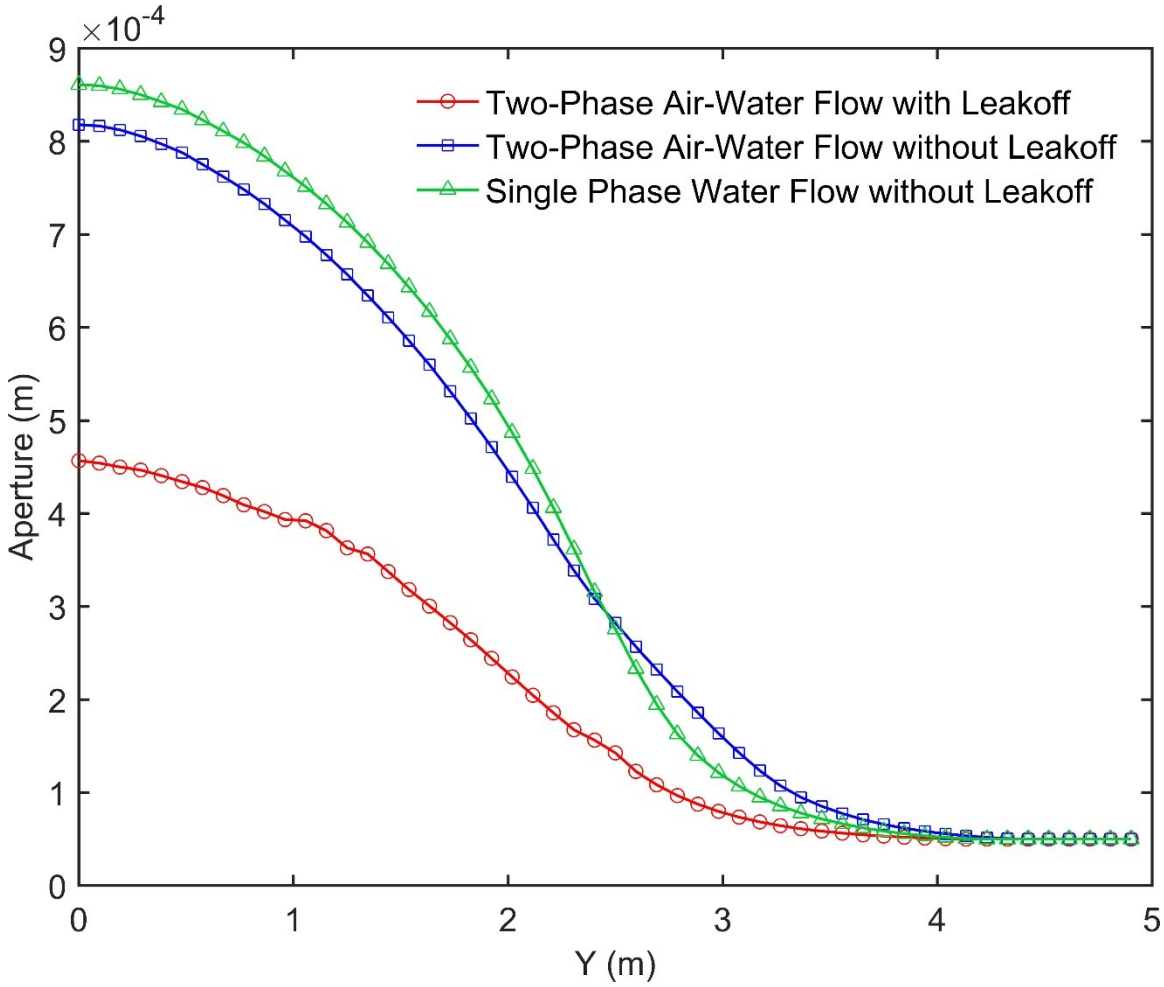

Figure 52: Mid-height aperture variation along a single fracture located inside porous matrix obtained by coupled hydro-mechanical analyses carried out by MPDES for three cases of two-phase air-water flow with and without fluid leakoff into porous matrix as well as single-phase water flow without fluid leakoff into porous matrix.

In Figure 52, the variation of mid-height aperture along the fracture obtained by MPDES is compared for three cases of two-phase air-water fluid flow with fluid leakoff, two-phase air-water fluid flow without fluid leakoff and single-phase water flow without fluid leakoff. In this figure, the effects of fluid leakoff and multi-phase fluid properties on fracture aperture is investigated in more details. As it can be observed, in spite of the very low permeability of porous matrix relative to fracture, fluid leakoff has a significant influence on pressure decrease inside fracture leading to dramatic fracture aperture decrease. This is due to the fact that the pore spaces inside the porous matrix can absorb remarkable amounts of the injected water. According to Figure 52, another factor affecting fracture aperture is the compressibility of invading and resident fluid. As it can

be observed, if the fluid flow inside the fracture is simulated taking into account separate fluid phases, particularly in the case of the existence of gas phase which is highly compressible, fracture aperture predicted by hydro-mechanical analyses is lower in the case of multi-phase flow than single phase flow. Although the effect of multi-phase fluid flow on fracture aperture is not as significant as the effect of fluid leakoff, it is still an influential factor to be taken into account in the analyses.

The numerical results presented in this section demonstrates the stability and reasonable accuracy of the numerical solution obtained by MPDES. In order to further assess the stability of the numerical solution, the change in material balance error for air and water fluid phases has been plotted in Figure 53.

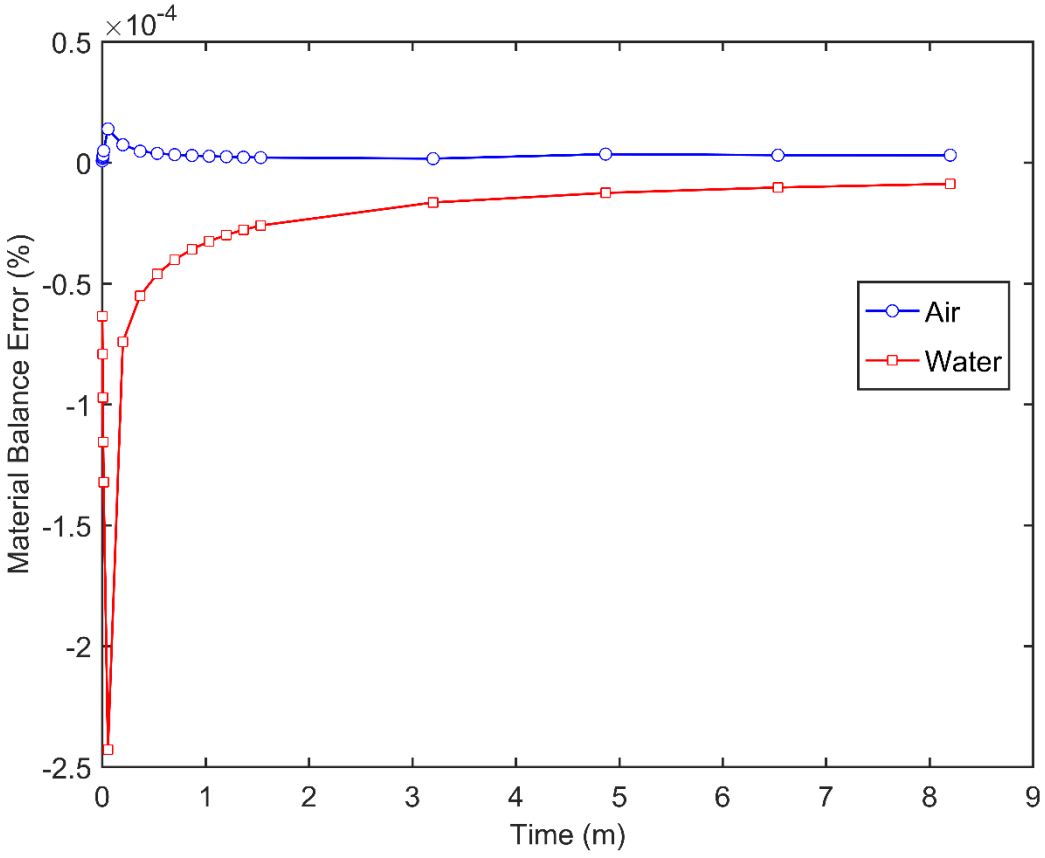

Figure 53: Material balance error generated by the numerical solution performed by MPDES.

As it can be seen in Figure 53, material balance error generated by the numerical solution is negligible and decreases by time demonstrating the numerical stability of the solution

obtained by MPDES.

The effects of fluid leakoff and multi-phase fluid properties on hydro-mechanical response of fractured porous media demonstrated in this section have not been properly accounted for in previous research works and available computational codes so far. This is due to the fact that the available computational codes are not properly equipped with multi-phase discrete fracture-matrix methods considering multi-phase fluid flow through both pore spaces of porous matrix and fractures. Another superior feature of MPDES differentiating it from the available computational codes is the unique hydro-mechanical simulation capabilities of this code which is resulted from the utilization of discrete element approach for solid mechanical analyses. This feature enables MPDES to deal with highly complex discrete fracture networks as it will be demonstrated in the following section.

6.3 Simulation of Coupled Hydro-Mechanical Multi-Phase Fluid Flow in Porous Media Containing Stochastically Generated Discrete Fracture Network

In the previous section, the developed coupled hydro-mechanical multi-phase simulation approach implemented in MPDES was verified for the case of multi-phase flow through a porous matrix block containing a single fracture. It was also demonstrated that the effect of fluid leakoff into porous matrix, compressibility of multi-phase fluid and hydro-mechanical coupling play crucial roles in the simulation of multi-phase fluid flow through fractured porous media. In this section, the capabilities of MPDES in dealing with coupled hydro-mechanical multi-phase fluid flow through both pore spaces and complex fracture networks is assessed.

As it was discussed in section 5.4.7, in the numerical model of multi-phase fluid flow through porous matrix and stochastically generated discrete fracture network created by FVBOS, the effects of hydro-mechanical coupling was neglected which brought about unrealistic pore fluid pressure, fracture aperture and fluid saturation fields. In this section the same problem is numerically simulated by MPDES taking into account the effects of displacement field in solid phase which is dependent, not only on the pore fluid pressure, but also on the constitutive behavior, stress field and boundary conditions in solid phase. To this end, the fractured porous matrix block is assumed to be located at the

depth of 1000 m below the ground surface. The vertical in situ stress at any material points in the solid phase was determined based on the weight of the column of porous media above the point, i.e. $\sigma_v = \int \gamma d\zeta$ where γ is the bulk density of porous media and ζ denotes the depth below the ground surface. The minimum and maximum horizontal in situ stresses were determined using the maximum and minimum horizontal stress ratios, i.e. $\sigma_{hmax} = K_{hmax}\sigma_v$ and $\sigma_{hmin} = K_{hmin}\sigma_v$. With this aim, the values of the minimum and maximum horizontal stress ratios are assumed to be equal to 1 and 0.5, respectively. The multi-phase fluid properties, geometry of the model and discrete fracture network as well as fluid mechanical initial and boundary conditions used in this numerical model are the same as those used in section 5.4.7. Moreover, the material properties of the intact rock as well as the fractures are the same as the ones reflected in Table 4. In this problem, Mohr-Coulomb model was used to simulate the constitutive behavior of fractures with friction angle of 20 degrees and negligible cohesion, dilation angle and tensile strength. Also, the boundary conditions of the solid phase are defined as zero velocity at all the six boundary surfaces of the fractured porous block. The 3DEC codes used to generate the solid mechanical model for this problem are reflected in Appendix G.

In this problem, the stochastic discrete fracture network created by 3DEC is comprised of a number of disc-shaped fractures, as it is shown in Figure 39, with limited sizes represented by their diameters. Although these fractures cut the whole block, two different solid mechanical joint constitutive behaviors are assigned to inside and outside of the discs. The constitutive behavior assigned to the area inside the disc allows the normal displacement in the joint which is governed by the stress state in the solid phase and normal stiffness of the joint while it is bounded between minimum and maximum apertures. In contrast, in the area located outside of the disc, shear and normal displacements are restricted. The shear displacement of the joints inside the discs are governed by an elastic-perfectly plastic Mohr-Coulomb model. Therefore, shear displacements inside the discs elastically changes as a function of stress field in solid phase and shear stiffness of the joints, and as soon as the stress state is located on the failure surface, shear displacement changes based on the perfectly plastic constitutive equations which can also produce normal displacements depending on the amount of dilation angle. In these circumstances, water is injected at the center of the fractured block with the injection rate of 0.001 m^3/s and the numerical results are reflected in

pressure and saturation contours of fluid phases shown in Figure 54.

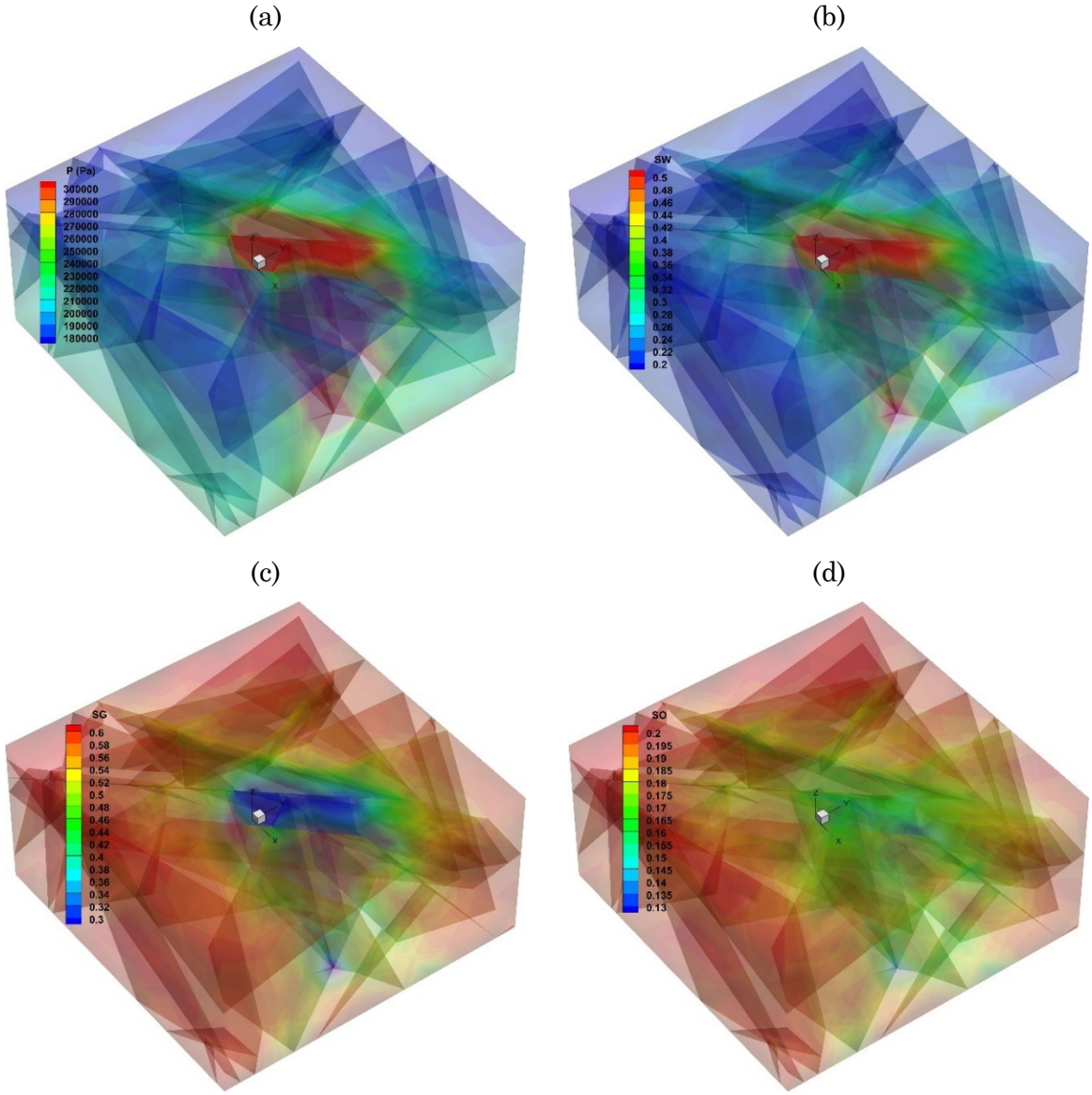

Figure 54: Numerical results obtained by MPDES for coupled hydro-mechanical multi-phase fluid flow through porous matrix and stochastically generated discrete fracture network.
(a) Pressure contour (b) Water saturation contour (c) Gas saturation contour (d) Oil saturation contour.

As it can be seen from the saturation contours, most of the injected water is hindered in an area around the center of the block. Another area with high water saturation can be detected at the bottom of the block where the intersection of multiple fractures is existing. According to Figure 54, in the areas with higher water saturation, pressure is higher which is due to the fact that pressure gradient can more effectively influence the points

which are connected to the injection source with more permeable paths provided by fracture network. The pressure expansion pattern implies that the effectiveness of the stimulation of the fractured formation by the injection of water relies on the connectivity of the fracture network. The more the connectivity of the fracture networks, the more the effectiveness of pressure gradient applied by the injection, and the more the efficiency of the stimulation of the fractured formation.

By comparing the pressure expansion and saturation distribution patterns approximated by MPDES with those obtained by FVBOS, it can be realized that the distribution of pressure and saturation of fluid phases predicted by MPDES are mostly concentrated at the center of the block while FVBOS results show remarkable expansion of these parameters towards the boundaries of the fractured porous block. This is due to the fact that, first, solid mechanical constitutive model assigned to the joints in MPDES restricts the normal displacements in the joints beyond the diameter of the fractures which in turn limits the fluid flow in these regions. Also, in numerical models created by FVBOS, it is only possible to consider the effects of pore pressure and fracture normal stiffness on fracture aperture growth. In contrast, in the numerical model created by MPDES, the effects of stress field, material model and boundary conditions in the solid phase are taken into account which considerably influence the aperture growth and fluid flow pattern.

In the coupled hydro-mechanical model available in MPDES, the effects of stress singularity at the fractures tips, released strain energy and developed surface energy due to fracture propagation are not considered because these effects are neglected in the distinct element formulation implemented in 3DEC. In spite of such negligence, MPDES can be utilized to estimate the stimulated reservoir volume created by hydraulic fracturing by analyzing the displacement field achieved by coupled hydro-mechanical simulations in the joints. For this purpose, the most important displacement-dependent parameter is fractures apertures calculated by hydro-mechanical simulations demonstrated in Figure 55.

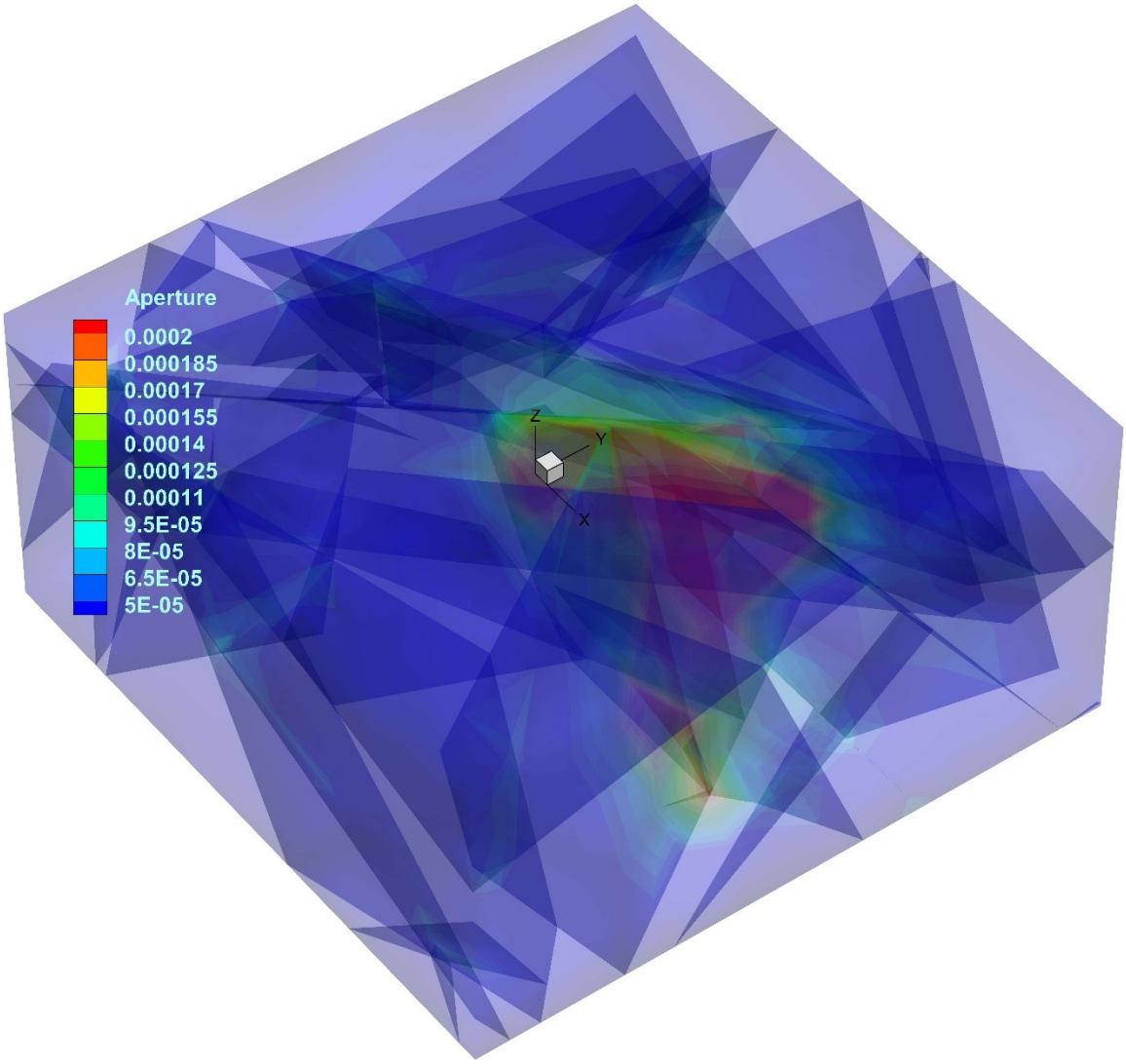

Figure 55: Aperture contour obtained by the numerical simulation of coupled hydro-mechanical multi-phase fluid flow through porous matrix and stochastically generated discrete fracture network using MPDES.

It can be observed that fracture aperture increases mostly in x direction which is aligned with the maximum far-field, i.e. in situ, stress. This is due to the fact that the fracture aperture tends to increase in a direction where the stresses normal to its faces is minimum. Such phenomena cannot be simulated by FVBOS because it neglects geomechanical stress field in the fluid flow simulation. The aperture contour obtained by MPDES demonstrates that, by the injection of water, only a limited area extended from the injection point to the bottom of the fractured block at the right of the y-z plane is effectively stimulated, i.e. considerable aperture increase has been induced. This is due to the fact that stress filed and boundary conditions in solid phase as well as limited

fractures lengths and connectivity prevents the aperture increase in the area located on the left side of y-z plane. The comparison of the aperture contour obtained by MPDES shown in Figure 55 and those obtained by FVBOS displayed in Figure 43 illuminates why, in the case of neglecting hydro-mechanical coupling, the distribution of pressure and water saturation is more expanded towards the outer boundaries of the the fractured porous block compared to the case considering hydro-mechanical coupling. In order to better evaluate the stimulated area around the injection point, both normal and shear displacements at the joints shall be analyzed. To this end, the vector plot of the displacements of the joints is depicted in Figure 56.

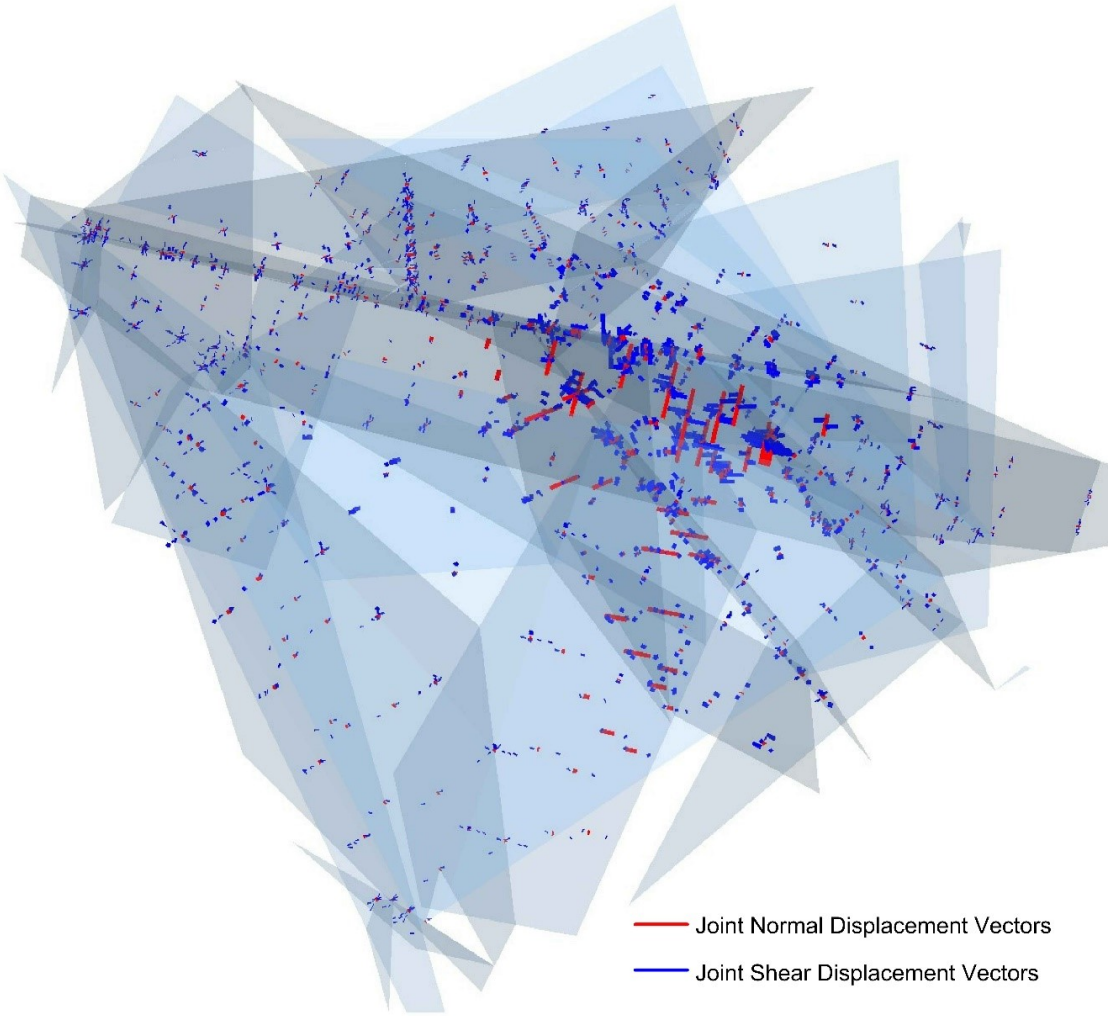

Figure 56: Vector plot of normal and shear displacement of fractures obtained by the numerical simulation of coupled hydro-mechanical multi-phase fluid flow through porous matrix and stochastically generated discrete fracture network using MPDES.

The vector plot of the displacement field demonstrates that the highest concentration of

normal and shear displacements in the joints are located in an area with a high concentration of fractures intersections near the injection point. In this area, the amount of normal displacements is higher than shear displacements while shear displacements are distributed over a larger area. Another area with high concentration of joint normal displacement is located at the bottom of the fractured block at the right side of y-z plane. The comparison of the displacement vector with aperture, pressure and water saturation contours implies that normal displacements inducing fracture aperture increase have a significant effect on the fluid flow as well as pressure distribution and stimulated area.

It is also worth mentioning that because of neglecting joints dilation under shear displacements, i.e. neglecting dilation angle of the joints, the effects of shear displacements on aperture change and fluid flow is not directly taken into account in the present numerical analysis. Such aperture change due to shear displacements can also be taken into account by assuming a dilation angle greater than zero as well as implementing proper 3DEC fish functions in MPDES models. Furthermore, despite the fact that water saturation increase is concentrated in a limited area near the injection point, shear displacement is distributed over a large area. The reason behind the existence of such movements in the areas which are not effectively accessible by the injected water is that the displacement filed is calculated by the numerical solution of the equations of motion of the solid phase under the applied pore fluid pressure, stress state and boundary conditions and it is not necessarily limited to the accessible areas by injected water.

Finally, it should be emphasized that the numerical simulation carried out by MPDES takes into account the fluid leakoff into porous matrix and multi-phase fluid compressibility. Such capability makes it feasible to more realistically approximate the effectiveness of the pressure gradient created by the injection with the aim of stimulating the fractured porous media. As it was clearly demonstrated in the previous section through a simplified model, fluid leakoff into porous matrix significantly decreases the fracture aperture growth which in turn brings about the less efficient stimulation of the fractured formation. It was also shown that how multi-phase fluid compressibility and coupled hydro-mechanical response affects the aperture growth pattern in fractured porous media. Taking into account all these effects, MPDES has provided a novel powerful numerical method to more realistically approximate the pressure expansion

pattern, saturation changes of fluid phases as well as aperture change distribution due to the injection. These capabilities provide an effective methodology to assess the efficiency of the stimulation of the fractured formations by water injection.

7 Conclusions and Recommendations

In recent years, shale gas reservoirs have played a vitally important role in dealing with the increasing demand for energy. However, in these reservoirs, due to the extremely low permeability of shale rock, devising an efficient production scheme is a challenging task for the industry. A practical resolution for this issue, extensively used by the industry, is to enhance the interconnection between natural fractures exiting in shale reservoirs by hydraulic fracturing providing the properly permeable fluid flow paths required for reliable production. In theory, it might be born in mind that creation of large areas of interconnected fracture networks by hydraulic fracturing can significantly improve production in shale reservoirs. However, in practice, creation of larger interconnected fracture networks does not necessarily result in more efficient production strategy. Indeed, production plans in hydraulically fractured shale reservoirs shall be developed on the basis of comprehensive fluid flow simulations to strike a delicate balance between the extent of induced interconnected fracture networks and the area over which pressure gradient can effectively yield economical production.

Taking into account the high level of uncertainty and complexity surrounding shale formations, it is essential to develop sophisticated numerical models for fluid flow simulation in shale reservoirs. In particular, simulation of fluid flow through fractured shale reservoirs during both hydraulic fracturing and production phases involve compressible multi-phase fluid flow through porous matrix and complex deformable fracture networks considering hydro-mechanical coupling, viscous forces, gravity, interfacial tension as well as aqueous and non-aqueous liquids and dissolved and free gas. In spite of considerable industrial demand for such comprehensive numerical models, very few research works have yielded such models so far. In this research, a numerical approach was developed for the simulation of coupled hydro-mechanical multi-phase fluid flow through porous matrix and complex deformable fracture networks to address this shortcoming.

7.1 Multi-Phase Fluid Flow Formulation

In this research, a numerical formulation compatible with discrete element method was developed based on finite volume discrete fracture-matrix approach capable of simulating multi-phase fluid flow through both porous matrix and complex fracture systems. To formulate the discrete fracture-matrix method, momentum conservation law for single phase fluid flow was derived in integral form for an Eulerian control volume in space using Reynolds transport theorem. The momentum conservation law was combined with Stokes constitutive equation to derive the Navier-Stokes equations of motion for single phase fluid flow. The Navier-Stokes equations were simplified into Darcy's law in the case of fluid flow through porous matrix and Reynolds equation or cubic law for fluid flow through fractures. Then, the Darcy's law and cubic law were extended for the case of immiscible multi-phase fluid flow using the concept of relative permeability.

In the next stage, mass conservation equations for immiscible multi-phase fluid flow comprised of aqueous and non-aqueous liquids together with dissolved and free gas was derived in integral form using Reynolds transport theorem with the aid of defining reservoir volume factor and gas solubility in liquid phases. The resulting set of partial differential equations governing the multi-phase fluid flow was formulated based on the pressure and saturation of the fluid phases by combining mass conservation equations and Darcy's or cubic law. The governing partial differential equations were combined into a compact partial differential equation with only one unknown, i.e. pressure of one of the fluid phases, with the aid of capillary pressure concept.

Afterwards, a finite volume discrete fracture-matrix method was formulated to spatially discretize the governing partial differential equations taking into account matrix-matrix, matrix-fracture and fracture-fracture multi-phase fluid transfer. To this end, the partial differential equations were integrated over discrete finite volumes representing either porous matrix or fracture subdomains and the volume integrals of divergence terms were replaced by their equivalent surface integrals using Gauss's theorem. Then, the resulting integral equations were discretized in space using Gaussian numerical integration. It was also shown how the spatially discretized equations of motion of the multi-phase fluid flow are discretized in time domain using implicit pressure-explicit saturation method. A conceptual parameter was also introduced to replace porosity in the equations of motion

in the case of multi-phase fluid flow through fractures. In mass conservation equations, this conceptual parameter numerically takes into account the effects of aperture change, as a function of pressure and fracture normal stiffness, on accumulation term in fracture finite volumes. A numerical treatment was also formulated to more efficiently define fracture-fracture transmissibility in the case of multiple intersecting fractures by satisfying mass conservation equation at fracture intersections.

7.2 Implementation of Multi-Phase Fluid Flow Model

In the next stage, an object-oriented C++ code called Finite Volume Black-Oil Simulator (FVBOS) was developed implementing the formulated multi-phase discrete fracture-matrix approach. With the aid of object-oriented programming method, the structure of FVBOS was designed based on the interconnection of a number of C++ objects each of which dealing with specific tasks, e.g. processing grid data, setting multi-phase fluid material model, applying initial and boundary conditions, performing fluid mechanical analysis, post processing of results and so on. The C++ objects can be created based on a number of predefined C++ classes specifying the blueprints of the objects involving member functions and variables.

The object-oriented structure of FVBOS along with intuitive names of the classes, member functions and variables make the source code highly readable and organized. In particular, the utilized object-oriented programming approach makes it feasible to share the object files of the compiled classes of FVBOS with other software developers. These object files can be employed inside other programs without being involved in the detailed codes behind the classes provided that an instruction is given clarifying the available member functions and variables of the classes and their purpose. For instance, FVBOS can be easily implemented into Itasca's codes 3DEC and FLAC to equip these codes with the capability of multi-phase fluid flow simulation in fractured porous media. The inheritance concept in object-oriented programming can also facilitate upgrading FVBOS, e.g. by implementing different multi-phase fluid flow models in FVBOS. Using the inheritance concept, new C++ classes can be developed based on parent classes available in FVBOS inheriting the member functions and variables of the parent class and defining new member functions and variables inside the new class without being engaged in the detailed codes of the parent class.

The finite volume discrete fracture-matrix method implemented into FVBOS can handle two types of finite volume grids to spatially discretize fractured porous media, namely structured grids using hexahedral finite volumes for porous matrix and quadrilateral finite volumes for fractures as well as unstructured grids using tetrahedral finite volumes for porous matrix and trilateral finite volumes for fractures. The structured grids are mostly used in the case of simple geometries and fracture systems with simple configurations, particularly for the purpose of verification of numerical results with theoretical solutions. However, if complex fracture networks have to be considered in a model, unstructured grids must be utilized to discretize the the fractured porous media. In fact, the unstructured discretization enables FVBOS to model multi-phase fluid flow through stochastically generated complex discrete fracture networks representing natural and hydraulic fractures as well as rock joints representing probable hydraulic fractures trajectories.

After implementing the devised numerical formulation of multi-phase fluid flow through fractured porous media into FVBOS, a comprehensive study was carried out to verify the accuracy and assess the capabilities of the developed software. In this verification study, various benchmark problems were numerically modeled using FVBOS and the results were compared with either available theoretical solutions or the widely used commercial reservoir simulation software CMG-IMEX. The benchmark problems were chosen to investigate the capabilities and performance of FVBOS in simulating different components influencing multi-phase fluid flow through fractured porous media. In particular, the performance of FVBOS in modeling the effects of viscous forces, gravity, interfacial tension, multi-phase fluid compressibility and mass conservation at multiple fractures intersections were separately assessed. The verification results demonstrated the acceptable accuracy and unique capabilities of FVBOS in the analysis of multi-phase fluid flow through fractured porous media.

7.3 Multi-Phase Discrete Element Computational Tool

The compatibility of the finite volume discrete fracture-matrix approach implemented in FVBOS with discrete element solid mechanical simulation codes made it feasible to develop a powerful computational tool capable of modeling coupled hydro-mechanical multi-phase fluid flow through both porous matrix and highly complex discrete fracture

networks. To develop such computational tool, the source code of FVBOS can be implemented into discrete element solid mechanical computational codes based on fully coupled hydro-mechanical approach. However, since it is not feasible to have access to the source code of commercial discrete element codes such as 3DEC, and since it is out of the scope of this research to develop such codes, sequential coupling approach was used instead. To this end, a novel sequential hydro-mechanical coupling approach closely analogous to fully coupled methods was developed based on which the devised discrete fracture-matrix approach can be coupled with discrete element computational codes.

Using the developed sequential coupling approach, a multi-phase discrete element computational tool called MPDES was developed. To this end, multi-process programming was utilized in MPDES to handle the multitasking needed for coupling FVBOS and 3DEC. The multi-process programming method implemented into MPDES manages the synchronization of fluid and solid mechanical numerical analyses carried out by FVBOS and 3DEC for coupled hydro-mechanical simulations. With this aim, MPDES creates a parent process in which computational threads of FVBOS are executed performing fluid mechanical analyses using finite volume multi-phase discrete fracture-matrix approach. Then, at the end of fluid mechanical analysis time steps, MPDES temporarily pauses the computational threads of FVBOS and creates a child process where 3DEC runs its computational threads carrying out solid mechanical analyses using distinct element method. Afterwards, parameters updated by 3DEC are transferred to FVBOS and the child process together with computational threads of 3DEC are terminated. Then, MPDES reactivates computational threads of FVBOS to proceed with the coupled hydro-mechanical simulations.

Using the developed coupling approach, first, the space occupied by discrete porous matrix blocks and fracture network separating the blocks are discretized by an Eulerian finite volume mesh. The finite volume mesh is generated based on the coordinates of the grid points of the Lagrangian discrete element mesh produced by 3DEC. For this purpose, an algorithm was developed and implemented into MPDES which generates the Eulerian finite volume zones and determines the connectivity of the zones required for transmissibility calculations. Then, MPDES can be employed to solve coupled hydro-mechanical problems where changes in either stress or pore pressure field affect multi-phase fluid flow through pore spaces and fractures. In this research, the major focus was

on the simulation of problems where pore pressure changes under somewhat constant stress field due to the injection of an invading fluid either pushing the resident fluid towards a production well or inducing hydraulic fractures.

In order to numerically solve these problems, while the displacement field in solid phase is remained constant, MPDES first runs FVBOS to solve the equations of motion of multi-phase fluid moving relative to solid phase through pore spaces and complex fracture networks using Eulerian finite volume zones discretizing fractures and porous matrix. Then, MPDES transfers the updated pore pressure field and saturation of fluid phases obtained by fluid mechanical analyses to 3DEC to solve the equations of motion of porous media containing multi-phase fluid, which is immobile relative to solid phase, using Lagrangian zones discretizing discrete blocks and fractures. In this stage, equations of motion are obtained by integrating momentum conservation equations for differential elements of porous media under total stress field over the Lagrangian zones. To solve these equations, total stresses are related to strains of the differential elements using constitutive equations and effective stress concept postulating that total stresses are equilibrated by a fraction of pore pressure and the effective stresses developed between the contacts of constituents of solid phase inside the elements. Strains are also related to derivatives of displacement or velocity field of porous media using proper kinematic relations depending on small or large strain assumptions used in the analyses. Afterwards, displacement field in the porous media is obtained by numerically solving the equations of motion using distinct element method considering deformations in both fracture system and discrete blocks.

At the end of the first iteration of coupled hydro-mechanical analysis described above, two choices are available in MPDES to proceed with the analysis. The first choice is to use one-way coupling approach neglecting the effects of updated displacement field in porous media on the pore pressure redistribution. Using this approach, parameters updated by solid mechanical analysis is transferred to FVBOS to start the next time step of fluid mechanical analysis. The next choice is to utilize iterative coupling approach in which, before starting new time step of fluid mechanical analysis, pore fluid pressure field and displacement field in porous media are iteratively updated based on fluid and solid mechanical analyses until a predefined maximum iteration number or a convergence tolerance limit is reached. While iterative coupling approach consumes more

computational time than one-way method, it solves the coupled hydro-mechanical problem closely similar to fully coupled method. It is also worth mentioning that either at the end of each iteration of coupled hydro-mechanical analyses or at the beginning of fluid mechanical analysis time steps, the Eulerian fluid mechanical mesh can be updated based on the displacement field updated by solid mechanical analyses matching this grid system with the Lagrangian solid mechanical mesh during the analyses. Such a mesh updating makes the sequential coupling approach to behave more closely analogous to fully coupled approach in case large displacements are taken into account in the analysis.

MPDES updates three sets of data in FVBOS based on the solid mechanical analysis either at each iterations of hydro-mechanical coupling or at the beginning of fluid mechanical time steps, namely coordinates of finite volume grid points as well as porosity and aperture at the finite volume midpoints. In particular, the updated porosity and aperture are used to calculate absolute permeability and accumulation term in mass conservation equations of pore fluid moving through pore spaces and fractures in the finite volume zones.

In the calculation of the accumulation term in mass conservation equation, the compressibility of porous matrix can be updated based on the relation between porosity change and effective stress field. In this regard, constitutive relations can be defined for the compressibility of porous matrix as a function of effective stress field. However, compressibility of fracture finite volumes depends not only on stress and pore pressure fields, but also on solid mechanical boundary conditions and constitutive relations which makes it difficult to define a direct relation for the purpose of fracture compressibility updating in sequential coupling scheme. In this research, in order for the developed sequentially coupled hydro-mechanical approach to behave closely analogous to fully coupled approach, compressibility in fracture finite volume zones are approximated based on consecutive solid mechanical solutions during the hydro-mechanical coupling iterations.

It should also be mentioned that, in the numerical analysis results presented in this research, since the major focus has been on the reservoir simulation of fractured shale formations, it was assumed that porosity remains constant during the analyses. This is due to the fact that the injection of fluid into fractured shale formations mostly results in

changes in the configuration of fracture networks while the porosity of matrix blocks barely changes. In addition, large deformation was not taken into account in the numerical simulations due to the fact that 3DEC neglects this effect during hydro-mechanical simulations.

7.4 Application of the Developed Computational Tool

After the implementation of the developed coupled hydro-mechanical method into MPDES, the accuracy and capabilities of MPDES were assessed by the simulation of coupled hydro-mechanical multi-phase fluid flow problems encountered in fractured unconventional formations. The numerical results demonstrated the reasonable accuracy and unique computational capabilities of the developed multi-phase discrete element computational code. Indeed, MPDES has provided a novel powerful numerical approach to more realistically approximate the extent and distribution of fracture aperture change induced by water injection in fractured formations taking into account the effects of fluid leak off into porous matrix, multi-phase fluid properties as well as displacement field in solid phase.

Hydro-mechanical coupling of the finite volume discrete fracture-matrix approach devised in this research and distinct element method enabled MPDES to deal with numerical modeling of coupled hydro-mechanical multi-phase fluid flow through highly complex deformable fracture networks and discrete porous matrix blocks. It was also demonstrated that, in spite of neglecting stress singularity at fractures tips, released strain energy and developed surface energy during fracture propagation, the numerical modeling capacity of MPDES can be utilized to evaluate the effectiveness of the pressure gradient created by water injection, in the stimulation of fractured reservoirs. In particular, the effects of connectivity of fracture networks on the pressure and fracture aperture expansion pattern was evaluated through numerical modeling by MPDES.

The specific industrial applications of MPDES are listed as follows:

- Analysis of coupled hydro-mechanical multiphase fluid flow in fractured reservoirs considering complex deformable fracture networks and fluid transmissibility between fracture and porous matrix.
- Evaluation of the effectiveness of stimulation of fractured reservoirs performed by

water injection.

- Upscaling of hydro-geomechanical properties of fractured reservoir rocks.
- Caprock integrity and micro-seismic analyses in petroleum reservoirs.
- Unsaturated soil and rock mechanical analyses applied in dam and foundation engineering, particularly in soil and rock slope stability analyses.

7.5 Limitations of the Developed Numerical Approach

In the numerical approach developed for the simulation of coupled hydro-mechanical multi-phase fluid flow in fractured porous media, the following phenomena are not taken into account:

- The effects of stress singularity at fracture tips, released strain energy and developed surface energy on fracture initiation and propagation.
- Thermal effects in the equations of states of multi-phase fluid, heat transfer, and coupled thermo-hydro-mechanical processes in fractured porous media.
- Solid particles, i.e. proppant, transport in fractures and its effects on multi-phase fluid flow.
- Compositional multi-phase fluid flow.

7.6 Contributions

In this research, a novel numerical approach was developed in the framework of discrete element method for the simulation of coupled hydro-mechanical multi-phase fluid flow through fractured reservoirs taking into account complex deformable fracture networks. In this regard, the present research has made the following theoretical and industrial contributions:

- Developing a Finite Volume Discrete Fracture-Matrix Method for the simulation of compressible multi-phase fluid flow comprised of aqueous liquid, none-aqueous liquid as well as free and dissolved gas through highly complex fracture networks and porous matrix considering fluid transmissibility between fractures and porous matrix.
- Enriching Discrete Element Method with the capability of coupled hydro-mechanical multi-phase fluid flow simulation through both pore spaces and

complex deformable fracture networks taking into account matrix-matrix, matrix-fracture and fracture-fracture multi-phase fluid transmissibility.

- Utilizing an Eulerian Finite Volume mesh of fluid phase updated by current Lagrangian discrete element mesh of solid phase in the framework of Discrete Element Method.
- Taking into account the effects of fracture aperture changes in the pressure partial differential equation by a fracture normal stiffness updated based on displacement and stress filed in solid phase.
- Providing a more sophisticated alternative for the conventional reservoir simulators for the evaluation of the effectiveness of stimulation of fractured reservoirs performed by water injection.

7.7 Recommendations for Future Research

In spite of the remarkable numerical capacity of distinct element method in dealing with highly complex deformable fracture systems, this method has not been equipped with proper computational approach to undertake coupled hydro-mechanical multi-phase fluid flow through both fractures and pore spaces of fractured porous media so far. In this research, with the aim of exploiting the capabilities of distinct element method to provide a powerful computational tool to be used in the efficiency assessment of hydraulic fracturing and production schemes in fractured reservoirs, this method has been enriched with a powerful computational multi-phase fluid flow simulation approach developed based on finite volume discrete fracture-matrix method. The computational tool developed in this research offers a novel methodology for more sophisticated numerical simulations required in developing efficient exploitation strategies in fractured unconventional formations, particularly in shale reservoirs.

This research has opened new pathways in the reservoir simulation of fractured formations which can be further developed through the following proposed future research activities:

- Calibrate MPDES based on systematic experimental research on coupled hydro-mechanical multi-phase fluid flow through fractured porous media. With this aim, it is proposed to utilize 3-D printing technology of GeoPrint Facility at Reservoir Geomechanics Research Group (RG^2), University of Alberta, to produce repeatable

precise fractured porous samples which are essential for this purpose.

- Enrich MPDES with artificial intelligence (AI) and machine learning (ML) approaches to perform automated coupled hydro-mechanical simulations aimed at upscaling of hydro-geomechanical properties of fractured reservoir rocks. To this end, it is proposed to train the artificially intelligent computational tool by the experimental data provided by centrifuge facility available at Reservoir Experimental Facility (GeoRef) at Reservoir Geomechanics Research Group, University of Alberta.
- Upgrade MPDES by implementing a computational approach accounting for stress singularity, released strain energy and developed surface energy due to fracture propagation to devise a numerical approach for the simulation of highly complex hydraulic fracturing processes in unconventional reservoir formations.
- Upgrade MPDES by implementing compositional multi-phase fluid models along with a computational heat transfer method enabling the computational tool to deal with coupled thermo-hydro-mechanical simulations in fractured unconventional reservoirs.

References

Azad, A., Chalaturnyk R. 2012. An improved SAGD analytical simulator: Circular steam chamber geometry. J. Petrol. Sci. Eng. 82-83, 27-37.

Babadagli, T., Ren, X., Develi, K. 2015. Effect of fractal surface roughness and lithology on single and multiphase flow in a single fracture: An experimental investigation. Int. J. Multiphase Flow 68, 40-58.

Bailey, C., Cross, M. 1995. A finite volume procedure to solve elastic solid mechanics problems in three dimensions on an unstructured mesh. Int. J. Numer. Meth. Eng. 38, 1757-1776.

Bandis, S.C., Lumsden, A.C., Barton, N. R. 1983. Fundamentals of rock joint deformation. Int. J. Rock Mech. Min. Sci. 20, 249-268.

Barenblatt, G.I., Zheltov, Y.P. 1960. Basic equations of homogeneous flow in fissured rocks. Doklady Akademii Nauk SSSR 132, 545.

Bathe K.J. 1996. Finite element procedures. Prentice-Hall, New Jersey.

Bazant ZP, Ohtsubo H. 1978. Geothermal heat extraction by water circulation through a large crack in dry hot rock mass. Int. J. Numer. Anal. Meth. Geomech. 2, 317–27.

Belytschko, T., Liu, W.K., Moran, B., Elkhodary, K. 2013. Nonlinear finite elements for continua and structures. John Wiley and Sons.

Bergamaschi, L., Mantica, S., Manzini, G. 1999. A mixed finite element finite volume for simulation of the black-oil model. SIAM J. Sci. Comput. 20, 970-997.

Biot, M.A. 1941. General theory of three-dimensional consolidation. J. App. phys. 12, 155-164.

Buckley, S.E., Leverett, M.C. 1941. Mechanism of Fluid Displacement in Sands. SPE. doi: SPE-942107-G.

Chalaturnyk, R.J., Wagg, B.T., Dusseault, M.B. 1992. The Mechanisms of Solids Production in Unconsolidated Heavy-Oil Reservoirs. SPE. doi:10.2118/23780-MS.

Chalaturnyk, R., Scott, J.D. 1995. Geomechanics Issues of Steam Assisted Gravity Drainage. SPE. doi:10.2118/30280-MS.

Cho, Y., Ozkan, E., Apaydin, O.G. 2013. Pressure-dependent natural-fracture permeability in shale and its effect on shale-gas well production. SPE Reserv. Eval. Eng. 16, 216-228.

Chopra, A.K. 2012. Dynamics of structures: theory and applications to earthquake engineering. Prentice Hall, Boston.

Clough, R.W., Penzien, J. 2003. Dynamics of structures. Computers and Structures Inc., Berkeley.

Crisfield M.A. 1991. Non-linear finite element analysis of solids and structures. Essentials, vol. 1. John Wiley & Sons, New York.

Cundall P.A. 1971. A computer model for simulating progressive large-scale movement in blocky rock systems. In: Proceedings of the symposium of the international society of rock mechanics (Nancy, France, 1971) vol. 1, Paper No. II-8.

Cundall P.A., Strack, O. 1979. A discrete numerical model for granular assemblies. Geotechnique 29, 47-65.

Cundall, P.A. 1988. Formulation of a three-dimensional distinct element method-Part I: A scheme to detect and represent contacts in a system composed of many polyhedral blocks. Int. J. Rock Mech. Min. Sci. 25, 107-116.

Curtis, M.E., Cardott, B.J., Sondergeld, C.H., Rai, C.S., 2012. Development of organic porosity in the Woodford shale with increasing thermal maturity. Int. J. Coal Geol. 103, 26–31.

Damjanac, B., 1996. A three-dimensional numerical model of water flow in a fractured rock mass. PhD thesis, University of Minnesota, Minneapolis.

Damjanac, B., Cundall, P. 2016. Application of distinct element methods to simulation of hydraulic fracturing in naturally fractured reservoirs. Comput. Geotech. 71, 283-294.

Deisman, N., Ivars, D.M., Darcel, C., Chalaturnyk, R. 2010. Empirical and numerical approaches for geomechanical characterization of coal seam reservoirs. Int. J. Coal Geolo.

82, 204-212.

Demirdzic, I., Martinovic, D. 1993. Finite volume method for thermo-elasto-plastic stress analysis. Comput. Meth. Appl. Mech. Eng. 109, 331-349.

Fanchi, J.R., Harpole, K.J., Bujnowski, S.W. 1982. BOAST: A three-dimensional, three-phase black oil applied simulation tool (Version 1.1). Volume I: Thechnical description and fortran code. US Department of Energy, Bartlesville, Oklahoma, USA.

Franquet, M., Ibrahim, M., Wattenbarger, R.A., Maggard, J.B. 2004. Effect of pressure-dependent permeability in tight gas reservoirs transient radial flow. In: Canadian International Petroleum Conference. Petroleum Society of Canada.

Galerkin, B.G. 1915. Rods and plates. Series occurring in various questions concerning the elastic equilibrium of rods and plates. Eng. Bull.(Vestnik Inzhenerov) 19, 897-908.

Griffith A.A. 1921. The phenomena of rupture and flow in solids. The Philosophical Transactions of the Royal Society London (Series A), 221, 163-98.

Gutierrez, M., Oino, L.E., Nygard, R. 2000. Stress-dependent permeability of a demineralized fracture in shale. Mar. Petrol. Geol. 178, 895-907.

Guo, T., Zhang, S., Qu, Z., Zhou, T., Xiao, Y., Gao, J. 2014. Experimental study of hydraulic fracturing for shale by stimulated reservoir volume. Fuel 128, 373–80.

Hart, R., Cundall, P.A., Lemos, J. 1988. Formulation of a three-dimensional distinct element model – Part II: Machanical calculations for motion and interaction of a system of many polyhedral blocks. Int. J. Rock Mech. Min. Sci. 25, 117–26.

Hamidi, F., Mortazavi, A. 2014. A new three-dimensional approach to numerically model hydraulic fracturing process. J. Petrol. Sci. Eng. 124, 451-467.

Hoek, E., Martin, C.D. 2014. Fracture initiation and propagation in intact rock – A review. J. Rock Mech. Geotech. Eng. 6, 287-300.

Hu, Y., Chen G., Cheng W., Yang Z. 2014. Simulation of hydraulic fracturing in rock mass using a smeared crack model. Comput. Struct. 137, 72–7.

Hubbert, M.K. 1956. Darcy's law and the field equations of the flow of underground fluids. Petrol. Trans., AIME 207, 22-239.

Itasca Consulting Group Inc., 2016. 3DEC (Three-Dimensional Distinct Element Code), Version 5.2. Minneapolis, Minnesota, USA.

Javadpour, F., Fisher, D., Unsworth, M. 2007. Nanoscale gas flow in shale gas sediments. J. Can. Petrol. Technol. 46, 55–61.

Jing, L., Stephansson, O. 2007. Fundamentals of discrete element methods for rock engineering. Elsevier, Amsterdam.

Kaiser, M.J. 2012. Haynesville shale play economic analysis. J. Pet. Sci. Eng. 8, 75-89.

Karimi-Fard, M., Durlofsky, L.J., Aziz, K. 2004. An efficient discrete-fracture model applicable for general-purpose reservoir simulators. SPE Journal 9, 227-236.

Khazaei, C., Hazzard, J., Chalaturnyk, J. 2015. Damage quantification of intact rocks using acoustic emission energies recorded during uniaxial compression test and discrete element modeling. Comput. Geotech. 67, 94-102.

Kazemi, H., Seth, M. S., Thomas, G.W. 1969. The interpretation of interference tests in naturally fractured reservoirs with uniform fracture distribution. SPE Journal 463–472.

Khoei, A.R., Hosseini, N., Mohammadnjead, T. 2016. Numerical modeling of two-phase fluid flow in deformable fractured porous media using the extended finite element method as an equivalent continuum model. Adv. water Resour. 94, 510-528.

Kim, J., Tchelepi, H.A., Juanes, R. 2013. Regorous coupling of geomechanics and multiphase flow with strong capillary. SPE Journal 18.

Lecampion B. 2009. An extended finite element method for hydraulic fracture problems. Commun. Numer. Meth. Eng. 25, 121–33.

Le B.D., Dau, F., Charles, J.L., Iordanoff, I. 2016. Modeling damages and cracks growth in composite with a 3D discrete element method. Composites Part B 91, 615-630.

Li, P., Chalaturnyk, R.J. 2007. Gas-Over-Bitumen Geometry and Its SAGD Performance Analysis with Coupled Reservoir Geomechanical Simulation. Petroleum Society of Canada. doi:10.2118/07-01-05.

Lie, K.A. 2016. An introduction to reservoir simulation using MATLAB, user guide for the MATLAB reservoir simulation toolbox(MRST). SINTEF ICT, Department of Applied

Mthematics, Oslo, Norwey.

Liu, M., Xiao, C., Wang, Y., Li, Z., Zhang, Y., Chen, S., Wang, G. 2015. Sensitivity analysis of geometry for multi-stage fractured horizontal wells with consideration of finite-conductivity fractures in shale gas reservoirs. J. Nat. Gas Sci. Eng. 22, 182-195.

Liu, P., Liu, F., She, C., Zhao, L., Luo, Z. Guan, W., Li, N. 2016. Multi-phase fracturing fluid leakoff model for fractured reservoir using extended finite element method. J. Nat. Gas Sci. Eng. 28, 548-557.

Loucks, R.G., Reed, R.M., Ruppel, S.C., Jarvie, D.M. 2009. Morphology, genesis, and distribution of nanometer-scale pores in siliceous mudstones of the mississippian barnett shale. J. Sediment Res. 79, 848–61.

Ma, Y.Z., Holditch, S.A. 2015. Unconventional oil and gas resources handbook: evaluation and development. Elsevier, New York.

Mayerhofer, M.J., Lolon, E.P., Youngblood, J.E., Heinze, J.R., 2006. Integration of microseismic-fracture-mapping results with numerical fracture network production modeling in the Barnett Shale. In: SPE Annual Technical Conference and Exhibition. SPE.

McCain, W.D. 1991. Reservoir-Fluid Property Correlations-State of the Art. SPE Reservoir Eng. 6, 266-272.

Minkoff, S.E., Stone, C.M., Bryant, S., Peszunska, M., Wheetle, M.F. 2003. Coupled fluid flow and geomechanical deformation modeling. J. Petrol. Sci. Eng. 38, 37-56.

Morgan, W.E., Aral, M.M. 2015. An implicitly coupled hydro-geomechanical model for hydraulic fracture simulation with the discontinuous deformation analysis. Int. J. Rock. Mech. Min. Sci. 73, 82–94.

Munjiza, A., Owen, D., Bicanic, N. 1995. A combined finite-discrete element method in transient dynamics of fracturing solids. Eng. Comput. 12, 145–74.

Nazary Moghadam, S., Asgarian, B., Nazokkar, K. 2012. Simulation of overall and lockal buckling behavior of cylindrical tubular members using fuzzy inference system. Adv. Eng. Softw. 45, 349–359.

Nazary Moghadam, S., Mirzabozorg, H., Noorzad, A. 2013. Modeling time-dependent behavior of gascaverns in rock salt considering creep, dilatancy and failure. Tunnel. Undergr. Space Technol. 33, 171–185.

Nazary Moghadam, S., Nazokkar, K., Chalaturnyk, R.J., Mirzabozorg, H. 2015. Parametric assessment of salt cavern performance using a creep model describing dilatancy and failure. Int. J. Rock Mech. Min. Sci. 79, 250–267.

Newmark, N. M. 1959. A method of computation for structural dynamics. J. Eng. Mech. Div. 85, 67-94.

Nicot, J.P., Scanlon, B.R. 2012. Water use for shale-gas production in Texas, US. Environ. Sci. Technol. 46, 3580–6.

Noorishad, J., Mehran, M. 1982. An upstream finite element method for solution of transient transport equation in fractured porous media. Water Resour. Res. 18, 588-596.

Owen, D.R.J., Hinton, E. 1980. Finite Elements in Plasticity: Theory and Practice. Pineridge Press, Swansea.

Ozkan, E., Brown, M.L., Raghavan, R.S., Kazemi, H. 2009, January. Comparison of fractured horizontal-well performance in conventional and unconventional reservoirs. In: SPE Western Regional Meeting. SPE.

Perkins, T. K., Kern, L. R. 1961. Width of hydraulic fractures. SPE Journal 89-PA.

Pine, R.J., Cundall, P.A. 1985. Applications of the fluid-rock interaction program (FRIP) to the modelling of hot dry rock geothermal energy systems. In: Proceedings of the International Symposium on Fundamentals of Rock Joints, Bjorkliden; p. 293–302.

Peirce, A., Siebrits, E. 2005. A dual mesh multigrid preconditioner for the efficient solution of hydraulically driven fracture problems. Int. J. Numer. Meth. Eng. 63, 1797–823.

Reddy, J. N. 2007. An introduction to continuum mechanics. Cambridge University Press.

Reynolds, O. 1886. On the Theory of Lubrication and Its Application to Mr. Beauchamp Tower's Experiments, Including an Experimental Determination of the Viscosity of Olive Oil. Philosophical Transactions of the Royal Society of London.

Rutqvist, J., Wu, Y.S., Tsang, C.F., Bodvarsson, G. 2002. A modeling approach for analysis of coupled multiphase fluid flow, heat transfer, and deformation in fractured porous rock. Int. J. Rock Mech. Min. Sci. 39, 429-442.

Sakhaee-Pour, A., Bryant, S.L. 2015. Pore structure of shale. Fuel 143, 467–75.

Sandve, T.H., Berre, I., Nordbotten, J.M. 2012. An efficient multi-point flux approximation method for discrete fracture-matrix simulations. J. of Comput. Phys. 231, 3784-3800.

Savitski, A.A., Lin, M., Riahi, A., Damjanac, B., Nagel, N.B. 2013. Explicit modeling of hydraulic fracture propagation in fractured shales. IPTC-17073-MS.

Shabro, V., Javadpour, F., Torres-Verdin, C. 2009. A generalized finite-difference diffusive-advective (FDDA) model for gas flow in micro-and nano-porous media. World J. Eng. 6, 7–15.

Shames, I.H. 2003. Mechanics of fluids. McGraw Hill, New York.

Shilko, E.V., Psakhie, S.G., Schmauder, S., Popov, V.L., Astafurov, S.V., Smolin, A.Y. 2015. Overcoming the limitations of distinct element method for multiscale modeling of materials with multimodal internal structure. Comput. Mat. Sci. 102, 267-285.

Sneddon, I.N. 1946. The distribution of stress in the neighborhood of a crack in an elastic solid. Proceedings of the Royal Society of London. Series A. Mathematical and Physical Sciences 187, 229-260.

Snow, D.T. 1965. A Parallel Plate Model of Fractured Permeable Media. Ph. D. thesis, University of California, Berkeley.

Sondergeld, C.H., Ambrose, R.J., Rai, C.S., Moncrieff, J.M. 2010. Micro-structural studies of gas shales, SPE 131771. In: SPE Unconventional gas conference. Pittsburgh (Pennsylvania, USA): SPE.

Spencer, A.J.M. 2004. Continuum mechanics. Courier Corporation.

Terzaghi, K. 1943. Theoretical Soil Mechanics. John Wiley & Sons. New York, 11-15.

Trangenstein, J.A., Bell, J.N. 1989. Mathematical structure of the Black-Oil model for petroleum reservoir simulations. SIAM J. Appl. Math. 3, 749–786.

Wang T., Zhou W., Chen J., Xiao X., Li Y., Zhao X. 2014. Simulation of hydraulic fracturing using particle flow method and application in a coal mine. Int. J. Coal. Geol. 121, 1–13.

Wang, F., Reed, R. 2009. Pore networks and fluid flow in gas shales. SPE 124253. In: Annual technical conference and exhibition. New Orleans (Louisiana): SPE.

Warpinski, N.R., Mayerhofer, M.J., Vincent, M.C., Cipolla, C.L., Lolon, E.P., 2009. Stimulating unconventional reservoirs: Maximizing network growth while optimizing fracture conductivity. J. Can. Pet. Technol. 48, 39-51.

Wen, Q., Zhang, S., Wang, L., Liu, Y., Li, X. 2007. The effect of proppant embedment upon the long-term conductivity of fractures. J. Petrol. Sci. Eng. 55, 221-227.

Wong, D.L.Y., Doster, F., Geiger, S., Francot, E., Gouth, F. 2020. Fluid Flow Characterization Framework for Naturally Fractured Reservoirs Using Small-Scale Fully Explicit Models. Transp. Porous Media, 1-36.

Wu, Y.S. 2016. Multiphase fluid flow in porous and fractured reservoirs. Elsevier, New York.

Xu, J., Guo, C., Wei, M., Jiang, R. 2015. Production performance analysis for composite shale gas reservoir considering multiple transport mechanisms. J. Nat. Gas Sci. Eng. 26, 382-395.

Xu, M., Dehghanpour, H. 2014. Advances in understanding wettability of gas shales. Energy Fuels 28, 4362–75.

Young, D. M. 2014. Iterative solution of large linear systems. Elsevier.

Yu, W., Zhang, T., Du, S., Sepehrnoori, K. 2015. Numerical study of the effect of uneven proppant distribution between multiple fractures on shale gas well performance. Fuel 142, 189-198.

Zanganeh, N., Eberhardt, E., Bustin, R.M. 2015. Investigation of the influence of natural fractures and in situ stress on hydraulic fracture propagation using a distinct element approach. Can. Geotech. J. 52, 926–946.

Zhang, F., Maxwell, S.C., Damjanac, B. 2015. Modeling of fault activation induced by

hydraulic fracturing – a Horn River basin case study. Hyd. Fract. J. 2, 26–33.

Zienkiewicz, O. C., & Shiomi, T. 1984. Dynamic behavior of saturated porous media; the generalized Biot formulation and its numerical solution. Int. J. Num. Anal. Meth. Geomech. 8, 71-96.

Zienkiewicz, O.C., Paul, D.K., Chan, A.H.C. 1988. Unconditionally stable staggered solution procedure for soil-pore interaction problems. Int. J. Numer. Mech. Eng. 26, 1039-1055.

Zienkiewicz, O.C., Onate, E. 1992. Finite elements versus finite volumes. Is there really a choice? In: Nonlinear computational mechanics. State of the art. P. Wriggers, R. Wagner and E. Stein (Eds.), Chapter IV, Beam, Plate and Shell Formulations, pp. 240-254, Springer Verlag URL.

Zienkiewicz, O.C., Taylor, R.L. 2005. The finite element method for solid and structural mechanics. Elsevier, New York.

Zimmerman, R.W., Bodvarsson, G.S., 1996. Review article: hydraulic conductivity of rock fractures. Transp. Porous Media 23, 1-30.

Appendix A Derivation of Biot's Coefficient

As it was discussed in chapter 3, in the formulation of constitutive equations relating the stresses and strains in solid phase, the contribution of pore pressure in the deformation of solid phase cannot be neglected in fractured rock mass. Therefore, by subtracting the part of the pore fluid pressure that does not contribute in the deformation of solid phase from total stress tensor, and relating the resulting stress tensor and the strain tensor in the solid phase, assuming elastic material behavior, the Biot's effective stress and coefficient can be derived. To this end, as it is schematically shown in Figure 6, the total stress tensor can be decomposed into the part that is equilibrated by pore fluid pressure, developing volumetric deformation in undrained condition, and the part that is equilibrated solely by the stresses developed between solid constituents, developing volumetric and shear deformations in drained condition. Therefore, it can be assumed that the total strains in solid phase is obtained as the sum of the drained and undrained strains as follows:

$$\varepsilon_{ij} = \varepsilon_{ij}^{u} + \varepsilon_{ij}^{d} \qquad \text{Eq. 213}$$

where ε_{ij}^{u} and ε_{ij}^{d} are undrained and drained strains, respectively. The drained strains are developed due to the compressibility of pore fluid and solid particles as well as rearrangement of solid skeleton due to isotropic and deviatoric deformation of solid skeleton. Taking into account all the strains developed in solid constituents in drained, $\varepsilon_{ij}^{\mathcal{S}d}$, and undrained conditions, $\varepsilon_{ij}^{\mathcal{S}u}$, as well as the strains developed in the pore fluid, $\varepsilon_{ij}^{\mathcal{F}}$, which is immobile relative to the solid phase, the following relation can be defined for the total strains:

$$\varepsilon_{ij} = \varepsilon_{ij}^{\mathcal{F}} + \varepsilon_{ij}^{\mathcal{S}u} + \varepsilon_{ij}^{\mathcal{S}d} \qquad \text{Eq. 214}$$

$$\varepsilon_{ij}^{\mathcal{F}} = \frac{P}{3K_{\mathcal{F}}}\delta_{ij} \qquad \text{Eq. 215}$$

$$\varepsilon_{ij}^{\mathcal{S}u} = \frac{P}{3K_{\mathcal{S}}}\delta_{ij} \qquad \text{Eq. 216}$$

$$\varepsilon_{ij}^{\mathcal{S}d} = S_{ijkl}(\sigma_{kl} - P\delta_{kl}) \qquad \text{Eq. 217}$$

where $K_{\mathcal{F}}$ is the bulk modulus of pore fluid, $\varepsilon_{ij}^{\mathcal{F}}$ represents strains developed due to the compressibility of pore fluid, $K_{\mathcal{S}}$ is bulk modulus of solid constituents, $\varepsilon_{ij}^{\mathcal{S}u}$ denotes the strains developed due to the compressibility of solid constituents under pore pressure, and S_{ijkl} is elastic drained compliance tensor of solid phase. In the above equations, it should be noted that since the fluid phase is assumed to be inviscid, i.e. the viscosity of fluid is negligible, the deviatoric stresses develop in immobile pore fluid phase due to the velocity gradient of the fractured porous solid element is neglected. Therefore, the contribution of pore fluid in shear deformation of fractured porous media is ignored. Using the above equations, the total elastic strains developed in the solid phase can be formulated as follows:

$$\varepsilon_{ij}^{\mathcal{S}} = \varepsilon_{ij}^{\mathcal{S}u} + \varepsilon_{ij}^{\mathcal{S}d} = \frac{P}{3K_{\mathcal{S}}}\delta_{ij} + S_{ijkl}(\sigma_{kl} - P\delta_{kl}) \qquad \text{Eq. 218}$$

By multiplying the two sides of the above equation by elastic drained stiffness tensor of solid phase, $C_{ijkl} = \left(S_{ijkl}\right)^{-1}$, and rearranging the resulting equation, the following relations are derived:

$$C_{ijkl}\varepsilon_{kl}^{\mathcal{S}} = \frac{P}{3K_{\mathcal{S}}}C_{ijkl}\delta_{kl} + C_{ijkl}S_{klmn}(\sigma_{mn} - P\delta_{mn}) \qquad \text{Eq. 219}$$

$$\sigma_{ij} + \frac{P}{3K_{\mathcal{S}}}C_{ijkl}\delta_{kl} - P\delta_{ij} = C_{ijkl}\varepsilon_{kl}^{\mathcal{S}} \qquad \text{Eq. 220}$$

In the above equation, by extending the term $C_{ijkl}\delta_{kl}$, it can be simplified as follows:

$$C_{ijkl}\delta_{kl} = \frac{E}{(1+\nu)(1-2\nu)}\begin{bmatrix}\begin{bmatrix}(1-\nu) & 0 & 0\\ 0 & \nu & 0\\ 0 & 0 & \nu\end{bmatrix} & \begin{bmatrix}0 & \frac{1-2\nu}{2} & 0\\ 0 & 0 & 0\\ 0 & 0 & 0\end{bmatrix} & \begin{bmatrix}0 & 0 & \frac{1-2\nu}{2}\\ 0 & 0 & 0\\ 0 & 0 & 0\end{bmatrix}\\ \begin{bmatrix}0 & 0 & 0\\ \frac{1-2\nu}{2} & 0 & 0\\ 0 & 0 & 0\end{bmatrix} & \begin{bmatrix}\nu & 0 & 0\\ 0 & (1-\nu) & 0\\ 0 & 0 & \nu\end{bmatrix} & \begin{bmatrix}0 & 0 & 0\\ 0 & 0 & \frac{1-2\nu}{2}\\ 0 & 0 & 0\end{bmatrix}\\ \begin{bmatrix}0 & 0 & 0\\ 0 & 0 & 0\\ \frac{1-2\nu}{2} & 0 & 0\end{bmatrix} & \begin{bmatrix}0 & 0 & 0\\ 0 & 0 & 0\\ 0 & \frac{1-2\nu}{2} & 0\end{bmatrix} & \begin{bmatrix}\nu & 0 & 0\\ 0 & \nu & 0\\ 0 & 0 & (1-\nu)\end{bmatrix}\end{bmatrix} : \begin{bmatrix}1 & 0 & 0\\ 0 & 1 & 0\\ 0 & 0 & 1\end{bmatrix} \quad \text{Eq. 221}$$

$$C_{ijkl}\delta_{kl} = \frac{E}{(1-2\nu)}\begin{bmatrix}1 & 0 & 0\\ 0 & 1 & 0\\ 0 & 0 & 1\end{bmatrix} = \frac{E}{(1-2\nu)}\delta_{ij} = 3K_{\mathcal{B}}\delta_{ij} \quad \text{Eq. 222}$$

where E, ν and $K_{\mathcal{B}}$ are Young's modulus, Poison's ratio and bulk modulus of the drained fractured porous solid element. Therefore, the stress-strain relation in fractured porous solid element is simplified as follows:

$$\sigma_{ij} + 3K_{\mathcal{B}}\frac{P}{3K_{\mathcal{S}}}\delta_{ij} - P\delta_{ij} = C_{ijkl}\varepsilon^{\mathcal{S}}_{kl} \quad \text{Eq. 223}$$

$$\sigma_{ij} - \left(1 - \frac{K_{\mathcal{B}}}{K_{\mathcal{S}}}\right)P\delta_{ij} = C_{ijkl}\varepsilon^{\mathcal{S}}_{kl} \quad \text{Eq. 224}$$

Based on the above equation, the Biot's effective stress, σ''_{ij}, can be defined as the portion of the total stress which is responsible for the development of deformation in solid phase as follows:

$$\sigma_{ij} - \alpha P\delta_{ij} = \sigma''_{ij} = C_{ijkl}\varepsilon^{\mathcal{S}}_{kl} \quad \text{Eq. 225}$$

$$\alpha = 1 - \frac{K_{\mathcal{B}}}{K_{\mathcal{S}}} \quad \text{Eq. 226}$$

where α is Biot's coefficient. If the bulk modulus of solid constituents is much larger than the bulk modulus of drained fractured porous solid element, i.e. $K_{\mathcal{S}} \gg K_{\mathcal{B}}$, e.g. in the case of loose sand, the term $\frac{K_{\mathcal{B}}}{K_{\mathcal{S}}}$ tends to zero and $\alpha = 1$. Biot's coefficient is mostly in the range of $\alpha = [0.5,0.8]$, and for concrete it is equal to $2/3$.

Appendix B Mathematical Derivation of Pressure Equation

In the fourth chapter of this thesis, three partial differential equations of motion of multi-phase fluid flow through fractured porous media were derived by satisfying mass conservation law. Combining these equations with Darcy's or Reynolds equations, depending on the case of fluid flow through porous matrix or fractures, and substituting water and gas pressures by the corresponding expressions in terms of oil pressure using capillary pressure equations, the following partial differential equations are achieved:

$$\nabla.\left[-\frac{Kk_r^w}{B^w\mu^w}\nabla(P^o - P_c^{ow} - \rho^w gZ)\right] + \frac{q^w}{\rho_{SC}^w} = -\frac{\partial}{\partial t}\left(\frac{S^w\phi}{B^w}\right) \quad \text{Eq. 227}$$

$$\nabla.\left[-\frac{Kk_r^o}{B^o\mu^o}\nabla(P^o - \rho^o gZ)\right] + \frac{q^o}{\rho_{SC}^o} = -\frac{\partial}{\partial t}\left(\frac{S^o\phi}{B^o}\right) \quad \text{Eq. 228}$$

$$\nabla.\left[-\frac{Kk_r^g}{B^g\mu^g}\nabla(P^o - P_c^{go} - \rho^g gZ) - \frac{R_s^w Kk_r^w}{B^w\mu^w}\nabla(P^o - P_c^{ow} - \rho^w gZ) - \frac{R_s^o Kk_r^o}{B^o\mu^o}\nabla(P^o - \rho^o gZ)\right] + \frac{q^g}{\rho_{SC}^g} = -\frac{\partial}{\partial t}\left[\left(\frac{S^g}{B^g} + \frac{R_s^w S^w}{B^w} + \frac{R_s^o S^o}{B^o}\right)\phi\right] \quad \text{Eq. 229}$$

By utilizing the parameters CG^w, CG^o and CG^g, defined in the fourth chapter, representing the gravity and capillary pressures effects, the above set of partial differential equations can be rewritten as follows:

$$-\nabla.\left[\frac{Kk_r^w}{B^w\mu^w}\nabla P^o\right] - CG^w + \frac{q^w}{\rho_{SC}^w} = -\frac{\partial}{\partial t}\left(\frac{S^w\phi}{B^w}\right) \quad \text{Eq. 230}$$

$$-\nabla.\left[\frac{Kk_r^o}{B^o\mu^o}\nabla P^o\right] - CG^o + \frac{q^o}{\rho_{SC}^o} = -\frac{\partial}{\partial t}\left(\frac{S^o\phi}{B^o}\right) \quad \text{Eq. 231}$$

$$-\nabla.\left[\frac{Kk_r^g}{B^g\mu^g}\nabla P^o + \frac{R_s^w Kk_r^w}{B^w\mu^w}\nabla P^o + \frac{R_s^o Kk_r^o}{B^o\mu^o}\nabla P^o\right] - CG^g + \frac{q^g}{\rho_{SC}^g} = -\frac{\partial}{\partial t}\left[\left(\frac{S^g}{B^g} + \frac{R_s^w S^w}{B^w} + \frac{R_s^o S^o}{B^o}\right)\phi\right] \quad \text{Eq. 232}$$

Combining the above partial differential equations and equalizing the sum of fluid phases' saturations with unity, the pressure partial differential equation is obtained in which the only unknown is one of the fluid phases pressure. With this aim, the parameters ξ^w, ξ^o

and ξ^{g} are defined as follows:

$$\xi^{w} = \frac{\partial}{\partial t}\left(\frac{S^{w}\phi}{B^{w}}\right) = \nabla.\left[-\frac{Kk_r^{w}}{B^{w}\mu^{w}}\nabla P^{o}\right] + CG^{w} - \frac{q^{w}}{\rho_{SC}^{w}} \quad \text{Eq. 233}$$

$$\xi^{o} = \frac{\partial}{\partial t}\left(\frac{S^{o}\phi}{B^{o}}\right) = \nabla.\left[-\frac{Kk_r^{o}}{B^{o}\mu^{o}}\nabla P^{o}\right] + CG^{o} - \frac{q^{o}}{\rho_{SC}^{o}} \quad \text{Eq. 234}$$

$$\xi^{g} = \frac{\partial}{\partial t}\left[\left(\frac{S^{g}}{B^{g}} + \frac{R_s^{w}S^{w}}{B^{w}} + \frac{R_s^{o}S^{o}}{B^{o}}\right)\phi\right] = \nabla.\left[\frac{Kk_r^{g}}{B^{g}\mu^{g}}\nabla P^{o} - \frac{R_s^{w}Kk_r^{w}}{B^{w}\mu^{w}}\nabla P^{o} - \frac{R_s^{o}Kk_r^{o}}{B^{o}\mu^{o}}\nabla P^{o}\right] + CG^{g} - \frac{q^{g}}{\rho_{SC}^{g}} \quad \text{Eq. 235}$$

By extending the partial derivatives with respect to time in the above equations using chain rule, the following equations are obtained:

$$\xi^{w} = \frac{\partial}{\partial t}\left(\frac{S^{w}\phi}{B^{w}}\right) = \frac{S^{w}}{B^{w}}\frac{\partial\phi}{\partial P^{o}}\frac{\partial P^{o}}{\partial t} - \frac{S^{w}\phi}{(B^{w})^2}\frac{\partial B^{w}}{\partial P^{o}}\frac{\partial P^{o}}{\partial t} + \frac{\phi}{B^{w}}\frac{\partial S^{w}}{\partial t} \quad \text{Eq. 236}$$

$$\xi^{o} = \frac{\partial}{\partial t}\left(\frac{S^{o}\phi}{B^{o}}\right) = \frac{S^{o}}{B^{o}}\frac{\partial\phi}{\partial P^{o}}\frac{\partial P^{o}}{\partial t} - \frac{S^{o}\phi}{(B^{o})^2}\frac{\partial B^{o}}{\partial P^{o}}\frac{\partial P^{o}}{\partial t} + \frac{\phi}{B^{o}}\frac{\partial S^{o}}{\partial t} \quad \text{Eq. 237}$$

$$\xi^{g} = \frac{\partial}{\partial t}\left[\left(\frac{S^{g}}{B^{g}} + \frac{R_s^{w}S^{w}}{B^{w}} + \frac{R_s^{o}S^{o}}{B^{o}}\right)\phi\right] = \frac{S^{g}}{B^{g}}\frac{\partial\phi}{\partial P^{o}}\frac{\partial P^{o}}{\partial t} - \frac{S^{g}\phi}{(B^{g})^2}\frac{\partial B^{g}}{\partial P^{o}}\frac{\partial P^{o}}{\partial t} + \frac{\phi}{B^{g}}\frac{\partial S^{g}}{\partial t} + \frac{R_s^{w}S^{w}}{B^{w}}\frac{\partial\phi}{\partial P^{o}}\frac{\partial P^{o}}{\partial t} - \frac{R_s^{w}S^{w}\phi}{(B^{w})^2}\frac{\partial B^{w}}{\partial P^{o}}\frac{\partial P^{o}}{\partial t} + \frac{R_s^{w}\phi}{B^{w}}\frac{\partial S^{w}}{\partial t} + \frac{S^{w}\phi}{B^{w}}\frac{\partial R_s^{w}}{\partial P^{o}}\frac{\partial P^{o}}{\partial t} + \frac{R_s^{o}S^{o}}{B^{o}}\frac{\partial\phi}{\partial P^{o}}\frac{\partial P^{o}}{\partial t} - \frac{R_s^{o}S^{o}\phi}{(B^{o})^2}\frac{\partial B^{o}}{\partial P^{o}}\frac{\partial P^{o}}{\partial t} + \frac{R_s^{o}\phi}{B^{o}}\frac{\partial S^{o}}{\partial t} + \frac{S^{o}\phi}{B^{o}}\frac{\partial R_s^{o}}{\partial P^{o}}\frac{\partial P^{o}}{\partial t} \quad \text{Eq. 238}$$

By taking time derivative from the relation equalizing the saturation of fluid phases with unity, the following equation is obtained:

$$S^{w} + S^{o} + S^{g} = 1 \rightarrow \frac{\partial S^{g}}{\partial t} = -\left(\frac{\partial S^{w}}{\partial t} + \frac{\partial S^{o}}{\partial t}\right) \quad \text{Eq. 239}$$

By rearranging the equation for ξ^{g} and substitution of the above relation for time derivative of gas saturation, the following equation is achieved:

$$\xi^{g} = \frac{\partial S^{w}}{\partial t}\left(\frac{R_s^{w}\phi}{B^{w}} - \frac{\phi}{B^{g}}\right) + \frac{\partial S^{o}}{\partial t}\left(\frac{R_s^{o}\phi}{B^{o}} - \frac{\phi}{B^{g}}\right) + \left(\frac{S^{g}}{B^{g}}\frac{\partial\phi}{\partial P^{o}} - \frac{S^{g}\phi}{(B^{g})^2}\frac{\partial B^{g}}{\partial P^{o}} + \frac{R_s^{w}S^{w}}{B^{w}}\frac{\partial\phi}{\partial P^{o}} - \frac{R_s^{w}S^{w}\phi}{(B^{w})^2}\frac{\partial B^{w}}{\partial P^{o}} + \frac{S^{w}\phi}{B^{w}}\frac{\partial R_s^{w}}{\partial P^{o}} + \frac{R_s^{o}S^{o}}{B^{o}}\frac{\partial\phi}{\partial P^{o}} - \frac{R_s^{o}S^{o}\phi}{(B^{o})^2}\frac{\partial B^{o}}{\partial P^{o}} + \frac{S^{o}\phi}{B^{o}}\frac{\partial R_s^{o}}{\partial P^{o}}\right)\frac{\partial P^{o}}{\partial t} \quad \text{Eq. 240}$$

By combining the derived relations for the parameters ξ^{w}, ξ^{o} and ξ^{g}, the following equation is obtained:

$$(B^{w} - R_s^{w} B^{g})\xi^{w} + (B^{o} - R_s^{o} B^{g})\xi^{o} + B^{g}\xi^{g} = \left[\frac{\partial \phi}{\partial P^{o}} + \left(\frac{B^{g} S^{w} \phi}{B^{w}} \frac{\partial R_s^{w}}{\partial P^{o}} - \frac{S^{w} \phi}{B^{w}} \frac{\partial B^{w}}{\partial P^{o}}\right) + \left(\frac{B^{g} S^{o} \phi}{B^{o}} \frac{\partial R_s^{o}}{\partial P^{o}} - \frac{S^{o} \phi}{B^{o}} \frac{\partial B^{o}}{\partial P^{o}}\right) + \left(-\frac{S^{g} \phi}{B^{g}} \frac{\partial B^{g}}{\partial P^{o}}\right)\right] \frac{\partial P^{o}}{\partial t} \quad \text{Eq. 241}$$

The above equation can be rearranged as follows:

$$(B^{w} - R_s^{w} B^{g})\xi^{w} + (B^{o} - R_s^{o} B^{g})\xi^{o} + B^{g}\xi^{g} = \left[\frac{\partial \phi}{\partial P^{o}} + S^{w} \phi \left(\frac{B^{g}}{B^{w}} \frac{\partial R_s^{w}}{\partial P^{o}} - \frac{1}{B^{w}} \frac{\partial B^{w}}{\partial P^{o}}\right) + S^{o} \phi \left(\frac{B^{g}}{B^{o}} \frac{\partial R_s^{o}}{\partial P^{o}} - \frac{1}{B^{o}} \frac{\partial B^{o}}{\partial P^{o}}\right) + S^{g} \phi \left(-\frac{1}{B^{g}} \frac{\partial B^{g}}{\partial P^{o}}\right)\right] \frac{\partial P^{o}}{\partial t} \quad \text{Eq. 242}$$

Using the definitions given in the fourth chapter for oil, water, gas and rock compressibility, the final pressure partial differential equation is achieved as follows:

$$(B^{w} - R_s^{w} B^{g})\xi^{w} + (B^{o} - R_s^{o} B^{g})\xi^{o} + B^{g}\xi^{g} = \phi[C^{r} + S^{w} C^{w} + S^{o} C^{o} + S^{g} C^{g}] \frac{\partial P^{o}}{\partial t} \quad \text{Eq. 243}$$

Appendix C Iterative Solution of Systems of Linear Equations

After the discretization of the governing equations of motion by finite volume method, the pressure at the center of finite volume zones can be calculated by numerical solution of the following nonsingular linear system of equations:

$$\boldsymbol{\mathcal{A}p} = \boldsymbol{b} \qquad \text{Eq. 244}$$

where $\boldsymbol{\mathcal{A}}$ is the coefficient matrix, $\boldsymbol{p}$ is unknown pressure vector and $\boldsymbol{b}$ is constant vector. The resulting system of equations can be solved either by direct or iterative methods. Although utilization of direct methods is practical in solving the system of equations with small sizes, it is cumbersome to utilize these methods in solving problems with large number of finite volume zones. This is due to the fact that direct methods demand excessive amount of memory and computational effort when the size of the system of equations is large which is usually the case in three-dimensional problems. Therefore, to solve the problems with large number of finite volume zones, it is more efficient to apply iterative methods. The simplest iterative method for the solution of the final system of equations is Jacoby method. In order to formulate the Jacoby method, the coefficient matrix $\boldsymbol{\mathcal{A}}$ is decomposed into the strictly lower triangular matrix $\boldsymbol{\mathcal{L}}$, the diagonal matrix $\boldsymbol{\mathcal{D}}$ with a nonzero determinant and the strictly upper triangular matrix $\boldsymbol{\mathcal{U}}$ as follows:

$$(\boldsymbol{\mathcal{L}} + \boldsymbol{\mathcal{D}} + \boldsymbol{\mathcal{U}})\boldsymbol{p} = \boldsymbol{b} \qquad \text{Eq. 245}$$

By rearranging the above equation, the iterative procedure to approximate the unknown vector $\boldsymbol{p}$ is achieved as follows:

$$\boldsymbol{\mathcal{D}p}^{\mathfrak{n}+1} = \boldsymbol{b} - (\boldsymbol{\mathcal{L}} + \boldsymbol{\mathcal{U}})\boldsymbol{p}^{\mathfrak{n}} \qquad \text{Eq. 246}$$

$$\boldsymbol{p}^{\mathfrak{n}+1} = \boldsymbol{\mathcal{D}}^{-1}[\boldsymbol{b} - \boldsymbol{\mathcal{L}p}^{\mathfrak{n}} - \boldsymbol{\mathcal{U}p}^{\mathfrak{n}}] \qquad \text{Eq. 247}$$

where $\mathfrak{n}$ represents the iteration number and the Jacobi matrix is defined as follows:

$$\boldsymbol{\mathcal{J}} = \boldsymbol{\mathcal{D}}^{-1}(\boldsymbol{\mathcal{L}} + \boldsymbol{\mathcal{U}}) \qquad \text{Eq. 248}$$

The Jacoby method can also be written in the following indexical form:

$$p_i^{n+1} = \frac{1}{a_{ii}}\left[b_i - \sum_{j=1}^{m} a_{ij} p_j^{n}\right] \quad \text{Eq. 249}$$

where m represents the number of finite volume zones. In order to utilize the updated values of the unknowns obtained in the most recent iteration to accelerate the convergence of solution, the Jacoby method can be modified as follows:

$$\boldsymbol{p}^{n+1} = \boldsymbol{\mathcal{D}}^{-1}[\boldsymbol{b} - \boldsymbol{\mathcal{L}}\boldsymbol{p}^{n+1} - \boldsymbol{\mathcal{U}}\boldsymbol{p}^{n}] \quad \text{Eq. 250}$$

$$p_i^{n+1} = \frac{1}{a_{ii}}\left[b_i - \sum_{j=1}^{i-1} a_{ij} p_j^{n+1} - \sum_{j=i+1}^{m} a_{ij} p_j^{n}\right] \quad \text{Eq. 251}$$

The iterative method represented by the above equations is called Gauss-Seidel method. One of the widely-used iterative methods in solving large-sized system of equations is successive over-relaxation (SOR) method. In order to formulate the SOR method, the discretized system of equations is written as (Young, 2014)

$$\omega(\boldsymbol{\mathcal{L}} + \boldsymbol{\mathcal{D}} + \boldsymbol{\mathcal{U}})\boldsymbol{p} = \omega\boldsymbol{b} \quad \text{Eq. 252}$$

where ω is a scalar parameter called over-relaxation parameter. Rearranging the above equation leads to the following equation:

$$(\omega\boldsymbol{\mathcal{L}} + \omega\boldsymbol{\mathcal{D}} + \omega\boldsymbol{\mathcal{U}} + \boldsymbol{\mathcal{D}} - \boldsymbol{\mathcal{D}})\boldsymbol{p} = \omega\boldsymbol{b} \quad \text{Eq. 253}$$

Consequently, the unknown vector $\boldsymbol{p}$ can be iteratively approximated using the successive over-relaxation method represented by the following relation:

$$(\omega\boldsymbol{\mathcal{L}} + \boldsymbol{\mathcal{D}})\boldsymbol{p}^{n+1} = \omega\boldsymbol{b} - [\boldsymbol{\mathcal{D}}(\omega - 1) + \omega\boldsymbol{\mathcal{U}}]\boldsymbol{p}^{n} \quad \text{Eq. 254}$$

The above relation is equivalent to the following equations which are appropriate for computer programming:

$$\boldsymbol{p}^{n+1} = \omega\boldsymbol{\mathcal{D}}^{-1}[\boldsymbol{b} - \boldsymbol{\mathcal{L}}\boldsymbol{p}^{n+1} - \boldsymbol{\mathcal{U}}\boldsymbol{p}^{n}] + (1 - \omega)\boldsymbol{p}^{n} \quad \text{Eq. 255}$$

$$p_i^{n+1} = \frac{\omega}{a_{ii}}\left[b_i - \sum_{j=1}^{i-1} a_{ij} p_j^{n+1} - \sum_{j=i+1}^{m} a_{ij} p_j^{n}\right] + (1 - \omega)p_i^{n} \quad \text{Eq. 256}$$

The above equation is iteratively solved until the difference between the solutions of two successive iterations satisfies the convergence criteria defined as follows:

$$\delta_i^{\pi} = p_i^{\pi+1} - p_i^{\pi} \quad \text{Eq. 257}$$

$$\Delta^{\pi} = |max_{i=1}^{m}(\delta_i)| < \tau \quad \text{Eq. 258}$$

Where δ_i^{π} denotes the pressure difference vector in time step π, Δ^{π} represents the norm of the pressure difference vector at time step π and τ is the convergence tolerance. It should also be mentioned that the over-relaxation parameter should be in the range $\omega \in (0,2)$ to have a convergent iterative solution. If the over-relaxation is assumed to be equal to one, it is simplified into Gauss-Seidel method. In order to have an efficient SOR method, the over-relaxation parameter should be optimally chosen. In this regard, if the Eigen values of Jacobi matrix are real and lower than one, an optimal value can be theoretically found for the over-relaxation parameter as follows (Young, 2014):

$$\omega_{opt} = \frac{2}{1 + \sqrt{1 - \rho^2}} \quad \text{Eq. 259}$$

where ρ is the spectral radius, i.e. the maximum Eigen value, of the Jacobi matrix. The parameter ρ can be approximated during each iteration as follows:

$$\Psi^{\pi+1} = \frac{\Delta^{\pi+1}}{\Delta^{\pi}} \quad \text{Eq. 260}$$

$$|\Psi^{\pi+1} - \Psi^{\pi}| < \varepsilon \rightarrow \bar{\Psi} = \Psi^{\pi+1} \quad \text{Eq. 261}$$

$$\rho \approx \frac{\bar{\Psi} + \omega - 1}{\omega\sqrt{\bar{\Psi}}} \quad \text{Eq. 262}$$

where the parameter ε represents the tolerance for over-relaxation parameter updating. Finally, the parameters τ and ε should be reasonably chosen to achieve fast convergence and economical numerical solution.

Appendix D Object-Oriented C++ Code for Theoretical Solution of One-Dimensional Incompressible Two-Phase Fluid Flow in Porous Media by Buckley-Leverett Method

An object-oriented C++ code was developed to implement the Buckley-Leverett solution for incompressible two-phase flow through porous media. The C++ code was used to generate analytical results needed for the verification of FVBOS. In the following, the source code of this program is reflected.

```
//*****************************************************
//Main function
//*****************************************************
#pragma once
#include"Input.h"
#include"Analysis.h"
#include"Output.h"

using namespace std;

int main()
{
	int iTS;
	double totTime, curTime, delTime, tsNum;
	ofstream outfile;
	outfile.open("outfile.txt");
	Input FlowInput;
	Analysis FlowAnalysis(FlowInput);
	Output FlowOutput;
	totTime = FlowInput.TotalTime();
	tsNum = FlowInput.TimeStepNum();
	delTime = totTime / tsNum;
	curTime = 0;
	FlowAnalysis.OilRelPermOutFile();
	FlowAnalysis.WatRelPermOutFile();
	for (iTS = 1; iTS <= tsNum; iTS++)
	{
		curTime = curTime + delTime;
		if (curTime > totTime)
			curTime = totTime;
		cout << "Time Step: " << setw(6) << iTS << "      Current Time: ";
		cout << setw(10) << setprecision(4) << curTime << endl;
		FlowAnalysis.SatProfCalc(FlowInput, curTime);     //Saturation Profile
		FlowAnalysis.PrsProfCalc(FlowInput, curTime);     //Pressure Profile
		//Output Result
		FlowOutput.AnalysisOutput(FlowAnalysis, outfile, curTime, delTime, iTS);
	}
```

```
	cout << endl << endl;
	cout << "================================================" << endl;
	cout << "        Buckley-Leverett Solution is Done!      " << endl;
	cout << "================================================" << endl;
	cin.get();
	return 0;
}

//*******************************************************
//Header file for class Analysis
//*******************************************************
#pragma once
#include <stdio.h>
#include <iostream>
#include <fstream>
#include <tchar.h>
#include <math.h>
#include <stdlib.h>
#include "Input.h"
#include <iomanip>

using namespace std;

class Analysis
{
private:
	double* PrsOil;
	double* PrsWat;
	double* SatOil;
	double* SatWat;
	double* XCoord;
	double swc, sor, krom, krwm, no, nw;
	double soi, swi, poi;
	double swMax, dsW;
	int capprsCh;
	int sDatNo;

public:
	Analysis(Input&);
	~Analysis();
	double RelPermOil(double);
	double RelPermWat(double);
	double DKrOilDsw(double);
	double DKrWatDsw(double);
	double CapPres(double);
	double DCapPresDsw(double);
	double D2CapPresDsw2(double);
	double WatCut(Input&, double, double);
	double DWatCutDSW(Input&, double, double);
	void SatProfCalc(Input&, double);
	void PrsProfCalc(Input&, double);
	double XCoordSat(int);
	double WatSat(int);
	double OilSat(int);
	double WatPrs(int);
	double OilPrs(int);
	int SatDataNum();
	void OilRelPermOutFile();
```

```
        void WatRelPermOutFile();
};

//*******************************************************
//Header file for class Input
//*******************************************************
#pragma once
#include <stdio.h>
#include <iostream>
#include <fstream>
#include <tchar.h>
#include <math.h>
#include <stdlib.h>

using namespace std;

class Input
{
private:
        int DelxNum;
        double CrsArea;
        double AbsPerm;
        double MouOil;
        double MouWat;
        double RhoOil;
        double RhoWat;
        double GrvAcel;
        double SlpAngl;
        double TotQ;
        double TotTim;
        double Lengt;
        double Poros;
        double TStpNum;
        double IniPrsOil;
        double IniSatOil;
        ifstream infile;

public:
        Input();
        ~Input();
        double CrosSectArea();
        double ResLength();
        double AbslPermablt();
        double ViscOil();
        double ViscWat();
        double DensOil();
        double DensWat();
        double GravtAcel();
        double SlopAngle();
        double TotFlowRate();
        double TotalTime();
        double TimeStepNum();
        double ResvLength();
        double Porosity();
        int LengtDivNum();
        double InitialPressOil();
        double InitialSatOil();
};
```

```
//*****************************************************
//Header file for class Output
//*****************************************************
#pragma once
#include <stdio.h>
#include <iostream>
#include <fstream>
#include <tchar.h>
#include <math.h>
#include <stdlib.h>
#include <iomanip>
#include "Analysis.h"

using namespace std;

class Output
{
private:
	ifstream outputcontrol;
	int outpTSCntr;
	int timeOutUnit;
	int tsNumOut;
	double* outTime;
public:
	Output();
	~Output();
	void AnalysisOutput(Analysis&, ofstream&, double, double, int);
	void PrintOutput(Analysis&, ofstream&);
};

//*****************************************************
//Source code of class Analysis
//*****************************************************
#include "Analysis.h"

Analysis::Analysis(Input& InputObj)
{
	int i;
	int n;
	int m;
	ifstream relperminfile;
	relperminfile.open("RelPermInfile.txt");
	ifstream capresinfile;
	capresinfile.open("CaPresInfile.txt");
	relperminfile >> swc >> sor >> krwm >> krom >> nw >> no;
	capresinfile >> capprsCh;
	n = InputObj.LengtDivNum();
	soi = InputObj.InitialSatOil();
	swi = 1 - soi;
	poi = InputObj.InitialPressOil();
	swMax = 1 - sor;
	dsW = 0.01;
	m = (swMax - swc) / dsW;
	if (m > n)
		n = m;
	sDatNo = n;
	PrsOil = new double[n];
	PrsWat = new double[n];
```

```
	SatOil = new double[n];
	SatWat = new double[n];
	XCoord = new double[n];
	for (i = 0; i < n; i++)
	{
		PrsOil[i] = poi;
		PrsWat[i] = poi;
		SatOil[i] = soi;
		SatWat[i] = swi;
		XCoord[i] = 0;
	}
}

Analysis::~Analysis()
{
	delete[] PrsOil;
	delete[] PrsWat;
	delete[] SatOil;
	delete[] SatWat;
}

double
Analysis::RelPermOil(double sw)
{
	double kro, temp;
	temp = (1 - sw - sor) / (1 - swc - sor);
	temp = pow(temp, no);
	kro = krom * temp;
	return kro;
}

double
Analysis::RelPermWat(double sw)
{
	double krw, temp;
	temp = (sw - swc) / (1 - swc - sor);
	temp = pow(temp, nw);
	krw = krwm * temp;
	return krw;
}

double
Analysis::DKrOilDsw(double sw)
{
	double DkroDsw, temp;
	temp = (1 - sw - sor) / (1 - swc - sor);
	temp = pow(temp, no - 1);
	DkroDsw = -temp * krom*no / (1 - swc - sor);
	return DkroDsw;
}

double
Analysis::DKrWatDsw(double sw)
{
	double DkrwDsw, temp;
	temp = (sw - swc) / (1 - swc - sor);
	temp = pow(temp, nw - 1);
	DkrwDsw = temp * krwm*nw / (1 - swc - sor);
```

```
	return DkrwDsw;
}

double
Analysis::CapPres(double sw)
{
	double Pc;
	if (capprsCh == 0)
		Pc = 0;
	return Pc;
}

double
Analysis::DCapPresDsw(double sw)
{
	double DPcDx;
	if (capprsCh == 0)
		DPcDx=0;
	return DPcDx;
}

double
Analysis::D2CapPresDsw2(double sw)
{
	double D2PcDx2;
	if (capprsCh == 0)
		D2PcDx2 = 0;
	return D2PcDx2;
}

double
Analysis::WatCut(Input& InputObj, double sw, double dswdx)
{
	double piNum = 3.14159265359;
	double fWat;
	double muOil, muWat, krOil, krWat, rhoWat, rhoOil;
	double gravAcel, resCA, totQ, absK, slpAngl;
	double DpcDx;
	muOil = InputObj.ViscOil();
	muWat = InputObj.ViscWat();
	krOil = this->RelPermOil(sw);
	krWat = this->RelPermWat(sw);
	rhoOil = InputObj.DensOil();
	rhoWat = InputObj.DensWat();
	gravAcel = InputObj.GravtAcel();
	resCA = InputObj.CrosSectArea();
	totQ = InputObj.TotFlowRate();
	absK = InputObj.AbslPermablt();
	slpAngl = InputObj.SlopAngle();
	DpcDx = this->DCapPresDsw(sw);    //Caplary pressure effects
	DpcDx = DpcDx*dswdx;              //Caplary pressure effects
	slpAngl = (slpAngl* piNum) / 180;
	fWat = DpcDx - (rhoWat - rhoOil)*gravAcel*sin(slpAngl);
	fWat = 1 + fWat * resCA*absK*krOil / (muOil*totQ);
	fWat = fWat / (1 + muWat * krOil / (muOil*krWat));
	return fWat;
}
```

```
double
Analysis::DWatCutDSW(Input& InputObj, double sw, double dswdx)
{
	double denom, nemer;
	double piNum = 3.14159265359;
	double DfwDsw;
	double muOil, muWat, krOil, krWat, rhoWat, rhoOil;
	double gravAcel, resCA, totQ, absK, slpAngl;
	double DpcDx, D2pcDsw2;
	double DkrWatDsw, DkrOilDsw;
	double temp1, temp2;
	muOil = InputObj.ViscOil();
	muWat = InputObj.ViscWat();
	krOil = this->RelPermOil(sw);
	krWat = this->RelPermWat(sw);
	rhoOil = InputObj.DensOil();
	rhoWat = InputObj.DensWat();
	gravAcel = InputObj.GravtAcel();
	resCA = InputObj.CrosSectArea();
	totQ = InputObj.TotFlowRate();
	absK = InputObj.AbslPermablt();
	slpAngl = InputObj.SlopAngle();
	DpcDx = this->DCapPresDsw(sw);		//Capillary pressure effects
	DpcDx = DpcDx * dswdx;			//Capillary pressure effects
	D2pcDsw2 = this->D2CapPresDsw2(sw);	//Capillary pressure effects
	slpAngl = (slpAngl* piNum) / 180;
	nemer = DpcDx - (rhoWat - rhoOil)*gravAcel*sin(slpAngl);
	nemer = 1 + nemer * resCA*absK*krOil / (muOil*totQ);
	denom = 1 + muWat * krOil / (muOil*krWat);
	DkrWatDsw = this->DKrWatDsw(sw);
	DkrOilDsw = this->DKrOilDsw(sw);
	temp1 = resCA * absK / (muOil*totQ);
	temp1 = temp1* DkrOilDsw * (DpcDx - (rhoWat - rhoOil)*gravAcel*sin(slpAngl));
	temp2 = (resCA*absK*krOil / muOil * totQ)*D2pcDsw2*dswdx;
	temp1 = (temp1 + temp2)*denom;
	temp2 = (muWat / muOil) * (DkrOilDsw*krWat - DkrWatDsw * krOil) / (pow(krWat,
2));
	temp2 = temp2 * nemer;
	DfwDsw = (temp1 - temp2) / (pow(denom, 2));
	return DfwDsw;
}

void
Analysis::SatProfCalc(Input& InputObj, double time)
{
	int i;
	double sW, sO, Qt, phi, A, X, X0, delX;
	double DfDsw;
	double DswDx;
	double cumWatCont, totWatCont;
	double length;
	length = InputObj.ResvLength();
	Qt = InputObj.TotFlowRate();
	phi = InputObj.Porosity();
	A = InputObj.CrosSectArea();
	totWatCont = Qt * time;
	X = 0;
	X0 = 0;
```

```
        sW = swMax;
        sO = 1 - sW;
        i = 0;
        cumWatCont = 0;
        while ((sW > swc && cumWatCont < totWatCont) && X <= length)
        {
                if (capprsCh == 0)
                        DswDx=0;
                DfDsw = this->DWatCutDSW(InputObj, sW, DswDx);
                if (i == 0)
                        X = 0;
                if (i > 0)
                        X = DfDsw * Qt*time / (phi*A);
                delX = X - X0;
                if (X <= length)
                {
                        XCoord[i] = X;
                        SatWat[i] = sW;
                        SatOil[i] = sO;
                }
                X0 = X;
                cumWatCont = cumWatCont + delX * A*phi*(sW - swc);
                sW = sW - dsW;
                sO = 1 - sW;
                i++;
        }
        sDatNo = i + 3;
        XCoord[sDatNo - 3] = XCoord[sDatNo - 4];
        SatWat[sDatNo - 3] = swi;
        SatOil[sDatNo - 3] = soi;
        XCoord[sDatNo - 2] = length;
        SatWat[sDatNo - 2] = swi;
        SatOil[sDatNo - 2] = soi;
        XCoord[sDatNo-1] = length;
        SatWat[sDatNo-1] = 0;
        SatOil[sDatNo-1] = 0;

}

int
Analysis::SatDataNum()
{
        return sDatNo;
}

double
Analysis::WatSat(int datno)
{
        int i;
        double watS;
        i = datno - 1;
        watS = SatWat[i];
        return watS;
}

double
Analysis::OilSat(int datno)
{
```

```
	int i;
	double oilS;
	i = datno - 1;
	oilS = SatOil[i];
	return oilS;
}

double
Analysis::WatPrs(int datno)
{
	int i;
	double watP;
	i = datno - 1;
	watP = PrsWat[i];
	return watP;
}

double
Analysis::OilPrs(int datno)
{
	int i;
	double oilP;
	i = datno - 1;
	oilP = PrsOil[i];
	return oilP;
}

double
Analysis::XCoordSat(int datno)
{
	int i;
	double x;
	i = datno - 1;
	x = XCoord[i];
	return x;
}

void
Analysis::WatRelPermOutFile()
{
	double delSW;
	double maxSW;
	double krw;
	ofstream watkroutfile;
	watkroutfile.open("WatKrOutfile.txt");
	watkroutfile.setf(ios::showpoint);
	watkroutfile.setf(ios::fixed, ios::floatfield);
	delSW = 0;
	krw = 0;
	watkroutfile << "   S_Wat   " << "   Kr_Wat   " << endl;
	watkroutfile << setw(10) << setprecision(7) << delSW << "   ";
	watkroutfile << setw(10) << setprecision(7) << krw << endl;
	delSW = swc;
	maxSW = 1 - sor;
	while (delSW <= maxSW)
	{
		krw = this->RelPermWat(delSW);
		watkroutfile << setw(10) << setprecision(7) << delSW<< "   ";
```

```
                watkroutfile << setw(10) << setprecision(7) << krw << endl;
                delSW = delSW + 0.001;
        }
}

void
Analysis::OilRelPermOutFile()
{
        double delSO, delSW;
        double maxSO;
        double kro;
        ofstream oilkroutfile;
        oilkroutfile.open("OilKrOutfile.txt");
        oilkroutfile.setf(ios::showpoint);
        oilkroutfile.setf(ios::fixed, ios::floatfield);
        delSO = 0;
        kro = 0;
        oilkroutfile << "   S_Oil    " << "   Kr_Oil    " << endl;
        oilkroutfile << setw(10) << setprecision(7) << delSO << "    ";
        oilkroutfile << setw(10) << setprecision(7) << kro << endl;
        delSO = sor;
        delSW = 1 - delSO;
        maxSO = 1 - swc;
        while (delSO <= maxSO)
        {
                kro = this->RelPermOil(delSW);
                oilkroutfile << setw(10) << setprecision(7) << delSO << "    ";
                oilkroutfile << setw(10) << setprecision(7) << kro << endl;
                delSO = delSO + 0.001;
                delSW = 1 - delSO;
        }
}

//*******************************************************
//Source code of class Input
//*******************************************************
#include "Input.h"

Input::Input()
{
        infile.open("Infile.txt");
        infile >> TotTim >> TStpNum >> CrsArea >> Lengt >> SlpAngl >> DelxNum;
        infile >> GrvAcel >> TotQ;
        infile >> Poros >> AbsPerm;
        infile >> RhoWat >> RhoOil;
        infile >> MouWat >> MouOil;
        infile >> IniPrsOil >> IniSatOil;
}

Input::~Input()
{
        infile.close();
}

double
Input::CrosSectArea()
{
        return CrsArea;
```

```
}

double
Input::AbslPermablt()
{
	return AbsPerm;
}

double
Input::ViscOil()
{
	return MouOil;
}

double
Input::ViscWat()
{
	return MouWat;
}

double
Input::DensOil()
{
	return RhoOil;
}

double
Input::DensWat()
{
	return RhoWat;
}

double
Input::GravtAcel()
{
	return GrvAcel;
}

double
Input::SlopAngle()
{
	return SlpAngl;
}

double
Input::TotFlowRate()
{
	return TotQ;
}

double
Input::TotalTime()
{
	return TotTim;
}

double
Input::TimeStepNum()
```

```
{
	return TStpNum;
}

double
Input::ResvLength()
{
	return Lengt;
}

double
Input::Porosity()
{
	return Poros;
}

int
Input::LengtDivNum()
{
	return DelxNum;
}

double
Input::InitialPressOil()
{
	return IniPrsOil;
}

double
Input::InitialSatOil()
{
	return IniSatOil;
}

double
Input::ResLength()
{
	return Lengt;
}

//*****************************************************
//Source code of class Output
//*****************************************************
#include "Output.h"

Output::Output()
{
	int i;
	outputcontrol.open("OutputControl.txt");
	outputcontrol >> outpTSCntr >> timeOutUnit >> tsNumOut;
	outTime = new double[tsNumOut];
	for (i = 0; i < tsNumOut; i++)
		outputcontrol >> outTime[i];
}

Output::~Output()
{
	outputcontrol.close();
```

```
	delete[] outTime;
}

void
Output::AnalysisOutput(Analysis& AnalObj, ofstream& file, double t, double delt, int
tsi)
{
	file.setf(ios::showpoint);
	file.setf(ios::fixed, ios::floatfield);
	int i;
	int tsiTarget1, tsiTarget2;
	double tUnit, deltUnit;
	tsiTarget1 = 0;
	tsiTarget2 = 0;
	if (timeOutUnit == 0)
	{
		tUnit = t;		//time in second
		deltUnit = delt;
	}
	if (timeOutUnit == 1)
	{
		tUnit = t / 60;		//time in minutes
		deltUnit = delt / 60;
	}
	if (timeOutUnit == 2)
	{
		tUnit = t / 3600;	//time in hours
		deltUnit = delt / 3600;
	}
	if (timeOutUnit == 3)
	{
		tUnit = t / 86400;	//time in days
		deltUnit = delt / 86400;
	}
	if (outpTSCntr == 0)
	{
		file << "time: " << setw(5) << setprecision(3) << tUnit << endl;
		file <<
"*****************************************************************" << endl;
		file <<
"*****************************************************************" << endl;
		this->PrintOutput(AnalObj, file);
	}

	if (outpTSCntr == 1)
	{
		for (i = 0; i < tsNumOut; i++)
		{
			tsiTarget1 = outTime[i] / deltUnit;
			tsiTarget2 = tsiTarget1 + 1;
			if (tsi == tsiTarget1 || tsi == tsiTarget2)
			{
				file << "time: " << setw(15) << setprecision(7) << tUnit
<< endl;
				file <<
"*****************************************************************" << endl;
				file <<
"*****************************************************************" << endl;
```

```
                        this->PrintOutput(AnalObj, file);
                    }
                }
            }
}

void
Output::PrintOutput(Analysis& AnalObj, ofstream& file)
{
        int i;
        double stNo, x, sw, so;
        stNo = AnalObj.SatDataNum();
        file << "X: " << endl;
        for (i = 1; i <= stNo; i++)
        {
                x = AnalObj.XCoordSat(i);
                file << "    " << setw(10) << setprecision(6) << x;
        }
        file << endl;
        file << "*************************************************************************"
<< endl;
        file << "SW: " << endl;
        for (i = 1; i <= stNo; i++)
        {
                sw = AnalObj.WatSat(i);
                file << "    " << setw(10) << setprecision(6) << sw;
        }
        file << endl;
        file << "*************************************************************************"
<< endl;
        file << "SO: " << endl;
        for (i = 1; i <= stNo; i++)
        {
                so = AnalObj.OilSat(i);
                file << "    " << setw(10) << setprecision(6) << so;
        }
        file << endl;
        file << "*************************************************************************"
<< endl;
}
```

Appendix E Black-Oil Correlations for Determination of Non-Aqueous Liquid and Gas Properties

The properties of non-aqueous liquid, e.g. oil, as well as gas utilized in the multi-phase fluid flow simulations by FVBOS and MPDES are determined with the aid of CMG-IMEX and based on the correlations gathered by McCain (1991). In the paper by McCain (1991), various black-oil correlations proposed by different authors were verified with a wide variety of data available for reservoir fluid properties. The correlations properly matching the data were proposed to be used for the purpose of reservoir simulation. Using the correlations proposed by McCain (1991), solution gas-oil ratio for pressures below bubble point pressure is defined by the following equation:

$$P^{o} = 18.2\left[\left(\frac{R_s^{o}}{\gamma^{g}}\right)^{0.83} 10^{0.00091T-0.0125\gamma_{API}^{o}} - 1.4\right] \quad \text{Eq. 263}$$

where γ^{g} is the specific gravity of gas, T represents temperature in degrees of Fahrenheit, and γ_{API}^{o} is specific gravity of stock tank oil in degrees of API. The volume factor of oil below bubble point pressure is defined by the following relation:

$$B^{o} = 0.9759 + 0.00012\left[R_s^{o}\left(\frac{\gamma^{g}}{\gamma^{o}}\right)^{0.5} + 1.25T\right]^{1.2} \quad \text{Eq. 264}$$

where γ^{o} is specific gravity of oil. Viscosity of oil is obtained using the following equation:

$$\mu^{o} = 10.715(R_s^{o} + 100)^{-0.515}\mu_d^{o\left[5.44(R_s^{o}+150)^{-0.338}\right]} \quad \text{Eq. 265}$$

where μ_d^{o} denotes the viscosity of dead oil which does not contain any dissolved gas. By assuming that the gas phase in the fractured porous media is dry, i.e. the gas does not condense into liquid, gas volume factor can be obtained by the following relation:

$$B^{g} = 0.282\frac{zT}{P} \quad \text{Eq. 266}$$

where B^{g} is gas volume factor defined as the ratio of the gas volume in cubic feet in reservoir pressure condition to gas volume in cubic feet in standard pressure condition.

In this equation, T is temperature in degrees of Kelvin, P is pressure, and z is gas compressibility factor. Finally, viscosity of gas is estimated using the following relations:

$$\mu^{g} = 0.0001A\exp\left(B\rho^{g^{C}}\right) \quad \text{Eq. 267}$$

$$A = \frac{(9.379 + 0.01607M_a)T^{1.5}}{209.2 + 19.26M_a + T} \quad \text{Eq. 268}$$

$$B = 3.448 + \frac{986.4}{T} + 0.01009M_a \quad \text{Eq. 269}$$

$$C = 2.447 - 0.2224B \quad \text{Eq. 270}$$

where ρ^{g} is gas density, T is temperature in degrees of Kelvin, and M_a is the apparent molecular weight of gas.

Appendix F Rock Joints Constitutive Parameters

The constitutive parameters of rock joints used in the coupled hydro-mechanical multi-phase fluid flow analyses by MPDES are assumed based on the values given in 3DEC manual as well as the correlations and experimental data reported by Bandis et al. (1983) for the deformation of rock joints under normal and shear loading for different rocks. In the paper by Bandis et al. (1983), the nonlinear relation between joint normal stress, σ_n, and joint normal displacement, δ_n, as well as joint shear stress, τ, and joint shear displacement, δ_t, were empirically formulated by defining nonlinear joint normal stiffness, K_n, and nonlinear joint shear stiffness, K_s, based on available compression and direct shear test data. In particular, for interlocked joints, the following relations for joint normal stress-normal deformation and joint normal stiffness were developed:

$$\sigma_n = \frac{K_{ni}\delta_{mn}\delta_n}{\delta_m - \delta_n} \quad \text{Eq. 271}$$

$$K_n = K_{ni}\left[1 - \frac{\sigma_n}{\delta_{mn}K_{ni} + \sigma_n}\right]^{-2} \quad \text{Eq. 272}$$

where δ_{mn} represents maximum joint closure and K_{ni} is joint stiffness at initial normal stress state. In this equation, maximum joint closure can be related to Joint Roughness Coefficient (*JRC*) and Joint Compressive Strength (*JCS*) as follows:

$$\delta_{mn} = A + B(JRC) + C\left(\frac{JCS}{e_0}\right)^D \quad \text{Eq. 273}$$

$$a_j = \frac{JRC}{5}\left(0.2\frac{\sigma_c}{JCS} - 0.1\right) \quad \text{Eq. 274}$$

In these equations, the coefficients *A*, *B*, *C* and *D* are determined by experimental tests, e_0 is initial aperture of the joint in mm under self-weight, and σ_c is the uniaxial compressive strength of the rock. The initial joint stiffness is empirically formulated as follows:

$$K_{ni} = -7.15 + 1.75(JRC) + 0.02\frac{JCS}{e_0} \quad \text{Eq. 275}$$

In addition, the normal stress-normal deformation as well as normal stiffness of dislocated joints are defined by the following empirical correlations:

$$log\sigma_n = p + q\delta_n \quad \text{Eq. 276}$$

$$K_n = \frac{q\sigma_n}{0.4343} \quad \text{Eq. 277}$$

In these equations, p and q are determined based on experimental data. The normal stiffness of dislocated joints can also be estimated based on the normal stiffness of interlocked joints as follows:

$$\frac{K_n^{int}}{K_n^{dis}} \simeq 2 + \frac{(JCS)(JRC)\sigma_n}{2500} \quad \text{Eq. 278}$$

where K_n^{int} and K_n^{dis} represent normal stiffness of interlocked and dislocated joints, respectively. Finally, the shear stress-shear deformation relation as well as joint shear stiffness are empirically defined as:

$$\tau = \frac{K_{si}\delta_{tm}\delta_t}{\delta_{tm} - \delta_t} \quad \text{Eq. 279}$$

$$K_s = K_j(\sigma_n)^{n_j}\left[1 - \frac{R_f\tau}{\tau_p}\right]^2 \quad \text{Eq. 280}$$

where K_j is the stiffness number, n_j is stiffness exponent, $R_f = \tau/\tau_{ult}$ is failure ratio, τ_{ult} is ultimate joint shear strength, and τ_p is peak joint shear strength.

Using the data given for moderately weathered siltstone in the paper by Bandis et al. (1983) and assuming interlocked joints, i.e. $JCS = 67\ MPa, K_{ni} = 11.2\ MPa/mm, \delta_{mn} = 0.28\ mm\ and\ \sigma_n = 25\ MPa$, normal stiffness of the joints is approximated as $K_n \cong 1\ MPa/mm$. Finally, based on the data given for moderately weathered slate in the paper by Bandis et al. (1983), the shear stiffness of the joints is approximated as $K_s \cong 1\ MPa/mm$ assuming the shear stiffness is represented by the secant peak shear stiffness.

Appendix G 3DEC Codes in MPDES

To implement the developed coupled hydro-mechanical multi-phase simulation approach in MPDES, 3DEC codes and fish functions were written to create the distinct element solid mechanical model and handle the pore pressure and fracture aperture exchange between FVBOS and 3DEC. In the following, the 3DEC codes are reflected.

```
;**************************************************************************
;FVBOS-3DEC Coupling
;**************************************************************************
;-------- -----Load 3DEC solid mechanics Model---------------------------
restore 3DECModel
;--------------Call FVBOS-3DEC pressure-aperture transfer functions-------
call PrsAprTransferFunctions.3dfis
;--------------Applying FVBOS proe pressure-------------------------------
;***Assign input parameters of PorePresAsgn fish function_Input***
set @numFVBOSZone = 4523  @disToler_FVBOS_3DEC_PrsMap = 0.1
@PorePresAsgn
;--------------Solid mechanics analysis by 3DEC---------------------------
set mech on flow off
;***Number of solid mechanics analysis type steps_Input***
cyc 2000
;--Outputing the calculated apertures by 3DEC in file to be used in FVBOS -
@ApertureOutput
;-------------quit 3DEC and return to FVBOS-----------------------------
Quit
```

```
; ************************************************************
; Fish function to transfer pressures from FVBOS to 3DEC
; ************************************************************
def PorePresAsgn
       nZn = numFVBOSZone
       nPr = 4
       distTol=disToler_FVBOS_3DEC_PrsMap
       pArray = get_array(nZn,nPr)
       sTemp  = get_array(1)
       inFile='PosPrsFVBOS.dat'
       stat = open( inFile, 0, 1 )            ;File for reading
       loop iZn(1,nZn)
              stat = read( sTemp,1)
              ;stat = read( sTemp,1,PosPrs)
              loop iPr(1,nPr)
                     pArray(iZn,iPr) = parse(sTemp(1),iPr)
              end_loop
       end_loop
       stat=close
       iFKn = knot_head
       loop while iFKn # 0
              fknXCrd = fk_x( iFKn )
              fknYCrd = fk_y( iFKn )
              fknZCrd = fk_z( iFKn )
              chkFKn=0
              sumFkD=0.0
              fknPrs=0.0
              loop iZn(1,nZn)
                     inXCrd=pArray(iZn,1)
                     inYCrd=pArray(iZn,2)
                     inZCrd=pArray(iZn,3)
                     inPres=pArray(iZn,4)
                     fknDist=(fknXCrd-inXCrd)^2+(fknYCrd-inYCrd)^2+(fknZCrd-inZCrd)^2
```

```
                fknDist=fknDist^0.5
                if fknDist < distTol
                        chkFKn = 1
                        sumFkD = sumFkD + 1/fknDist
                        fknPrs = fknPrs + inPres/fknDist
                end_if
        end_loop
        if chkFKn == 1
                fknPrs=fknPrs/sumFkD
        end_if
        if chkFKn == 0
                fknPrs=0
        end_if
        fk_pp( iFKn ) = fknPrs
        iFKn = fk_next( iFKn )
    end_loop
end


; ********************************************************************
; Fish function to write apertures calculated by 3DEC for FVBOS use
; ********************************************************************
def ApertureOutput
    outPosApr=get_array(1)
    outFile='PosAper3DEC.dat'
    stat = open( outFile, 1, 1 )
    iFP = flow_head
    loop while iFP # 0
        iFPV = fp_fpx(iFP)
        loop while iFPV # 0
            apr3DEC=fpx_aperture( iFPV )
            posVect=fpx_pos( iFPV,iFP )
            x3DECApr=xcomp( posVect )
```

```
                    y3DECApr=ycomp( posVect )
                    z3DECApr=zcomp( posVect )
                    outPosApr(1)=string(x3DECApr)+''+string(y3DECApr)+''+
                    string(z3DECApr)+''+string(apr3DEC)
                    stat = write(outPosApr, 1)
                    iFPV = fpx_next(iFPV)
             end_loop
             iFP = fp_next(iFP)
      end_loop
      stat=close
end


;*************************************************************************
;**3DEC initial model to be used for hydro-mechanical analyses by MPDES***
;***Problem: Simulation of coupled hydro-mechanical***********************
;***multi-phase fluid flow in porous media containing**********************
;***stochastically generated discrete fracture network*******************
;*************************************************************************
new
config fluid
;*************************************************************************
;***Creating solid mechanical geometry of the model***********************
;*************************************************************************
def creategeometry
  ;***Middle point of the model
  xmiddle=0.0
  ymiddle=0.0
  zmiddle=0.0
  ;***Size of the model
  xSize=10
  ySize=10
  zSize=5
```

```
  ;***Scale for extended boundary of model for DFN generation
  extboundescl=3
  ;***Injection id, DFN id and injection disc size
  injid=99999
  dfnid=100000
  injdiscsize=2
  ;***Discretization size
  dscrtsize=1
  ;***Boundary of the model
  x1=xmiddle-0.5*xSize
  x2=xmiddle+0.5*xSize
  y1=ymiddle-0.5*ySize
  y2=ymiddle+0.5*ySize
  z1=zmiddle-0.5*zSize
  z2=zmiddle+0.5*zSize
  ;***Extended boundary of the model for DFN generation
  extx1=xmiddle-xSize*extboundescl
  extx2=xmiddle+xSize*extboundescl
  exty1=ymiddle-ySize*extboundescl
  exty2=ymiddle+ySize*extboundescl
  extz1=zmiddle-zSize*extboundescl
  extz2=zmiddle+zSize*extboundescl
end
@creategeometry
;***Set tolerance
set atol 0.02
;***Create block
poly brick @x1 @x2 @y1 @y2 @z1 @z2
;*********************************************************************
;***DFN definition*****************************************************
;*********************************************************************
domain extent @extx1 @extx2 @exty1 @exty2 @extz1 @extz2
;***Stochatically generated dfn representing natural fractures
```

```
dfn template create name 'naturalfracturedfn'      &
                    id @dfnid                      &
                    size powerlaw 3 slimit 2 5     &
                    position uniform               &
                    orientation uniform
;***Add the disc where injection is applied
dfn addfracture dip 90 dipdir 0 id @injid           &
                position @xmiddle @ymiddle @zmiddle &
                size @injdiscsize
;***Generate discrete fracture network
dfn generate template name 'naturalfracturedfn' density 0.2
jset dfn @dfnid
jset dfn @injid
;************************************************************************
;***Model discretization*************************************************
;************************************************************************
gen edge @dscrtsize
;************************************************************************
;***Material properties of porous matrix, fractures and fluid************
;************************************************************************
def matpropset
  ;***Intact rock properties
  rockelmod = 1e9   ; Pa
  rocknu = 0.2
  rockrho = 2500.0  ;kg/m^3
  ;***Joint properties
  jointkn=1.e9
  jointks=1.e9
  jointcoh=0.0
  jointfric=20.0
  jointtens=0.0
  jap0=5.0e-5
  japmax = 10.0e-3
```

```
  ; fluid properties
  fluidblkmod= 0
  fluidrho= 1000.0
  fluidvisc=0
end
@matpropset
;***Assign rock props
prop mat 1 dens @rockrho ymod @rockelmod pratio @rocknu
;***Constant aperture for initial stress state
;***Active hydro-mechanical joints
prop jmat 1 jkn @jointkn jks @jointks
prop jmat 1 jfric @jointfric jcoh @jointcoh jten @jointtens
prop jmat 1 azero @jap0 ares @jap0 amax @jap0
;***Inactive hydro-mechanical joints and joints outside of the DFN
prop jmat 2 jkn @jointkn jks @jointks
prop jmat 2 jfric 40 jcoh 1e30 jten 1e30
prop jmat 2 azero @jap0 ares @jap0 amax @jap0
;***Hydro-mechanical properties of the joint where injection occurs
change dfn @injid jmat 1 2
;***Hydro-mechanical properties of natural fractures
change dfn @dfnid jmat 1 2
;***Fluid material properties
fluid bulk @fluidblkmod density @fluidrho viscosity @fluidvisc
;*********************************************************************
;***Assing insitu stress state*************************************
;*********************************************************************
def setinstrs
  depth = 1000.0  ; depth of model centre (m)
  gravaccel= 9.81 ; metric
  khmax=1.0       ; maximum ratio of horizontal to vertical stress
  khmin=0.5       ; minimum ratio of horizontal to vertical stress
  ;***Stresses at z = 0.  Compression is negative
  szz0 = -rockrho*depth*gravaccel
```

```
  sxx0 = khmax*szz0
  syy0 = khmin*szz0
  ;***fluid pressure at z = 0 (positive)
  pp0 = 200000
  ;***gradients (per m in positive z direction)
  szzgrd = rockrho*gravaccel
  syygrd = khmin*szzgrd
  sxxgrd = khmax*szzgrd
  ppgrd = -fluidrho*gravaccel
end
@setinstrs
;***In-situ stress
insitu stress @sxx0 @syy0 @szz0 0. 0. 0. &
              zgrad @sxxgrd @syygrd @szzgrd 0. 0. 0. nodisp
;***In-situ pore pressure
insitu pp @pp0 grad 0. 0. @ppgrd nodisp
;*********************************************************************
;***Assign bouundary conditions*************************************
;*********************************************************************
bou xvel 0.0 yvel 0.0 zvel 0.0  ran x @x1
bou xvel 0.0 yvel 0.0 zvel 0.0  ran x @x2
bou xvel 0.0 yvel 0.0 zvel 0.0  ran y @y1
bou xvel 0.0 yvel 0.0 zvel 0.0  ran y @y2
bou xvel 0.0 yvel 0.0 zvel 0.0  ran z @z1
bou xvel 0.0 yvel 0.0 zvel 0.0  ran z @z2
;*********************************************************************
;***Set Initial equilibrium state**********************************
;*********************************************************************
gravity 0 0 [-gravaccel]
set flow off mech on
fluid bulk 0
set small
cycle 2000
```

```
;*************************************************************************
;***Initialize the model for coupled hydro-mechanical analyses by MPDES***
;*************************************************************************
;***Reset joint apertures
def apreset
  local fp = flow_head
  loop while fp # 0
    local fpx = fp_fpx(fp)
    loop while fpx # 0
      fpx_apmech(fpx) = jap0
      fpx = fpx_next(fpx)
    end_loop
    fp = fp_next(fp)
  end_loop
end
@apreset
;***Reset joint displacements
reset disp jdisp
;***Reset time
set time 0
;***change joint material to allow for joint opening during hm analyses
prop jmat 1 amax @japmax
;*************************************************************************
;***Save the initial soild mechanical model*****************************
;*************************************************************************
save 3DECModel
;*************************************************************************
;***End******************************************************************
;*************************************************************************
```